

Internal deformation of salt bodies with large mechanical contrast: A case study of the Veendam salt Pillow, the Netherlands

Alexander S. F. Raith

Internal deformation of salt bodies with large mechanical contrast: A case study of the Veendam salt Pillow, the Netherlands

Von der Fakultät für Georessourcen und Materialtechnik der
Rheinisch -Westfälischen Technischen Hochschule Aachen
zur Erlangung des akademischen Grades eines

Doktors der Naturwissenschaften

genemigte Dissertation
vorgelegt von

M.Sc.
Alexander Sascha Frank Raith

aus Langenfeld

Berichter:
Univ.-Prof. Dr. Janos L. Urai
Prof. Dr. Christopher J. Spiers
Univ.-Prof. Dr. Christopher A.-L. Jackson

Tag der mündlichen Prüfung: 12 Juni 2017

Diese Dissertation ist auf der Internetseite der Hochschulbibliothek online verfügbar.

Acknowledgements

For the success of this work and the good memories of the last years working on it, I owe many thanks to a lot of friends, colleagues and family.

At first, I have to thank all colleagues and scientists that took the time to discuss my research, taught me valuable lessons and improved my publications with some very elaborate and constructive reviews.

The deepest thanks goes to Janos. I know that much of what I have achieved is based on your support, supervision and your tenacious ways to spur me on. But most off all, I like to thank you for all those discussions and arguments, when we were not sharing the same opinion. You always provided me with the freedom to argue for my ideas. From the beginning on you gave me the respect to let me convince you if my arguments were very good but never accepted anything less. I enjoyed our sparring, for I was always sure to get a fair and honest fight. I have the deepest respect for a professor that is still able after years of teaching to let himself be convinced in an argument with an overly motivated bachelor student. The same thanks goes to my other teachers, as Christoph Hilgers who believed in me from the beginning, promoted me and granted me with responsibilities that let me grow.

Manny thanks goes to my colleagues that fueled my work with a lot of discussions, but most of all, made the institute a great place to work and even stay long hours after work, developing other projects, talking and having fun. It is a great experience to work with friends! Simon, Max, Patrick, Ben, Sebastian, Michael, Susanne, Arne, Christoph, Frank and Moritz, thank you a lot. Special thanks to Werner Kraus who spend many hours with me in the dry lab covered in salt dust cutting cores and preparing samples.

However, behind all the work, there is much more to life, which brought me where I am today and hardly can be honored here. Yet I am afraid, many of them will never be reached by these words and my thanks would be best delivered in person. Nevertheless, deep thanks gose to my friends and family, most off all to Kira with her unflinching support and love.

At last, I want to thank Nedmag Industries that provided the funding for this PhD thesis, without their support this work would not have been possible. Even more thanks go to the great people at Nedmag for the many hours of discussions and shared knowledge. They provided me with the excellent motivation that my work is needed and highly appreciated.

Table of Contents

1. Introduction 5

1.1 Formation of Massive Evaporites Bodies 5

1.2 Concepts of salt tectonic through the centuries 6

1.3 Internal structure of evaporite bodies 11

1.4 Rheology of salt 12

1.5 About this work 15

1.6 References 16

2. Evolution of rheologically heterogeneous salt structures: a case study from the NE-Netherlands 23

2.1 Abstract 23

2.2 Introduction 24

2.3 Geological setting 27

2.4 Data and Methods 30

2.5 Results 32

2.6 Discussion 38

2.7 Conclusions 43

2.8 References 44

3. Interpretation of the ZIII-1b structure and content using acoustic impedance 49

3.1 Summary 49

3.2 Introduction 49

3.3 Methods and dataset 52

3.4 Results 55

3.5 Discussion 59

3.6 Conclusions 62

3.7 References 63

4. Handling and analysis of an extremely hygroscopic K-Mg salt core 73

4.1 The dry lab 73

4.2 Cutting the core pieces 75

4.3 Core photographs 76

4.4 Thin section and polished section preparation 76

5. Structure of K-Mg salt layers in the Zechstein III of the Veendam Pillow, NE Netherlands: development of a tectonic mélange during salt flow 79

5.1 Abstract 79
5.2 Introduction 79
5.3 Data & Methods 83
5.4 Results 89
5.5 Discussion 102
5.6 Conclusions 108
5.7 Acknowledgements 108
5.8 References 109
5.9 Appendix 113

6. Squeeze mining- induced stress changes in the faulted overburden of the Veendam salt Pillow 153

6.1 Summary 153
6.2 Method 153
6.3 FE model setup 154
6.4 Model Results 158
6.5 Faults in the overburden 160
6.6 Discussion 164
6.7 Conclusion 167
6.8 References 167

7. Finite element modeling of the deformation of ZIII-AC and ZIII K-Mg salts layers during pillow development 169

7.1 Summary 169
7.2 Introduction 169
7.3 The model 172
7.4 Results 181
7.5 Discussion 181
7.6 Conclusions 184
7.7 References 185

8. Outlook **195**

9. Zusammenfassung **199**

10. Summary **202**

Synopsis

The internal deformation of salt bodies is studied in three parts. In the first part seismic data is used to reconstruct the geologic history and visualize the internal structure of a mechanically stratified salt pillow. In the second part a drill core from the same salt pillow is analyzed in detail to understand the meter to microscale structure and deformation processes with an emphasis on potassium and magnesium salts. In the last part, numerical modelling, based on previous results, is used to analyze the conditions and processes leading to the observed structures.

1 Introduction

The Introduction gives a brief overview of our understanding of salt deformation today and in the past and a summary of salt rheology.

I SEISMIC INTERPRETATION

2 Evolution of rheologically heterogeneous salt structures: a case study from the NE-Netherlands (Journal Article)

In this chapter, the evolution of the Veendam and Slochteren salt pillows at the southern boundary of the Groningen High, northern Netherlands is studied with high-resolution 3D seismic and well data. The internal structure of the two salt pillows shows areas in which the K-Mg salt-rich ZIII 1b layer is much thicker than elsewhere, in combination with a complexly ruptured and folded ZIII Anhydrite - Carbonate stringer. Thickness maps of supra-salt sediments and well data are used to infer the initial depositional architecture of the K-Mg salts and their deformation history. Results suggest that faulting and the generation of depressions on the top Zechstein surface above a Rotliegend graben caused the local accumulation of bittern brines and precipitation of thick K-Mg salts. During the first phase of salt flow and withdrawal from the Veendam area, under the influence of differential loading by Buntsandstein sediments, the ZIII stringer was boudinaged while the lens of Mg salts remained relatively undeformed. This was followed by a convergence stage, when the K-Mg salt-rich layers were deformed within the inflating salt pillows. This deformation was strongly disharmonic and strongly influenced by folding of the underlying, ruptured ZIII stringer, leading to thickening and internal deformation of the K-Mg salt layers.

3 Interpretation of the ZIII-1b structure and content using acoustic impedance

This chapter presents the results of the reinterpretation of the internal structures of the Veendam Pillow based on acoustic impedance (AI) data focusing on the Zechstein III (ZIII) - 1b potassium

and magnesium (K-Mg) salt layer. The seismic inversion was performed in order to obtain calibrated acoustic impedance values whilst at the same time improving the temporal resolution compared to the reflectivity dataset. After seismic inversion, the structure of the Zechstein III- 1b subunit could be identified as a low acoustic impedance body. The unit's boundaries were interpreted by manually picking the threshold between low AI K-Mg salts and the higher AI halite layers. Elastic parameters were estimated of mineral mixtures typically found in the ZIII-1b subunit, such as carnallite with bischofite and kieserite and halite. Threshold values were based on these estimations, allowing identification of the most prospective intervals. In addition, tuning effects on AI values was taken into account in thin layers. This led to the definition of bodies within the ZIII – 1 b subunit that exhibit low and connected AI values, a strong indicator for the presence of bischofite. Results show that the interpretation of AI data refined the geometric model of the salt body's structure especially in areas where the original reflection data quality was weak. Layer thicknesses conducted from the interpretation correlate reasonably with thicknesses measured in wells. In absolute depth terms, depth values at top ZIII – 1b levels are around 45 m off. We suggest that areas of low AI values, in combination with an analysis of local deformation structures can be used, to identify the most prospective areas of high magnesium content

II CORE ANALYSIS

4 Handling and analysis of an extremely hygroscopic K-Mg salt core

In this chapter a short description of methods, techniques and facilities needed to safely handle extreme hydroscopic salts are given. The dry laboratory setup, core cutting, photography and thin section preparation are described in detail.

5 Structure of K-Mg salt layers in the Zechstein III of the Veendam Pillow, NE Netherlands: development of a tectonic mélange during salt flow (Journal Article)

In this chapter, we analyzed a unique Tr-9 carnallite- and bischofite- rich drill core from the Zechstein III-1b subunit in the Veendam Pillow in the Netherlands.

The slabbed core was analyzed by macroscale photography, bulk chemical methods, XRD and optical microscopy. Results show high strain in the weaker bischofite- and carnallite- rich layers, with associated dynamic recrystallization at very low differential stress, completely overprinting the original texture. Stronger layers formed by alternating beds of halite and carnallite show complex recumbent folding on different scales commonly interrupted by sub-horizontal shear zones with brittle deformation, veins and boudinage. We attribute this tectonic fragmentation to be associated with a softening of the complete ZIII-1b subunit during its deformation. The result is a tectonic mélange with cm - to

10 m size blocks with internal folds and boudinage. We infer that these structures and processes are common in deformed, rheologically strongly stratified evaporites.

III FINITE ELEMENT MODELING

6 Squeeze mining- induced stress changes in the faulted overburden of the Veendam salt Pillow

The content of this chapter is the quantification of stress changes in the faulted overburden of the Veendam Salt pillow, induced by squeeze mining in a salt cavern field, and the evaluation of those changes regarding the mechanical stability of the faulted overburden. Faults in the overburden were mapped in a 3D seismic dataset, and shown to be normal faults with N-S and NE-SW strikes. None of the faults can be shown to continue to the surface, in agreement with the absence of neotectonic activity in the area. A Finite Element model was used to calculate the stress changes in the Veendam Salt Pillow and its overburden, caused by squeeze mining. We built a model with radial symmetry, and let it develop a geologically stable in-situ stress field as a starting point for the squeeze mining simulations. Using reasonable values of the input geometry and the material properties, the model was ran until about 60 cm of subsidence in 50 years above a 2.4 km wide cavern field.

In most of the overburden, stress changes correspond to reduction of the shear stress and thus mechanically more stable conditions, in agreement with earlier simulations. In a limited volume of the overburden, shear stresses increase, but this increase is small. The calculated stress changes are therefore unlikely to lead to reactivation of the faults in the overburden.

7 Finite element modeling of the deformation of ZIII-AC and ZIII K-Mg salts layers during pillow development

In this chapter simplified 2D plain strain models containing the key components of the Veendam Pillow were performed to analyze the influence and behavior of hard and soft layers on the internal deformation. The results show that the pre-fractured stringer is folded and thrusted in the pillow center during the development of the pillow. Depending on the viscosity of the stringer, the shortening is either compensated by folding or thrusting. We supposed that the stress exponent of halite and stringer deformation are most likely not the same and we could therefore expect a strain dependency of the effective viscosity contrast. Under this conditions, strong strain-rate changes during the pillow evolution could produce different dominant wavelengths. Fold analysis can therefore be used to estimate the in situ rheology of stringers or if the in situ rheology of anhydrite and salt is well known, might be used to estimate the in situ strain rates. We concluded from the models that the folding of the ZIII-

AC observed in the Veendam pillow indicates an effective velocity contrast of about 100 between the stringer and the halite. Nevertheless, a much larger wavelength folding could have been produced by early slow deformation forming the large syncline in the NE of the Veendam Pillow. Both soft K-Mg salt layers and strong stringers influence the deformation and salt flow inside the salt pillow. Strain is accumulated in the soft layers leading to stronger salt flow near these layers and extensive deformation inside of them. Thus, if a soft layer is present near a stringer, it will experience more deformation. On the other hand, the structure of the soft K-Mg salt layers and the salt flow inside of them is strongly influenced by folding of a harder stringer. As a result, the soft K-Mg salts are withdrawn from areas above stringer anticlines to areas above stringer synclines.

1. Introduction

The research on evaporate bodies has been motivated by two major economical aspects that formed our perception on salt. One side is the salt mining industry, interested in the internal structure, stratigraphy, evaporation and metamorphic processes forming different paragenesis of evaporate minerals.

On the other side is the oil and gas producing industry. Many of the world´s great hydrocarbon provinces are located in salt basins (Gulf of Mexico, Persian Gulf, North Sea, Lower Congo Basin and Pricaspian Basin) (Hudec and Jackson 2007). Here, the evolution and shape of salt structures is of major interest due to their unique sealing and thermal properties and associated structures in the surrounding sediments forming great potential for hydrocarbon accumulation and affecting all aspects of the hydrocarbon system. The internal structure of salt bodies plays a secondary role, although it is partly of interest due to serious drilling issues caused by soft squeezing salts (Williamson et al. 1998) and overpressured floaters. These floaters, also called stringers, consist of carbonate and sulphate evaporates and can function as hydrocarbon reservoirs under special conditions. Nevertheless, this kind of reservoirs, like in the Ara salt in Oman, are rather exotic. The rising urgency to find a solution for long-term storage of highly radioactive waste yields even more motivation to understand the deformation and internal structure of salt bodies. In this case, the low permeability and unique self-sealing potential of salt bodies in tectonically quiet basins provides the potential for a save storage over the needed period.

Most of all, salt is a unique and easily deformable material that has a strong influence on the tectonic development where it is present. For all these reasons, we need a precise understanding of the rheology of all materials and their behavior during evaporation, diagenesis, metamorphism and deformation. Thus, the final goal is to be able to understand and predict the structure of evaporite bodies from micro to basin scale.

1.1 Formation of Massive Evaporites Bodies

Evaporites are defined as “rock originally precipitates from saturated surface or near-surface brines by hydrologies driven by solar evaporation” (Warren 2006). To form massive evaporite bodies several conditions have to be met (Warren 2006): (i) Arid to semi-arid climatic conditions and the right surface morphology and hydrology to provide large volumes of brine at or near the land surface. (ii) A sedimentary depression that is not filled by other sediments providing enough accommodation space. (iii) A preservative burial environment preventing dissolution. During the Earth history these conditions were met during several phases in restricted basins mostly around 30° latitude, where outflow of water by evaporation exceeds inflow (Hudec and Jackson 2007). The evaporation took place in

four tectonic settings: cratonic basins, synrift basins, postrift passive margins and continental collision zones and foreland basins (Hudec and Jackson 2007). During evaporation from sea water the rising concentration of the brine produces a predictable suite of primary evaporites (Usiglio 1849; Van't Hoff 1905; Borchert and Muir 1964; Carpenter and others 1978; McCaffrey et al. 1987) containing Na, Ca, Mg, K, Cl, SO_4 and CO_3 and less common B, Ba, Sr, Br and I (Warren 2006). The first mineral occurring in still mesohaline waters (twice the concentration as seawater) is $CaCO_3$, usually as aragonite. When a four to five times concentration is reached, gypsum starts to precipitate. Supersaline conditions are reached at 10 to 12 times concentration and halite begins to precipitate. If the brine reaches extremely high concentration of 70 to 90 times, bittern salts are formed. These bittern salts contain high amounts of potassium and magnesium and are commonly found as sylvite (KCl) and carnallite ($KMgCl_3*6H_2O$). Bischofite ($MgCl_2*6H_2O$) represents the endmember of evaporation and although a great amount of bischofite could be produced by full evaporation (30% vol. of the whole evaporite column)(Borchert and Muir 1964), it is very rare in most salt bodies. This can be explained by the extreme hot and dry conditions that have to be reached to completely evaporate the highly concentrated brine and the high solubility of bischofite leading to quick dissolution during a seawater refreshing event or in contact with ground water.

1.2 Concepts of salt tectonic through the centuries

"There is a theory which states that if ever anyone discovers exactly what the Universe is for and why it is here, it will instantly disappear and be replaced by something even more bizarre and inexplicable. There is another theory which states that this has already happened."

-Douglas Adams

Our understanding of salt tectonics today has a complex and exciting history of complementary and conflicting concepts. Although many concepts that are used today root back to very early theories and were developed ever since, the research history can be divided into three eras (Jackson 1995). First, the pioneering era starting in the mid of the 19th century, which developed towards the fluid era starting about 1933. The fluid era described salt and overburden as viscose fluids with no yield strength and dominated the scientific discussion for over 50 years. By the end of the 1980s, the idea that the overburden cannot be described as viscous fluid but is definitely a brittle material, won wide recognition marking the beginning of the brittle era and modern salt tectonics.

The pioneering era originated in the first scientific description of a salt dome in 1856 by Ville.

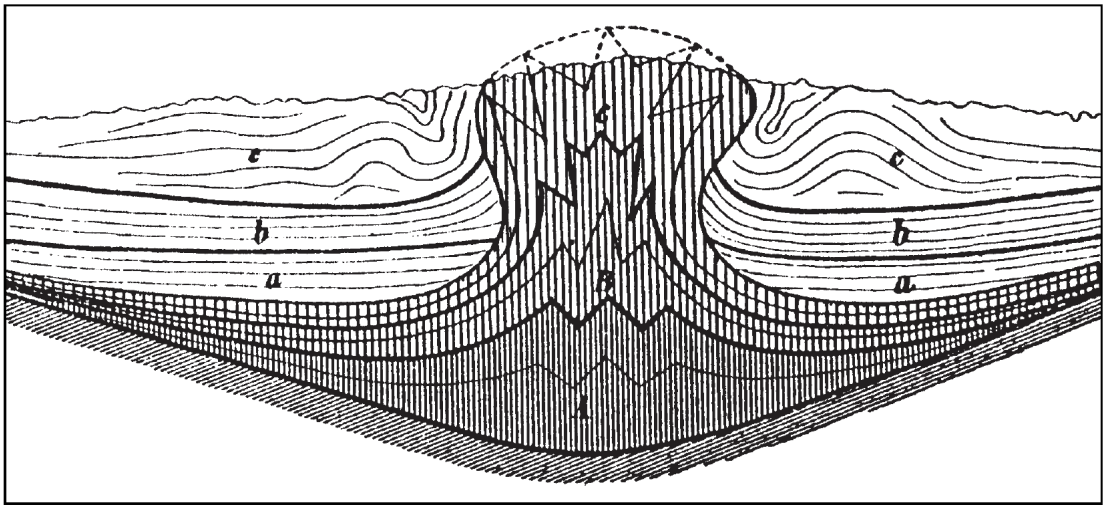


Fig. 1.1: Early schematic cross section with fundamental characteristics of salt diapirs (Posepny's 1871): internal folding inside the diapir, discordance and onlaps of the flanking strata anf folding around the shoulders of the diapir.

The early observations of salt structures, salt-glaciers and contact relations already led to the development of the fundamental concepts of downbuilding (Barton 1933) and erosional and depositional differential loading (Harrison 1927; Bailey 1931; Rettger 1935) (Fig. 1.1) for diapiric processes, driven by buoyancy (Lachmann 1910; Arrhenius 1913; Stille 1925) or regional contraction (Stille 1910; Stille 1917; Stille 1925). At the same time further hypotheses about the origin of salt structures based on igneous activity (Lerch 1892; DeGolyer 1925), residual islands (Lockett 1871; Hildgard 1872), in situ crystallization, osmotic pressures and expansive crystallization (Fenneman 1906; Harris 1907) were developed that had no relevance in later research. While the early concept of downbuilding was widely recognized by American geologists it was incompatible with the hypothesis that salt structures develop due to regional contraction for which strong evidence was found in Europe.

The fluid era started with Nettleton´s corn syrup and crude oil experiments 1934, demonstrating that a setup of two viscous fluids in which the overburden is represented by a slightly denser upper layer can produce diapir like shapes by gravity alone. This simple and on first look self-suggesting hypothesis explained salt tectonics by Rayleigh Taylor instabilities depending on viscosity contrast, density and dominant wavelength, focusing on active buoyant salt. In theory, the equilibrium between the two fluids is unstable at any perturbations of the interface, leading to infinitesimal stress differences and linear grows of the perturbations followed by later exponential grows. Following this process, first palinspastic restorations (Rios 1948) were performed and the concept of peripheral sinks was established as seismic imaging became possible. The concept was shaped by Trusheim´s (Trusheim 1957; Trusheim 1960) hypothesis of halokinesis, in which salt structures are the result of autonomous and isostatic rise and the evolution of salt structure can be reconstructed with the help of the sedimentary record of the surrounding strata (Fig. 1.2). While the mechanical properties of dry salt were studied

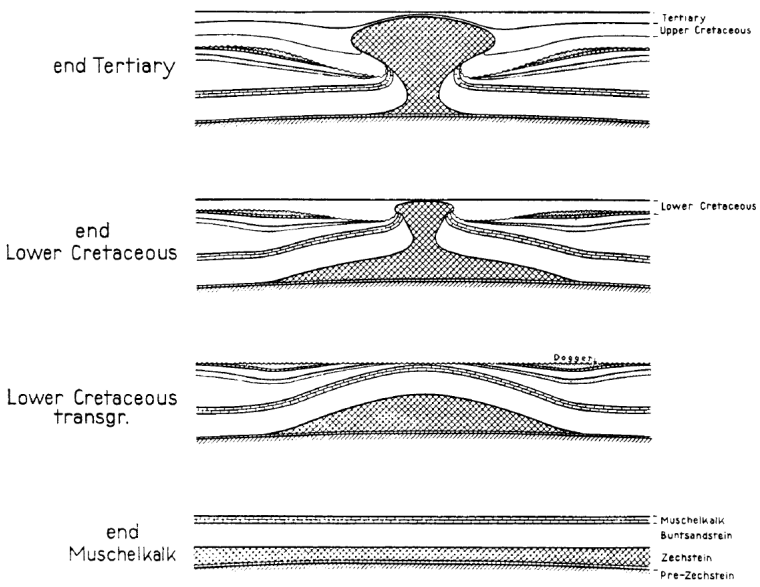


Fig. 1.2: Reconstruction of the evolution of flat-lying salt into a pillow and finally a diapir, demonstrating the concept of primary peripheral sinks (Dogger), secondary primary peripheral sinks (Lower Cretaceous) and the post diapiric stage with turtleback anticlines (Trusheim 1960).

in laboratory experiments (Handin and Hager 1958) producing higher viscosities than expected from field observations (Gussow 1968) thermal convection was discussed to take place inside some salt bodies (Talbot 1978; Talbot et al. 1982). Further research on salt deformation, in laboratory experiments and salt glaciers, revealed that under slightly damp conditions, salt not only deforms by dislocation creep (Carter and Hansen 1983) but also by fluid assisted solution –precipitation creep, that allowed much higher strain rates under low deviatoric stresses (Urai 1983; Urai 1985; Spiers et al. 1986; Urai et al. 1986). By the end of the 1980s the salt body shapes like pillows, domes, diapirs, walls, salt rollers and salt canopies are well known (Fig. 1.3) and explained by buoyancy and Rayleigh-Taylor instabilities, completely ignoring the actual mechanical properties of the overburden. In the case of a fluid-fluid interface, infinitesimal stresses at perturbations are able to grow over time. However, if one of the materials has a yield strength, it will withstand the small stresses and the perturbations are not able to grow. The fact that sediment rocks show yield strength in general brings the whole concept to a fundamental dilemma.

Around this time, the perception on the mechanical behavior of the overburden changed and its role as brittle encasement whose deformation controls the style of salt tectonics (Jackson 1995) won wide recognition. Nevertheless, this idea was not completely new. Faulting around salt domes was already recognized and modeled very early (Nettleton and Elkins 1947; Hubbert 1951; Parker and McDowell 1955; Bishop 1978), while the fact, that diapirs stopped rising if the roof was too thick, was observed repeatedly. Numerous analogue models using sand for the overburden above a viscous salt analog (McGill and Stromquist 1979; Vendeville and Cobbold 1987; Vendeville 1988; Vendeville and Cobbold 1988; Cobbold et al. 1989; Vendeville 1989) produces much more realistic salt structures defined by aggradation rate and the strength of the overburden. In contrary to older concepts buoy-

ancy was recognized to play a secondary role in the initial development of most diapirs. Although salt is less dense than most carbonates and fully compacted siliciclastic rocks, a burial depth of at least 650 to 1500 m is needed before the compaction in the lowest sediments is high enough to produce densities equivalent to salt. To produce gravitational unstable conditions, the average density of the whole overburden has to exceed the salt density which happens not before 1.6 to 3 km of burial (Hudec and Jackson 2007). It was therefore recognized, that the roof strength and regional deformation have major control on the development of salt structures. The importance of faulting of the brittle overburden producing salt rollers, the connection between sub salt and supra salt faults (Vendeville 1988) and raft tectonics (Burollet 1975) were discovered. Together with the computerized palinspastic reconstruction (Worrall and Snelson 1989; Hossack and McGuinness 1990) our understanding of complex salt tectonics was formed. Diapirism was classified into stages of (i) passive downbuilding diapirism (halokinesis) controlled by the interplay between sedimentation and upwelling salt, (ii) reactive diapirism due to regional extension and (iii) active diapirism, of super-lithostatic salt forcing itself into the surrounding strata near the surface (Nelson 1989; Vendeville and Jackson 1990; Vendeville and Jackson 1991; Vendeville and Jackson 1992). These concepts were refined leading to explanations of the different structural styles by the rates of extension or contraction and local amount of sedimentation (Fletcher et al. 1995; Letouzey et al. 1995; Talbot 1995; Vendeville and Nilsen 1995). Differential loading as a

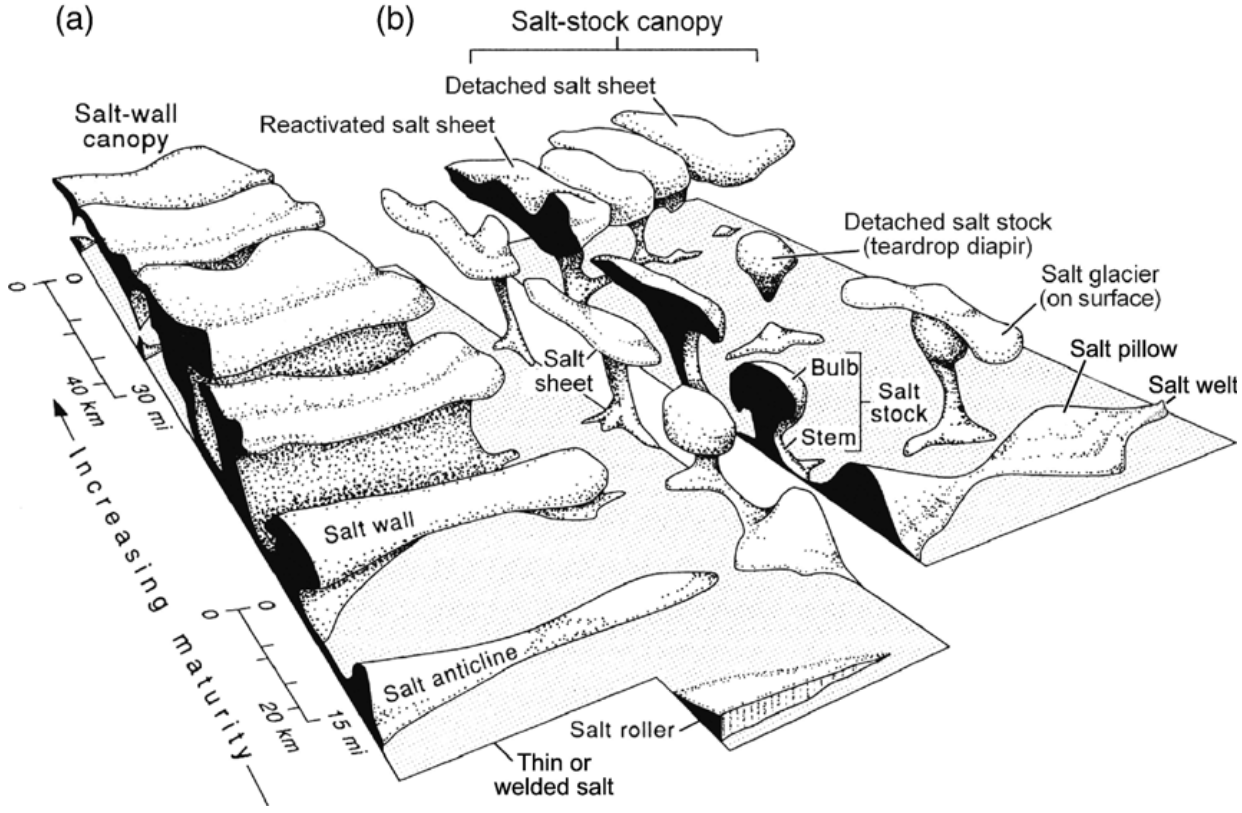


Fig. 1.3: Shapes of salt structures. (a) elongated line source structures (b) point source structures. (Hudec and Jackson 2007, simplified from Jackson and Talbot (1991)).

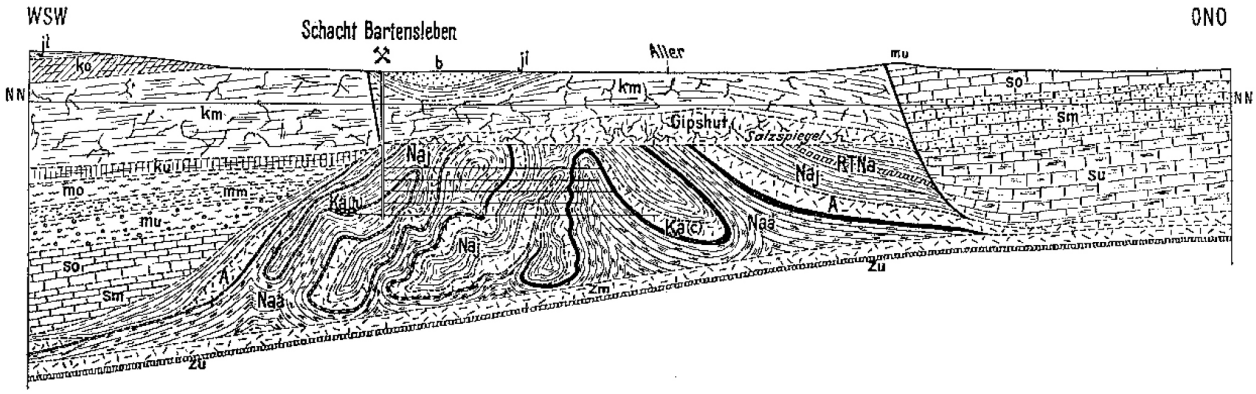


Abb. 16. Profil durch die Grubenbaue des Kaliwerkes Bartensleben im oberen Allertal. — Nach Fulda. Maßstab 1 : 20000.

Zeichenerklärung.

zu = Unterer Zechstein
zm = Mittlerer Zechstein
Naä = Älteres Steinsalz
Kä(c) = Älteres Kalilager (Carnallitgestein)
Kä(h) = Älteres Kalilager (Hartsalz)
A = Grauer Salzton und Hauptanhydrit
Naj = Jüngeres Steinsalz
RTNa = Roter Salzton
su = Unterer Buntsandstein
sm = Mittlerer Buntsandstein
so = Oberer Buntsandstein
mu = Unterer Muschelkalk
mm = Mittlerer Muschelkalk
mo = Oberer Muschelkalk
ku = Unterer Keuper
km = Mittlerer Keuper
ko = Oberer Keuper
jl = Lias
b = Tertiär
NN = Normalnull.

Fig. 1.4: Profile through the Bartensleben potassium mine (Fulda 1928).

driving force for salt expulsion towards a diapir was divided into gravitational loading by a hydraulic head in the salt (Kehle 1988), thermal loading by a strong temperature gradient (Talbot 1978; Talbot et al. 1982) and displacement loading by moving diapir flanks due to regional shortening or extension (Suppe 1985). Nevertheless, prove for thermal convection in diapirs encased in sediments is still missing (Hudec and Jackson 2007) and rather implausible in respect to known salt rheologies and realistic conditions. Although the deformation structures in the Boulby mine Potash salt were explained by thermal convection (Talbot et al. 1982) with very low Raleigh number values, the needed salt viscosities are orders of magnitude smaller than everything observed in deformation experiments with wet salt. These problematic assumptions combined with further inconsistent arguments and calculations of the authors make their concept of thermal convection under realistic conditions highly unlikely.

In summary, piercing of diapirs towards the surface takes place mostly during extensional events, while piercing driven by differential loading is only possible if the overburden is weakened or removed above the rising diapir. Without regional extension or shortening the grow of a diapir is stopped if the roof is too strong to be pierced or if the expulsion of salt reached an extend at which the remaining thin salt layer is too strong to be extruded.

Since this very productive period in the early nineties, our modern view of salt tectonics was formed. Nevertheless, recent research on many important aspects like the initial grows of mini basins, internal salt deformation, allochthonous salt or the role of salt in passive margins keeps our understanding of salt tectonics expanding.

1.3 Internal structure of evaporite bodies

As our understanding of salt body deformation and salt tectonics evolved tremendously, especially since the 90s, our knowledge of the internal deformation made much slower progress. Compared to other rocks, surface exposures of salt structures is rather rare and often of poor quality. Therefore, our view on the three dimensional internal structure of salt bodies had been mostly extrapolated from observations in mine galleries and drill cores. However, advances in the quality of modern industrial 3D seismic reflection data start to reveal the internal structures, although the resolution is still very limited (Van Gent et al., 2011; Cartwright et al., 2012; Fiduk and Rowan, 2012; Strozyk et al., 2012, 2014; Jackson et al., 2014, 2015). In addition, improvements in geomechanical modelling techniques, has allowed major advances to be made (Chemia et al. 2008; Albertz et al. 2010; Albertz and Ings 2012; Goteti et al. 2012; Li et al. 2012a; Li et al. 2012b).

Observations from mine galleries (Fig. 1.4) and drill cores revealed a variety of complex structures of shear-zones, boudinage and folding (Stier 1915; Fulda 1928; Balk 1949; Balk 1953; Martini 1953; Siemeister 1969; Kupfer 1976; Talbot and Jackson 1987; Bornemann and Fischbeck 1991; Burliga 1996; Zirngast 1996; Behlau and Mingerzahn 2001; Bornemann et al. 2008; Schléder et al. 2008; Hammer et al. 2014). Especially complex fold structures like curtain folds (Stier 1915) or constrictional sheath folds (Talbot and Jackson 1987) were observed in diapirs and the folded structure described as "resembling those in a handkerchief drawn vertically from the center through a small ring" (Kupfer 1968). Fist advances to understand these structures were originally made with the help of simple analogue models partly explaining the complex folding observed in salt mines (Dixon 1975).

The key to a deeper understanding of internal deformation lies in the varying mechanical properties of the different evaporite minerals typical present in a stratified buildup. The rheologies of these materials varies from rather strong and mostly brittle deforming carbonates and anhydrite, to soft creeping halite, up to extremely soft Potassium and Magnesium salts, creating effective viscosity contrasts of up to five orders of magnitude (van Eekelen et al. 1981; Müller et al. 1981; Spiers et al. 1983; Langbein 1987; Scott Duncan and Lajtai 1993; Schenk and Urai 2005; Urai et al. 2008).

The interaction of layers with such high contrasts in viscosity and rheology during deformation must lead to the development of complex fold and boudin structures. K-Mg salt-rich layers typically show complex internal folding on the meter to mm-scale, even if the entire package of layered evaporites is less deformed.

The role of high-viscosity, brittle-ductile layers (also called stringers) in salt deformation has been studied using 3D seismic data (Van Gent et al., 2011; Cartwright et al., 2012; Fiduk and Rowan,

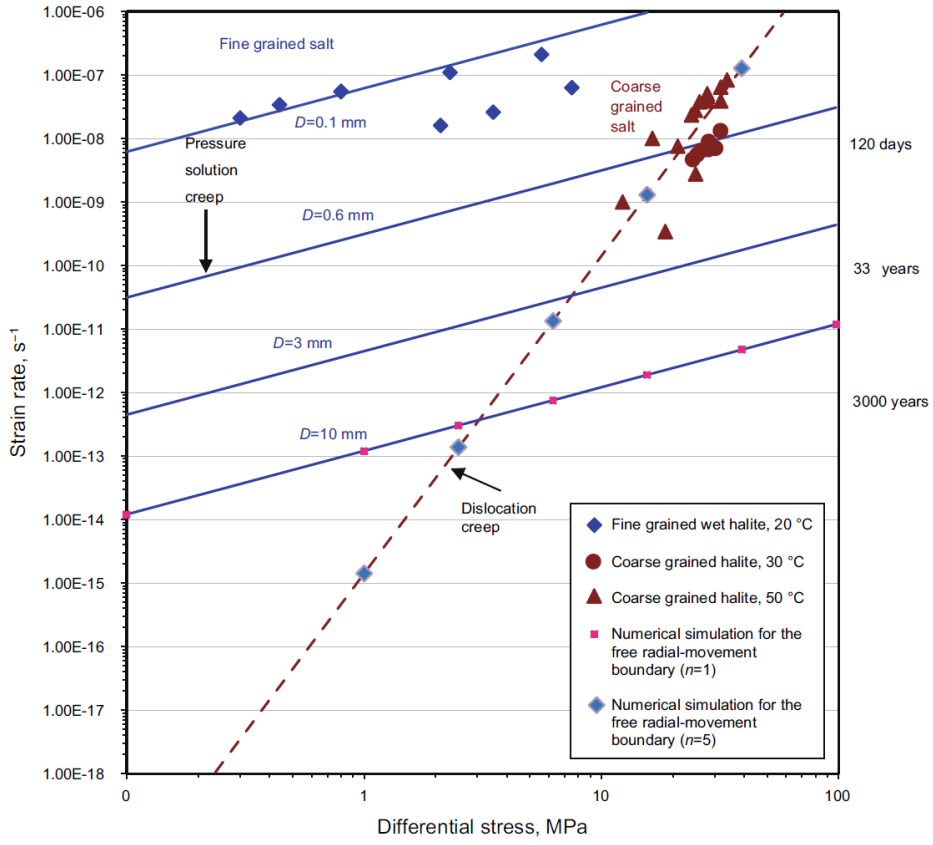


Fig. 1.5: Differential stress versus strain rate diagram. Solid lines are the pressure solution creep for fine and coarse grain sizes at room temperature. The broken line is the extrapolation of the dislocation creep. The red and blue dots represent numerical results with free radial-movement boundary condition (Li 2016 modified from Urai and Spiers 2007).

2012; Jackson et al., 2014, 2015; Strozyk et al., 2014), laboratory experiments, analogue models, and numerical modeling. More specifically, these techniques have been used to understand the complex folds, faults, and boudinage of stringers as a result of deformation of the surrounding salt. Deformation experiments on layered salt show the influence of different rheologies and the mechanics during stringer extension (Liang et al. 2007; Zulauf et al. 2010). Additionally, analogue and numerical models described the evolution of salt flow and stringer deformation (Jackson and Talbot 1989; Koyi 2001; Talbot and Aftabi 2004; Zulauf and Zulauf 2005; Chemia et al. 2008; Brun and Mauduit 2009; Chemia et al. 2009; Cartwright et al. 2012; Li et al. 2012a; Li et al. 2012b; Dooley et al. 2015).

1.4 Rheology of salt

Halite

Polycrystalline halite (Sodium chloride, NaCl), which is also called rock salt, is the main component of most evaporite bodies. Due to the low density, porosity and permeability in combination with low creep strength, the behavior of salt bodies differs strongly from other rocks in the upper earth crust. Therefore, the unique properties of halite play an important role in the tectonic deformation in salt bearing sediment basins.

The deformation of halite itself is influenced by a number of factors like temperature, stress,

grain size, fluid chemistry and impurity content (Urai et al. 2008). Although some aspects of halite rheology are object of current research and in many details controversial three long term deformation types can be distinguished: i) dilatant crystal plasticity and micro cracking, ii) dislocation creep and iii) fluid assisted solution /precipitation creep (also called pressure solution (PS) creep)(Heard 1972; Heard and Ryerson 1986; Wawersik and Zeuch 1986; Urai et al. 1987; Carter et al. 1993; Ter Heege et al. 2005a; Schléder et al. 2007). Dilatant halite plasticity with inter- and intergranular microcracking, grain rotation and intergranular slip can only take place under low effective confining pressure combined with high deviatoric stresses (>15-20 MPa) (Peach and Spiers 1996; Jin and Cristescu 1998) and plays therefore a minor role under the conditions present in the salt bodies discussed in this work.

Under the in situ conditions during salt tectonics, strain rates from 10^{-15} to 10^{-8} s^{-1} can be expected (Heard 1972; van Eekelen et al. 1981; Jackson and Talbot 1986; Carter et al. 1993) with, in our case, at least a few hundred meter of burial and temperatures between 20 - 200 °C. Under these conditions, a number of very different microphysical processes are involved in the deformation. The fundamental problem of studying these processes is the issue to perform deformation experiments with realistic deformation rates without exceeding the lifespan of the performing researcher. Thus, almost all deformation experiments were conducted under much higher deformation rates and deviatoric stresses. Only a few experiments, studying relaxation after deformation, reached strain rates of about 10^{-9} s^{-1} (Atkinson et al. 1978; Muhammad 2015). Taking this into account, flow laws for halite under realistic conditions are not only extrapolated from much faster experiments, it also cannot be determined which processes are dominant, due to the lack of data.

Under high deviatoric stresses and in dry salt (<10 ppm water) dislocation creep processes are dominant. They were analyzed and quantified in many laboratory experiments and are basis of most engineering creep laws used in the salt mining industry (Cristescu and Hunsche 1998; Hunsche and Hampel 1999). As the result, halite deformation is often described as non- Newtonian power law creep or visco-elastic material (Weijermars et al. 1993). The processes can be divided into dislocation climb (Senseny et al. 1992; Carter et al. 1993; Franssen 1994), dislocation cross-slip and dislocation glide (Auten et al. 1973; Wawersik and Zeuch 1986; Conrad and Yang 1999). The deformation is associated with the formation of subgrains (Pennock et al. 2006). The diameter of these subgrains has a near-linear, inverse correlation with the deviatoric stress and can therefore be used as stress piezometers (Carter et al. 1993). The different dislocation creep processes were analyzed in detail and summarized in deformation mechanism maps (Ter Heege et al. 2005a; Ter Heege et al. 2005b). As said before, the experiments were performed in a rather short-time and the extrapolated strain rates under in situ conditions vary strongly between the different mechanisms.

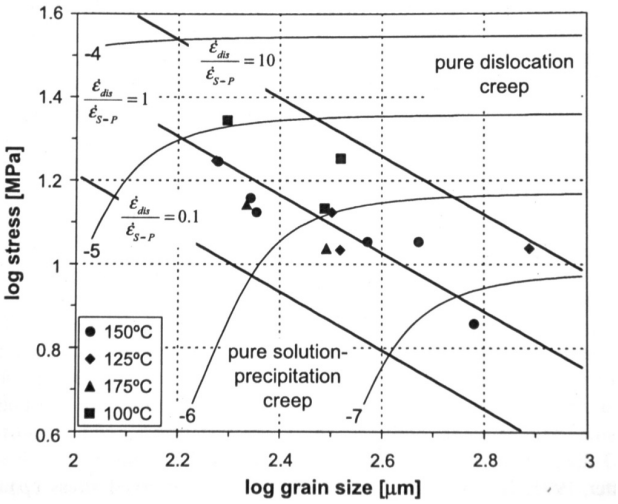


Fig. 1.6: Dynamically recrystallized grain size versus stress data for synthetic halite samples, superposed on a deformation mechanism map, showing that these samples deform in the transition region between dislocation creep and solution- precipitation creep (from ter Heege et al., 2005a).

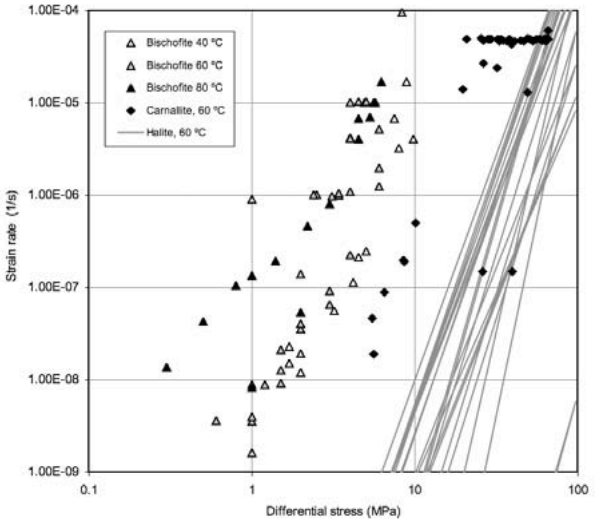


Fig. 1.7: Mechanical properties of bischofite and carnallite, compared with rock salt (Urai et al. 2008).

If the salt is not completely dry, which is the usual case in natural salt (Urai et al. 1986; Spiers et al. 1990), fluid assisted processes, involving mass transfer over and around grain boundaries, can take place. The fluids, in form of saturated brine inclusions or grain boundary films, enable fluid assisted grain boundary migration (Schenk and Urai 2004; Schenk and Urai 2005) and solution- precipitation creep to take place. By solution-precipitation or "pressure solution" (PS) creep material is dissolved at highly stressed grain boundaries and crystallizes at interfaces with low normal stresses after diffusion through the grain boundary fluid (Spiers et al. 1990; Spiers and Schutjens 1999). The deformation is typically associated with intergranular sliding and grain rotation. Although rarely seen in short term laboratory experiments, pressure solution creep is expected to play an important role under in situ conditions. Due to the linear Newtonian creep behavior the importance of pressure solution creep depends on the deviatoric stress. In particular at low deviatoric stress, pressure solution creep produces much higher strains than dislocation creep. Nevertheless, to allow mass transfer around grain boundaries, an interconnected fluid film or network is needed. Under absence of deviatoric stresses the fluids tend to separate into bubbles (Drury and Urai 1990; Spiers and Schutjens 1999; van Noort et al. 2007). Thus, the deviatoric stress must overcome a minimum threshold to form an interconnected fluid film and allow pressure solution processes to act. In contrast to dislocation creep processes, pressure solution creep is strongly dependent on the grain size (Fig. 1.5).

On the other hand, due to grain boundary migration and sub grain development, under the right conditions the grain size is dependent on the deviatoric stress.

In summary, the non-dilatant, steady state strain rate for dislocation creep is described by:

$$\dot{\varepsilon}_{DC} = A(\sigma)^n = A_0 e^{\left(-\frac{Q_{DC}}{RT}\right)} \cdot (\sigma)^n$$

While solution-precipitation creep is described by

$$\dot{\varepsilon}_{PS} = B(\sigma) = B_0 e^{\left(-\frac{Q_{PS}}{RT}\right)} \cdot \left(\frac{\sigma}{TD^m}\right)$$

Thus, the total strain rate is the sum of the two creep processes:

$$\dot{\varepsilon} = \dot{\varepsilon}_{DC} + \dot{\varepsilon}_{PS}$$

A_0 and B_0 are material parameters, Q_{DC} and Q_{PS} activation energies, R the gas constant, T absolute temperature, σ deviatoric stress, D grainsize and n and m are stress and grainsize exponents.

If both dislocation creep and fluid assisted deformation are taking place, dynamic recrystallization establishes a systematic relation between flow stress and grain size. As a result, the deformation often occurs at the boundary between the dislocation and pressure solution creep fields leading to an equilibrium of both processes (Fig. 1.6) (Ter Heege et al. 2005a; De Bresser et al. 2001).

Bischofite and Carnallite

Laboratory experiments with both materials revealed evidence for the same deformations acting in halite. Additional both materials develop mechanical twins. Compared to halite, carnallite has a lower viscosity and bischofite an even much lower (Fig. 1.7) (van Eekelen et al. 1981; Urai 1983; Urai and Boland 1985; Schenk et al. 2005; Muhammad 2015).

1.5 About this work

The aim of this work is to improve our understanding of the internal structures and dynamics inside mechanically layered evaporite bodies during deformation. A better understanding is needed to improve salt reservoir models, reduce drilling risks and to understand the long-term behavior of complex salt structures.

In detail, we address the questions: What is the influence of extreme soft or much harder layers during deformation? What happens during this deformation inside K-Mg salt dominated layers and which structures are formed? Under which conditions (rheology, viscosity contrast, strain rates, stresses, layering, multiphase deformation) can the observed structures be formed?

The study area chosen in this work fits the desired requirement in an optimal manner. We could access a broad dataset of well-logs, core pictures, 3D seismic and an extraordinary drill core from a K-Mg salt rich subunit. The structure itself experienced a complex deformation history, yet the deformation was simple enough to be reconstructed. In addition, the salt pillow is strongly mechanically layered. This layering could be used to study the deformation of the mechanically diverse layer and at

the same time enables visualization with seismic imaging.

With the synthesis of data from basin to micro scale structures, the salt body evolution, local salt flow, material mixing, stress indicators, strain concentration were analyzed on the basis of existing rheology models and concepts of salt body deformation. Thus, a model of salt deformation inside the Veendam salt pillow in the framework of local tectonics was developed together with a concept of conditions leading to the local extreme accumulation of bischofite. A fine stratigraphic analysis of the bischofite rich ZIII-1b layer was performed with a detailed examination of the existing deformational structures. Based on these results, the deformation of the ZIII-AC stringer was modeled revealing the influence on the internal deformation and the boundary conditions to produce the observed structures.

1.6 References

Albertz M, Beaumont C, Shimeld JW, et al (2010) An investigation of salt tectonic structural styles in the Scotian Basin, offshore Atlantic Canada: 1. Comparison of observations with geometrically simple numerical models. Tectonics 29:TC4017. doi: 10.1029/2009TC002539

Albertz M, Ings SJ (2012) Some consequences of mechanical stratification in basin-scale numerical models of passive-margin salt tectonics. Geol Soc London, Spec Publ 363:303–330. doi: 10.1144/SP363.14

Arrhenius S (1913) Zur Physik der Salzlagerstätten. Medd Vetensskapsakademiens Nobelinstitut 2:1–25.

Atkinson B, Mainprice D, Rutter E (1978) Use of the stress relaxation testing method in studies of the mechanical behavior of geological materials.

Auten TA, Davis LA, Gordon RB (1973) Hydrostatic pressure and the mechanical properties of NaCl polycrystals. Philos Mag 28:335–341. doi: 10.1080/14786437308217457

Bailey EB (1931) Salt-Plugs. Geol Mag 68:335. doi: 10.1017/S0016756800095613

Balk R (1949) Structure of grand saline salt dome, Van Zandt County, Texas. Am Assoc Pet Geol Bull 33:1791–1829.

Balk R (1953) Salt structure of Jefferson Island salt dome, Iberia and Vermilion parishes, Louisiana. Am Assoc Pet Geol Bull 37:2455–2475.

Barton D (1933) Mechanics of formation of salt domes with special reference to Gulf Coast salt domes of Texas and Louisiana. Am Assoc Pet Geol Bull 17:1025–1083.

Behlau J, Mingerzahn G (2001) Geological and tectonic investigations in the former Morsleben salt mine (Germany) as a basis for the safety assessment of a radioactive waste repository. Eng Geol 61:83–97. doi: 10.1016/S0013-7952(01)00038-2

Bishop RS (1978) Mechanism for emplacement of piercing diapiers. AAPG Bull. (American Assoc. Pet. Geol. 62:1561–1583.

Borchert H, Muir R (1964) Salt deposits: the origin, metamorphism and deformation of evaporites. D. Van Nostrand Company. Ltd, London.

Bornemann O, Behlau J, Fischbeck R, et al (2008) Projekt Gorleben, Standortbeschreibung Gorleben. Teil 3: Ergebnisse der über- und untertägigen Erkundung des Salinars. Bundesanstalt für Geowissenschaften und Rohstoffe (BGR), Hannover.

Bornemann O, Fischbeck R (1991) Zur geologie des salzstocks Gorleben nach den Bohrergebnissen. Deutschland Bundesamt für Strahlenschutz, Salzgitter.

Brun JP, Mauduit TPO (2009) Salt rollers: Structure and kinematics from analogue modelling. Mar Pet Geol 26:249–258. doi: 10.1016/j.marpetgeo.2008.02.002

Burliga S (1996) Kinematics within the Klodawa salt diapir, central Poland. Geol Soc London, Spec Publ 100:11–21. doi: 10.1144/GSL.SP.1996.100.01.02

Burollet PF (1975) Tectonique en radeaux en Angola. Bull la Soc Geol Fr S7–XVII:503–504. doi: 10.2113/gssgfbull.S7-XVII.4.503

Carpenter AB, others (1978) Origin and chemical evolution of brines in sedimentary basins. In: SPE Annual Fall Technical Conference and Exhibition.

Carter N., Horseman S., Russell J., Handin J (1993) Rheology of rocksalt. J Struct Geol 15:1257–1271. doi: 10.1016/0191-8141(93)90168-A

Carter NL, Hansen FD (1983) Creep of rocksalt. Tectonophysics 92:275–333. doi: 10.1016/0040-1951(83)90200-7

Cartwright J, Jackson MPA, Dooley T, Higgins S (2012) Strain partitioning in gravity-driven shortening of a thick, multilayered evaporite sequence. Geol Soc London, Spec Publ 363:449–470. doi: 10.1144/SP363.21

Chemia Z, Koyi H, Schmeling H (2008) Numerical modelling of rise and fall of a dense layer in salt diapirs. Geophys J Int 172:798–816. doi: 10.1111/j.1365-246X.2007.03661.x

Chemia Z, Schmeling H, Koyi H (2009) The effect of the salt viscosity on future evolution of the Gorleben salt diapir, Germany. Tectonophysics 473:446–456. doi: 10.1016/j.tecto.2009.03.027

Cobbold P, Rossello E, Vendeville B (1989) Some experiments on interacting sedimentation and deformation above salt horizons. Bull - Soc Geol Fr 5:453–460.

Conrad H, Yang D (1999) The rate-controlling mechanism(s) during plastic deformation of polycrystalline NaCl at 0.28–0.75 TM. J Mater Sci 34:821–826. doi: 10.1023/A:1004537300154

Cristescu N, Hunsche U (1998) Time effects in rock mechanics.

De Bresser J, Ter Heege J, Spiers C (2001) Grain size reduction by dynamic recrystallization: can it result in major rheological weakening? Int J Earth Sci 90:28–45. doi: 10.1007/s005310000149

DeGolyer E (1925) Origin of North American salt domes. Am Assoc Pet Geol Bull 9:831–874.

Dixon J (1975) Finite strain and progressive deformation in models of diapiric structures. Tectonophysics 28:89–124.

Dooley TP, Jackson MPA, Jackson CA-L, et al (2015) Enigmatic structures within salt walls of the Santos Basin—Part 2: Mechanical explanation from physical modeling. J Struct Geol 75:163–187. doi: 10.1016/j.jsg.2015.01.009

Drury MR, Urai JL (1990) Deformation-related recrystallization processes. Tectonophysics 172:235–253.

Fenneman NM (1906) Oil fields of the Texas Louisiana Gulf Coastal Plain. USGS Bull 282:146.

Fiduk JC, Rowan MG (2012) Analysis of folding and deformation within layered evaporites in Blocks BM-S-8 & -9, Santos Basin, Brazil. Geol Soc London, Spec Publ 363:471–487. doi: 10.1144/SP363.22

Fletcher R, Hudec M, Watson I (1995) Salt glacier and composite sediment-salt glacier models for the emplacement and early burial of allochthonous salt sheets. In: M.P.A.Jackson, Roberts DG, Snelson S (eds) Salt tectonics: a global perspective: AAPG Memoir 65. pp 77–108

Franssen RCMW (1994) The rheology of synthetic rocksalt in uniaxial compression. Tectonophysics 233:1–40. doi: 10.1016/0040-1951(94)90218-6

Fulda E (1928) Die Geologie der Kalisalzlagerstätten. In: Das Kali, II. Teil: Enke's Bibliothek für Chemie und Technik unter Berücksichtigung der Volkswirtschaft 7. p 24–136.

Goteti R, Ings SJ, Beaumont C (2012) Development of salt minibasins initiated by sedimentary topographic relief. Earth Planet Sci Lett 339–340:103–116. doi: 10.1016/j.epsl.2012.04.045

Gussow WC (1968) Salt diapirism: importance of temperature, and energy source of emplacement. In: O`Brien GD, Braunstein J (eds) Diapirism and diapirs: AAPG Memoir 8. pp 18–52.

Hammer J, Behlau J, Mingerzahn G, Mertineit M (2014) The mechanical behavior and geometry of anhydrite layers in rock salt: Observations from nature. In: Natural Analogues for Safety Cases of Repositories in Rock salt - "Salt Club" Workshop Proceedings Braunschweig, Germany, 05.-07.September 2012. Hosted by Gesellschaft für Anlagen und Reaktorsicherheit (GRS) mbH, Braunschweig and Project Management Agency.

Handin J, Hager R V. (1958) Experimental deformation of sedimentary rocks under confining pressure: tests at high temperature. Am Assoc Pet Geol Bull 42:2893–2934.

Harris GD (1907) Notes on the geology of the Winnfield Sheet.

Harrison T (1927) Colorado-Utah salt domes. Am Assoc Pet Geol Bull 11:111–133.

Heard HC (1972) Steady-State flow in polycrystalline halite at pressure of 2 kilobars. American Geophysical Union, pp 191–209.

Heard HC, Ryerson FJ (1986) Effect of cation impurities on steady-state flow of salt. In: Hobbs BE, Heard HC (eds) Mineral and rock deformation: laboratory studies. AGU Geophysical Monograph 36. American Geophysical Union, pp 99–115.

Hildgard EW (1872) On the geology of lower Louisiana and the salt deposits of Petite Anse Island. Smithson Contrib 248:32–34.

Hossack J, McGuinness D (1990) Balanced sections and the development of fault and salt structures in the Gulf of Mexico (GOM). In: Geological Society of America, 1990 annual meeting. p 48.

Hudec MR, Jackson MPA (2007) Terra infirma: Understanding salt tectonics. Earth-Science Rev 82:1–28. doi: 10.1016/j.earscirev.2007.01.001

Hunsche U, Hampel A (1999) Rock salt - the mechanical properties of the host rock material for a radioactive waste repository. Eng Geol 52:271–291. doi: 10.1016/S0013-7952(99)00011-3

Jackson CA-L, Jackson MPA, Hudec MR, Rodriguez C (2014) Internal structure, kinematics, and growth of a salt wall: Insights from 3-D seismic data. Geology 42:307–310. doi: 10.1130/G34865.1

Jackson CA-L, Jackson MPA, Hudec MR, Rodriguez CR (2015) Enigmatic structures within salt walls of the Santos Basin—Part 1: Geometry and kinematics from 3D seismic reflection and well data. J Struct Geol 75:135–162. doi: 10.1016/j.jsg.2015.01.010

Jackson MPA (1995) Retrospective salt tectonics. AAPG Mem 65:1–28.

Jackson MPA, Talbot C (1989) Anatomy of mushroom-shaped diapirs. J Struct Geol 11:211–230. doi: 10.1016/0191-8141(89)90044-8

Jackson MPA, Talbot CJ (1986) External shapes, strain rates, and dynamics of salt structures. Geol Soc Am Bull 97:305–323. doi: 10.1130/0016-710.1130/0016-7606(1986)97<305:ESSRAD>2.0.CO;2

Jin J, Cristescu ND (1998) An elastic/viscoplastic model for transient creep of rock salt. Int J Plast 14:85–107. doi: 10.1016/S0749-6419(97)00042-9

Kehle RO (1988) The origin of salt structures. In: Schreiber BC (ed) Evaporites and Hydrocarbons. Columbia University Press, New York, p 345–404.

KING HUBBERT M (1951) Mechanical basis for certain familliar geologic structures. Geol Soc Am Bull 62:355. doi: 10.1130/0016-7606(1951)62[355:MBFCFG]2.0.CO;2

Koyi H a. (2001) Modeling the influence of sinking anhydrite blocks on salt diapirs targeted for hazardous waste disposal. Geology 29:387–390. doi: 10.1130/0091-7613(2001)029<0387:MTIOSA>2.0.CO;2

Kupfer D (1976) Shear zones inside Gulf Coast salt stocks help to delineate spines of movement. Am Assoc Pet Geol Bull 60:1434–1447.

Kupfer D (1968) Relationship of internal to external structure of salt domes.

Lachmann R (1910) Über autoplaste (nichttektonische) Formelemente im Bau der Salzlagerstätten Norddeutschlands. Zeitschrift der Dtsch Geol Gesellschaft 62:113–116.

Langbein R (1987) The Zechstein sulphates: The state of the art. In: Peryt TM (ed) The Zechstein Facies in Europe, Lecture Notes in Earth Science, Vol .10. Springer- Verlag Berlin, Heidelberg, pp 143–188.

Lerch O (1892) A Preliminary Report Upon the Hills of Louisiana, North of the Vicksburg, Shreveport and Pacific Railroad.

Letouzey J, Colletta B, Vially R, Chermette J (1995) Evolution of salt-related structures in compressional settings. In: Jackson MPA, Roberts DG, Snelson S (eds) Salt tectonics: a global perspective: AAPG Memoir 65. pp 41–61.

Li S, Abe S, Reuning L, et al (2012a) Numerical modelling of the displacement and deformation of embedded rock bodies during salt tectonics: A case study from the South Oman Salt Basin. Geol Soc London, Spec Publ 363:503–520. doi: 10.1144/SP363.24

Li S, Abe S, Van Gent H, et al (2012b) A new method to evaluate the salt rheology during long term ceep by inversion of numerical models of gravitational sinking of carbonate-anhydrite inclusions (stringers) in salt. In: Proceedings of the 7th Conference on the Mechanical Behavior of Salt : Saltmech7 Paris, 16-19 April 2012. pp 215–220.

Liang W, Yang C, Zhao Y, et al (2007) Experimental investigation of mechanical properties of bedded salt rock. Int J Rock Mech Min Sci 44:400–411. doi: 10.1016/j.ijrmms.2006.09.007

Lockett S (1871) Second annual report of the Topographical Survey of Louisiana.

Martini HJ (1953) Salzsättel und Deckgebirge. In: Frühjahrestagung "Salzlagerstätten" der Deutschen Geologischen Gesellschaft in Goslar, Mai 1953. pp 823–836.

McCaffrey MA, Lazar B, Holland HD (1987) The evaporation path of seawater and the coprecipitation of Br (super-) and K (super+) with halite. J Sediment Res 57:928–937.

McGill GE, Stromquist AW (1979) The grabens of Canyonlands National Park, Utah: Geometry, mechanics, and kinematics. J Geophys Res 84:4547. doi: 10.1029/JB084iB09p04547

Muhammad N (2015) Deformation and transport processes in salt rocks : An experimental study exploring effects of pressure and stress relaxation. UU Dept. of Earth Sciences.

Müller WH, Schmid SM, Briegel U (1981) Deformation experiments on anhydrite rocks of different grain sizes: Rheology and microfabric. Tectonophysics 78:527–543. doi: 10.1016/0040-1951(81)90027-5

Nelson T (1989) Style of salt diapirs as a function of the stage of evolution and the nature of the encasing sediments. In: Gulf of Mexico salt tectonics, associated processes and exploration potential: Gulf Coast Section SEPM Foundation Tenth Annual Research Conference. pp 109–110

Nettleton LL, Elkins TA (1947) Geologic models made from granular materials. Trans Am Geophys Union 28:451. doi: 10.1029/TR028i003p00451

Parker T, McDowell A (1955) Model studies of salt-dome tectonics. Am Assoc Pet Geol Bull 39:2384–2470.

Peach CJ, Spiers CJ (1996) Influence of crystal plastic deformation on dilatancy and permeability development in synthetic salt rock. Tectonophysics 256:101–128. doi: 10.1016/0040-1951(95)00170-0

Pennock GM, Drury MR, Peach CJ, Spiers CJ (2006) The influence of water on deformation microstructures and textures in synthetic NaCl measured using EBSD. J Struct Geol 28:588–601. doi: 10.1016/j.jsg.2006.01.014

Reeve MT, Bell RE, Duffy OB, et al (2015) The growth of non-colinear normal fault systems ; What can we learn from 3D seismic reflection data? J Struct Geol 70:141–155. doi: 10.1016/j.jsg.2014.11.007

Rettger R (1935) Experiments on soft-rock deformation. Am Assoc Pet Geol Bull 19:271–292.

Rios JM (1948) Diapirismo. Inst Geológico y Min España Boletín 60:390.

Schenk O, Urai JL (2005) The migration of fluid-filled grain boundaries in recrystallizing synthetic bischofite: First results of in-situ high-pressure, high-temperature deformation experiments in transmitted light. J Metamorph Geol 23:695–709. doi: 10.1111/j.1525-1314.2005.00604.x

Schenk O, Urai JL, Evans B (2005) The effect of water on recrystallization behavior and grain boundary morphology in calcite–observations of natural marble mylonites. J Struct Geol 27:1856–1872. doi: 10.1016/j.jsg.2005.05.015

Schenk OO, Urai JL (2004) Microstructural evolution and grain boundary structure during static recrystallization in synthetic polycrystals of sodium chloride containing saturated brine. Contrib to Mineral Petrol 146:671–682. doi: 10.1007/s00410-003-0522-6

Schléder Z, Burliga S, Urai JL (2007) Dynamic and static recrystallization-related microstructures in halite samples from the Kłodawa salt wall (central Poland) as revealed by gamma-irradiation. Neues Jahrb für Mineral - Abhandlungen 184:17–28. doi: 10.1127/0077-7757/2007/0079

Schléder Z, Urai JL, Nollet S, Hilgers C (2008) Solution-precipitation creep and fluid flow in halite: A case study of Zechstein (Z1) rocksalt from Neuhof salt mine (Germany). Int J Earth Sci 97:1045–1056. doi: 10.1007/s00531-007-0275-y

Scott Duncan EJ, Lajtai EZ (1993) The creep of potash salt rocks from Saskatchewan. Geotech Geol Eng 11:159–184. doi: 10.1007/BF00531249

Senseny PE, Hansen FD, Russell JE, et al (1992) Mechanical behaviour of rock salt: Phenomenology and micromechanisms. Int J Rock Mech Min Sci Geomech Abstr 29:363–378. doi: 10.1016/0148-9062(92)90513-Y

Siemeister G (1969) Primärparagenese und Metamorphose des Ronnenberglagers nach Untersuchung im Grubenfeld Salzdetfurth. Bundesanstalt für Bodenforschung, Geologische Landesämter der Bundesrepublik Deutschland, Hannover.

Spiers C, Urai J, Lister G, et al (1986) The influence of fluid-rock interaction on the rheology of salt rock. Commission of the European Communities (CEC).

Spiers CJ, Schutjens P (1999) Intergranular pressure solution in NaCl: Grain-to-grain contact experiments under the optical microscope. Oil Gas Sci Technol 54:729–750.

Spiers CJ, Schutjens PMTM, Brzesowsky RH, et al (1990) Experimental determination of constitutive parameters governing creep of rocksalt by pressure solution. Geol Soc London, Spec Publ 54:215–227. doi: 10.1144/GSL.SP.1990.054.01.21

Spiers CJ, Urai JL, Lister GS, et al (1983) The influence of fluid-rock interaction on the rheology of salt rock and on ionic transport in salt. Report over the period nov. 1981- Dec. 1983. 131.

Stier K (1915) Strukturbild des Benther Salzgebirges. Jahresbericht des niedersächsischer Geol Verein, Hann 8:1–15.

Stille H (1925) The upthrust of the salt masses of Germany. Am Assoc Pet Geol Bull 9:417–441.

Stille H (1910) Faltung des Deutschen Bodens und des Salzgebirges. Kali Zeitschrift 5:17.

Stille H (1917) Injektivfaltung und damit zusammenhängende Erscheinungen. Geol Rundschau 8:89–142. doi: 10.1007/BF01801634

Strozyk F, Urai JL, Gent H Van, et al (2014) The internal structure of salt : insights from a regional 3D seismic study of the Permian Zechstein 3 intra-salt stringer in the Northern Netherlands and its implications for salt tectonics. Interpretation 2:101–117. doi: 10.1190/INT-2014-0037.1

Strozyk F, Van Gent H, Urai JL, Kukla PA (2012) 3D seismic study of complex intra-salt deformation: An example from the Upper Permian Zechstein 3 stringer, western Dutch offshore. Geol Soc London, Spec Publ 363:489–501. doi: 10.1144/SP363.23

Suppe J (1985) Principles of structural geology. Prentice Hall.

Talbot C (1995) Molding of salt diapirs by stiff overburden. In: M.P.A.Jackson, Roberts DG, Snelson S (eds) Salt tectonics: a global perspective: AAPG Memoir 65. pp 61–75

Talbot C, Jackson M (1987) Internal kinematics of salt diapirs. Am Assoc Pet Geol Bull 71:1068–1093.

Talbot CJ (1978) Halokinesis and thermal convection. Nature 273:739–741. doi: 10.1038/273739a0

Talbot CJ, Aftabi P (2004) Geology and models of salt extrusion at Qum Kuh, central Iran. J Geol Soc London 161:321–334. doi: 10.1144/0016-764903-102

Talbot CJ, Tully CP, Woods PJE (1982) The structural geology of boulby (potash) mine, Cleveland, United Kingdom. Tectonophysics 85:167–204. doi: 10.1016/0040-1951(82)90102-0

Ter Heege JH, De Bresser JHP, Spiers CJ (2005a) Rheological behaviour of synthetic rocksalt: The interplay between water, dynamic recrystallization and deformation mechanisms. J Struct Geol 27:948–963. doi: 10.1016/j.jsg.2005.04.008

Ter Heege JH, De Bresser JHP, Spiers CJ (2005b) Dynamic recrystallization of wet synthetic polycrystalline halite: Dependence of grain size distribution on flow stress, temperature and strain. Tectonophysics 396:35–57. doi: 10.1016/j.tecto.2004.10.002

Trusheim F (1957) Über Halokinese und ihre Bedeutung für die strukturelle Entwicklung Norddeutschlands. Dtsch Geol Gesellschaft Zeitschrift 109:111–151.

Trusheim F (1960) Mechanism of Salt Migration in Northern Germany. Am Assoc Pet Geol Bull 44:1519–1540. doi: 10.1306/0BDA61CA-16BD-11D7-8645000102C1865D

Urai JL (1983) Water assisted dynamic recrystallization and weakening in polycrystalline bischofite. Tectonophysics 96:125–157. doi: 10.1016/0040-1951(83)90247-0

Urai JL (1985) Water-enhanced dynamic recrystallization and solution transfer in experimentally deformed carnallite. Tectonophysics 120:285–317. doi: 10.1016/0040-1951(85)90055-1

Urai JL, Boland JN (1985) Development of microstructures and the origin of hematite in naturally deformed carnallite. Neues Jahrb für Mineral Monatshefte H.2:58–72.

Urai JL, Schléder Z, Spiers CJ, et al (2008) Flow and Transport Properties of Salt Rocks. In: Dynamics of Complex Intracontinental Basins: The Central European Basin System. Springer Science & Business Media, pp 277–290.

Urai JL, Spiers CJ, Peach CJ, et al (1987) Deformation mechanisms operating in naturally deformed halite rocks as deduced from microstructural investigations. Geologie en Mijnbouw 66:165–176.

Urai JL, Spiers CJ, Zwart HJ, Lister GS (1986) Weakening of rock salt by water during long-term creep. Nature 324:554–557. doi: 10.1038/324554a0

Usiglio MJ (1849) Etudes sur la composition de l'eau de la Mediterranee et sur l'exploitation des sels qu'elle contient. Ann Chim Phys, ser 3 27:172–191.

Van't Hoff JH (1905) Zur Bildung der ozeanischen Salzablagerungen. Zeitschrift f{ü}r Anorg Chemie 47:244–280.

van Eekelen HA, Urai JL, Hulsebos T (1981) Creep of Bischofite. In: Proceedings, 1st Conference on the Mechanical Behaviour of Salt. Pennsylvania.

Van Gent H, Urai JL, de Keijzer M (2011) The internal geometry of salt structures - A first look using 3D seismic data from the Zechstein of the Netherlands. J Struct Geol 33:292–311. doi: 10.1016/j.jsg.2010.07.005

van Noort R, Spiers CJ, Peach CJ (2007) Effects of orientation on the diffusive properties of fluid-filled grain boundaries during pressure solution. Phys Chem Miner 34:95–112. doi: 10.1007/s00269-006-0131-9

Vendeville B (1988) Scale models of basement-induced extension: Comptes Rendus de l'Academie des Sciences de Paris, serie II, v. 307. 1013–1019.

Vendeville B (1989) Scaled experiments on the interaction between salt flow and overburden faulting during syndepositional extension. In: SEPM Gulf Coast Section, 10th Annual Research Conference, Houston, Program and Extended Abstracts. pp 131–136.

Vendeville B, Cobbold P (1987) Synsedimentary gravitational sliding and listric normal growth faults -Insights from scaled physicak models. COMPTES RENDUS L Acad DES Sci Ser II 305:1313–1319.

Vendeville B, Cobbold PR (1988) How normal faulting and sedimentation interact to produce listric fault profiles and stratigraphic wedges. J Struct Geol 10:649–659. doi: 10.1016/0191-8141(88)90073-9

Vendeville B, Jackson M (1990) Physical modeling of the growth of extensional and contractional salt tongues on continental slopes (abs.). Am Assoc Pet Geol Bull 74:784.

Vendeville B, Jackson M (1991) Deposition, extension, and the shape of downbuilding salt diapirs. In: Annual meeting of the American Association of Petroleum Geologists (AAPG), Dallas, TX (United States).

Vendeville BC, Nilsen ET (1995) Episodic grows of salt diapiers driven by horizontal shortening.

Vendeville C, Jackson MPA (1992) The rise of diapirs during thin-skinned extension. Mar Pet Geol 9:331–354.

Ville L (1856) Notice géologique sur les salines des Zahrez et les gites de sel gemme de Rang el Melah et d'Ain Hadjera (Algérie). Ann des Mines 15:351–410.

Warren JK (2006) Evaporites:Sediments, Resources and Hydrocarbons. Springer Science & Business Media, Berlin Heidelberg.

Wawersik WR, Zeuch DH (1986) Modeling and mechanistic interpretation of creep of rock salt below 200°C. Tectonophysics 121:125–152. doi: 10.1016/0040-1951(86)90040-5

Weijermars R, Jackson MPA, Vendeville B (1993) Rheological and tectonic modeling of salt provinces. Tectonophysics 217:143–174. doi: 10.1016/0040-1951(93)90208-2

Williamson MDM, Murray SSJJ, Hamilton TAPAP, et al (1998) A Review of Zechstein Drilling Issues. In: Offshore Europe Conference in Aberdeen, Scotland, 9-12 September 1997. pp 189–196.

Worrall D, Snelson S (1989) Evolution of the northern Gulf of Mexico. In: Albert W. Bally ARP (ed) The geology of North America; an overview: Geological Society of America, v. A. pp 97–138.

Zirngast M (1996) The development of the Gorleben salt dome (northwest Germany) based on quantitative analysis of peripheral sinks. Geol Soc London, Spec Publ 100:203–226. doi: 10.1144/GSL.SP.1996.100.01.13

Zulauf G, Zulauf J, Bornemann O, et al (2010) Experimental deformation of a single-layer anhydrite in halite matrix under bulk constriction. Part 2: Deformation mechanisms and the role of fluids. J Struct Geol 32:264–277. doi: 10.1016/j.jsg.2009.12.001

Zulauf J, Zulauf G (2005) Coeval folding and boudinage in four dimensions. J Struct Geol 27:1061–1068. doi: 10.1016/j.jsg.2005.04.003

2. Evolution of rheologically heterogeneous salt structures: a case study from the NE-Netherlands

This chapter was publised as Raith AF, Strozyk F, Visser J, Urai JL (2016) Evolution of rheologically heterogeneous salt structures: A case study from the NE Netherlands. Solid Earth 7:67–82. doi: 10.5194/se-7-67-2016

2.1 Abstract

The growth of salt structures is controlled by the low flow strength of evaporites and by the tectonic boundary conditions. The potassium- magnesium salts (K-Mg salts) carnallite and bischofite are prime examples of layers with much lower effective viscosity than halite: their low viscosity presents serious drilling hazards but also allows squeeze solution mining. In contrast, intrasalt anhydrite and carbonate layers (stringers) are much stronger than halite. These rheological contrasts within an evaporite body have an important control on the evolution of the internal structure of salt, but how this mechanical layering affects salt deformation at different scales is not well known. In this study, we use high-resolution 3D seismic and well data to study the evolution of the Veendam and Slochteren salt pillows at the southern boundary of the Groningen High, northern Netherlands. Here the rock salt layers contain both the mechanically stronger Zechstein III Anhydrite - Carbonate stringer and the weaker K-Mg salts, thus we are able to assess the role of extreme rheological heterogeneities on salt structure growth. The internal structure of the two salt pillows shows areas in which the K-Mg salt-rich ZIII 1b layer is much thicker than elsewhere, in combination with a complexly ruptured and folded ZIII Anhydrite - Carbonate stringer. Thickness maps of supra-salt sediments and well data are used to infer the initial depositional architecture of the K-Mg salts and their deformation history. Results suggest that faulting and the generation of depressions on the top Zechstein surface above a Rotliegend graben caused the local accumulation of bittern brines and precipitation of thick K-Mg salts. During the first phase of salt flow and withdrawal from the Veendam area, under the influence of differential loading by Buntsandstein sediments, the ZIII stringer was boudinaged while the lens of Mg salts remained relatively undeformed. This was followed by a convergence stage, when the K-Mg salt-rich layers were deformed within the inflating salt pillows. This deformation was strongly disharmonic and strongly influenced by folding of the underlying, ruptured ZIII stringer, leading to thickening and internal deformation of the K-Mg salt layers.

2.2 Introduction

Salt bodies are often depicted as a homogeneous mass of mechanically weak rock salt, with deformation driven by buoyancy, differential loading, or gravity gliding (Jackson and Talbot, 1986; Hudec and Jackson, 2007). Our understanding of large-scale salt tectonics has grown tremendously over the last century (e.g. Jackson et al., 1996; Warren, 2006), but the internal deformation of evaporates, as commonly observed in outcrops in mines and rare surface exposures (Jackson et al., 1990), is less well known. Our knowledge of this domain is making some progress however, largely because the internal layering of salt bodies can now be studied at relatively high resolution using modern industrial 3D seismic reflection data (Van Gent et al., 2011; Cartwright et al., 2012; Fiduk and Rowan, 2012; Strozyk et al., 2012, 2014; Jackson et al., 2014, 2015). In addition, improvements in geomechanical modelling techniques, has allowed major advances to be made (Chemia et al., 2008; Albertz et al., 2010; Albertz and Ings, 2012; Goteti et al., 2012; Li et al., 2012a, 2012b).

Evaporites like carbonates and sulfates (anhydrite, polyhalite, tachydrite), and the K-Mg chlorides bischofite (MgCl2*6H2O) and carnallite (KMgCl3*6H2O), are rheologically and mechanically different from the polycrystalline halite and may impact the internal deformation of salt structures (Geluk, 1998; Strozyk et al., 2014). Compared to rock salt, the effective viscosity of K- and Mg-salts is up to three orders of magnitude lower (Eekelen et al., 1981; Urai 1983; Urai 1985; Urai and Boland 1985; Urai 1987; Spiers et al., 1983; Langbein, 1987; Scott Duncan and Lajtai, 1993; Schenk and Urai, 2005; Urai et al., 2008), while anhydrite and carbonates have much higher viscosity than rock salt and thus form buckle folds during compression. Furthermore, anhydrates and carbonates are brittle, thus they may rupture in extension or compression (Müller et al., 1981). The interaction of layers with such contrasts in viscosity and rheology during deformation must lead to the development of complex fold and boudin structures. At the meso-scale, these complex internal geometries in layered evaporites are documented in mine galleries and in drill cores (Martini, 1953; Siemeister, 1969; Bornemann and Fischbeck, 1991; Burliga, 1996; Zirngast, 1996; Behlau and Mingerzahn, 2001; Bornemann et al., 2008; Schléder et al., 2008; Hammer et al., 2014). K-Mg salt-rich layers typically show complex, internal folding on the meter to mm-scale, even if the entire package of layered evaporites is less deformed.

The role of high-viscosity, brittle-ductile layers (also called stringers) in salt deformation has been studied using 3D seismic data (Van Gent et al., 2011; Cartwright et al., 2012; Fiduk and Rowan, 2012; Jackson et al., 2014, 2015; Strozyk et al., 2014), laboratory experiments, analogue models, and numerical modeling. More specifically, these techniques have been used to understand the complex folds, faults, and boudinage of stringers as a result of deformation of the surrounding salt. Deforma-

tion experiments on layered salt show the influence of different rheologies and the mechanics during stringer extension (Liang et al., 2007; Zulauf et al., 2010). Additionally, analogue and numerical models described the evolution of salt flow and stringer deformation (Jackson and Talbot, 1989; Koyi, 2001; Talbot and Aftabi, 2004; Zulauf and Zulauf, 2005; Chemia et al., 2008, 2009; Brun and Mauduit, 2009; Cartwright et al., 2012; Li et al., 2012a, 2012b; Dooley et al., 2015).

In contrast, we have a poorer understanding of the influence of low-viscosity layers of K-Mg salts. In this study we focus on bischofite and carnallite, although we note that other salts like tachydrite (Poiate et al., 2006) have also a very low viscosity, which have been described in evaporites offshore Brazil. The low viscosity of deeply buried K-Mg salts combined with their high solubility is a well known source of drilling problems and casing instability (Williamson et al., 1998). On the other hand, carnallite and bischofite are economically interesting and are mined in a number of locations (Vysotskiy and Kislik, 1987; Cerqueira et al., 1997).

There are a few known bischofite deposits with economically significant thickness worldwide, these occur in the Caspian and Kaidak basins in Kaszakhstan, the Dneiper-Donets and Pripyat in Ukraine, the Gabon and Congo basins on the African platform, the Sergipe Basin in Brazil and the West European basin (Vysotskiy and Kislik, 1987). One of these rare occurrences of thick bischofite layers occurs on the southern edge of the Groningen High in the NE Netherlands, where it is solution mined by the squeeze mining technique (Fokker, 1995). Bischofite is the last mineral precipitating during a full evaporation cycle (Lotze, 1957; Warren, 2006). For its precipitation out of bittern brines, extremely arid conditions are required. Seawater refreshing events in salt basins normally prevent the deposition of bischofite or dissolve it, while carnallite is more frequently formed (Borchert and Muir, 1964). Besides climate, tectonic processes that change the surface morphology play an important role in the depositional architecture of evaporites (Geluk et al., 2000).

In this project we studied two salt pillows, the Veendam Pillow and Slochteren Pillow in the NE-Netherlands. Here, meter-thick layers of carnallite and bischofite were discovered in the Veendam Pillow in the 1970s (Coelewij et al., 1978). Today the K-Mg salts are produced by NEDMAG Industries using the squeeze mining technique (cf. Geluk et al., 2007). The bischofite layers in the Veendam Pillow are part of uppermost Zechstein III cycle, interbedded with carnallite and halite. Coelewij et al. (1978) studied this structure based on 2D seismic data and data from wells (VDM-1 to VDM-4), which are located on the eastern flank of the Veendam Pillow. The local Top Salt geometry and the occurrence of thick K-Mg salts were said to be the result of a combination of preferential and differential salt flow. Preferential flow is caused by differences in salt viscosity: for example due to higher temperature in the lower part of the Zechstein, this interval takes up most of the strain, while the upper sec-

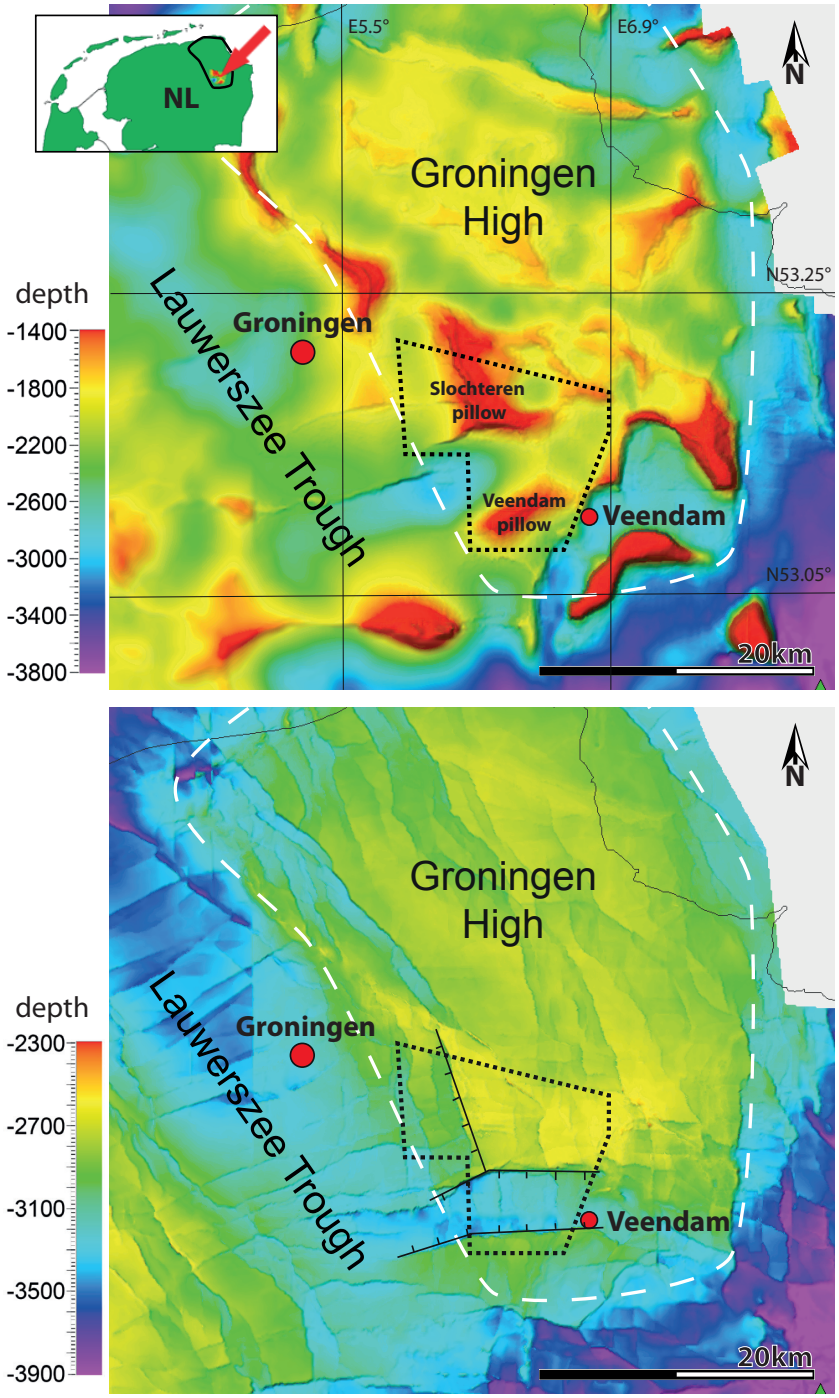


Fig. 2.1: (a) Top Salt map from the Groningen High (outline marked by white dotted line) and surrounding areas (modified after Strozyk et al. (2014)). The black dotted line indicates the outlines of 3D seismic volumes covering the study area; (b) Base Salt map from the Groningen High and surrounding areas (modified after Strozyk et al. (2014)). Major normal faults (offset < 100m) in the study area are marked.

tion folds with much less internal strain. Differential flow is caused by differences in viscosity between layers leading to local strain differences. The result of preferential flow was interpreted to cause the strong thickness variation in the lower ZII halite. In the top part of the Zechstein section, ZIII layers of strongly different composition and viscosities are present. The high viscosity contrast between the layers was proposed to lead to strain concentrated in the softer carnallite and bischofite-rich layers. The result is the formation of "sub-pillows" of low-viscosity evaporites during halokinesis. While these interpretations represented the state of the art in the seventies, the role that the primary sedimentary architecture had on the initial thickness differences was not addressed, and no quantitative analysis or

prediction of the "sub-pillows" was provided.

In summary, studying the deformation of evaporites with extreme mechanical stratification will contribute to our understanding of salt tectonics, by exploring how the original compositional variations control rheology and styles of salt structures that form. Furthermore, it will contribute to exploration and production of potassium-magnesium salts by helping predict lithologies that often lead to drilling problems. In addition, it contributes to develop techniques that will assist to predict the internal structure of potential nuclear waste repositories in salt (Gärtner et al., 2008; Kukla et al., 2011).

The aim of this study is to gain a better understanding of the initial architecture and structural evolution of layered evaporite deposits, focusing on K-Mg salts and on the role of the anhydrite-carbonate stringer in the formation of intrasalt structure.

2.3 Geological setting

The study area is 10 km southeast of the city of Groningen, in the area between Veendam and Slochteren in the NE Netherlands. Geologically, the area is located at the southernmost edge of the Groningen High (Fig. 2.1), between the northwest-southeast trending Lauwerszee Trough in the west and the Lower Saxony Basin in the south-east (Fig. 2.1). As part of the Lower Permian Basin it has a complex geological history, with multiple tectonic phases of extension, compression, and halokinesis (Ziegler, 1978; Mohr et al., 2005; De Jager, 2007; Geluk et al., 2007). This complex history can be

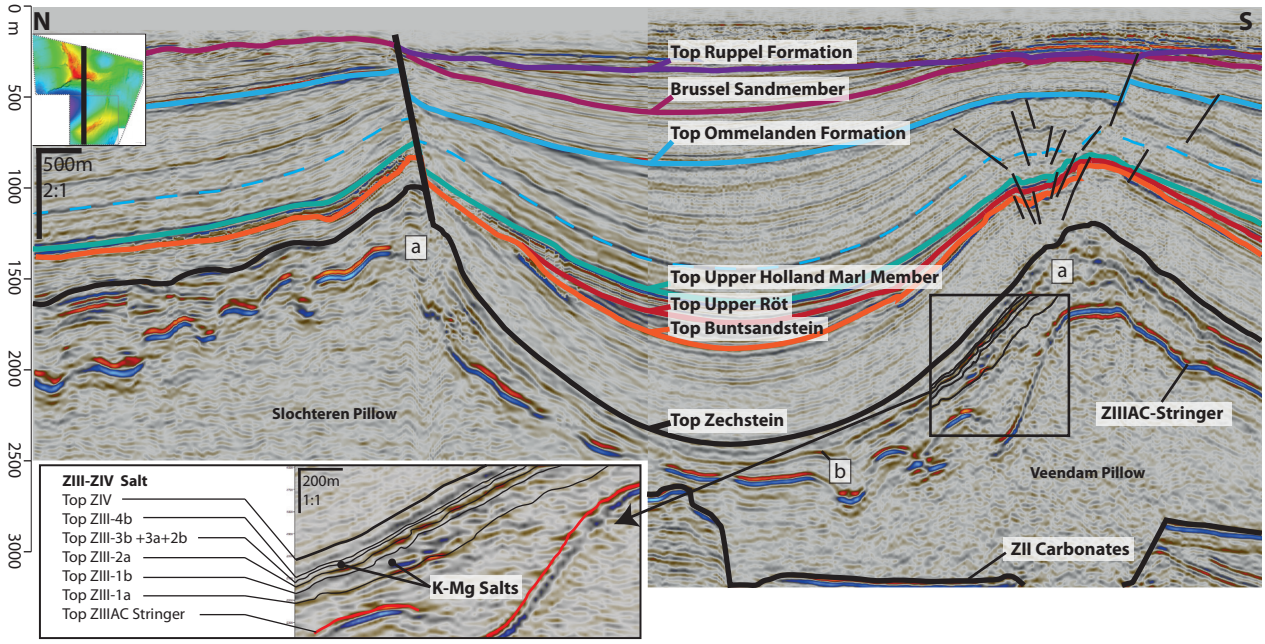


Fig. 2.2: N–S profile through the study area with the Slochteren Pillow in the north (volume 2) and the Veendam Pillow in the south (volume 1). The black lines indicate a normal fault at the south margin of the Slochteren Pillow and smaller faults above the Veendam Pillow forming a crestal collapse graben. The basin between the pillows shows significant thickening of most layers. The Z3 stringer is separated under the basin and folded and thrusted in the pillows. Bottom: Detailed view of the salt layers in the top of the salt bodies. (a): decline of seismic quality in the pillow crest. (b): merging of reflections under the basin.

summarized in four main tectonic phases (De Jager, 2007): (1) The Paleozoic Caledonian and Variscian orogenies caused by the assembly of the Pangea supercontinent, (2) rifting during the breakup of Pangea in the Mesozoic, (3) the collision of Africa and Europe that led to the Alpine inversion during the late cretaceous and Early Tertiary, and (4) the development of the Rhine Graben rift system from the Oligocene to recent. Key structural processes included the formation and reactivation of basement faults, deformation of Zechstein salts, and strongly decoupled extensional and transpressional faulting in the suprasalt sediments. Halokinesis is interpreted to have been triggered by reactivation of basement faults, which led to differential loading and salt withdrawal (Geluk et al., 2000).

The subsalt Permian Rotliegend is strongly deformed by E-W and N-S to NNW-SSE striking normal and strike-slip faults that form a network of graben to half-graben structures (Fig. 2.1; also see (De Jager, 2007; M. C. Geluk, 2007; Biehl et al., 2014). The Zechstein section in the study area contains fully developed Z-I to Z-IV cycles. The thin and well-stratified ZI and lower ZII sequences are seismically harmonic with the Rotliegend-Zechstein contact, and are mechanically considered to be part of the subsalt. A prominent high-amplitude reflector commonly interpreted as "Base Salt" represents the transition from the ZII salt to Top ZIIC carbonates (Fig. 2.2 & Fig. 2.4). The thickness of the overlaying, seismically chaotic to transparent ZII rock salt varies from c. 50 m below salt withdrawal basins to up to 1.8 km in flanking salt pillows. In general, the ZII salts are mainly composed of halite (>95%; Geluk et al., 2000).

The ZIIIAC stringer represents the base of the ZIII unit and consists of the gray Salt Clay, overlain by the 0.5-20 m thick Plattendolomit and the 15-130 m thick Hauptanhydrit (Van Gent et al., 2011). As the stringer is thick and encased in rock salt, it produces a high-amplitude reflection in the seismic data (Van Gent et al., 2011; Strozyk et al., 2012, 2014).

The ZIII and ZIV units above the stringer are compositionally and mechanically layered (Coelewij et al., 1978), and are traditionally subdivided into several subunits (Fig. 2.3). The seismically transparent lower ZIII is 100 to 300 m thick. The ZIII-1 to -4 show a number of seismic reflections thought to reflect interbedding of halite with K-Mg salt-rich layers in the ZIII-1b, -2b and -3b. Besides halite, the most common minerals here are carnallite, kieserite, and anhydrite, whereas in ZIII-1b bischofite is also present (Coelewij et al., 1978). Drill cores in the study area were used to differentiate varying evaporation conditions for the ZIII-1b compared to the ZIII-2b and 3b (Coelewij et al., 1978). ZIII-1b shows numerous alterations of bischofite, carnallite and halite as result of a regularly reversed evaporation process caused by intermittent influx of fresh seawater with a subsequent drop in salinity. The result are thin layers composed of one or two minerals such as halite, kieserite, which is indicative of shallow water co-precipitation (Coelewij et al., 1978). In ZIII-2b and -3b, indistinct bedding and

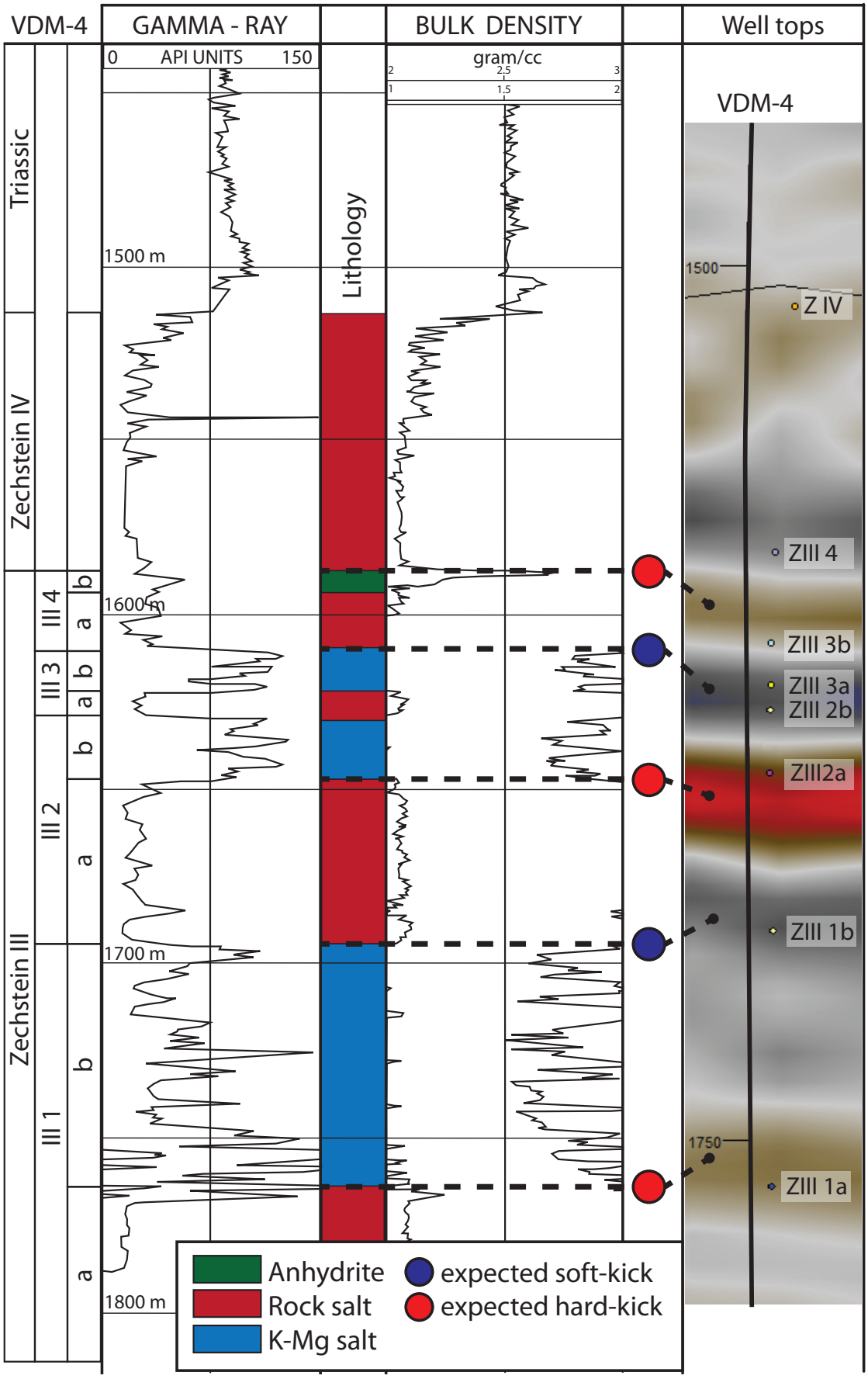


Fig. 2.3: VDM-4 Well-log and expected seismic response compared to the real seismic response.

weak development of cycles with intimate mixing of carnallite and halite crystals is thought to be the result of co-precipitation. Co-precipitation was interpreted to be caused by concentration stratification and simultaneous precipitation in two brine layers (Coelewij et al., 1978). The halite forms in the higher, less concentrated stratum, while the carnallite forms in the lower, higher-concentration/density stratum (Coelewij et al., 1978). This means that the water column during the ZIII-2b and 3b precipitation was higher than during the ZIII-1b precipitation. Coelewij et al. (1978) used seismic acoustic impedance (AI) to evaluate the K-Mg grade of the layer. The percentage of carnallite and bischofite in a layer was interpreted to be inversely proportional to the AI and only disturbed by the high AI of kieserite.

The Zechstein is overlain by Triassic (Buntsandstein and upper Röt), Cretaceous (Rijnland and Chalk) the Tertiary units (Lower/Middle and Upper North Sea Group) and the Quaternary. The Jurassic is not present in the study area (Wong, 2007a).

2.4 Data and Methods

We used two PSDM (pre-stack depth migrated) 3D seismic volumes of different sizes and ages, provided by Nederlandse Aardolie Maatschappij (NAM). The southern seismic volume mainly covers the Veendam Pillow covers of 46 km² and images down to 3.25 km depth. The northern volume covers 135 km² and images down to 2.5 km depth (Fig. 2.2 & Fig. 2.5). Both seismic volumes overlap by 30 km² and display vertical offsets between reflections due to differences in the velocity model during data processing. This offset is, however less than 30 m.

Furthermore, over 100 wells and side-tracks from 15 well locations, were provided by NEDMAG and are publically available on the TNO online database. The included well tops and well log data were mainly used for well-to-seismic tie. Stratigraphic boundaries of the upper Zechstein cycles (ZIII-1 to ZIV) were identified from existing well top information or were interpreted from well logs (GR, DEN). Interpreted log data showing the lithological composition was available for wells TRC-1 to -9 (TRC = Tripscompagnie) and VDM-1 to -4 (VDM = Veendam). Most wells were drilled into the Rotliegend penetrating the whole Zechstein salt, except the TRC and VDM wells, which terminate in the ZIII-1a.

Based on the well-to-seismic tie 15, Zechstein seismic horizons were interpreted using Schlumberger's Petrel. Horizons were picked by a combination of manual and automated methods based on the continuity and connectivity of reflections. The interpreted horizons are Base Salt (= Top ZII-A), Top ZIII-AC ("stringer"), Top ZIII-1a, Top ZIII-1b, Top ZIII-2a, Top ZIII-2b+ ZIII-3a + ZIII-3b, Top ZEIII-4b and Top Salt (Top ZIV) (Fig. 2.2 & Fig. 2.3). Layers ZIII-2b to ZIII-4b are not resolved in the seismic volume 2.

Major stratigraphic units in the Zechstein's overburden were interpreted to help us reconstruct the study areas salt tectonic evolution: (i) Top Buntsandstein (Triassic), (ii) Top Upper Röt (Triassic), (iii) Top Upper Marl Member (Cretaceous), (iv) Top Chalk (Cretaceous), (v) Top Mid Brussels Sand Member (Tertiary), and (vi) Top Rupel Formation (Tertiary). Additionally, one intermediate reflection within the Chalk was interpreted (Fig. 2.2 and Fig. 2.6). Stratigraphic thickness maps were calculated to identify sediment thickness changes. These changes were used to identify the timing and special variations in subsidence and uplift. The thinning of sediments above salt highs is used to identify reduced or non-deposition, or even uplift and erosion.

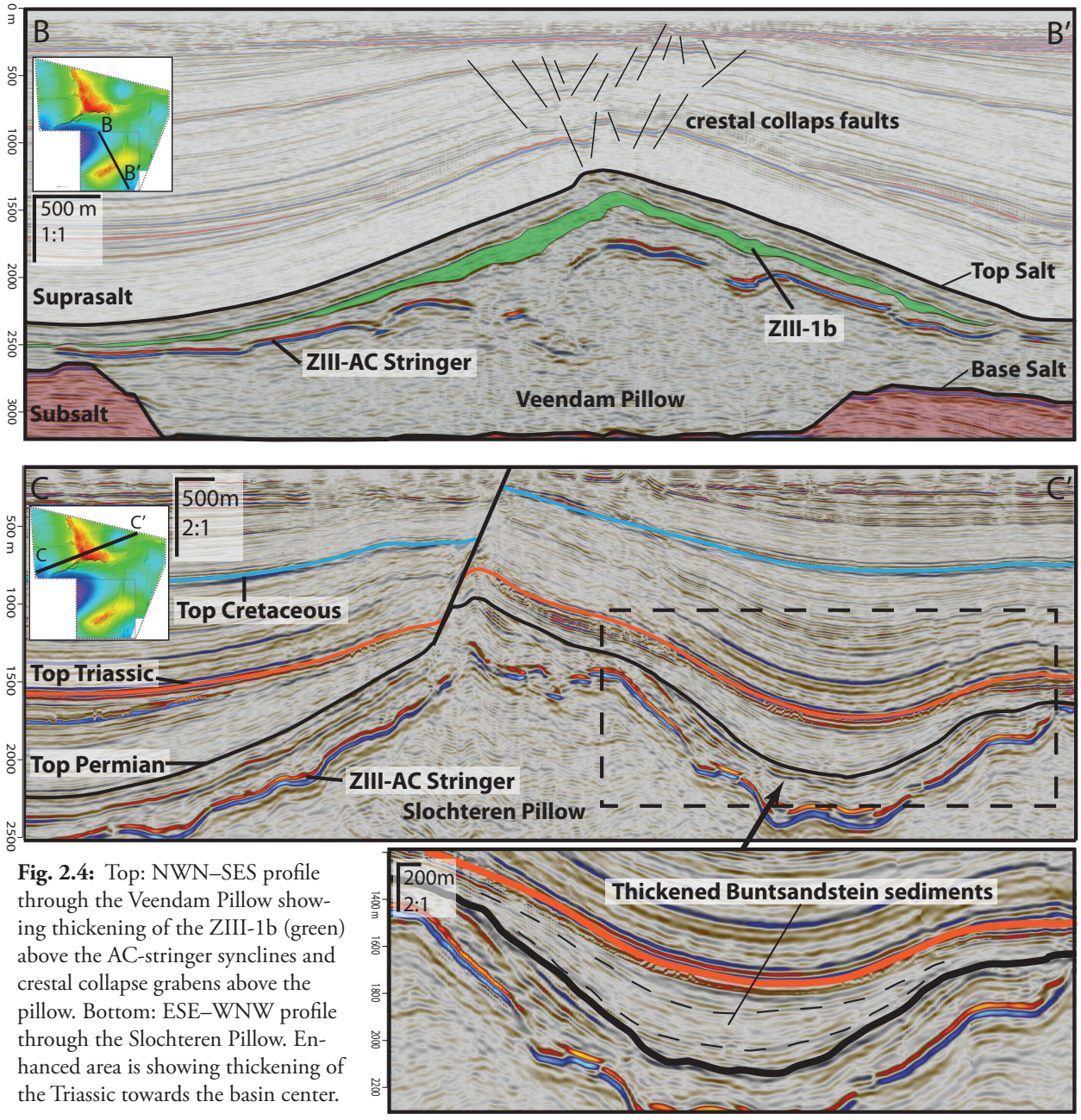


Fig. 2.4: Top: NWN–SES profile through the Veendam Pillow showing thickening of the ZIII-1b (green) above the AC-stringer synclines and crestal collapse grabens above the pillow. Bottom: ESE–WNW profile through the Slochteren Pillow. Enhanced area is showing thickening of the Triassic towards the basin center.

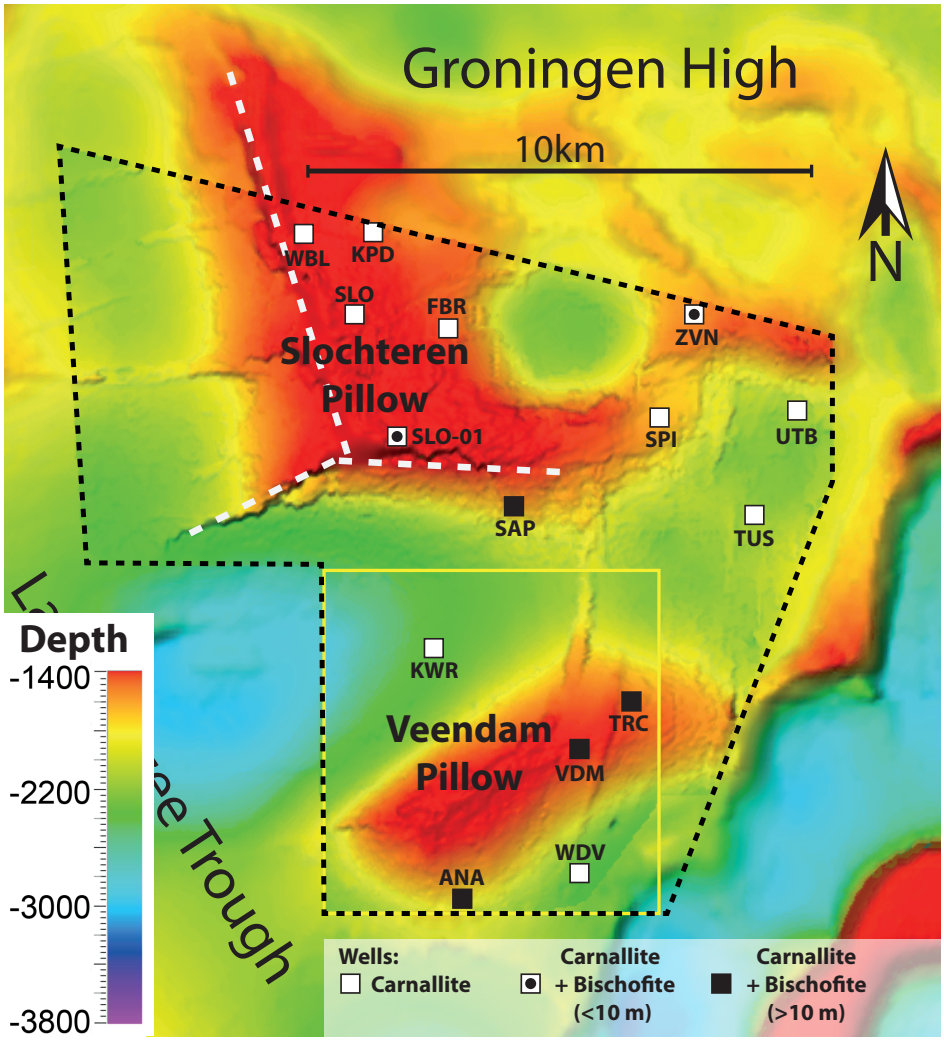


Fig. 2.5: Top Salt surface map compiled after Strozyk et al. (2014) and this study, with well head locations. White dotted lines indicate major suprasalt faults at the Slochteren Pillow. The black dashed box indicates the study area and the yellow box indicates the location of seismic volume 1.

2.5 Results

2.5.1 Structural overview of the study area

The Rotliegend is crosscut by mainly E-W and N-S to NNW-SSE striking normal and occasionally strike-slip faults (Fig. 2.1). The faults generally have offsets smaller than 100 m, with two larger, E-W striking normal faults bounding a 400 m deep graben below the Veendam Pillow (Fig. 2.1 & Fig. 2.7).

Two salt pillows are identified in the study area, the Veendam (cf. Coelewij et al., 1978) and Slochteren pillows (Fig. 2.5), which are surrounded by salt withdrawal basins filled by up to 3 km of post-salt strata (Fig. 2.5). Post-salt sediments are generally thicker in the basins and thinner above the salt pillows (Fig. 2.6). The Veendam Pillow strikes SW-NE and is 10 km long in the NE-SW direction and 5 km wide. The Zechstein is 2600 m in the pillow core, and the top of the pillow is at 1100 m depth. The Slochteren Pillow extends 10 km in the E–W and 14 km in the N–S direction. The Zechstein is of 1800m in the pillow core and the top of the pillow is 1000 m below the surface. The overburden of the Slochteren pillow is deformed by a large, N-S striking fault and a smaller E-W strik-

ing fault are located on its eastern and southern flank (Fig. 2.1 & Fig. 2.7).

The Top Salt surface of the two pillows is generally smooth, locally offset by faults in the post-salt sediments. These faults can be divided into two groups: (1) normal faults with small offsets (< 100 m) forming grabens above the pillows (Fig. 2.2 right side,Fig. 2.5 top), and (2) normal faults with throws that can be traced from Top Salt up to the Mid Tertiary (Fig. 2.2 left side, Fig. 2.5 bottom), offsetting the postsalt sediments by up to 350 m and 200 m for the N–S and E–W trending faults, respectively. The smaller normal faults are associated with elongated anticlines in the Top Salt surface (Fig. 2.5&Fig. 2.7a), these anticlines are up to 500 m wide and up to 100 m high, showing classic reactive piercement geometries (Hudec and Jackson, 2007). The crest of the Slochteren Pillow is dominated by bigger faults (Fig. 2.2 & Fig. 2.5), but lack an anticline at top salt.

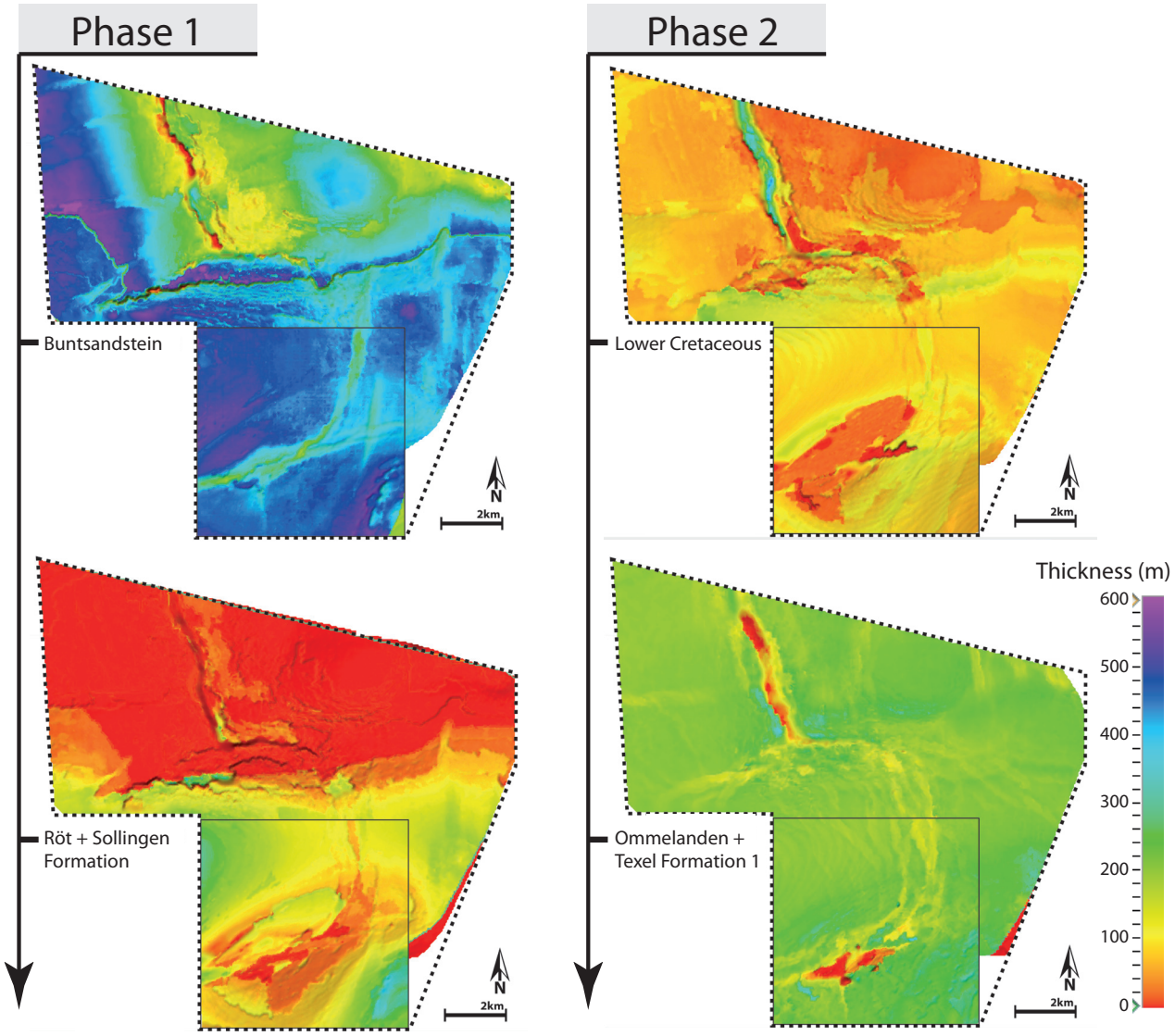
2.5.2 Stratigraphic units

ZIII-AC stringer

The fragmented ZIII stringer has an average thickness of 40 m. Below salt withdrawal basins the stringer is rather flat and parallel to Top Salt, while it shows complex patterns of rupture folding and tectonic duplication in the pillows. Fold axes have a wide range of strikes, are often curved in harmony with Top Salt (Fig. 2.8). N-S and ENE-WSW striking folds are more common in the Veendam Pillow, whereas E-W and NNW-SSE striking folds occur in the Slochteren Pillow. Fold amplitudes are mostly < 100 m, reaching up to 300 m in the northern flank of the Veendam Pillow. Stringer fragments that overlap a few tens of meters as well as a complex pattern of gaps are observed. In the Veendam pillow, the largest NE-SW striking gaps occur on the NW-flank of the pillow, whereas gaps in the center of the Slochteren pillow gaps define an almost polygonal pattern (Fig. 2.8).

ZIII-1 to IV

The ZIII-1a, -2a, and -3a halite layers represent are inferred to relatively strong units, whereas the K-Mg salt-rich ZIII-1b, -2b and -3b layers are interpreted to be relatively weak (Fig. 2.3). The reflectors, representing the boundaries between these units are mostly continuous, with two exceptions: (i) reflection continuity and amplitudes decrease strongly towards the tops of salt pillows (i.e., reflections cannot be traced in the Veendam Pillow crest, show several gaps in the Slochteren crest, and are not visible below suprasalt faults at the Slochteren Pillow) (Fig. 2.2), and (ii) under sedimentary basins the top ZIII-1a and Top ZIII-2a reflections merge, and Top ZIII-1b becomes invisible (Fig. 2.2). The top ZIII-1b to -3b reflectors principally follow Top Salt, and the units in between thicken towards the pillows' crests. In general, the thickness variation of <30 m to ca. 400 m in the K-Mg salt-bearing



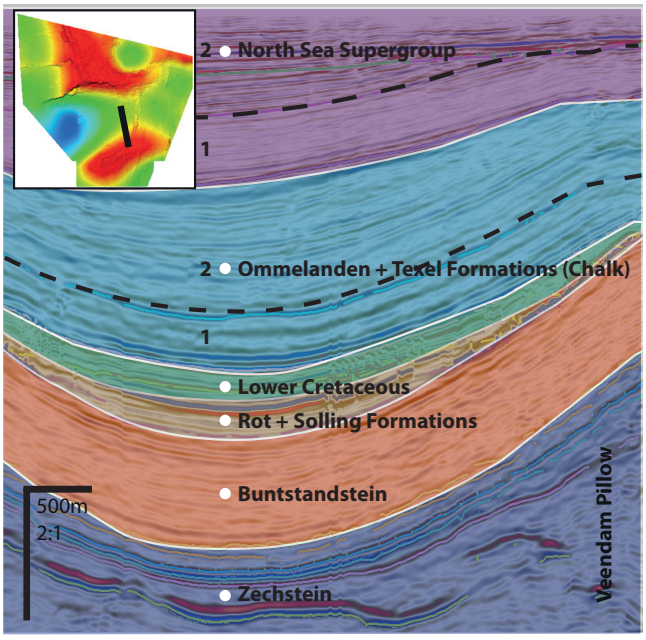
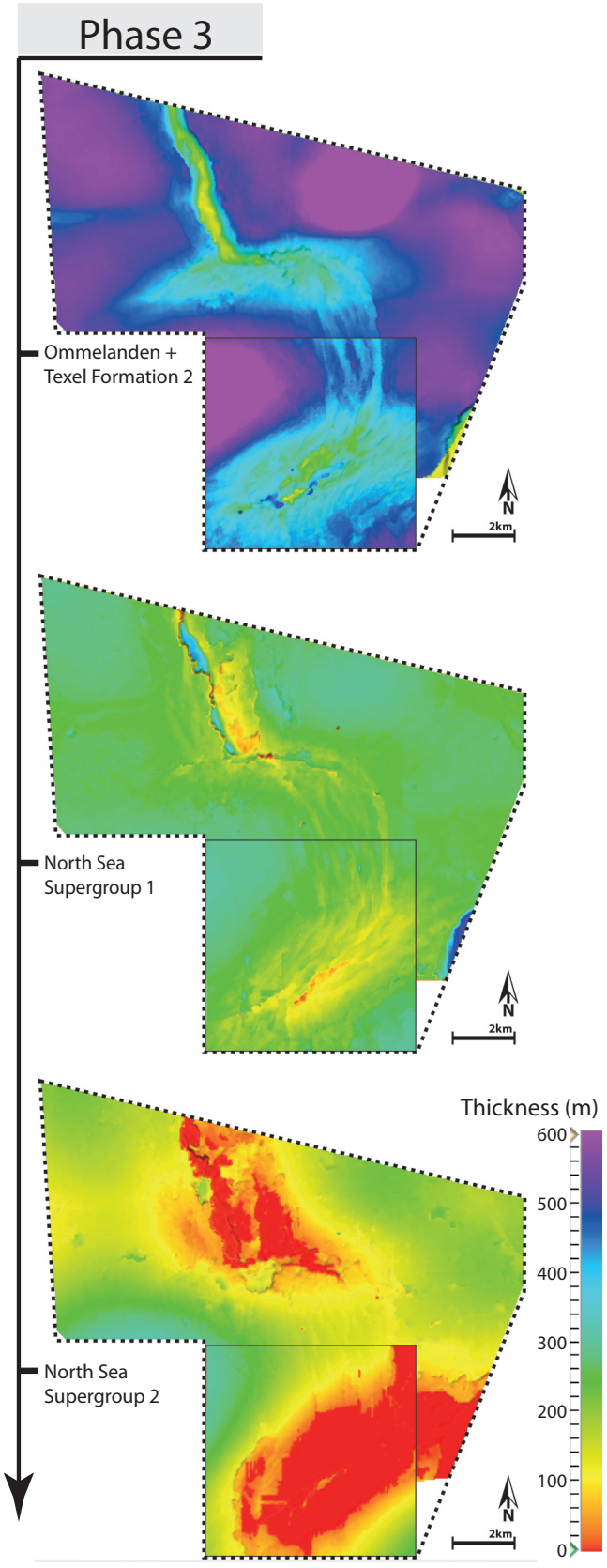


Fig. 2.6: Supersalt thickness maps of the units mark in the profile at the bottom. Due to the influence of faults in the superasalt the thickness information in the center of the pillows is faulty. The dotted line in the chalk indicates the change from phase 2 to phase 3. The thickness maps show substantial thickening above the basins in phase 1 and 3 and constant thicknesses in phase 2.



ZIII-1b is much larger than in other units and partially correlates with the stringer geometry (Fig. 2.7d & Fig. 2.8). More specifically, the ZIII-1b is thicker above stringer fold synclines than above fold anticlines. The ZIII-1b thickness reaches its maximum (Fig. 2.7d) above the deep stringer anticline at the north-western flank of the Veendam Pillow (Fig. 2.8, profile B). In addition, ZIII-1b is thicker directly below the small anticlines of Top Salt (see section: Discussion, Phase 3). The ZIV generally marks Top Salt, except in parts of the Slochteren Pillow, where this unit is absent.

Postsalt

The Lower Triassic Buntsandstein sediments represent the oldest Postsalt sediments above the salt with an average thickness of ca. 100 m above the Slochteren Pillow. Above the Veendam Pillow the Buntsandstein is around 400 m thick, in the surrounding basins the unit is up to 550 m thick (Fig. 2.6). Above the Top Salt anticlines (see section: Discussion, Phase1; Fig. 2.7) the Buntsandstein can be as little as 200 m thick. Adjacent to the anticlines it shows a minimum thickness of 400 m at the western flank of the Veendam Pillow (Fig. 2.6). Top Bundsandstein has a conformable upper contact with the Upper Triassic Upper Röt Formation, whereas it has an erosional contact with the Upper Marl Member in the northern part of the study area (Fig. 2.2), where the Upper Röt is missing (Fig. 2.6).

The Upper Triassic Upper Röt and Solling formations together have an average thickness of 200-

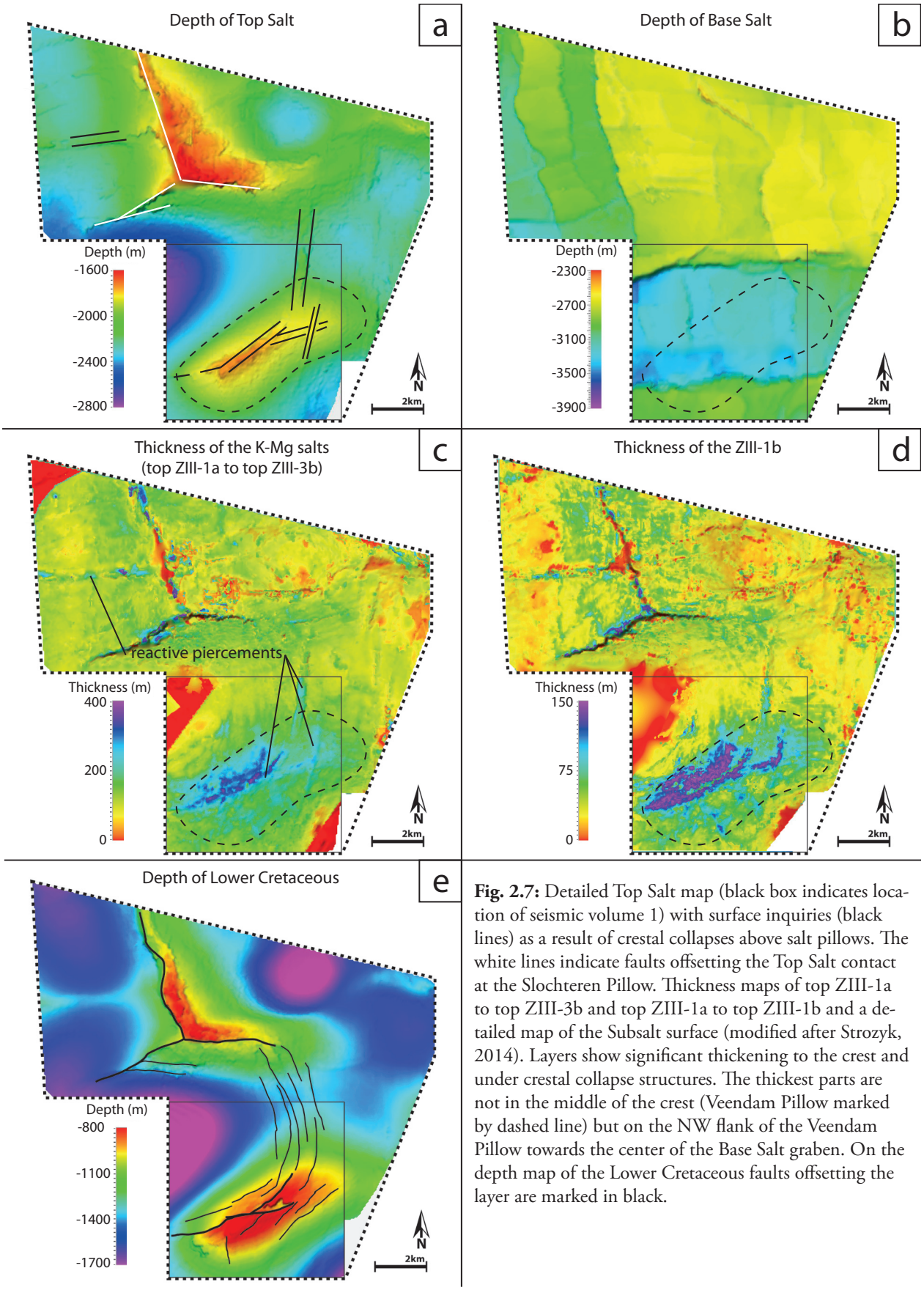


Fig. 2.7: Detailed Top Salt map (black box indicates location of seismic volume 1) with surface inquiries (black lines) as a result of crestal collapses above salt pillows. The white lines indicate faults offsetting the Top Salt contact at the Slochteren Pillow. Thickness maps of top ZIII-1a to top ZIII-3b and top ZIII-1a to top ZIII-1b and a detailed map of the Subsalt surface (modified after Strozyk, 2014). Layers show significant thickening to the crest and under crestal collapse structures. The thickest parts are not in the middle of the crest (Veendam Pillow marked by dashed line) but on the NW flank of the Veendam Pillow towards the center of the Base Salt graben. On the depth map of the Lower Cretaceous faults offsetting the layer are marked in black.

300 m in the salt withdrawal basins, whereas it is significantly thinner above the Veendam Pillow (Fig. 2.6). This unit is not present above the Slochteren Pillow (Fig. 2.6).

The Cretaceous Upper Marl Member varies in thickness from 50 to 140 m. In contrast to the underlying units, it is not preferentially thicker in the basins (Fig. 2.6). The units upper and lower contacts are mostly concordant (Fig. 2.2 & Fig. 2.5).

The Cretaceous Chalk is 300 to 850 m thick and is divided into two seismically different subunits. The lower subunit shows no significant change in thickness across the study area (Fig. 2.6), while the upper subunit is thicker in the salt withdrawal basins and is truncated at its top by the Base Tertiary (Fig. 2.2&Fig. 2.4).

The Mid Brussels Sand Member of the Tertiary North Sea Supergroup shows a thickness of 100 m above the pillows, which increases up to 270 m in the flanking basins (Fig. 2.6). The unit's top is mostly concordant to overlying strata. An exception can be observed at the Slochteren Pillow where thinning and toplaps in footwall position of the supra salt truncating faults is visible (Fig. 2.2 & Fig. 2.4).

The Rupel Formation of the Tertiary North Sea Supergroup is thick in the basins and significantly thins and terminates towards the salt pillows, (Fig. 2.6). Younger sediments are not or are only partly resolved in the seismic data, and were thus not interpreted.

2.5.3 ZIII K-Mg salts in well data

Bischofite: Well data show abundant bischofite in the southern part of the study area (Fig. 2.5). Highest concentrations were identified in TRC wells on the eastern flank of the Veendam Pillow, where bischofite shows a cumulative thickness of up to 58 m. Significant cumulative bischofite thicknesses (i.e., >10 m) are also present in the VDM wells, the Annerveen-Anlo (ANA -01) well at the south flank of the Veendam Pillow, and the Sappemeer (SAP) wells on the south-eastern flank of the Slochteren Pillow. Furthermore, bischofite is present with 5 m cumulative thickness in a Slochteren (SLO-01) well in the crest of the Slochteren Pillow and in the Zuiderveen (ZVN-01) well (i.e., 6 m) in a small salt high at the north-eastern boundary of the study area. Wells on the Slochteren Pillow north of SLO-01 (i.e., Froombosch (FBR), Kooipolder (KPD) and Woudbloem (WBL)) show no significant bischofite occurrences. Also, no bischofite is present in the basins east of the Slochteren Pillow at Spitsbergen (SPI), Tusschenklappen (TUS) and Uiterburen (UTB), in the basin west between the two pillows at Kiel-Windeweer (KWR), and south of the Veendam Pillow at Annerveen-Wildervank (WDV).

Carnallite: Carnallite is present in all wells in the study area. Cumulative thicknesses are generally higher in the pillows than in the basins. The highest concentrations of 70 to 136 m cumulative thickness are found in the southern part of the study area in TRC and VDM wells in the Veendam Pil-

low. South of this, thicknesses of 30 to 65 m occur. In the Slochteren Pillow, around 50 m cumulative thickness were identified in SLO, FRB, KPD, and SAP. In the basins east of the pillow, only 10 to 30 m cumulative carnallite thicknesses are present in the TUS and UTB wells.

2.6 Discussion

2.6.1 Sedimentary architecture and K-Mg salt deposition

As the K-Mg salt layers have a much lower viscosity than the halite, there is the potential for high strains in these layers. Therefore, the observed spatial variation in thickness can be either sedimentary or tectonic in origin, for both the carnallite and bischofite layers.

To allow for precipitation of a fully developed evaporitic cycle, including the deposition of significant amounts of bischofite, a pond-like morphological depression and prolonged arid conditions without seawater refreshing events is required. This could have been the case above the basement graben below the study area, where subsalt faulting may have produced gentle depressions in the evolving evaporites. Recent studies show that at least some subsalt faults in the study area were active during ZII and ZIII precipitation (Biehl et al., 2014; Strozyk et al., 2014) providing support for this hypothesis.. Mg-enriched residual brines are interpreted to have collected inside the depression of the carnallite-rich ZIII-1b layers above the basement graben, in the area where the Veendam Pillow later formed, with bischofite precipitation in local lenses (Fig. 2.9a). Smaller bischofite occurrences in other parts of the study area suggest the presence of several smaller ponds, or that later strains squeezed parts of the bischofite deposit towards some distal areas. Unlike the bischofite, carnallite was deposited regionally as continuous layers of varying thickness across the entire study area. The high concentration of bittern brines needed for bischofite concentration, explains why the ZIII and ZIV units are continuously present in the study area, while the bischofite was just locally accumulated. During the precipitation of the halite layers (ZIII-1a,2a,3a,4 and ZIV), the water level was high enough to flood the entire area and allow equal precipitation. We can expect the same situation during the carnallite + halite precipitation in the ZIII-2b and 3b. It is most likely that during the ZIII-1b the water level was lowered to an amount that marginal topography could impact the distribution of the last remaining brine. Thus, only affecting the bischofite distribution but not the occurrence of other minerals that were evaporated from less concentrated brine.

2.6.2 Salt tectonic evolution

To analyze the relative salt movements in the study area we consider the spatial and temporal changes in postsalt sediment thickness and the associated withdrawal and accumulation of salt pillows with thinning of sediments above. The resulting history of salt-tectonics can be summarized in three main phases (Fig. 2.6):

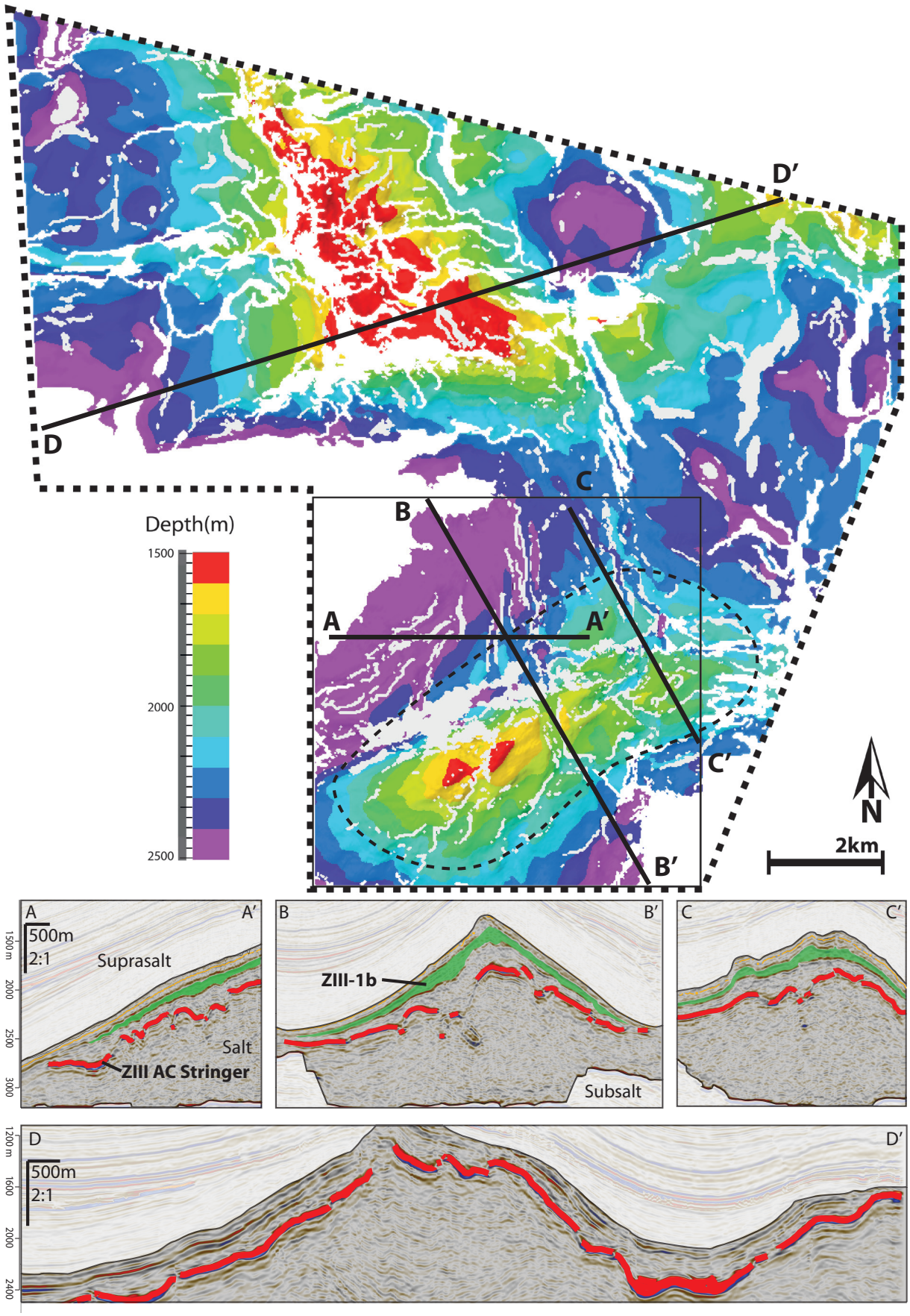


Fig. 2.8: Map view of the ZIII stringer showing the different rupture patterns in the two pillows with several profiles. The Veendam Pillow is outlined with the black dashed line.

Phase 1:

During the Triassic, localized differential loading in the early postsalt sediments induced salt withdrawal below the Veendam area, while salt flowed towards the area of the later Slochteren pillow, as indicated by strong variations in Buntsandstein thickness (Fig. 2.9). Regional extension during the Triassic (Mohr et al., 2005; M.C. Geluk, 2007; Vackiner et al., 2011) was described to cause faulting and rafting of the Triassic sediments. Thickening of Buntsandstein towards the basin center in the north (Fig. 2.5 bottom) indicates that salt movements occurred in the study area in this time. However, the rather tabular Buntsandstein geometries in the southern and western study area indicate that large areas were not affected by early differential loading and salt flow, and that most of the salt deformation took place later in the Late Triassic and Jurassic. The significantly thinner (i.e., 100 m) Triassic sediments above the Slochteren Pillow are therefore result of erosion of a tabular sediment layer that was truncated during the Jurassic hiatus. We infer that salt withdrawn from beneath the subsiding basins flowed mainly from the south and the east towards the Slochteren Pillow and also into the much more slowly inflating Veendam Pillow. Absence of Upper Röt sediments above the Slochteren Pillow indicates that, during the Late Triassic the pillow continued to rise. At the same time, reactive piercement structures in Triassic sediments above the Veendam Pillow evolved and formed small-scale Top Salt anticlines. These reactive piercement structures caused by regional extension fit into the rafting tectonics described by literature (Mohr et al., 2005; Vackiner et al., 2011).

Phase 2:

The Jurassic is absent (cf. Wong et al., 2007), whereas the Lower Cretaceous interval is 50 to 140 m thick and does not thicken into the salt withdrawal basins. The layer has a rather continuous thickness compared to the surrounding units in the study area. Constant sediment thicknesses in the lower part of the overlying Chalk is another sign that the salt movement was very slow.

Phase 3:

Significant thickening of upper Chalk sediments into the salt withdrawal basins indicates renewed salt flow into the Veendam and the Slochteren pillows (Fig. 2.9), caused by regional compression during the Late Cretaceous inversion (Wong, 2007b). The regional compressional buckling of the postsalt sediments led to salt rising together with local extensional bending in the sediments above the salt pillows and produced crestal collapses (cf. Mohr et al., 2005).

Salt tectonics continued during the Tertiary, but slowed during the deposition of the Lower North Sea Group. During deposition of the Middle and upper North Sea Group, faults above the Slochteren Pillow offsetting Top Salt were active (Fig. 2.2 & Fig. 2.5). The N-S striking and the E-W

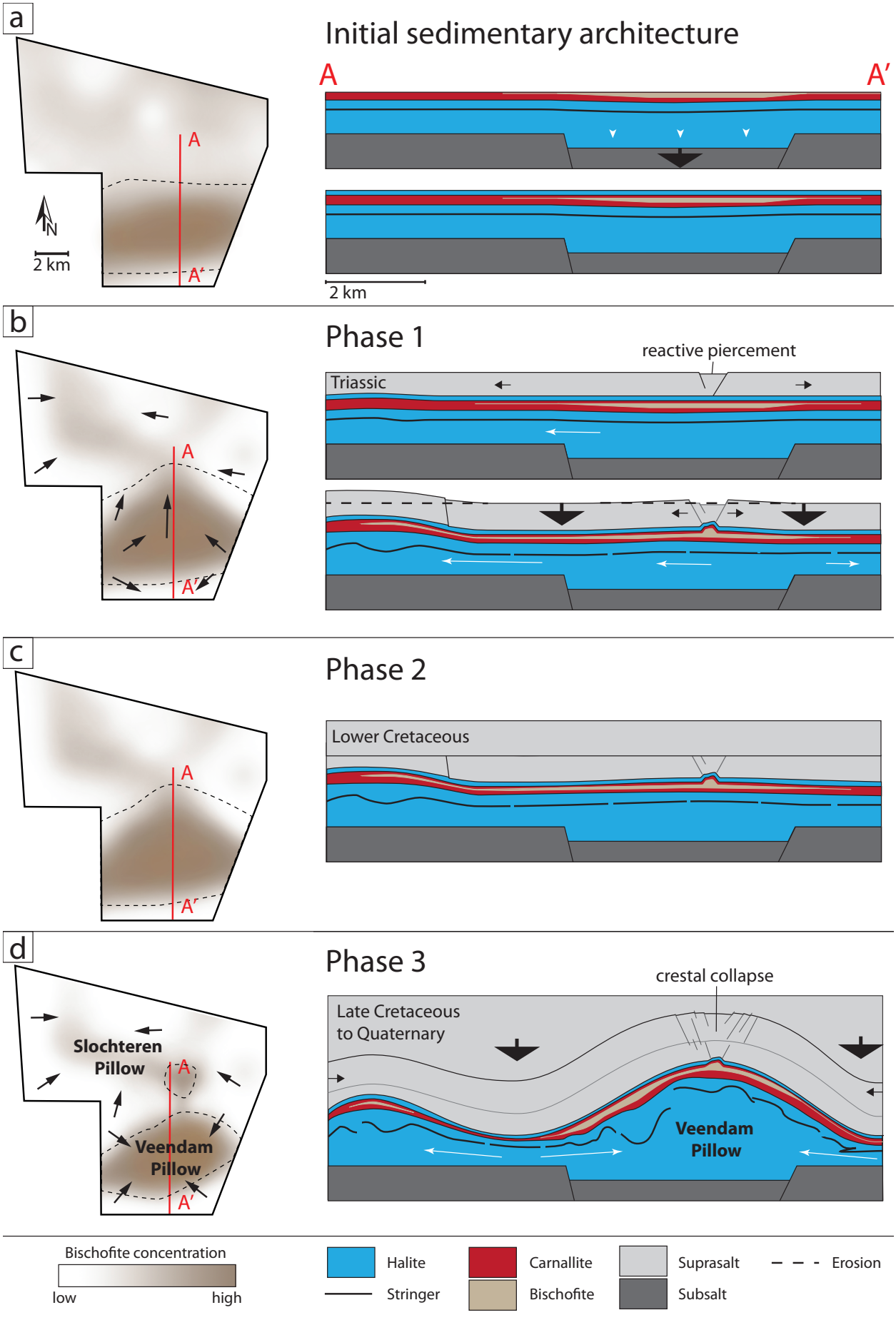

a
Initial sedimentary architecture
A
A′
N
2 km
2 km
b
Phase 1
reactive piercement
Triassic
c
Phase 2
Lower Cretaceous
d
Phase 3
crestal collapse
Late Cretaceous
to Quaternary
Slochteren
Pillow
Veendam
Pillow
Veendam
Pillow
Bischofite concentration
low
high
Halite
Stringer
Carnallite
Bischofite
Suprasalt
Subsalt
Erosion

Fig. 2.9: Conceptual sketch (depth not to scale) of salt deformation in the study area: maps on the left indicate movements in the bischofite deposit; the profile sketches on the right side indicate corresponding deformation of the Zechstein (incl. ZIII AC stringer and K-Mg salts) and the suprasalt sediments. Black arrows indicate movements in the suprasalt sediments (e.g., extension and subsidence), white lines movements in the salt (e.g. salt withdrawal below sediment basins): (a) tectonic movements in the subsalt allow for localized bischofite deposition in the area of the later Veendam Pillow; (b) differential loading and extension in the Triassic sediments and during Jurassic erosion cause salt withdrawal and boudinage of the ZIII stringer in the area of the later Veendam Pillow, while salt accumulation and doming farther north triggers the formation of the Slochteren Pillow; K-Mg salts are initially deformed by extensional features in the salt's overburden; (c) No deformation during stable phase 2; (d) ongoing subsidence and salt withdrawal below sedimentary basins cause the formation of the Veendam Pillow and further grow of the Slochteren Pillow. The bischofite deposits are dragged into the Veendam Pillow, where they deform due to ZIII stringer deformation and structures in the suprasalt.

striking fault are both parallel to faults in the Base Salt at the Slochteren pillow and offset into the hanging walls. Post-Tertiary sediments are significantly thicker in the basins than above the pillows indicating ongoing salt movement into the Quaternary.

2.6.3 Evolution of the internal structure of the salt

In addition to the location of the bischofite layers above the subsalt graben, the second argument for a locally confined carnallite-bischofite lens is the deformation history. If the original bischofite layer had been continuous over the study area, the first stage of deformation would have removed it from the area of the future Veendam pillow, and enriched it in the incipient Slochteren Pillow, which is not the case.

Coelewij et al. (1978) suggests that truncation of a salt body in contact with groundwater could lead to a loss of the highly soluble bischofite. However, the bischofite-rich ZIII-1b layer does not thin towards the faults offsetting the Top Salt in Slochteren (Fig. 2.2 & Fig. 2.5). Furthermore, it is more likely that only thin layers of bischofite were deposited here in the first place (Fig. 2.9). The up to 36 m thick bischofite encountered in the SAP wells, which are located on the south-eastern flank of the Slochteren Pillow, are interpreted as local fold hinge or boudin-neck (Fig. 2.9).

Coelewij et al. (1978) suggested the thick bischofite occurrences were caused by thickening in the fold hinges. From our thickness maps (Fig. 2.7c&d) however it is clear that the ZIII-1b layer's thickness does not conform to the salt pillow (Fig. 2.7a), it is rather located on the NW flank. This argues against redistribution at the scale of the pillow. An alternative explanation is related to the structural evolution of the anhydrite-carbonate stringer located deeper in the structure (Fig. 2.8).

A closer look at the rupture patterns of the stringer shows a strikingly different pattern in the Veendam and the Slochteren pillows (Fig. 2.8). In the Slochteren Pillow, the rupture pattern is consistent with stretching of the layer during the rise of the pillow (Abe et al. 2013), with two major boudin zones parallel to the crest, and smaller polygonal fractures in the crestal zone. In the Veendam Pillow, however, the largest ruptures are clearly off from the crest of the structure (Fig. 2.7d). To explain these,

we recall that the initial phase of salt flow was withdrawal from the Veendam area, which has led to boudinage and rupture of the stringer before the start of growth of the Veendam pillow (Fig. 2.9b).

The presence of the broken stringer fragments at the start of pillow growth is interpreted to have made the internal deformation of the Veendam pillow more heterogeneous. This led to the nucleation of smaller scale (few 100 m) folds in the surrounding halite, which in turn formed saddle reef structures where the bischofite was tectonically thickened (Fig. 2.8, profiles). During salt flow from the location of the later Veendam Pillow towards the Slochteren Pillow the ZIII stringer is dragged with the salt and boudinaged. Later, the salt flowed from the subsiding basins also into the Veendam Pillow. The ZIII stringer was dragged with the salt, which locally led to compression structures like folds and thrusts (Fig. 2.9d). This deformation localized flows in the overlaying mobile K-Mg salts to significantly thicken above stringer synclines.

A secondary effect of the extension during Late Triassic and the formation of reactive piercements is flow in topmost salts that were dragged into the bottom of these structures. We propose that especially the highly mobile K-Mg salts filled the space formed by the faulted sediments above Top Salt.

While all these processes may affect the entire salt section, the low viscosity of the K-Mg-rich salts amplifies and speeds up these effects by magnitudes:

1. On large scale, K-Mg salts are passively dragged with the general salt flows, and thus preferably occur inside salt highs. Here, their thickness further increases towards the crest, which results from radial salt flows towards the center of the salt high.

2. In addition, faulting in the salt's overburden may trigger the mobile K-Mg salts to flow into the space created by the deformation of the overlying rocks.

3. K-Mg salts can be highly influenced by deformation of high-viscosity layers in their vicinity (e.g., anhydrite and carbonates). Folding of such layers may lead to strong thickness variations in the K-Mg salts on local scale.

2.7 Conclusions

In the NE Netherlands, two Zechstein salt pillows show exceptional thickness of carnallite and bischofite in the uppermost salt section. Initial precipitation of bischofite in the area of the future Veendam Pillow occurred from Mg-rich residual brines concentrated in surface depressions above an active basement graben. The rock salt layers contain the much weaker carnallite and bischofite layers and the much stronger Zechstein III Anhydrite - Carbonate stringer, providing an example of extreme rheological heterogeneities in a salt structure.

During a first stage of salt tectonics differential loading by Triassic sediments induced salt withdrawal from the area of the future Veendam Pillow, which led to boudinage of the ZIII Anhydrite - Carbonate stringer while the K-Mg lens remained relatively undeformed. This was followed by two phases of pillow growth separated by limited salt flow during the Jurassic to mid Cretaceous. The K-Mg salt layers were deformed with the evolving salt pillows. Deformation of K-Mg salt-rich layers in the evolving salt pillows was strongly disharmonic and strongly influenced by folding of the underlying ruptured ZIII stringer. The second phase of pillow growth triggered crestal collapse above both salt anticlines and large-scale faulting above the Slochteren Pillow. The highly mobile K-Mg salts were thickened in salt anticlines below the collapse structures.

Acknowledgements

The authors thank Nedmag Industries for the financial support and further thank NEDMAG and Nederlandse Aardolie Maatschappij (NAM) for providing the data. Schlumberger is thanked for providing Petrel seismic interpretation software under academic license. Furthermore, we are deeply grateful to the editors and reviewer Christopher Jackson as well as a second unknown reviewer for their many fruitful comments and suggestions that strongly improved our manuscript.

2.8 References

Abe, S., Urai, J.L., Kettermann, M., (2013). Fracture patterns in nonplane strain boudinage-insights from 3-D discrete element models. J. Geophys. Res. Solid Earth 118, 1304–1315. doi:10.1002/jgrb.50126

Albertz, M., Beaumont, C., Shimeld, J.W., Ings, S.J., Gradmann, S., (2010). An investigation of salt tectonic structural styles in the Scotian Basin, offshore Atlantic Canada: 1. Comparison of observations with geometrically simple numerical models. Tectonics 29, TC4017. doi:10.1029/2009TC002539

Albertz, M., Ings, S.J., (2012). Some consequences of mechanical stratification in basin-scale numerical models of passive-margin salt tectonics. Geol. Soc. London, Spec. Publ. 363, 303–330. doi:10.1144/SP363.14

Behlau, J., Mingerzahn, G., (2001). Geological and tectonic investigations in the former Morsleben salt mine (Germany) as a basis for the safety assessment of a radioactive waste repository. Eng. Geol. 61, 83–97. doi:10.1016/S0013-7952(01)00038-2

Biehl, B.C., Reuning, L., Strozyk, F., Kukla, P.A., (2014). Origin and deformation of intra-salt sulphate layers: an example from the Dutch Zechstein (Late Permian). Int. J. Earth Sci. 103, 697–712. doi:10.1007/s00531-014-0999-4

Borchert, H., Muir, R., (1964). Salt deposits: the origin, metamorphism and deformation of evaporites. D. Van Nostrand Company. Ltd, London.

Bornemann, O., Behlau, J., Fischbeck, R., Hammer, J., Jaritz, W., Keller, S., Mingerzahn, G., Schramm, M., (2008). Projekt Gorleben, Standortbeschreibung Gorleben. Teil 3: Ergebnisse der über- und untertägigen Erkundung des Salinars., Geologisches Jahrbuch. Bundesanstalt für Geowissenschaften und Rohstoffe (BGR), Hannover.

Bornemann, O., Fischbeck, R., (1991). Zur geologie des salzstocks Gorleben nach den Bohrergebnissen. Deutschland Bundesamt für Strahlenschutz, Salzgitter.

Brun, J.P., Mauduit, T.P.O., (2009). Salt rollers: Structure and kinematics from analogue modelling. Mar. Pet. Geol. 26, 249–258. doi:10.1016/j.marpetgeo.2008.02.002

Burliga, S., (1996). Kinematics within the Klodawa salt diapir, central Poland. Geol. Soc. London, Spec. Publ. 100, 11–21. doi:10.1144/GSL.SP.1996.100.01.02

Cartwright, J., Jackson, M.P.A., Dooley, T., Higgins, S., (2012). Strain partitioning in gravity-driven shortening of a thick, multilayered evaporite sequence. Geol. Soc. London, Spec. Publ. 363, 449–470. doi:10.1144/SP363.21

Cerqueira, R.M., Chaves, A.P.V., Pessoa, A.F.C., Monteiro, J.L.A., Pereira, J.C., Wanderley, M.L., (1997). Principais depositos minerais do Brasil, in: Rochas E Minerais Industriais [Pricipal Mineral Deposits of Brazil, v. 4, Industrial Rocks and Minerals]: Brasilia, [Brazil] Departamento Nacional de Producao Mineral. pp. p. 277–312.

Chemia, Z., Koyi, H., Schmeling, H., (2008). Numerical modelling of rise and fall of a dense layer in salt diapirs. Geophys. J. Int. 172, 798–816. doi:10.1111/j.1365-246X.2007.03661.x

Chemia, Z., Schmeling, H., Koyi, H., (2009). The effect of the salt viscosity on future evolution of the Gorleben salt diapir, Germany. Tectonophysics 473, 446–456. doi:10.1016/j.tecto.2009.03.027

Coelewij, P., Haug, G., Kuijk, H. Van, (1978). Magnesium-salt exploration in the northeastern Netherlands. Geol. en Mijnb. 57, 487–502.

De Jager, J., (2007). Geological development, in: Wong, T.E., Batjes, D.A.J., De Jager, J. (Eds.), Geology of the Netherlands. Royal Netherlands Academy of Arts and Sciences, pp. 5–26.

Dooley, T.P., Jackson, M.P.A., Jackson, C.A.-L., Hudec, M.R., Rodriguez, C.R., (2015). Enigmatic structures within salt walls of the Santos Basin—Part 2: Mechanical explanation from physical modeling. J. Struct. Geol. 75, 163–187. doi:10.1016/j.jsg.2015.01.009

Fiduk, J.C., Rowan, M.G., (2012). Analysis of folding and deformation within layered evaporites in Blocks BM-S-8 & -9, Santos Basin, Brazil. Geol. Soc. London, Spec. Publ. 363, 471–487. doi:10.1144/SP363.22

Fokker, P.A., (1995). The behaviour of salt and salt caverns. Dissertation, Delft University of Technology.

Gärtner, G., Stockmann, N., Fricke, H., Wallmüller, R., (2008). Geological characterization of the Asse salt mine for mining, disposal of radioactive waste, and proof of long-term safety, in: Reviews in Engineering Geology Volume XIX: Deep Geologic Repositories. pp. 41–52. doi:10.1130/2008.4119(05)

Geluk, M.. C., (2007). Triassic, in: Wong, T.E., Batjes, D.A.J., De Jager, J. (Eds.), Geology of the Netherlands. Royal Netherlands Academy of Arts and Sciences, pp. 85–106.

Geluk, M.C., 2(007). Permian, in: Wong, T.E., Batjes, D.A.J., De Jager, J. (Eds.), Geology of the Netherlands. Royal Netherlands Academy of Arts and Sciences, pp. 63–83.

Geluk, M.C., (1998). Internal tectonics of salt structures. J. Seism. Explor. 7, 237–250.

Geluk, M.C., Paar, W.A., Fokker, P.A., (2007). Salt, in: Wong, T.E., Batjes, D.A.J., De Jager, J. (Eds.), Geology of the Netherlands. Royal Netherlands Academy of Arts and Sciences, pp. 283–294.

Geluk, M.C., Röhling, H., Brückner-Röhling, S., (2000). Salt occurrences in the Netherlands and Germany: new insights in the formation of salt basins, in: Geertman, R.M. (ed.): Proceedings of the 8th World Salt Symposium, May 2000, The Hague. Elsevier, pp. 126–131.

Goteti, R., Ings, S.J., Beaumont, C., (2012). Development of salt minibasins initiated by sedimentary topographic relief. Earth Planet. Sci. Lett. 339-340, 103–116. doi:10.1016/j.epsl.2012.04.045

Hammer, J., Behlau, J., Mingerzahn, G., Mertineit, M., (2014). The mechanical behavior and geometry of anhydrite layers in rock salt: Observations from nature, in: Natural Analogues for Safety Cases of Repositories in Rock Salt - “Salt Club” Workshop Proceedings Braunschweig,

Germany, 05.-07.September 2012. Hosted by Gesellschaft Für Anlagen Und Reaktorsicherheit (GRS) mbH, Braunschweig and Project Management Agency.

Hudec, M.R., Jackson, M.P.A., (2007). Terra infirma: Understanding salt tectonics. Earth-Science Rev. 82, 1–28. doi:10.1016/j.earscirev.2007.01.001

Jackson, C.A.-L., Jackson, M.P.A., Hudec, M.R., Rodriguez, C., (2014). Internal structure, kinematics, and growth of a salt wall: Insights from 3-D seismic data. Geology 42, 307–310. doi:10.1130/G34865.1

Jackson, C.A.-L., Jackson, M.P.A., Hudec, M.R., Rodriguez, C.R., (2015). Enigmatic structures within salt walls of the Santos Basin—Part 1: Geometry and kinematics from 3D seismic reflection and well data. J. Struct. Geol. 75, 135–162. doi:10.1016/j.jsg.2015.01.010

Jackson, M.P.A., Cornelius, R.R., Craig, C.H., Gansser, A., Stöcklin, J., Talbot, C.J., (1990). 177 : Salt Diapirs of the Great Kavir, Central Iran, Memoir of the Geological Society of America. doi:10.1130/MEM177

Jackson, M.P.A., Roberts, D., Snelson, S., (1996). Salt Tectonics: A Global Perspective: Based on the Hedberg International Research Conference, Bath, UK, September 1993, No. 65. Amer Assn of Petroleum Geologists, Tulsa, Oklahoma.

Jackson, M.P.A., Talbot, C., (1989). Anatomy of mushroom-shaped diapirs. J. Struct. Geol. 11, 211–230. doi:10.1016/0191-8141(89)90044-8

Jackson, M.P.A., Talbot, C.J., (1986). External shapes, strain rates, and dynamics of salt structures. Geol. Soc. Am. Bull. 97, 305–323. doi:10.1130/0016-710.1130/0016-7606(1986)97<305:ESSRAD>2.0.CO;2

Koyi, H. a., (2001). Modeling the influence of sinking anhydrite blocks on salt diapirs targeted for hazardous waste disposal. Geology 29, 387–390. doi:10.1130/0091-7613(2001)029<0387:MTIOSA>2.0.CO;2

Kukla, P., Pechnig, R., Urai, J., (2011). Analysis and evaluation of the Gorleben site characteristics. Report on the working package 2. Preliminary safety analysis Gorleben. Gesellschaft fuer Anlagen-und Reaktorsicherheit mbH (GRS), Koeln (Germany). Funding organisation: Bundesministerium fuer Umwelt, Naturschutz und Reaktorsicherheit, Berlin (Germany). ISBN 978-3-939355-52-6.

Langbein, R., (1987). The Zechstein sulphates: The state of the art, in: Peryt, T.M. (Ed.), The Zechstein Facies in Europe, Lecture Notes in Earth Science, Vol .10. Springer- Verlag Berlin, Heidelberg, pp. 143–188.

Li, S., Abe, S., Reuning, L., Becker, S., Urai, J.L., Kukla, P. a., (2012a). Numerical modelling of the displacement and deformation of embedded rock bodies during salt tectonics: A case study from the South Oman Salt Basin. Geol. Soc. London, Spec. Publ. 363, 503–520. doi:10.1144/SP363.24

Li, S., Abe, S., Van Gent, H., Strozyk, F., Kukla, P.A., Urai, J.L., (2012b). A new method to evaluate the salt rheology during long term ceep by inversion of numerical models of gravitational sinking of carbonate-anhydrite inclusions (stringers) in salt, in: Proceedings of the 7th Conference on the Mechanical Behavior of Salt : Saltmech7 Paris, 16-19 April 2012. pp. 215–220.

Liang, W., Yang, C., Zhao, Y., Dusseault, M.B., Liu, J., (2007). Experimental investigation of mechanical properties of bedded salt rock. Int. J. Rock Mech. Min. Sci. 44, 400–411. doi:10.1016/j.ijrmms.2006.09.007

Lotze, F., (1957). Steinsalz und kalisalze, Part I, in: Berlin: Gebruder Borntrager, 446p.

Martini, H.J., (1953). Salzsättel und Deckgebirge, in: Frühjahrestagung “Salzlagerstätten” Der Deutschen Geologischen Gesellschaft in Goslar, Mai 1953. pp. 823–836.

Mohr, M., Kukla, P.A., Urai, J.L., Bresser, G., (2005). Multiphase salt tectonic evolution in NW Germany: Seismic interpretation and retro-deformation. Int. J. Earth Sci. 94, 917–940.

doi:10.1007/s00531-005-0039-5

Müller, W.H., Schmid, S.M., Briegel, U., (1981). Deformation experiments on anhydrite rocks of different grain sizes: Rheology and microfabric. Tectonophysics 78, 527–543. doi:10.1016/0040-1951(81)90027-5

Poiate, E.J., Costa, A.M., Falcao, J.L., Petrobrás, S.A., (2006). Well Design for Drilling Through Thick Evaporite Layers in Santos Basin- Brazil, in: IADC/SPE Drilling Conference , 21-23 February 2006, Miami, Florida, USA. Society of Petroleum Engineers, p. 16. doi:10.2523/99161-MS

Reeve, M.T., Bell, R.E., Duffy, O.B., Jackson, C.A.-L., Sansom, E., (2015). The growth of non-colinear normal fault systems ; What can we learn from 3D seismic reflection data? J. Struct. Geol. 70, 141–155. doi:10.1016/j.jsg.2014.11.007

Schenk, O., Urai, J.L., (2005). The migration of fluid-filled grain boundaries in recrystallizing synthetic bischofite: First results of in-situ high-pressure, high-temperature deformation experiments in transmitted light. J. Metamorph. Geol. 23, 695–709. doi:10.1111/j.1525-1314.2005.00604.x

Schléder, Z., Urai, J.L., Nollet, S., Hilgers, C., (2008). Solution-precipitation creep and fluid flow in halite: A case study of Zechstein (Z1) rocksalt from Neuhof salt mine (Germany). Int. J. Earth Sci. 97, 1045–1056. doi:10.1007/s00531-007-0275-y

Scott Duncan, E.J., Lajtai, E.Z., (1993). The creep of potash salt rocks from Saskatchewan. Geotech. Geol. Eng. 11, 159–184. doi:10.1007/BF00531249

Siemeister, G., (1969). Primärparagenese und Metamorphose des Ronnenberglagers nach Untersuchung im Grubenfeld Salzdetfurth, Beihefte zum Geologischen Jahrbuch, Beiheft 62. Bundesanstalt für Bodenforschung, Geologische Landesämter der Bundesrepublik Deutschland, Hannover.

Spiers, C.J., Urai, J.L., Lister, G.S., Boland, J.N., Zwart, H.J., (1983). The influence of fluid-rock interaction on the rheology of salt rock and on ionic transport in salt. Report over the period nov. 1981- Dec. 1983 131.

Strozyk, F., Urai, J.L., Gent, H. Van, Keijzer, M. De, Kukla, P.A., (2014). The internal structure of salt : insights from a regional 3D seismic study of the Permian Zechstein 3 intra-salt stringer in the Northern Netherlands and its implications for salt tectonics. Interpretation 2, 101–117. doi:10.1190/INT-2014-0037.1

Strozyk, F., Van Gent, H., Urai, J.L., Kukla, P.A., (2012). 3D seismic study of complex intra-salt deformation: An example from the Upper Permian Zechstein 3 stringer, western Dutch offshore. Geol. Soc. London, Spec. Publ. 363, 489–501. doi:10.1144/SP363.23

Talbot, C.J., Aftabi, P., (2004). Geology and models of salt extrusion at Qum Kuh, central Iran. J. Geol. Soc. London. 161, 321–334. doi:10.1144/0016-764903-102

Urai, J.L., Schléder, Z., Spiers, C.J., Kukla, P.A., Lange, J.-M., Röhling, H.-G., (2008). Flow and Transport Properties of Salt Rocks, in: Dynamics of Complex Intracontinental Basins: The Central European Basin System. Springer Science & Business Media, pp. 277–290.

Vackiner, A.A., Antrett, P., Stollhofen, H., Back, S., Kukla, P.A., Bärle, C., (2011). Syndepositional tectonic controls and palaeo-topography of a permian tight gas reservoir in nw germany. J. Pet. Geol. 34, 411–428. doi:10.1111/j.1747-5457.2011.00512.x

van Eekelen, H.A., Urai, J.L., Hulsebos, T., (1981). Creep of Bischofite, in: Proceedings, 1st Conference on the Mechanical Behaviour of Salt. Pennsylvania.

Van Gent, H., Urai, J.L., de Keijzer, M., (2011). The internal geometry of salt structures - A first look using 3D seismic data from the Zechstein of the Netherlands. J. Struct. Geol. 33, 292–311. doi:10.1016/j.jsg.2010.07.005

Vysotskiy, E.A., Kislik, V.Z., (1987). Epochs of bischofite deposition in geologic history. Int. Geol.

Rev. 29, 134–139. doi:10.1080/00206818709466130

Warren, J.K., (2006). Evaporites:Sediments, Resources and Hydrocarbons. Springer Science & Business Media, Berlin Heidelberg.

Williamson, M.D., Murray, S.J.J., Hamilton, T.A.P.A.P., Copland, M.A.A., Wil, M.D., Murray, S.J.J., Science, W.S.A., Hamilton, T.A.P.A.P., Copland, M.A.A., (1998). A Review of Zechstein Drilling Issues, in: Offshore Europe Conference in Aberdeen, Scotland, 9-12 September 1997. pp. 189–196. doi:10.2118/51182-PA

Wong, T.E., (2007a). Jurassic, in: Wong, T.E., Batjes, D.A.J., De Jager, J. (Eds.), Geology of the Netherlands. Royal Netherlands Academy of Arts and Sciences, pp. 107–125.

Wong, T.E., (2007b). Cretaceous, in: Wong, T.E., Batjes, D.A.J., De Jager, J. (Eds.), Geology of the Netherlands. Royal Netherlands Academy of Arts and Sciences, pp. 127–150.

Ziegler, P. a., (1978). North-Western Europe: Tectonics and Basin Development. Geol Mijnb. 57, 589–626.

Zirngast, M., (1996). The development of the Gorleben salt dome (northwest Germany) based on quantitative analysis of peripheral sinks. Geol. Soc. London, Spec. Publ. 100, 203–226. doi:10.1144/GSL.SP.1996.100.01.13

Zulauf, G., Zulauf, J., Bornemann, O., Brenker, F.E., Höfer, H.E., Peinl, M., Woodland, a. B., (2010). Experimental deformation of a single-layer anhydrite in halite matrix under bulk constriction. Part 2: Deformation mechanisms and the role of fluids. J. Struct. Geol. 32, 264–277. doi:10.1016/j.jsg.2009.12.001

Zulauf, J., Zulauf, G., (2005). Coeval folding and boudinage in four dimensions. J. Struct. Geol. 27, 1061–1068. doi:10.1016/j.jsg.2005.04.003

3. Interpretation of the ZIII-1b structure and content using acoustic impedance

3.1 Summary

This report presents the results of the reinterpretation of the internal structures of the Veendam Pillow based on acoustic impedance (AI) data focusing on the Zechstein III (ZIII) - 1b potassium and magnesium (K-Mg) salt layer. The seismic inversion was performed in order to obtain calibrated acoustic impedance values whilst at the same time improving the temporal resolution compared to the reflectivity dataset. After seismic inversion, the structure of the Zechstein III- 1b subunit could be identified as a low acoustic impedance body. The unit's boundaries were interpreted by manually picking the threshold between low AI K-Mg salts and the higher AI halite layers.

Elastic parameters were estimated of mineral mixtures typically found in the ZIII-1b subunit, such as carnallite with bischofite and kieserite and halite. Threshold values were based on these estimations, allowing identification of the most prospective intervals.. In addition, tuning effects on AI values was taken into account in thin layers.This led to the definition of bodies within the ZIII – 1 b subunit that exhibit low and connected AI values, a strong indicator for the presence of bischofite.

Results show that the interpretation of AI data refined the geometric model of the salt body's structure especially in areas where the original reflection data quality was weak. Layer thicknesses conducted from the interpretation correlate reasonably with thicknesses measured in wells. In absolute depth terms, depth values at top ZIII – 1b levels are around 45 m off. We suggest that areas of low AI values, in combination with an analysis of local deformation structures can be used, to identify the most prospective areas of high magnesium content.

3.2 Introduction

3.2.1 Previous work:

In a first step the structure of the Veendam area was interpreted based on seismic reflection data. Key horizons in the supra salt and all visible horizons inside the Zechstein salt body were interpreted and identified with the help of well log data of several Veendam and Tripscompagnie wells. Details of this work were presnted in the 2014 project report and published in Raith et al. 2016. The conclusions of the interpretations were that the bischofite was initially precipitated from an Mg- rich brine pond above a basement graben at the location of the Veendam Pillow. The mechanically strongly stratified salt body underwent a complex deformation history of early extension and later contraction leading to fracturing and folding of internal layers. Results show that buckling of the central ZIII Anhydrite/ Carbonate stringer (ZIII-AC) led to local concentrations of the mobile K-Mg salt above the stinger synclines.

Although the quality of the reflections was fluctuating and their exact position indistinctive in some areas, the results correlated well with the well tops of the Tripscompagne and Veendam wells (Table 2). Nevertheless, at the VDM -01 well, the depth and thickness values deviated strongly indicating that the present structure (e.g. strongly folded layers in the crest of the structure) could not be imaged and interpreted with the given data quality.

3.2.2 Materials

Contrasts in elastic properties give rise to seismic reflections of which the am plitudes are related to the difference in acoustic impedance provided the thickness of the layer exceeds the tuning thickness. It is still possible to identify a layer with thickness less than the tuning thickness, however, amplitudes are no longer proportional to reflection coefficients. Inversion to acoustic impedance largely alleviates tuning effects (Latimer et al., 2000) Whilst the ZII is mostly consisting of halite (>95%), and therefore seismically transparent, the ZIII also contains thick layers beyond than the tuning thickness of about 30 m consisting of anhydrite and carbonate, halite and Potassium and Magnesium salts (K-Mg salts) (Geluk et al., 2007). Out of these K-Mg salts carnallite (KMgCl3*6H2O), bischofite (MgCl2*6H2O) and kieserite (MgS04) are present in a large enough quantity to have an impact on the seismic response (Table 1).

	Kieserite	Halite	Carnallite	Bischofite	Mg- Brine
Density [kg/m³]	2579	2100	1570	1550	1400
Bulk mod. K [GPa]	53.3	24.7	13.3	8	4.3
Shear mod. μ [Gpa]	32	14.8	8	4.8	---
Young´s mod. E [Gpa]	90	37.1	20	12	---
Compr. Vel. Vp [m/s]	6110	4540	3905	3055	1750
Shear Vel. Vs [m/s]	3530	2655	2255	1760	---
Acoustic Imp. [MPas/m³]	15.7	9.53	6.13	4.74	2.5

Table 1:

A few notes on the values in table 1. Whereas elastic properties of halite are rather well known and relatively widely published (Mavko et al., 1998), equivalent properties of the other evaporitic minerals have not been traced. Moreover, published values of compressional velocities vary wildly. Hence a choice had to be made from published data as far as Vp is concerned on the basis of the most plausible value. The published properties of halite imply a Poisson ration of 0.25 (Mavko et all, 1998), which subsequently has been applied for the estimation of the shear velocities of the other evaporitic minerals. The last column contains the elastic properties of bischofite brine, calculated according to the Batzle and Wang equations (1992)

In summary, a layer with high content of carnallite has a significant lower AI value than a pure

halite layer. If also bischofite is present in the layer the effect is much stronger. Nevertheless, a high content of carnallite and bischofite can be masked by the high AI values of kieserite, which is also common in these layers.

3.2.3 Study area

The study area is 10 km southeast of the city of Groningen, near Veendam in the NE Netherlands. Geologically, the area is located at the southernmost edge of the Groningen High, between the northwest- southeast trending Lauwerszee Trough in the west and the Lower Saxony Basin in the southeast. The subsalt Permian Rotliegend is strongly deformed by E-W and N-S to NNW-SSE striking normal and strike-slip faults that form a network of graben to half-graben structures (Geluk, 2007; Geluk et al., 2007; Biehl et al., 2014).

The Veendam Pillow strikes SW-NE and is 10 km long in the NE-SW direction and 5 km wide (Fig. 3.1). The Zechstein is 2600 m thick in the pillow core, and the top of the pillow is at 1100 m depth. The Top Salt surface of the pillows is generally smooth, but locally offset by faults in the post-salt sediments occur.

The Zechstein section in the study area contains fully developed Z-I to Z-IV cycles. The thin and well-stratified ZI and lower ZII sequences are seismically harmonic with the Rotliegend-Zechstein contact and are mechanically considered to be part of the subsalt. A prominent high-amplitude re-

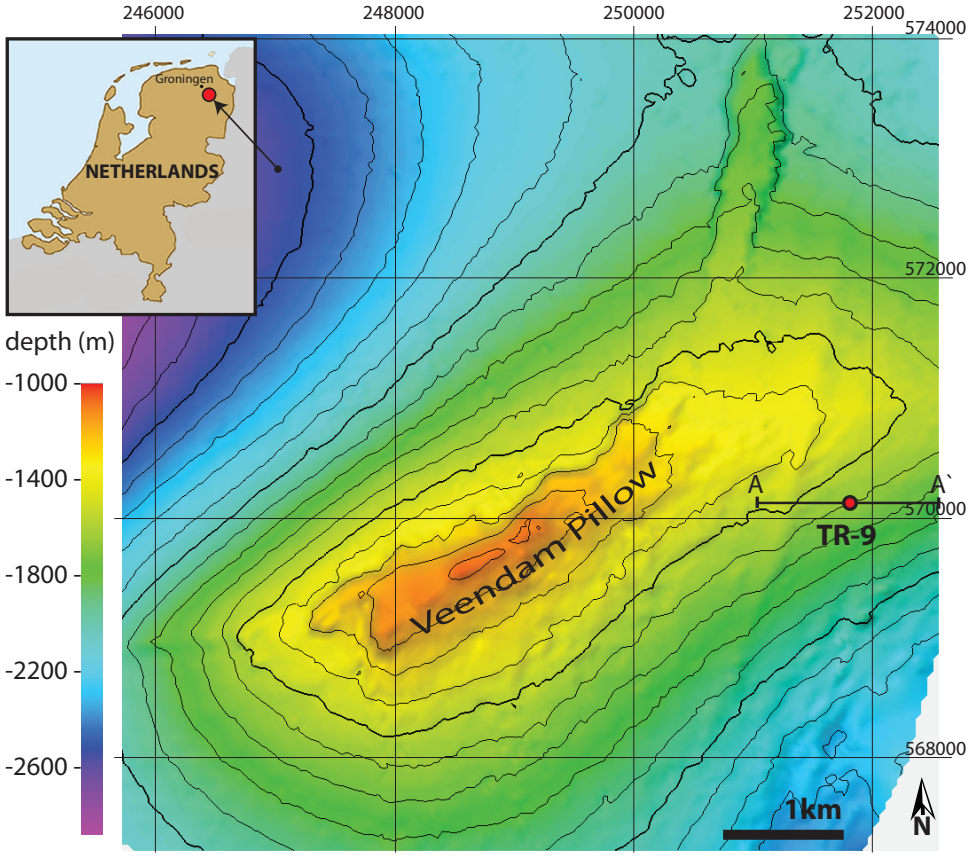


Fig. 3.1: Depth map of the top salt surface of the Veendam Pillow.

flector commonly interpreted as “Base Salt” represents the transition from the ZII salt to Top ZIIC carbonates. The thickness of the overlaying seismically chaotic to transparent ZII rock salt varies from ca. 50 m below salt withdrawal basins to up to 1.8 km in flanking salt pillows. In general, the ZII salts are mainly composed of halite (> 95 %; (Geluk et al., 2000)). The ZIIIAC stringer represents the base of the ZIII unit and consists of the gray Salt Clay, overlain by the 0.5–20 m thick Plattendolomit and the 15–130 m thick Hauptanhydrit (Van Gent et al., 2011). As the stringer is thick and encased in rock salt, it produces a high-amplitude reflection in the seismic data (Van Gent et al., 2011; Strozyk et al., 2012, 2014). The ZIII and ZIV units above the stringer are compositionally and mechanically layered (Coelewij et al., 1978), and are traditionally subdivided into several subunits. The seismically transparent lower ZIII is 100 to 300 m thick. The ZIII-1 to -4 show a number of seismic reflections thought to reflect interbedding of halite with K-Mg salt-rich layers in the ZIII-1b, -2b and -3b. Besides halite, the most common minerals here are carnallite, kieserite, and anhydrite, whereas in ZIII-1b bischofite is also present (Coelewij et al., 1978). The Zechstein is overlain by Triassic (Buntsandstein and upper Röt), Cretaceous (Rijnland and Chalk) the Tertiary units (Lower/Middle and Upper North Sea Group) and the Quaternary. The Jurassic is not present in the study area (Wong, 2007).

3.3 Methods and dataset

3.3.1 Dataset

For the initial interpretation, two PSDM (pre-stack depth migrated) 3-D seismic volumes of different size were used, provided by Nederlandse Aardolie Maatschappij (NAM). The southern seismic depth volume of 46 km² mainly covers the Veendam Pillow and images down to 3.25 km depth (R868). The northern depth volume covers 135 km² and images down to 2.5 km depth (R2437). Both seismic volumes overlap by 30 km² and display vertical offsets between reflections due to differences in the velocity model during data processing. This offset is, however, less than 30 m.

Inversion to acoustic impedance was performed on the PSDM dataset R2437 by CGG in Massy, France. Apart from the R2437 reflectivity dataset, the PSDM velocity cube was available. Using that cube, the top Zechstein Halite was interpreted and used in combination with the already interpreted horizon to construct a low-frequency model. Input data stretched from approximately top Cretaceous to top Zechstein 2 (Basal) Anhydrite. A wavelet was derived using welldata from well KWR-01. In view of the deconvolution applied on the reflectivity dataset, little was gained on the high frequency side. Gains on the low frequency side were substantial through use of the low-frequency model, resulting in a substantial suppression of sidelobes in the final wavelet. The last step comprised a layer-based, deterministic inversion, calibrated against wellresults from KWR-01. In addition a so-called synthetic

reflection volume was generated by differentiating the AI dataset. Subsequently these calibrated acoustic impedance values were converted to depth using the PSDM velocity cube.

3.3.2 Interpretation

In the first interpretation performed on the R868 dataset, it was possible to identify the ZIII-1b layer using a soft kick reflection on the top and a hard kick reflection on the bottom and well log data (see (Raith et al., 2016)). On basis of this first interpretation the position of the ZIII-1b layer was identified in the new dataset (Fig. 3.2).

3.3.3 Identification of the ZIII-1b with AI

The interpretation of top ZIII 1b and top ZIII 1a was performed by manual single line picking (25m grid) based on the AI value (Fig. 3.2). The value of acoustic impedance of pure halite is well established at around 9.53 MPas/m³ by Mavko (1998) and many others. The values for carnallite, 6,13 MPas/m³ and bischofite, 4.74 MPas/m³ have been estimated based on assumptions described above. Typically these values are much lower than those for halite and kieserite, 15.7 MPas/m³. Analysis of core pictures and well logs from several cores in the area have shown that tenth of meter thick layers of pure carnallite are not observable. On the scale relevant for seismic imaging, carnallite is always mixed with halite (and/or kieserite) leading to higher AI values. Therefore, if the observed AI value reaches values typical for carnallite we can assume that these values can only be reached by the existence of bischofite in the layer. Based on these observations the threshold value to identify K-Mg salt was picked at 9000 kPas/m³. If the values lower than 6130 kPas/m³ are reached, bischofite must be present. Considering the influence of halite and kieserite (AI values about 14700 kPas/m³) which are associated with carnallite and bischofite in all wells, the AI values for an Mg rich layer can still be much higher than 6130 kPas/m³. Nevertheless, due to the effect of noise, artefacts and complex structures the threshold value had to be chosen more flexible in some locations. Instead of this fixed threshold value, locations of strong AI value drop (Top 1b) or rise (Top 1a) were picked, representing the extreme values of the first derivative of the AI. (Fig. 3.2)

3.3.4 Material mixture calculations

The calculations were carried out to evaluate the effect of material mixing and layer thickness below seismic tuning thickness on the resulting AI signal. In the first part, the bulk AI of a mixture of carnallite, bischofite and kieserite (up to 10%) with 15 % halite was calculated. Bulk and shear modulus of the mixed material was calculated using effective medium approximations of Hashin and Shtrikman (1963) and Berryman (1995).These calculations yield an upper and a lower bound for each

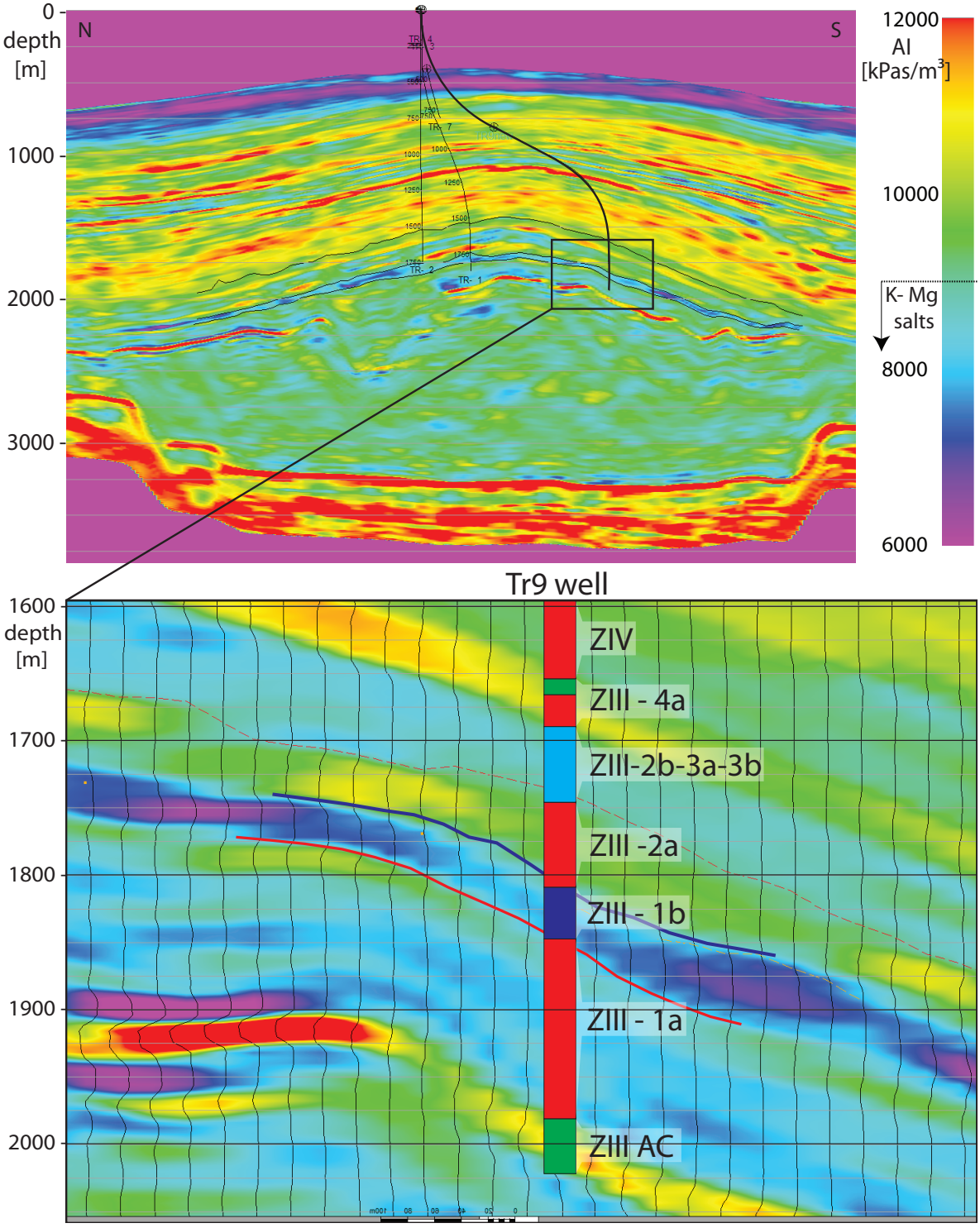


Fig. 3.2: Interpretation of the ZIII layers at the Tr-9 well and the AI data.

elastic modulus. In absence of other information, the average values of the two bounds were taken subsequentlty.

In the second part, the AI values of three layers imbedded in halite were modelled representing typical compositions found in Veendam drill cores (Fig. 3.3). The uppermost layer consists of a mixture with 43% carnallite, 40% bischofite, 15% halite and 2% kieserite. It is wedge shaped to analyse the influence of layer thickness. The middle layer consists of 75% carnallite with 20% halite and 5%

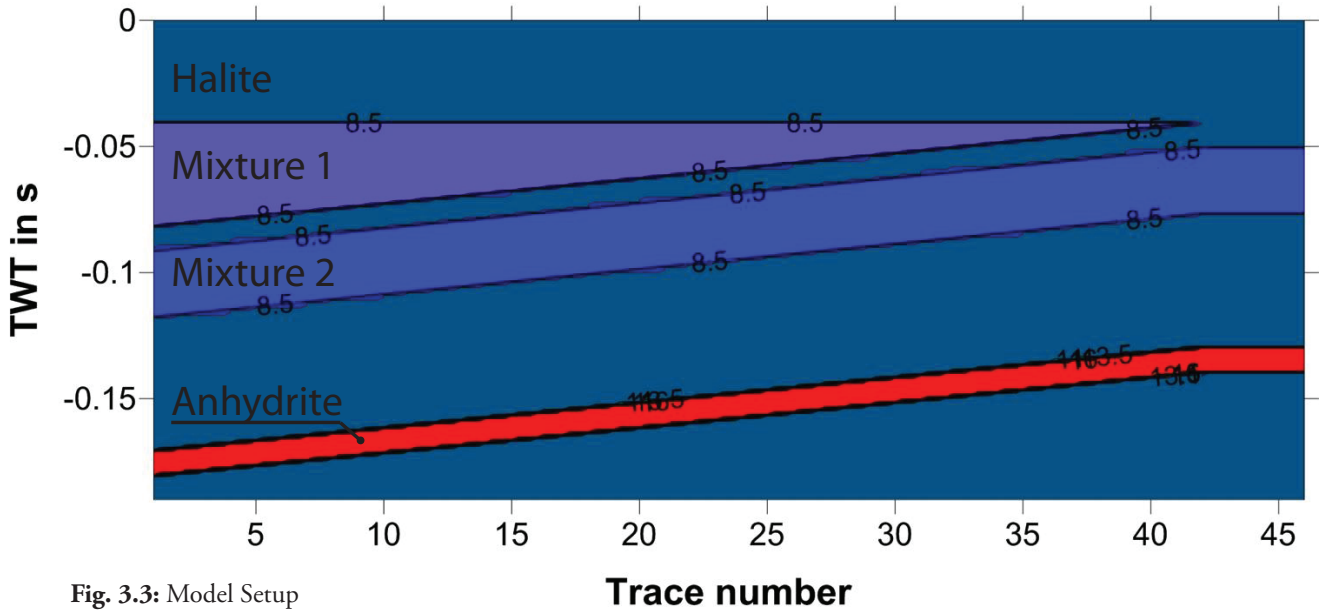


Fig. 3.3: Model Setup

kieserite and is inclined by 10°. The lowest layer represents the anhydrite dominated ZIII-AC, which is also inclined by 10°.

3.3.5 Body checking

After the interpretation of the top and bottom boundaries of the ZIII-1b the volume was further processed to extract bodies of connected low AI voxels (Fig. 3.10). In this technique, bodies are determined of spatially connected voxels below a threshold value. The work has been carried out by DGB in Enschede, The Netherlands. The choice of the threshold value was based on modelling results, reported above, as well as on analysis of acoustic impedance values with in the ZIII-1b sequence. For this analysis an AI threshold of 7850 kPas/m³ was selected to detect the volume of high interest. An AI value of 7850 kPas/m³ represents a mixture of carnallite with 15% halite and about 9% kieserite, lower AI values therefore indicate less kieserite and/or a higher content of bischofite. The analysis produced discrete bodies with a minimum size of 200 voxels (voxel size =25 * 25 * 8 m = 5000 m³) with information of volume average AI, minimum AI and maximum vertical thickness.

3.4 Results

3.4.1 Material mixture calculations

The results show the margin of AI values in which high Mg contents can be expected (Fig. 3.4). Although pure carnallite has a mineral value of 6135 kPas/m³ for its acoustic impedance, presence of halite and/or kieserite will increase that value strongly. Consequently AI values lower than 7500 kPas/m³ are likely to indicate presence of bischofite.

In view of the fact that some layers in the objective sequence are just around the tuning thick-

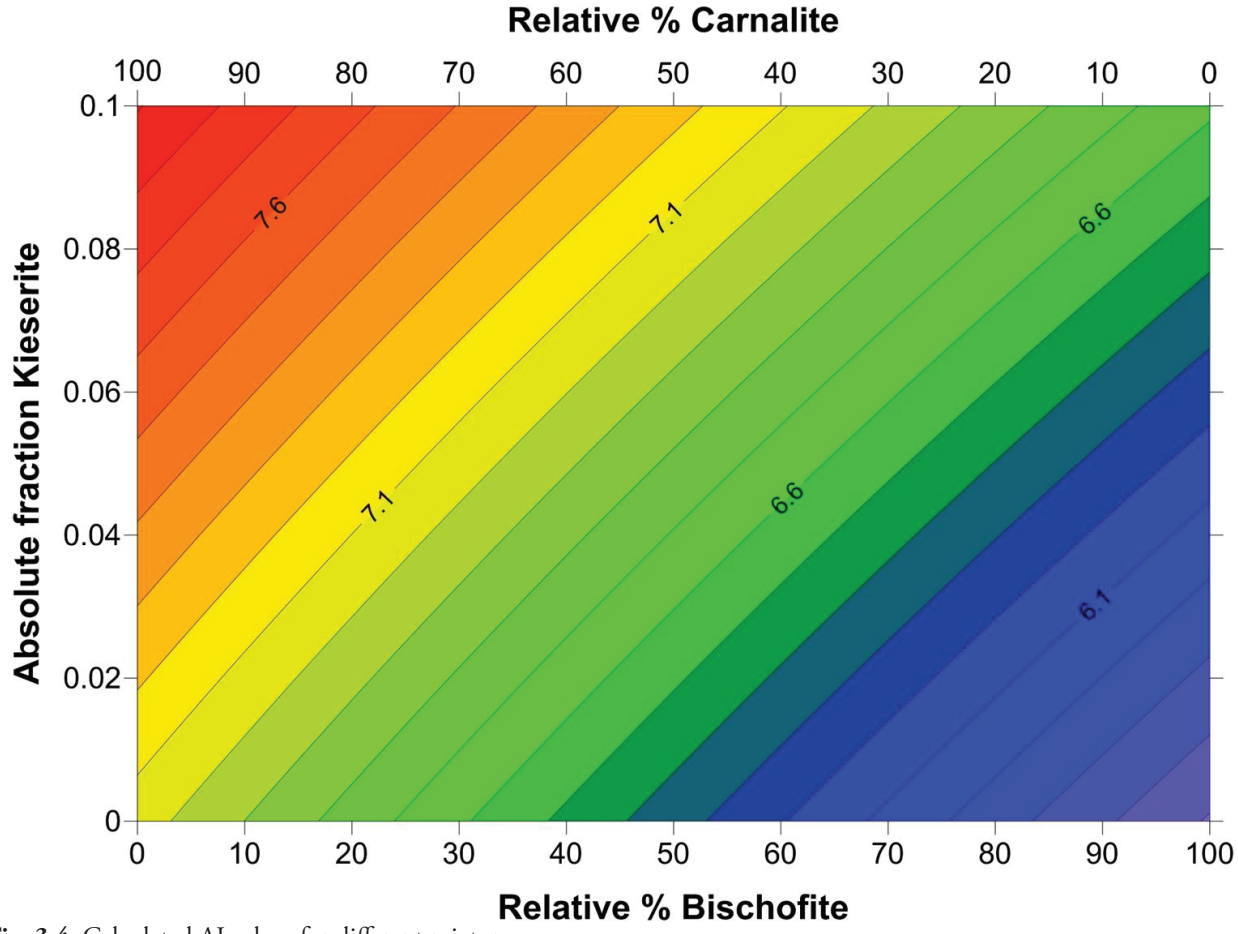


Fig. 3.4: Calculated AI values for different mixtures.

ness, a zero-incidence wedge model has been made based on acoustic impedance data, shown in Fig. 3.5. The layer containing bischofite is the top layer, wedging out to the right. The bottom most, high AI value layer consists of anhydrite – modelled for reference purposes. Inversion to acoustic impedance largely alleviates tuning effects on reflectivity data.

The results show that layers above 40 m thickness are needed to produce reliable AI values (Fig.

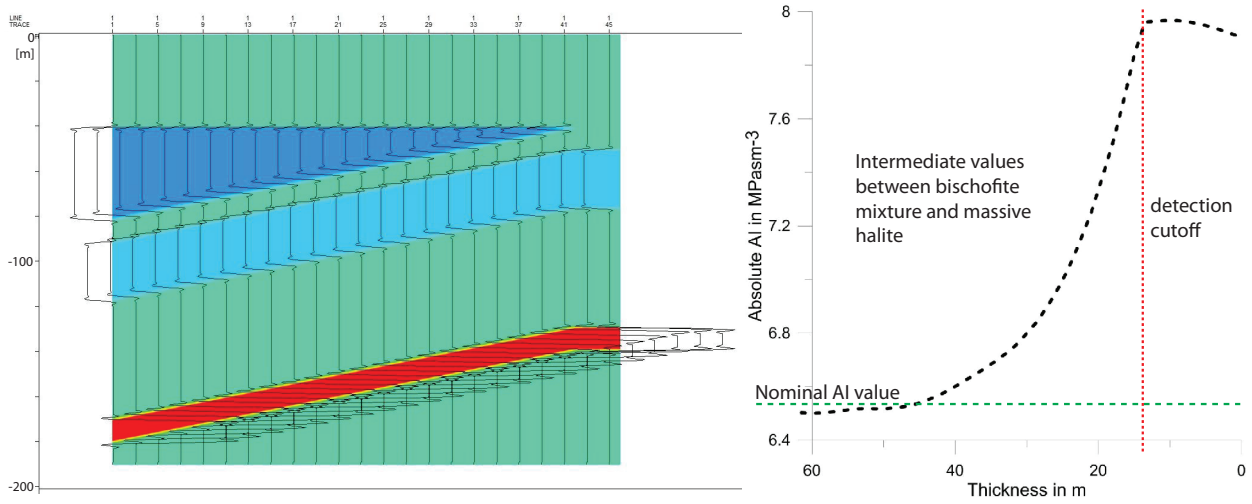


Fig. 3.5: Model results

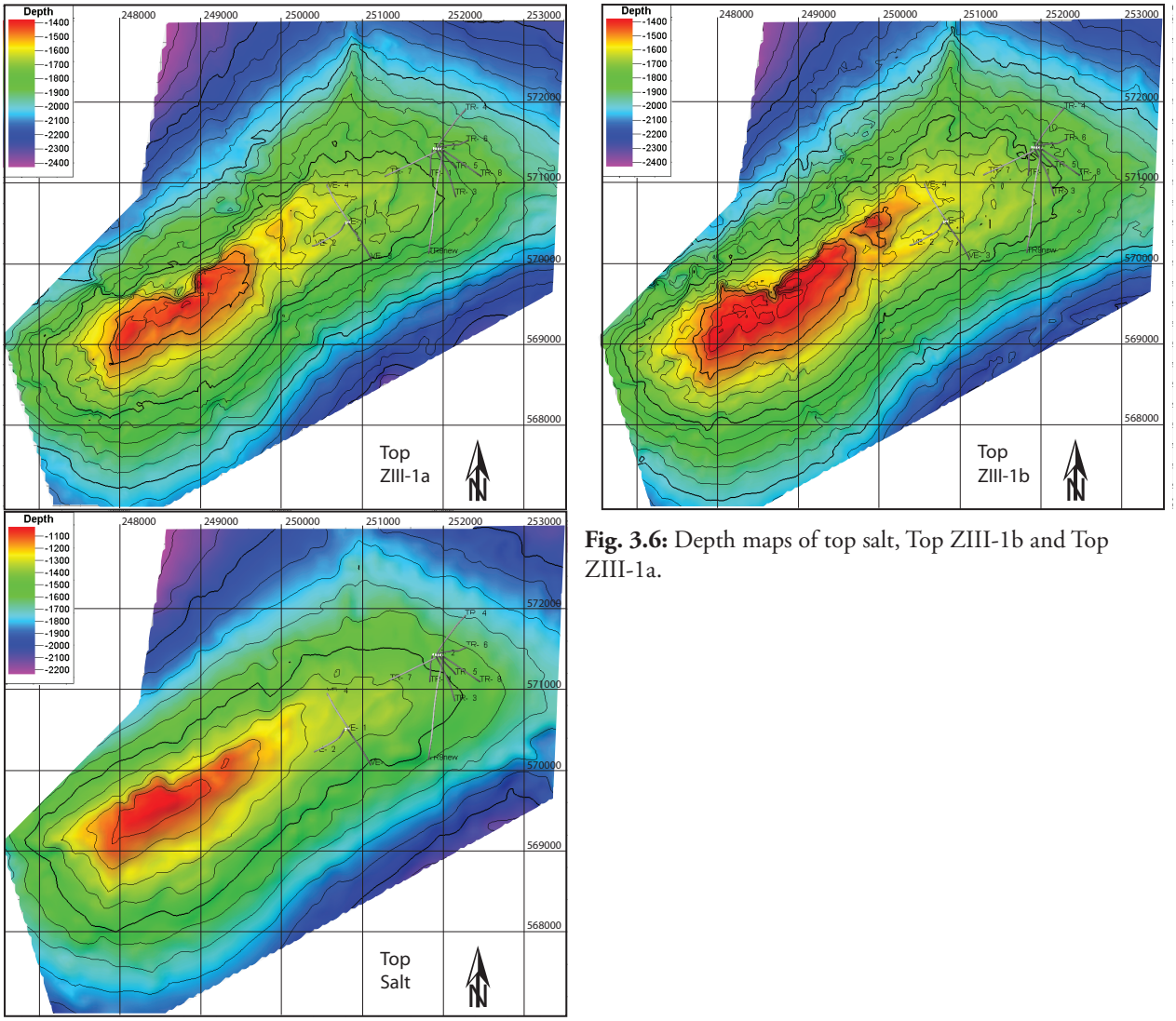


Fig. 3.6: Depth maps of top salt, Top ZIII-1b and Top ZIII-1a.

3.5). Layers thinner than this value will produce higher values until they get too thin and will go undetected if thinner than 14 m.

3.4.2 Interpreted layers

The top salt horizon reveals a NE – SW elongated pillow structure with a number of NE – SW to N-S striking synclines and offsets parallel to suprasalt faults (Fig. 3.6). These structures were already discussed in Raith (2016).

Table 2

		VND1	VND2	VND3	VND4	Tr1	Tr2	Tr3	Tr4	Tr5	Tr6	Tr7	Tr8	Tr9
Top ZIII-1a	well	1665.2	1616.7	1728.7	1629.4	1693	1766.7	1744	1934	1784.5	1828.8	1660	1817.2	1837.7
	old	1656	1592	1724	1636	1720	1764	1745	1927	1785	1855	1636	1796	1800
	new	1691	1650	1760	1662	1754	1836	1776	1965	1803	1875	1684	1836	1848
Top ZIII-1b	well	1629.9	1498.4	1673.2	1556.8	1610	1697	1670	1839	1685	1754.8	1573	1752.9	1766.7
	old	1603	1487	1644	1550	1636	1700	1655	1855	1675	1772	1563	1736	1731
	new	1647	1560	1720	1595	1680	1762	1707	1893	1720	1795	1590	1772	1790
difference	1a old-well	9.17	24.66	4.65	-6.58	-27	2.7	-1	7	-0.5	-26.2	24	21.2	37.68
	1b old well	26.87	11.36	29.15	6.82	-26	-3	15	-16	10	-17.2	10	16.9	35.68
	1a new-well	18.17	-33.34	-31.35	-32.58	-61	-69.3	-32	-31	-18.5	-46.2	-24	-18.8	-10.32
	1b new-well	-61.13	-61.64	-46.85	-38.18	-70	-65	-37	-54	-35	-40.2	-17	-19.1	-23.32
thickness	Well	35.3	118.3	55.5	72.6	83	69.7	74	95	99.5	74	87	64.3	71
	old	53	105	80	86	84	64	90	72	110	83	73	60	69
	new	44	90	40	67	74	74	69	72	83	80	94	64	58
difference	old-well	17.7	-13.3	24.5	13.4	1	-5.7	16	-23	10.5	9	-14	-4.3	-2
	new-well	8.7	-28.3	-15.5	-5.6	-9	4.3	-5	-23	-16.5	6	7	-0.3	-13

3.4.3 Thickness of the ZIII-1b

Compared to the old interpretation, the new ZIII- 1b interpretation shows strongly reduced thickness in the thickened areas (Fig. 3.7). The change is most obvious in the NW part of the pillow, where the ZIII- 1b is most thickened.

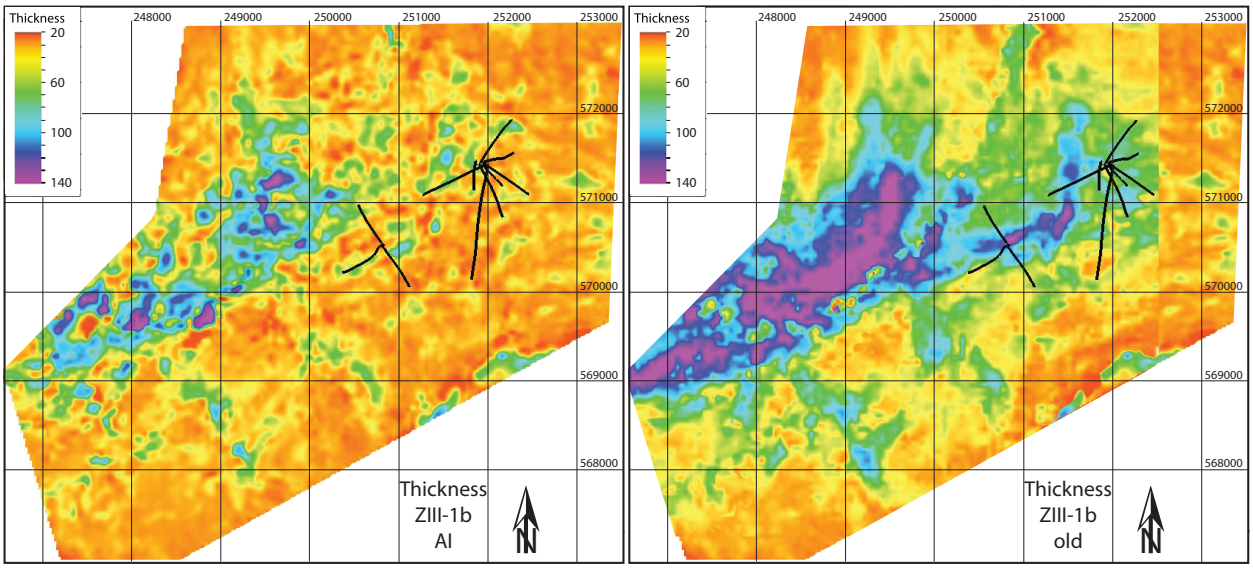


Fig. 3.7: Thickness-maps of the new interpretation performed on AI data and the old performed on reflection data.

3.4.4 Low AI bodies

The body checking produced 36 (Fig. 3.10) bodies with a maximum volume of 33.5 106 m^3. A detailed table of the bodies is in the appendix

3.5 Discussion

3.5.1 Uncertainties of the material mixing calculations

As shown above, the calculation of elastic moduli of the highly soluble minerals has been done on an assumption regarding the Poisson ratio, in absence of well-established published values. Obviously this assumption could not be valid, with consequence for the subsequent analysis. Furthermore, in absence of any other indication, it has been assumed that the subsurface values for the elastic moduli would be in the middle between the calculated upper and lower bounds. This assumption may not be completely valid either. On the other hand, a contradiction in the form of logdata over comparable intervals, has not been found.

Given the presence of four evaporitic minerals, there is a non-uniqueness in the interpretation of seismically derived acoustic impedance data. Even though the four minerals can be grouped in two groups of two according to their acoustic impedance values, the non-uniqueness problem persists. As a result, the presence of bischofite is only assured if the acoustic impedance value of the objective sequence falls below the mineral value of carnallite, i.e. below 6130 kPas/m^3.

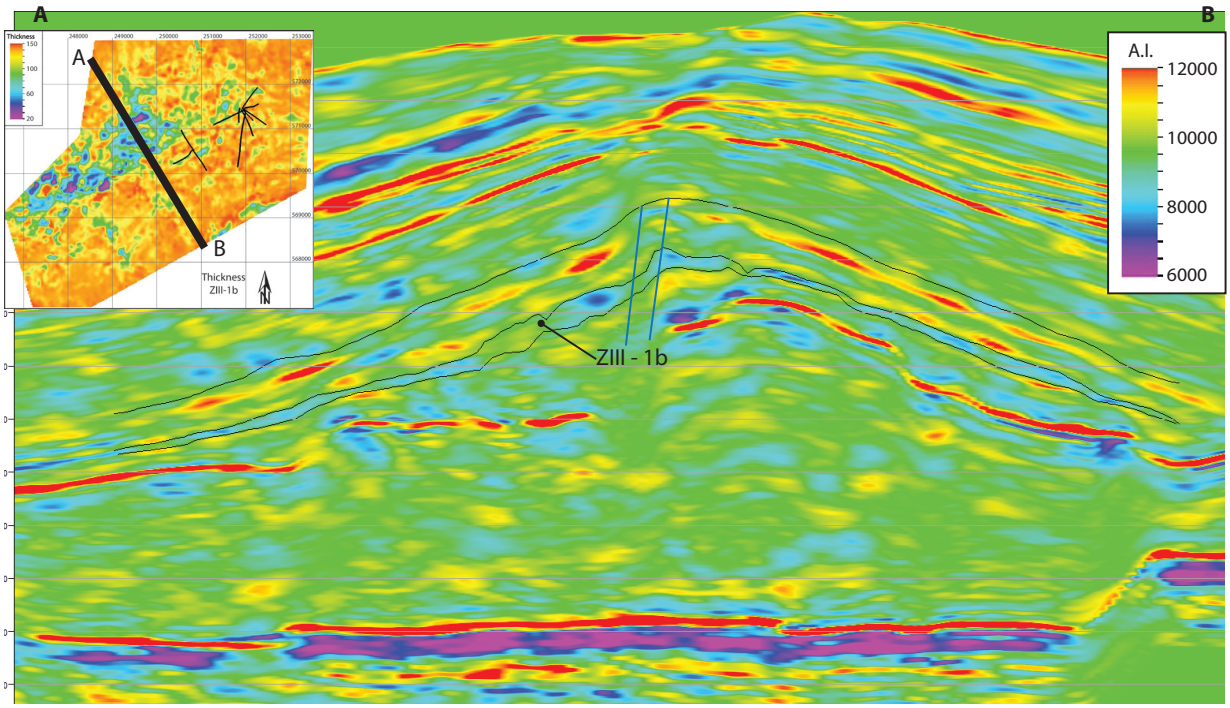


Fig. 3.8: Profile showing the thick ZIII-1b in the NW part of the pillow. The blue lines indicate a normal shear zone in the crest.

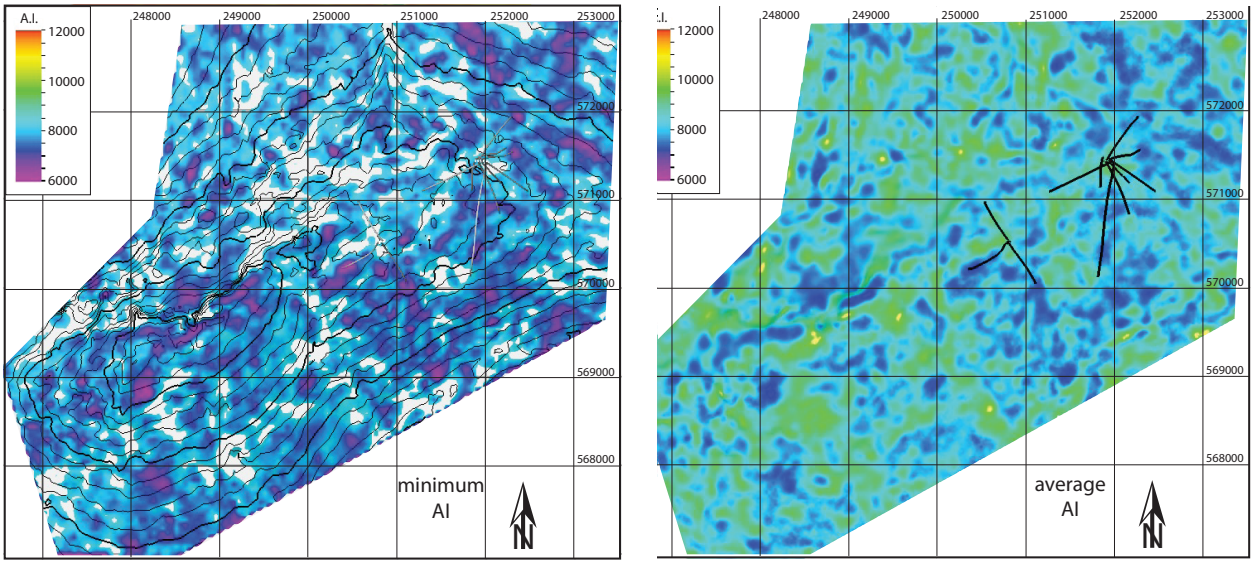


Fig. 3.9: Maps showing the minimum and average AI values.

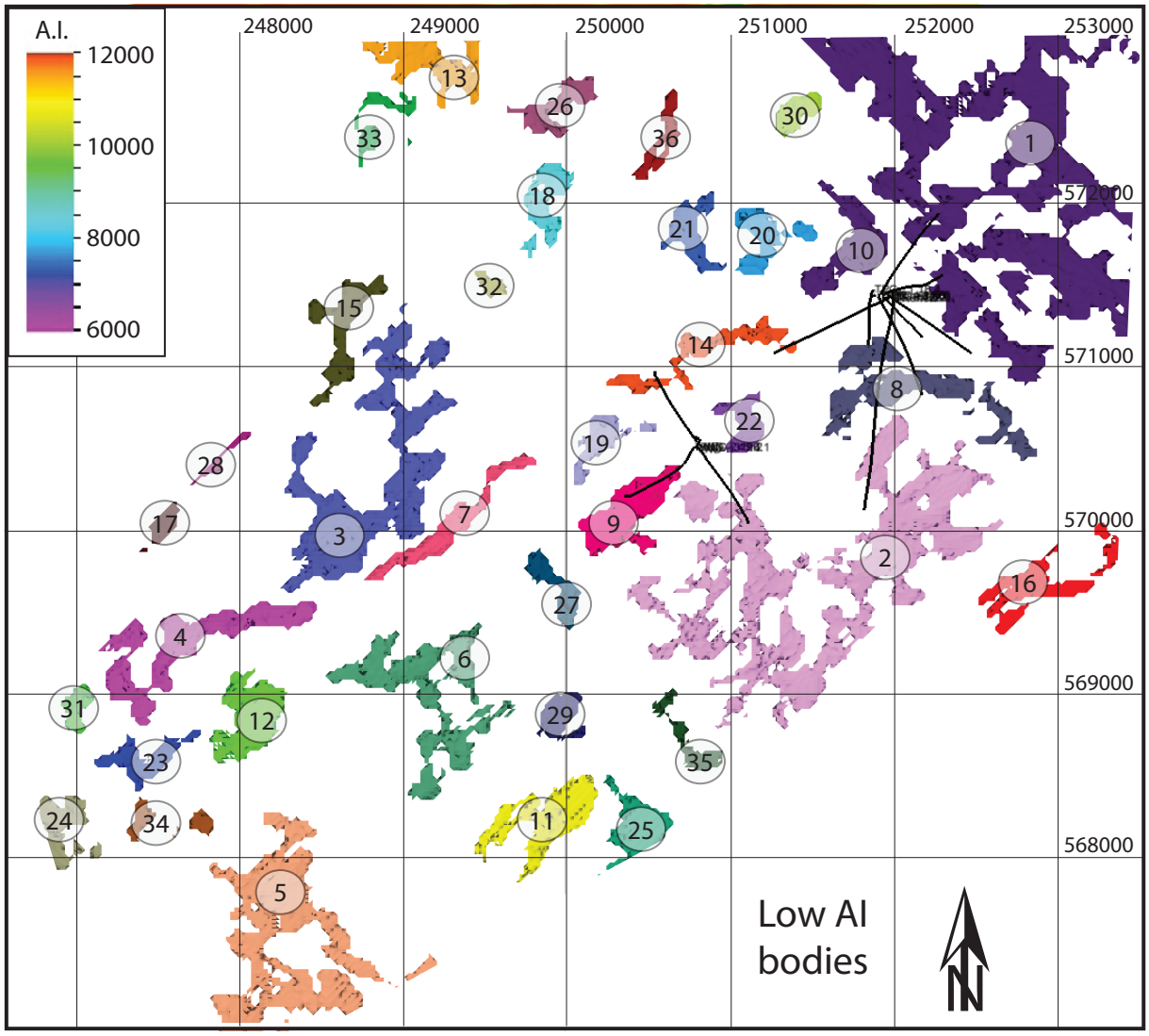


Fig. 3.10: Low AI bodies

3.5.2 Quality increase in the new interpretation

The new interpretation enhanced the quality of the model in many important details. While, the geometries hardly changed in areas where the quality of the original reflection data was good, we see a strong improvement in areas where the original interpretation was problematic.

Pillow crest: The original reflection data was almost seismically transparent in the centre of the salt structure leading to a vague interpretation of the top salt reflector and the internal structure. The new interpretation revealed a sharp offset of the salt pillow roof in the crest parallel to a large fault, crosscutting the suprasalt sediments up into the Tertiary. The offset is continued inside the salt body leading to a shear zone in the internal ZIII layers, parallel to the fault (Fig. 3.8).

The interpretation based on reflectors is especially complicated in areas were multiple close amplitude maxima (or minima) are present masking the reflector of interest. Using thresholds of AI values to identify layer boundaries eliminates these uncertainties and gives much better results. This improvement can best be seen on the NW flank of the pillow (Fig. 3.7). Here, the interpretation of the ZIII- 1a changed strongly, resulting in a different and much more detailed structure of the ZIII-1b layer.

One weakness of the seismic imaging is that steeply dipping reflectors cannot be imaged completely correctly even though PSDM was applied. This can be problematic in folded layers were the steep fold flanks get transparent. As a result of this effect, folding of the upper most ZIII layers leading to a strong thinning of the ZIII-1b at the VDM-1 well could not be detected in the original reflection data but was clearly visible in the AI images (Appendix VDM-1).

3.5.3 Problems to compare the AI value to bischofite content of existing wells

On first look, the AI values inside the ZIII-1b layer at the location of the wells should correlate with the amount of bischofite present, only masked by kieserite. On second look, the values can be altered by the brine filled caverns (AI of Mg-brine about 2.5 MPas/m³) that were already present at almost all wells at the times the seismic surveys were shot. This effect can for example, clearly be seen at the locations of well VDM-1 (Fig. 3.9), where body #9 is presumably the result of the cavern (see well path and body on Fig. 3.10). Taking this into account the AI values at the positions of the wells cannot be compared to the bischofite content found in the cores.

3.5.4 Body checking, lowest or average AI value UE

Given the evaporitic environment in which bischofite was precipitated and the manner in which this mineral is being mined by solution and squeezing, it is clear that large, connected volumes are the most attractive from a development point of view. Given the fact that neither the ZIII-1b thickness nor its average acoustic impedance is constant in space, a body-checking technique was applied on the sequence. This resulted in the identification of 36 different bodies, ranging in volume from 33.5 to

1.1 million cubic meters. A view of these bodies is given in Fig. 3.11 superimposed on the base surface of the objective sequence.

3.5.5 Depth discrepancy

While the seismic survey used for the first study had an excellent correlation between reflection depth and well tops, the reflections in the survey used for the new interpretation are about 30 to 60 m lower than observed in the wells. Fortunately this only affects the uncertainty on the depth of the layer but has no effect on the interpreted thicknesses and structures. The depth discrepancies are shown in Table 2. On average over the Veendam and Tripscompagnie wells, the interpreted seismic depths were 61 m shallow. Consequently a static correction has been applied on top and base ZIII-1b maps. When comparing the abovementioned wells with the corrected maps, the maximum difference is some 40 m shallower or deeper.

3.5.6 Applications for magnesium exploration

From well data we can recognize a correlation between ZIII – 1b thickness and Mg content. This leads to the assumption, that we can expect high bischofite contents in thick ZIII – 1b lenses and the Mg concentration is controlled by the structure. If we combine this model with the now available distribution of AI values we get a much more complex result. The AI signal is strongly fluctuating inside the layer showing no clear correlation to the thickness. Core analysis reveals that the internal structure of the ZIII – 1b is a rather complex mélange of folds fractures and veins (see chapter 5). A patchy distribution caused by internal deformation inside the subunit can therefore be presumed. Due to the lack of physical data, to prove the correlation between AI value and Mg content in the study area, the AI values produced in this study have to be used with precaution.

We conclude that best results can be achieved by a combination of the factors: local structure and expected salt flow leading to Magnesium concentration and low AI values.

3.6 Conclusions

It was possible to refine the geometric model of the ZIII-1b K-Mg salt with the help of the AI dataset. Complex structures were visible more clearly and therefore structural uncertainties are lowered.

If the layer is thicker than the seismic tuning thickness, the average AI value and the lowest AI value should correlate with the bischofite grade of the layer.

The highest Magnesium concentrations are therefore expected in areas that offer a combination of low AI values and a thickened ZIII – 1b layer.

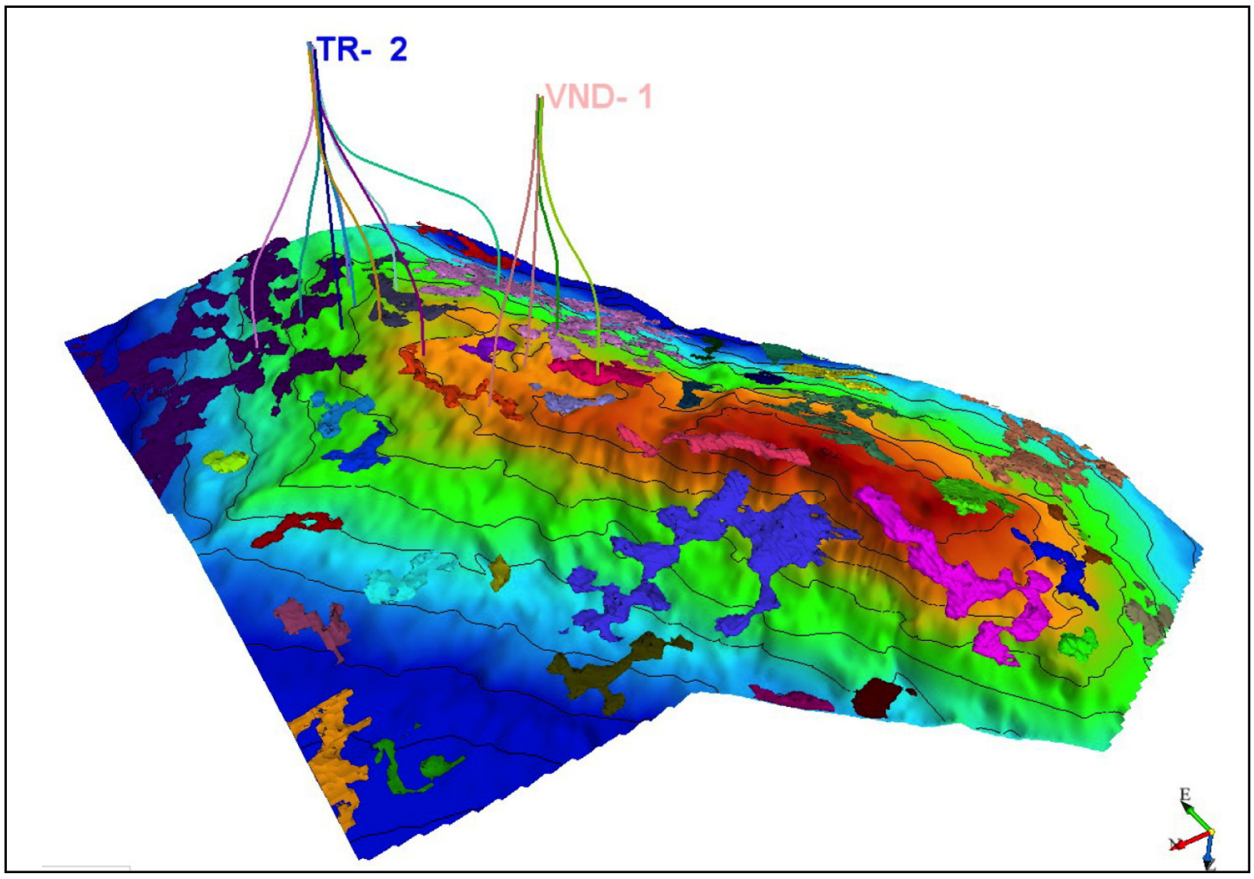


Fig. 3.11: In this figures, bodies of different sizes can be clearly distinguished. It should be noted that the seismic data were acquired after the start of bischofite production from the Veendam (VDM) wells. Hence it is very possible that the body, apparently penetrated by well VDM-01, largely is caused by the presence of a brine-filled cavern. From this diagram it is also clear that very extensive bodies are located at the northern (left) side of the salt-diapir. A full list of the 36 bodies and their properties is given in in the appendix.

3.7 References

Berryman, J.G., (1995). Mixture theory for rock properties, in Handbook of Physical Constants, T.J. Arends, ed., American Geophysical Union, Washington D.C., 205-228

Breunese, J., and Schroot, B., (Eds.), (2004), Proceedings "Squeezing salts" - an expensive problem. Pubished by TNO-NITG

Biehl, B.C., Reuning, L., Strozyk, F., Kukla, P.A., (2014). Origin and deformation of intra-salt sulphate layers: an example from the Dutch Zechstein (Late Permian). Int. J. Earth Sci. 103, 697–712. doi:10.1007/s00531-014-0999-4

Coelewij, P., Haug, G., Kuijk, H. Van, (1978). Magnesium-salt exploration in the northeastern Netherlands. Geol. en Mijnb. 57, 487–502.

Geluk, M.C., (2007). Permian, in: Wong, T.E., Batjes, D.A.J., De Jager, J. (Eds.), Geology of the Netherlands. Royal Netherlands Academy of Arts and Sciences, pp. 63–83.

Geluk, M.C., Paar, W. a, Fokker, P.A., (2007). Salt, in: Wong, T.E., Batjes, D.A.J., De Jager, J. (Eds.), Geology of the Netherlands. Royal Netherlands Academy of Arts and Sciences, pp. 283–294.

Geluk, M.C., Röhling, H., Brückner-Röhling, S., (2000). Salt occurrences in the Netherlands and Germany: new insights in the formation of salt basins, in: Geertman, R.M. (Ed.): Proceedings of the 8th World Salt Symposium, May 2000, The Hague. Elsevier, pp. 126–131.

Hashin, Z., and Shtrikman, S., (1963), A variational approach to the elastic behavious of multiphase matreials,. J. Mech. Phys. Solids, 11, 127-140

Latimer, R.B., Davison, R. and Van Riel, P., (2000), An interpreter's guide to understanding and working with seismic-derived acoustic impedance data, The Leading Edge, V 19, nr2, pp 242-256

Mavko, G., (1998), The Rock Physics Handbook, Cambridge University Press, ISBN 0 521 62068 6

Raith, A.F., Strozyk, F., Visser, J., Urai, J.L., (2016). Evolution of rheologically heterogeneous salt structures: A case study from the NE Netherlands. Solid Earth 7, 67–82. doi:10.5194/se-7-67-2016

Strozyk, F., Urai, J.L., Gent, H. Van, Keijzer, M. De, Kukla, P.A., (2014). The internal structure of salt : insights from a regional 3D seismic study of the Permian Zechstein 3 intra-salt stringer in the Northern Netherlands and its implications for salt tectonics. Interpretation 2, 101–117. doi:10.1190/INT-2014-0037.1

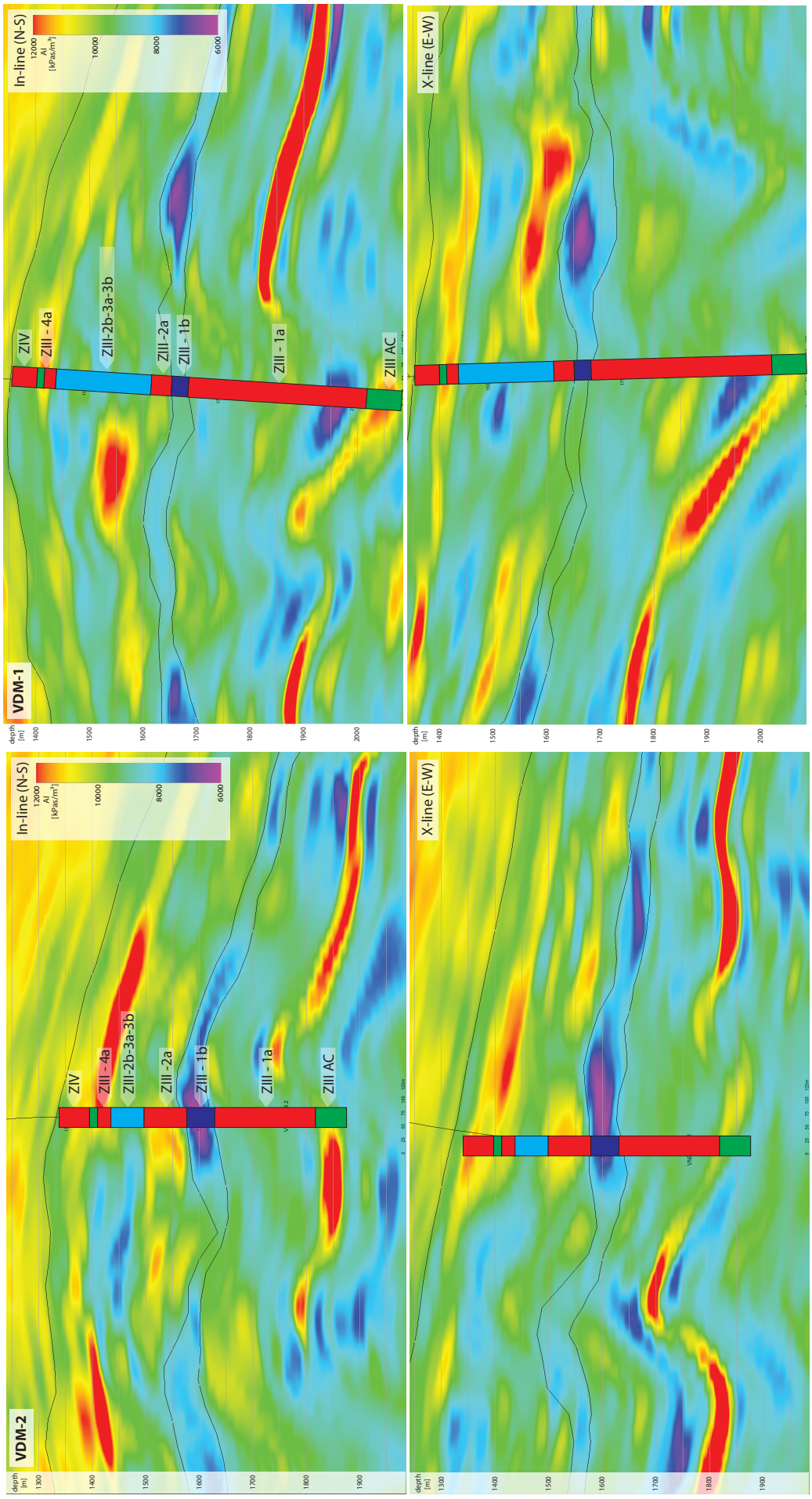
Strozyk, F., Van Gent, H., Urai, J.L., Kukla, P.A., (2012). 3D seismic study of complex intra-salt deformation: An example from the Upper Permian Zechstein 3 stringer, western Dutch offshore. Geol. Soc. London, Spec. Publ. 363, 489–501. doi:10.1144/SP363.23

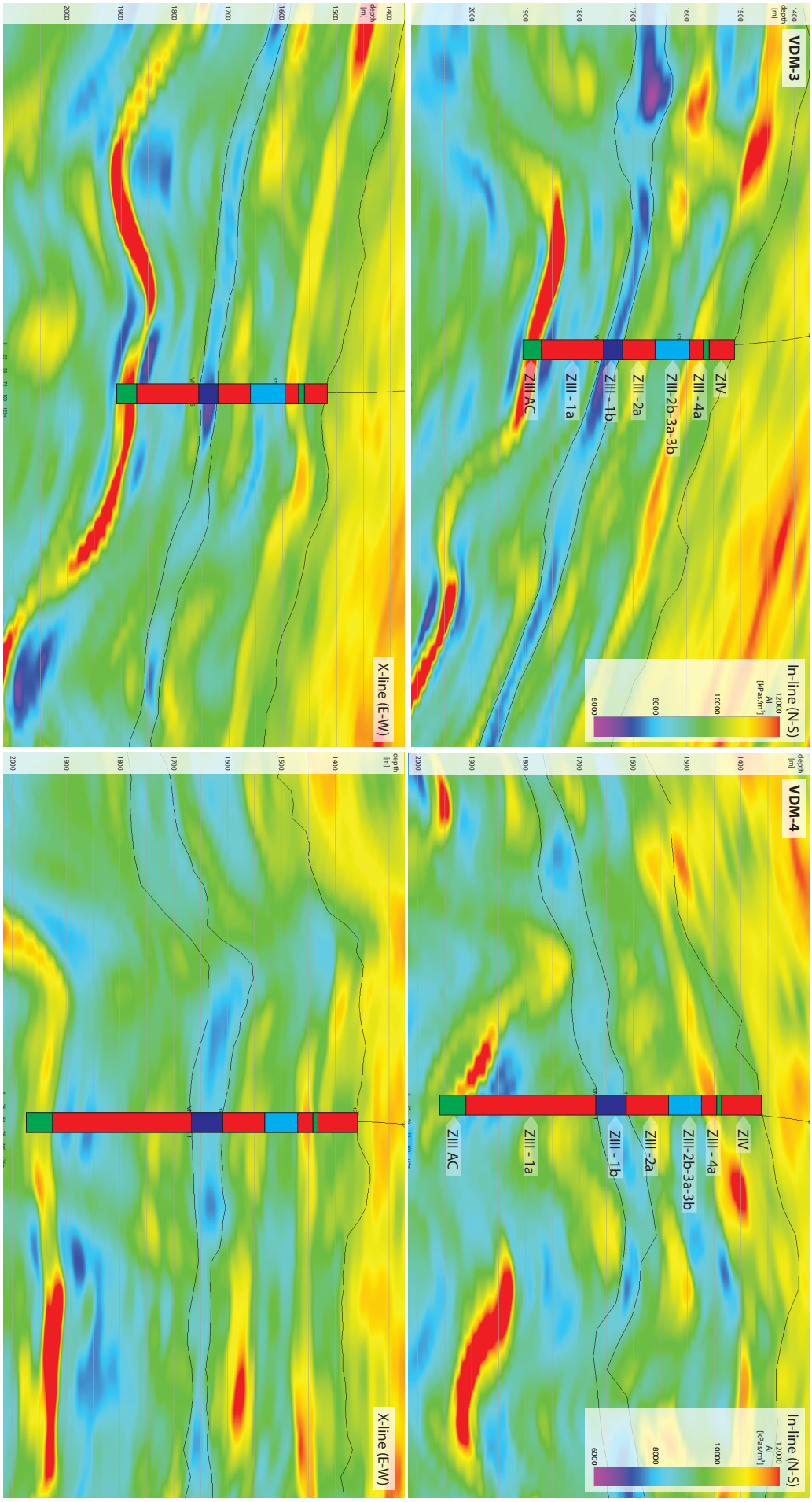
Van Gent, H., Urai, J.L., de Keijzer, M., (2011). The internal geometry of salt structures - A first look using 3D seismic data from the Zechstein of the Netherlands. J. Struct. Geol. 33, 292–311. doi:10.1016/j.jsg.2010.07.005

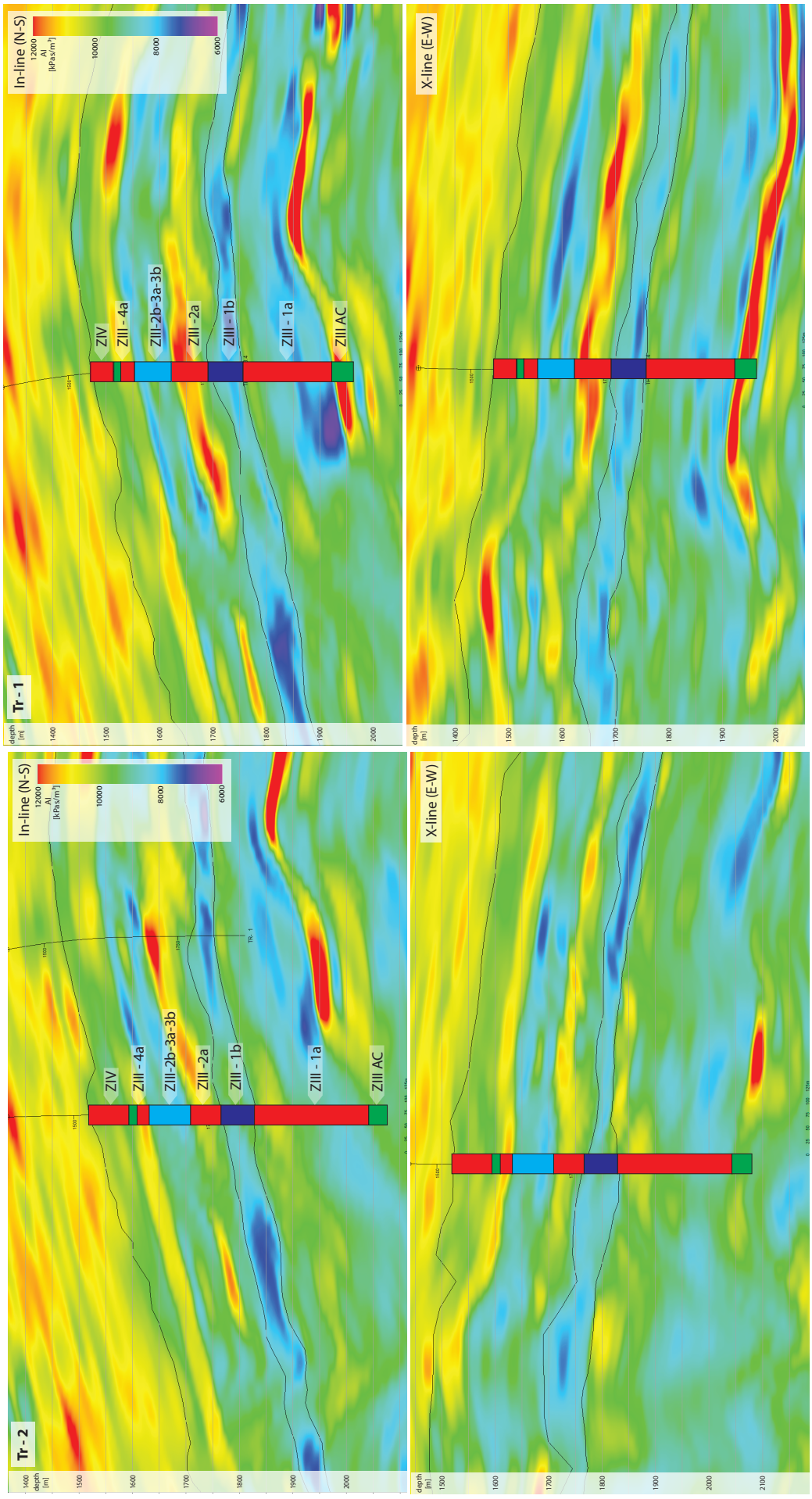
Wong, T.E., (2007). Jurassic, in: Wong, T.E., Batjes, D.A.J., De Jager, J. (Eds.), Geology of the Netherlands. Royal Netherlands Academy of Arts and Sciences, pp. 107–125.

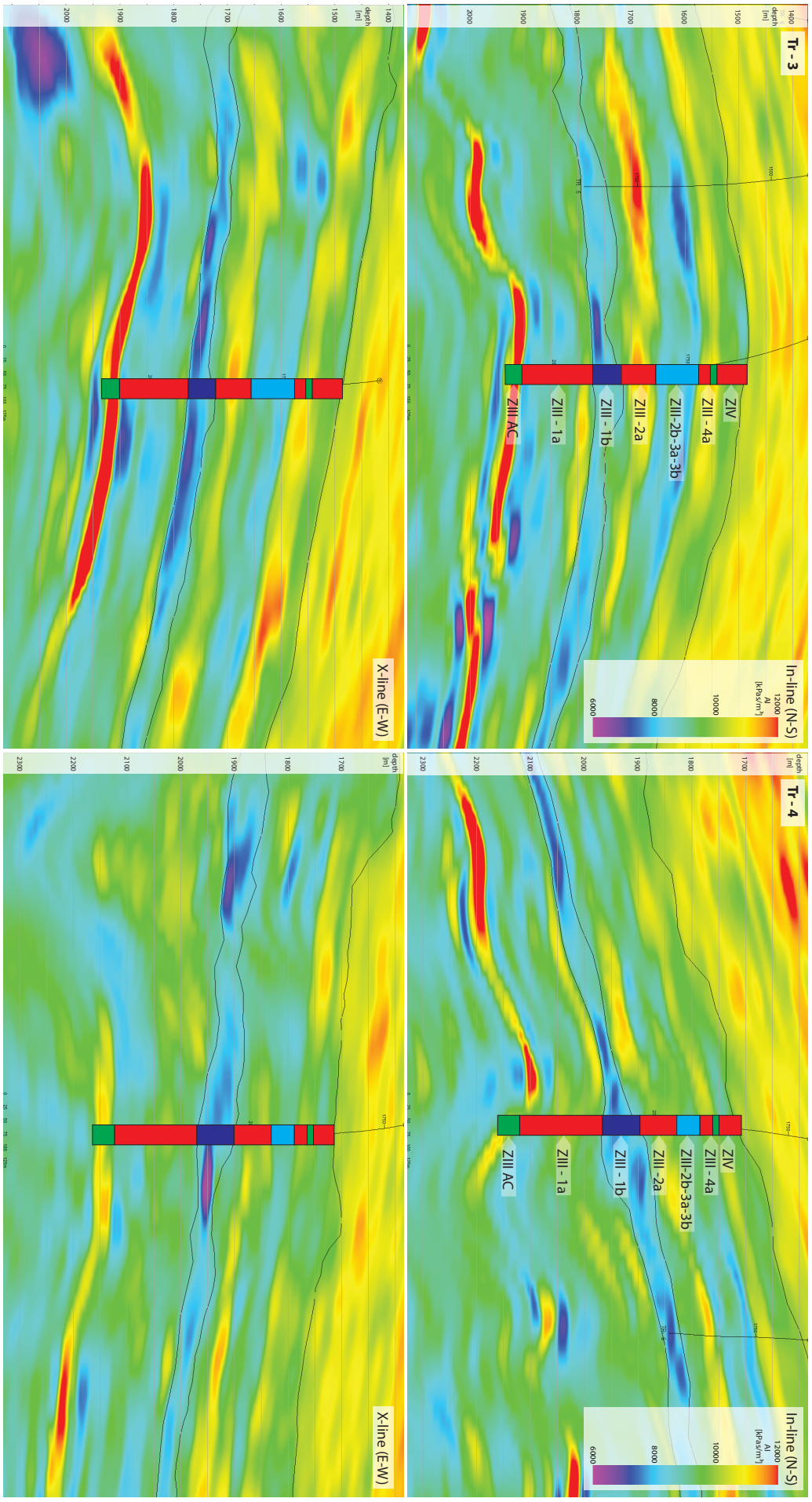
Appendix

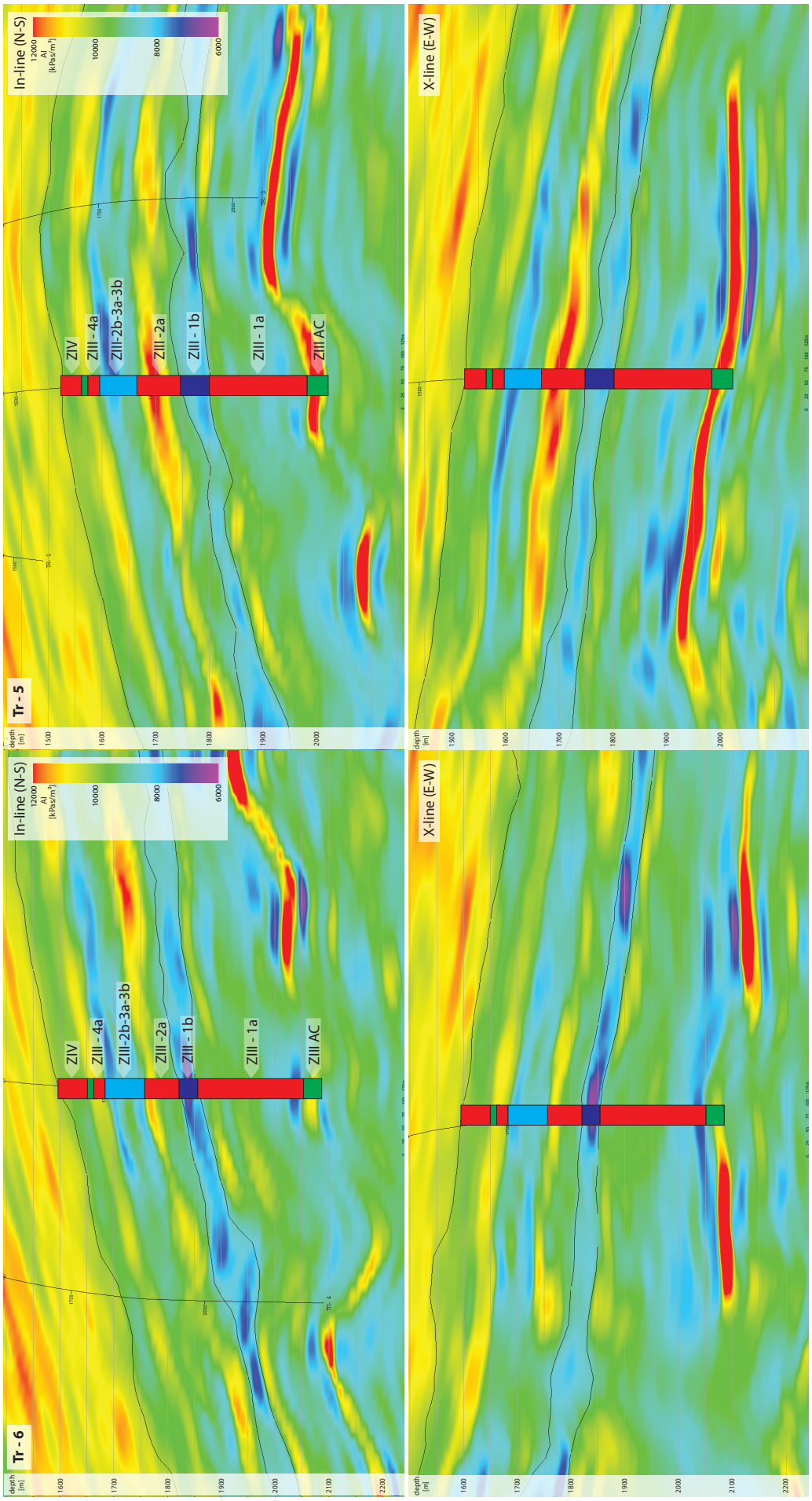
Body [-]	Max Thickness [m]	Assoc. AI [kPasm^-3]	Minimum AI [kPasm^-3]	Assoc. Thickness [m]	Average Thickness [m]	Average AI [kPasm^-3]	Volume isopachs [10^6 m^3]	Volume voxels [10^6 m^3]
0	90.3	7704.0	6084.0	29.5	37.7	7466.4	92.82	33.53
1	69.6	6772.0	6012.0	28.0	39.7	7451.1	84.53	29.17
2	163.9	7584.0	6340.0	108.8	96.7	7494.4	183.73	27.90
3	126.2	7236.0	6184.0	106.0	88.3	7504.4	84.31	14.05
4	85.9	7408.0	6404.0	31.2	37.5	7485.9	33.45	12.35
5	77.5	7708.0	6788.0	38.9	43.9	7547.5	25.36	7.97
6	263.8	7460.0	6208.0	55.0	90.8	7364.6	37.58	5.96
7	70.0	7792.0	6616.0	27.9	39.3	7548.8	16.25	5.49
8	81.8	6544.0	5944.0	55.0	51.7	7362.7	18.10	4.99
9	110.7	7168.0	6504.0	59.3	64.9	7516.3	21.99	4.74
10	55.8	7164.0	7076.0	53.9	40.6	7608.7	11.52	3.86
11	94.8	7716.0	5864.0	29.4	39.1	7303.4	10.91	3.81
12	56.8	7824.0	6588.0	38.5	39.7	7508.0	10.67	3.71
13	103.8	7708.0	6780.0	52.7	65.6	7628.8	17.37	3.69
14	83.4	7808.0	6044.0	41.9	45.9	7434.8	12.19	3.65
15	47.0	7840.0	6768.0	31.2	33.1	7534.6	7.85	3.27
16	166.0	7684.0	6604.0	119.4	105.0	7376.3	18.89	2.73
17	104.7	7152.0	6620.0	63.3	67.6	7485.6	12.41	2.53
18	100.2	6608.0	6384.0	82.5	66.6	7422.8	11.42	2.37
19	93.4	7596.0	6488.0	55.0	46.6	7455.2	7.48	2.27
20	80.9	7744.0	6768.0	62.7	63.8	7486.8	10.26	2.15
21	108.8	7744.0	6156.0	103.8	71.8	7465.9	10.57	2.10
22	105.7	7424.0	6424.0	47.4	58.1	7460.6	8.51	2.00
23	58.2	7720.0	6756.0	33.9	35.8	7465.6	5.31	1.95
24	37.8	7640.0	6824.0	26.0	29.3	7530.4	3.90	1.87
25	60.6	7716.0	7016.0	27.0	37.8	7608.9	4.84	1.77
26	76.2	7492.0	6756.0	46.3	49.1	7562.7	6.16	1.76
27	102.5	7164.0	6264.0	61.8	56.8	7322.4	6.41	1.61
28	50.6	7524.0	6556.0	30.8	37.9	7402.4	4.47	1.57
29	62.5	7496.0	6476.0	44.2	43.6	7368.7	4.75	1.49
30	110.9	6852.0	6716.0	84.6	71.3	7439.1	6.97	1.44
31	111.6	6576.0	6576.0	111.6	99.2	7395.2	9.08	1.35
32	46.8	7564.0	6976.0	38.1	37.4	7597.2	3.62	1.32
33	57.1	7792.0	6708.0	30.9	39.6	7550.7	3.76	1.25
34	79.8	7720.0	6920.0	25.2	45.8	7551.5	4.25	1.20
35	66.5	7280.0	7264.0	41.7	46.3	7645.2	3.99	1.13

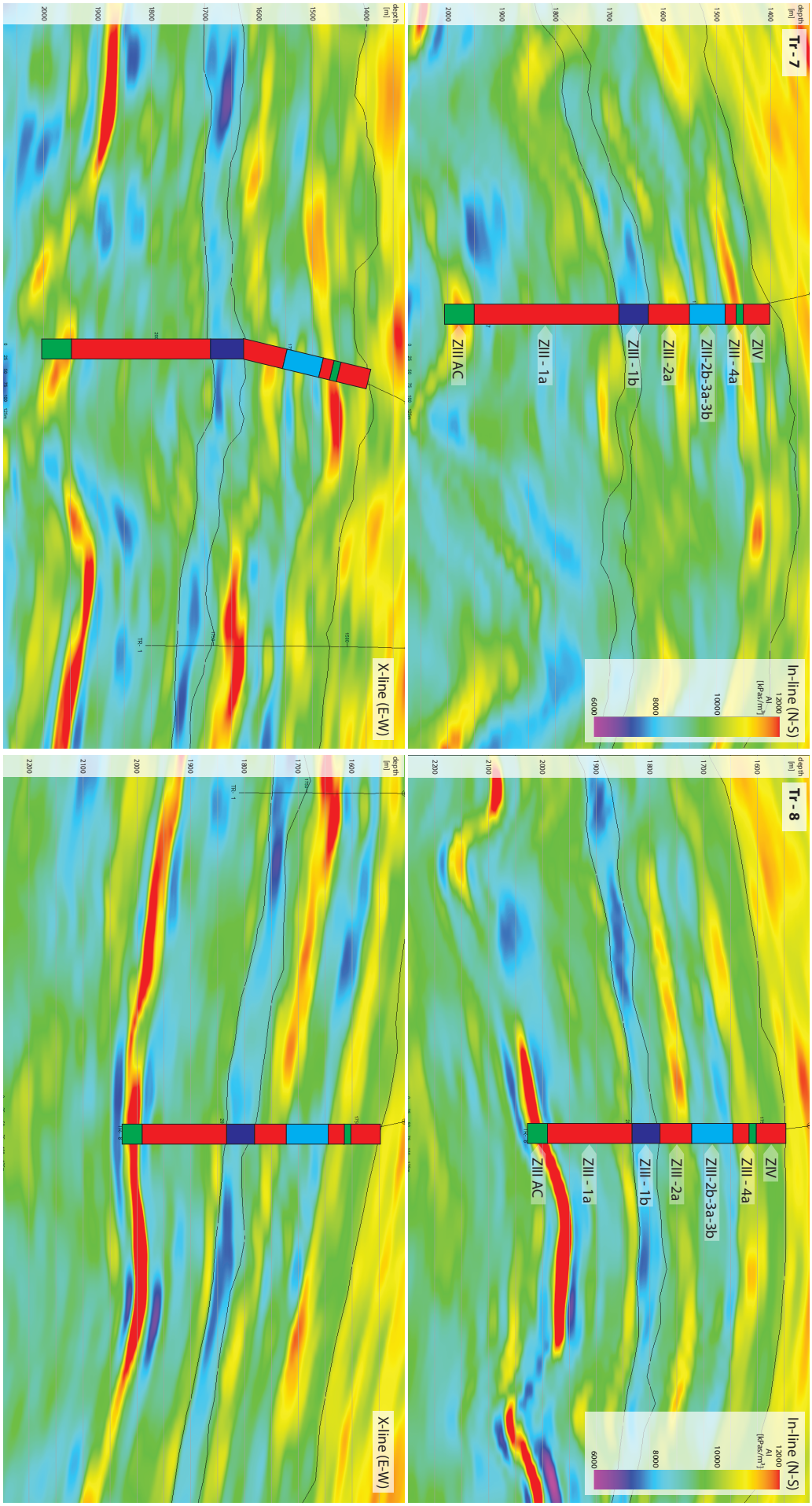

In-line (N-S)
AI [kPas/m³]
12000
10000
8000
6000
VDM-1
ZIV
ZIII - 4a
ZIII-2b-3a-3b
ZIII -2a
ZIII - 1b
ZIII - 1a
ZIII AC
depth [m]
X-line (E-W)
VDM-2

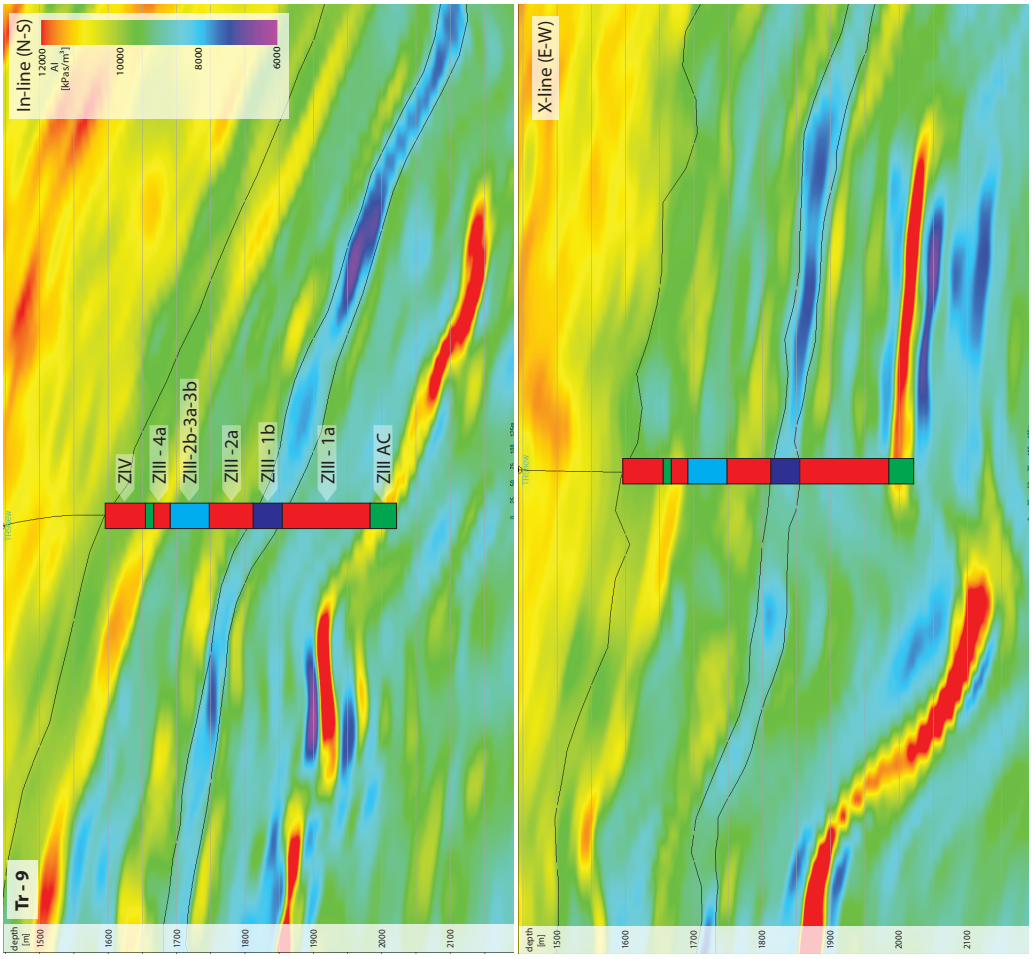

VDM-3
In-line (N-S)
X-line (E-W)
ZIV
ZIII - 4a
ZIII-2b-3a-3b
ZIII - 2a
ZIII - 1b
ZIII - 1a
ZIII AC
AI [kPa.s/m]
depth [m]
VDM-4
In-line (N-S)
X-line (E-W)
ZIV
ZIII - 4a
ZIII-2b-3a-3b
ZIII - 2a
ZIII - 1b
ZIII - 1a
ZIII AC
AI [kPa.s/m]
depth [m]


In-line (N-S)
X-line (E-W)
Tr - 1
Tr - 2
ZIV
ZIII - 4a
ZIII-2b-3a-3b
ZIII -2a
ZIII - 1b
ZIII - 1a
ZIII AC
depth [m]


Tr - 3
ZIV
ZIII - 4a
ZIII-2b-3a-3b
ZIII -2a
ZIII - 1b
ZIII - 1a
ZIII AC
In-line (N-S)
X-line (E-W)
Tr - 4
ZIV
ZIII - 4a
ZIII-2b-3a-3b
ZIII -2a
ZIII - 1b
ZIII - 1a
ZIII AC
In-line (N-S)
X-line (E-W)


Tr - 5
In-line (N-S)
12000
10000
8000
6000
ZIV
ZIII - 4a
ZII-2b-3a-3b
ZIII -2a
ZIII - 1b
ZIII - 1a
ZIII AC
depth [m]
1500
1600
1700
1800
1900
2000
X-line (E-W)
Tr - 6
In-line (N-S)
12000
10000
8000
6000
ZIV
ZIII - 4a
ZII-2b-3a-3b
ZIII -2a
ZIII - 1b
ZIII - 1a
ZIII AC
depth [m]
1600
1700
1800
1900
2000
2100
2200
X-line (E-W)


Tr - 7
ZIV
ZIII - 4a
ZIII-2b-3a-3b
ZIII -2a
ZIII - 1b
ZIII - 1a
ZIII AC
In-line (N-S)
X-line (E-W)
Tr - 8
ZIV
ZIII - 4a
ZIII-2b-3a-3b
ZIII -2a
ZIII - 1b
ZIII - 1a
ZIII AC
In-line (N-S)
X-line (E-W)


In-line (N-S)
12000
AI
[kPa·s/m]
10000
8000
6000
ZIV
ZIII - 4a
ZIII-2b-3a-3b
ZIII-2a
ZIII - 1b
ZIII - 1a
ZIII AC
Tr - 9
depth
[m]
1500
1600
1700
1800
1900
2000
2100
X-line (E-W)
depth
[m]
1500
1600
1700
1800
1900
2000
2100

4. Handling and analysis of an extremely hygroscopic K-Mg salt core

4.1 The dry lab

The extremely hygroscopic properties of most K-Mg salts require an extremely dry workplace. A relative humidity of more than 30% would cause water absorption and immediate damage to thin-sections or powdered samples. To avoid this, the workplace should be kept below a relative humidity of about 20% at any time. Considering that the humidity could rise locally by transpiration, wet cutting and cleaning, we achieved good results with a target rel. humidity of about 10%. Under these condition safe handling of the cores was possible while several persons, wet rags and wet cutting equipment were present.

These dry conditions could be achieved by either working in freezing temperatures, constant influx of dry air or constant air-drying. For practical reasons we decided for the last option. To achieve efficient constant dryness, intrusion of moisture into the room through the walls or by air influx must be prevented. Intrusion through the walls was prevented by watertight aluminum wallpapers on the walls and ceiling of the dry labor.

To keep a more or less constant climate in the labor unaffected by frequent opening of the door, a room with a separate entrance area that functioned as a climate lock was chosen (Fig. 4.1). In this entrance area, an adsorption air dryer and a conventional air-conditioning unit were present. The air-conditioning is needed to ensure semidry (30-40 % rel.) fresh air supply during longtime working and to provide cooling during the summer.

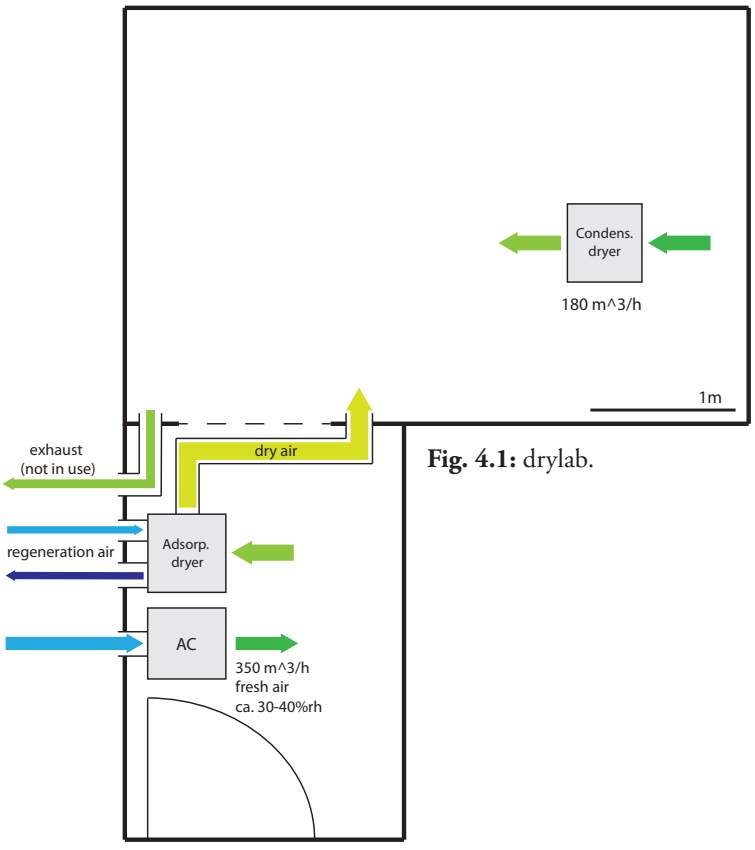


Fig. 4.1: drylab.

The adsorption air dryer sucks the air in the entrance area and exhaust very dry (3-10 % rel.) air into the main room. This constant air influx causes a slight overpressure in the main room preventing semidry air from the air conditioning or door opening to enter. The air dryer itself has a separate in- and exhale connection to the outside to dispose moist air without changing the total vol-

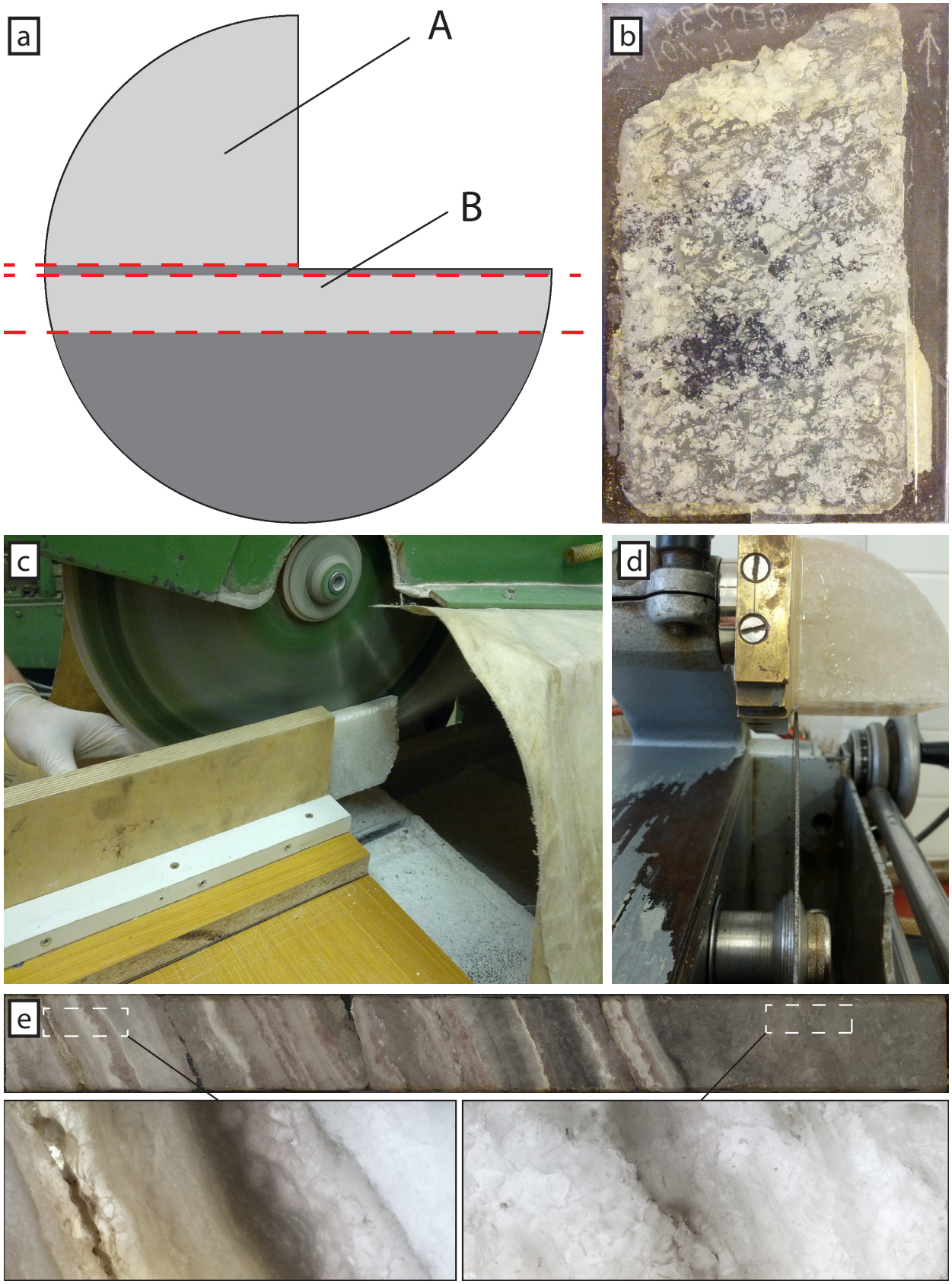


Fig. 4.2: Figure 9) (a) Scheme of core cutting: “A” is used for thin section preparation; ”B” is used for thick section preparation. (b)Thinn section. (c) dry core cutting with a circular saw. (d) Thinn section cutting. (e) Thick slice (B) from one core 1/3 from 2449 to 2450 m and two enhanced areas photographed with transmitted light. Left: thin layers of Carnallite with Bischofite and rock salt. Right: coarse rock salt with grains up to 6 mm.

ume of air in the laboratory. To prevent damage during adsorption dryer failure a simple condensation dryer was present that was able to keep the humidity below 30 % rel.

4.2 Cutting the core pieces

The core cutting was executed depending on the material content and core condition. Of all core pieces that belong to the ZIII-1b (above1835 m depth) one quarter along the drill axis was already cut out directly after drilling (Fig. 4.2). The deeper ZIII-1a halite core pieces were left intact. Due to the lack of extremely hygroscopic K-Mg salts in these pieces they were cut parallel to the drill axis during dry weather conditions outside of the dry lab with a huge compressed air-cooled diamond saw (Fig. 4.2c). The rest of the core had to be cut inside the dry laboratory with a smaller diamond blade table saw (Fig. 4.3). Dry cutting with the used diamond blade is only possible in almost pure halite parts. If carnallite or bischofite is present, the blade is clogged immediately, heads up and is unable to cut through the material. To provide sufficient cooling and cleaning a slightly under saturated Na-Mg-K brine was used. Alternatively, oil can be used for cooling but was dismissed due to possible problems during later sample gluing. The brine was applied to the blade by a reservoir under the blade in which the blade was dipped about 2-3 mm. To minimize contact of brine with the core and to reduce mist, the blade was run through a vacuum device during cutting (Fig. 4.3 d&e).

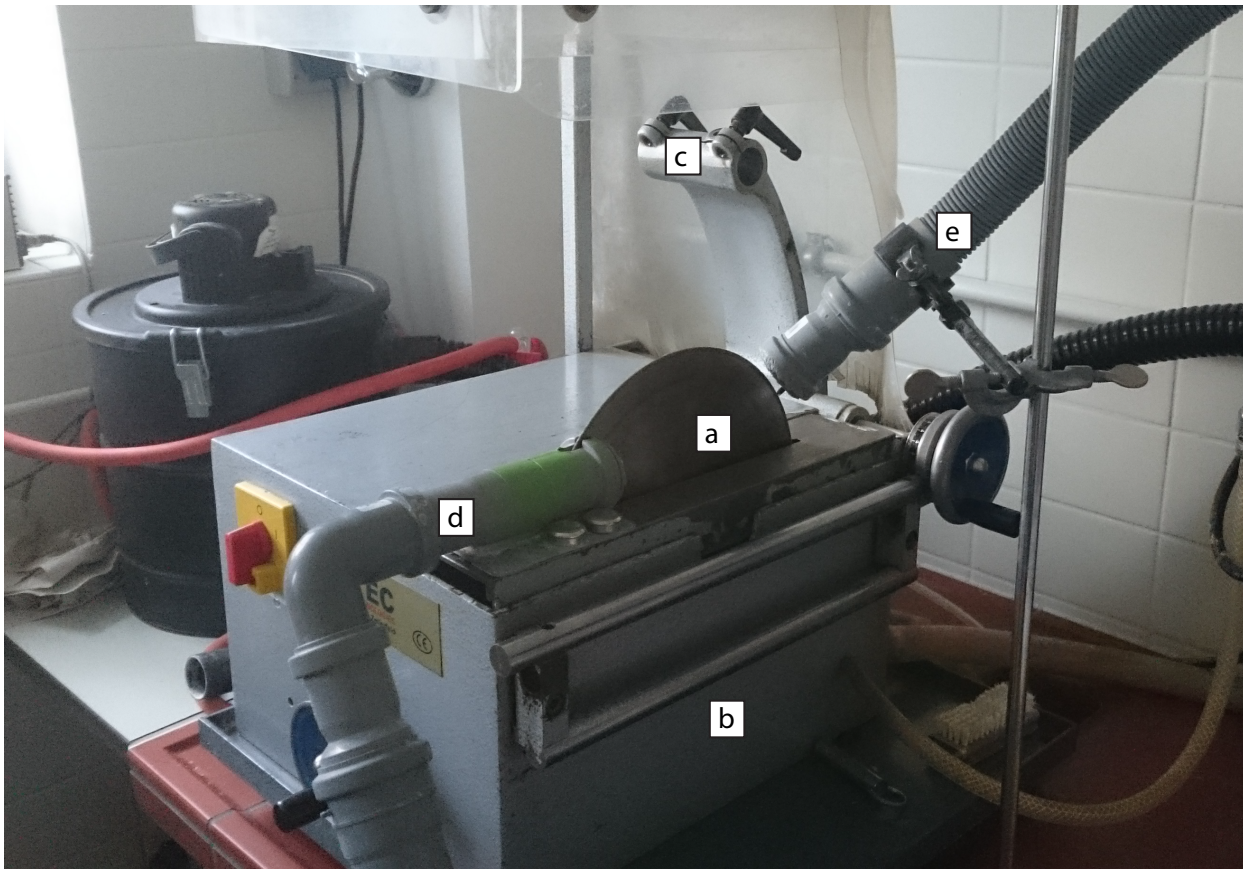


Fig. 4.3: a: diamond blade saw. b: fluid reservoir. c: movable arm for thin section preperation. d&e: vacuum suction.

We note that when cutting the core, the 1 m core segments were unfortunately not marked to allow orienting the segments with respect to north. When preparing for slabbing, the core segments were matched as well as possible. This was complicated by fact that the quarter of the core that was extracted directly after drilling was cut randomly and the slabs had to be aligned with the existing cuts for technical reasons. Hence, the slabs and photos shown do not always match in orientation and therefore, dipping directions are random. As a result, it is not possible to recognize folds directly by change of dip angle if the fold wavelength exceeds the core segment length of about 1m.

4.3 Core photographs

The photographs of the core were taken with a Nikon D800 camera with a 60 mm macro lens (36MP). Due to limitations of the depth of focus with this lens setup each picture had to be taken perpendicular to the core slab surface. This was complicated by thickness variations in and between the core pieces of up to 1 cm due to the manual cutting. Additionally, the autofocus was unfit to work in very homogeneous core parts. To establish perfect conditions the core pieces were placed on a horizontal glass plate und photographed from below. The camera was placed on a rail parallel to the core and the about 1 m long core parts were photographed in 15 cm steps and later stitched together using the Adobe Photoshop Photomerge (reposition only) function. The cores were aligned parallel to a cm scale that also functioned as reference for the autofocus. To establish constant conditions all pictures were taken with the same shutter speed, white balance and light condition. For lighting, a 2x36 watt 1.2 m long halogen lamp (6400 k) in a shaded room was used. The lamp was either placed directly on top of the core slabs for transmitted light pictures or placed under the core for reflective conditions. To avoid reflections of the lamp in the reflective light photographs the lamp must not be placed too close to the camera rail.

4.4 Thin section and polished section preparation

For thin section preparation core pieces were cut to the right size as described before. In the next step, one side of the sample manually was polished using dry grinding paper with degreasing grid size from 320 to 2400. If the sample contained bischofite an additional finishing step is needed. During the grinding of bischofite, the top few µm of the polished surface immediately recrystallized, this fine grained recrystallized layer was removed in a last step with a slightly damp polishing cloth as described in Urai (1983).

When the polishing is finished, the polished side of the sample is glued to a glass slide with

transparent epoxy glue (Fig. 4.2b). After hardening the sample is cut to a thickness of about 2-3 mm. The glass slide is placed in a vacuum holder that can be moved parallel to a diamond blade saw (Fig. 4.2d). As mentioned before carnallite and bischofite cannot be cut dry but the amount of brine used during the core cutting might cause damage to the thin sample. Instead of brine reservoir below the blade a brine sprinkler was positioned at the blade directly behind the cut sample. With this setup, the blade was wetted after coming in contact with the sample and had time to dry of during the at least 300° turn also going through vacuum suction. After the rough cutting, the top side of the thin section had to be polished and brought to the right thickness. The thinning of the thin section was performed by grinding the section on 300 to 800 grid size paper until interference colors of first to third order were observable. As a time saving measure the thin section was not repeatedly checked with a polarized light microscope. Instead, to survey the interference color, a combination of a polarized light source and polarizing glasses (conventional 3D shutter glasses) in crossed orientation were used. If the sample was placed in front of the light source, the interference colors could be observed directly without interrupting the grinding and polishing process. When the desired thickness was reached and the sample polished down to a grit size of 2400 to 4000 it was either left uncovered for reflected light microscopy or covered with epoxy glue and a thin glass plate. If bischofite was present in the sample the top surface was removed with a damp cloth as described above before the covering. Additionally, polished-sections from halite-dominated samples were etched with a slightly under saturated NaCl brine for about 30 seconds and dried using a jet of n-Hexane to remove all brine. The etching makes halite sub-grain boundaries visible in reflective light microscopy and the halite sub-grain sizes were used for halite sub-grain piezometry (Carter et al. 1993; Franssen 1993; Schléder and Urai 2005).

References

Carter N., Horseman S., Russell J., Handin J (1993) Rheology of rocksalt. J Struct Geol 15:1257–1271. doi: 10.1016/0191-8141(93)90168-A

Franssen RCMW (1993) Rheology of synthetic rocksalt with emphasis on the influence of deformation history and geometry on on the flow behaviour. Rijksuniversiteit Utrecht

Schléder Z, Urai JL (2005) Microstructural evolution of deformation-modified primary halite from the Middle Triassic Röt Formation at Hengelo, The Netherlands. Int J Earth Sci 94:941–955. doi: 10.1007/s00531-005-0503-2

Urai JL (1983) Deformation of wet salt rocks. Rijksuniveriteit te Utrecht

5. Structure of K-Mg salt layers in the Zechstein III of the Veendam Pillow, NE Netherlands: development of a tectonic mélange during salt flow

This chapter was published as: Raith AF, Urai JL, Visser J (2018) Structural and microstructural analysis of K–Mg salt layers in the Zechstein 3 of the Veendam Pillow, NE Netherlands: development of a tectonic mélange during salt flow, Netherlands Journal of Geosciences, 96- 4, pp. 331-351, doi: 10.1017/njg.2017.31

5.1 Abstract

In fully developed evaporite cycles, effective viscosity contrasts of up to five orders of magnitude are possible between different layers, but the structures and mechanics in evaporites with such extreme mechanical stratification are not well understood. The Zechstein 3 unit in the Veendam salt pillow in the Netherlands contains anhydrite, halite, carnallite and bischofite, showing this extreme mechanical stratification. The Veendam Pillow has a complex multiphase salt tectonic history as shown by seismic reflection data: salt withdrawal followed by convergent flow into the salt pillow produced ruptures and folds in the underlying Z3-anhydrite–carbonate stringer and deformed the soft Z3-1b layer

We analysed a unique carnallite- and bischofite-rich drill core from the soft Z3-1b layer by macroscale photography, bulk chemical methods, X-ray diffraction and optical microscopy. Results show high strain in the weaker bischofite- and carnallite-rich layers, with associated dynamic recrystallisation at very low differential stress, completely overprinting the original texture. Stronger layers formed by alternating beds of halite and carnallite show complex recumbent folding on different scales commonly interrupted by sub-horizontal shear zones with brittle deformation, veins and boudinage. We attribute this tectonic fragmentation to be associated with a softening of the complete Z3-1b subunit during its deformation. The result is a tectonic mélange with cm- to 10 m-size blocks with frequent folds and boudinage. We infer that these structures and processes are common in deformed, rheologically strongly stratified evaporites.

5.2 Introduction

Metre-thick layers of potassium–magnesium (K–Mg) salts are common in salt giants like the European Zechstein or the Cretaceous of offshore Brazil (Cerqueira et al., 1997; Geluk et al., 2000, 2007; Warren, 2006). Consisting of carnallite or sylvite, these layers are locally exploited by potash mining. They are also known to generate problems while drilling subsalt wells, caused by their high solubilities and very low viscosities (Williamson et al., 1998). Occasionally, even less viscous layers of tachyhydrite or bischofite are included in this sequence (Coelewij et al., 1978; Vysotskiy & Kislik, 1987; Poiate et al., 2006; Geluk et al., 2007).

The K–Mg salts carnallite and bischofite deform in the laboratory with viscosities up to three orders of magnitude lower than halite (Van Eekelen et al., 1981; Spiers et al., 1983; Urai, 1983, 1985; Urai & Boland, 1985; Langbein, 1987; Urai et al., 1987, 2008; Scott Duncan & Lajtai, 1993; Schenk & Urai, 2005; Muhammad, 2015). Together with the much stronger carbonates and sulphates that are precipitated in the same evaporation cycle, a highly stratified mechanical layering can develop inside salt bodies (Richter-Bernburg, 1987; Geluk, 1998, 2000; Warren, 2006; Bérest et al., 2012). During deformation, evaporites form complex structures including folds, faults, veins and breccias that are often visible in mine galleries and drill cores (Martini, 1953; Roth, 1968; Siemeister, 1969; Coelewij et al., 1978; Talbot et al., 1982; Richter-Bernburg, 1987; Jackson & Talbot, 1989; Bornemann & Fischbeck, 1991; Burliga, 1996; Zirngast, 1996; Behlau & Mingerzahn, 2001; et al.Bornemann et al., 2008; Schléder et al., 2008; Hammer et al., 2014). However, there are no mine galleries and very few drill cores in evaporites rich in bischofite, due to mechanical and chemical instability. Although mine and core observations give excellent insights into the structures and deformation processes present, the full internal structure of the salt bodies can only be extrapolated from these limited data.

While the external morphology of salt bodies is relatively well understood and can be imaged using 3D reflection seismic data, internal structures in 3D have only recently begun to be studied, using internal reflectors with high acoustic impedance contrasts (anhydrite + carbonate stringers) (Van Gent et al., 2011; Cartwright et al., 2012; Fiduk & Rowan, 2012; Jackson et al., 2014, 2015; Strozyk et al., 2014). A recent study (Raith et al., 2016) using high-resolution 3D seismic data, described the large-scale structure of the K–Mg salt-rich Zechstein 3, inside the Veendam salt pillow in the north European Zechstein basin. Nevertheless, the spatial resolution of 3D reflection seismic is limited and structures smaller than 25–30 m cannot be imaged.

In this project, we analysed 81 m of core drilled through the K–Mg salt-rich Zechstein III-1b subunit in the Veendam Pillow. This combination of 3D seismic and a drill core provides a unique opportunity to study the deformation of a salt body with extreme rheological layering at km to 0.1 mm scales, over six orders of magnitude. The core was analysed with the aid of chemical analyses, X-ray diffraction (XRD) and optical microscopy.

The following two questions are addressed: (1) how is strain partitioned in a salt body with extreme rheological layering? and (2) does strain partitioning result in strongly deformed but continuous layers or do pinches or fractures disrupt the original layering to produce a tectonic mélange?

Our results can help us to better understand the impact of thin soft layers on the behaviour of a deforming salt body and to improve prediction of the geometries of ore bodies made up of K–Mg salts. The results of this study may help us to improve the understanding of well-bore stability in K–Mg

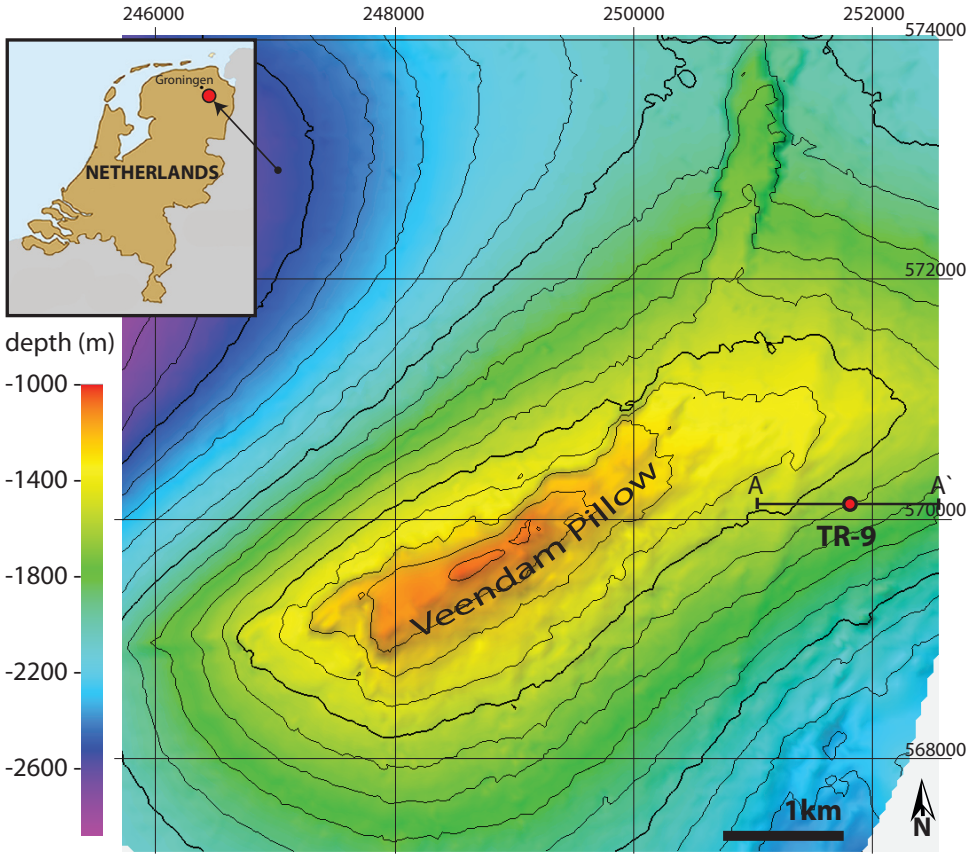


Fig. 5.1: Depth map of Top Salt at the Veendam Pillow. The TR9 well (red dot) was drilled at the SE flank. The profile A–A` is shown in (b). (b) E–W profile (A–A`) at the core location from seismic interpretation (Raith et al., 2016).

salts and to predict the long-term evolution of abandoned solution-mining caverns and nuclear waste repositories.

5.2.1 Study area

The Tripscompagnie 9 (Tr-9) core was drilled in the SE flank of the Veendam salt pillow 10 km southeast of the city of Groningen in the NE Netherlands (Fig. 5.1). The Veendam Pillow is located at the southernmost edge of the Groningen High in the Lower Permian Basin. The Southern Permian Basin has undergone four tectonic phases with extension, compression and halokinesis (Ziegler, 1978; Mohr et al., 2005; De Jager, 2007; Geluk et al., 2007). Three major tectonic phases (break-up of Pangaea in the Mesozoic, the Alpine inversion in the late Cretaceous and Early Tertiary and the Rhine Graben rift development from the Oligocene to recent times) took place after salt deposition and triggered renewed salt movement. The Zechstein section in the Veendam Pillow contains Z-I to Z-IV overlain by Lower Triassic (Buntsandstein and upper Röt), Cretaceous (Rijnland and Chalk), Tertiary units (Lower/Middle and Upper North Sea Group) and the Quaternary (Raith et al., 2016) with an important erosional unconformity between the Triassic and the base of the Cretaceous.

The focus of this study is on the Z3 unit, which contains the Zechstein 3 anhydrite–carbonate (Z3-AC) layer (also called Z3 AC stringer or floater since it is a distinct reflector in the typically seismically transparent rock salt) at the base, overlain by four Z3 subunits (Fig. 5.2). The Z3 subunits typical-

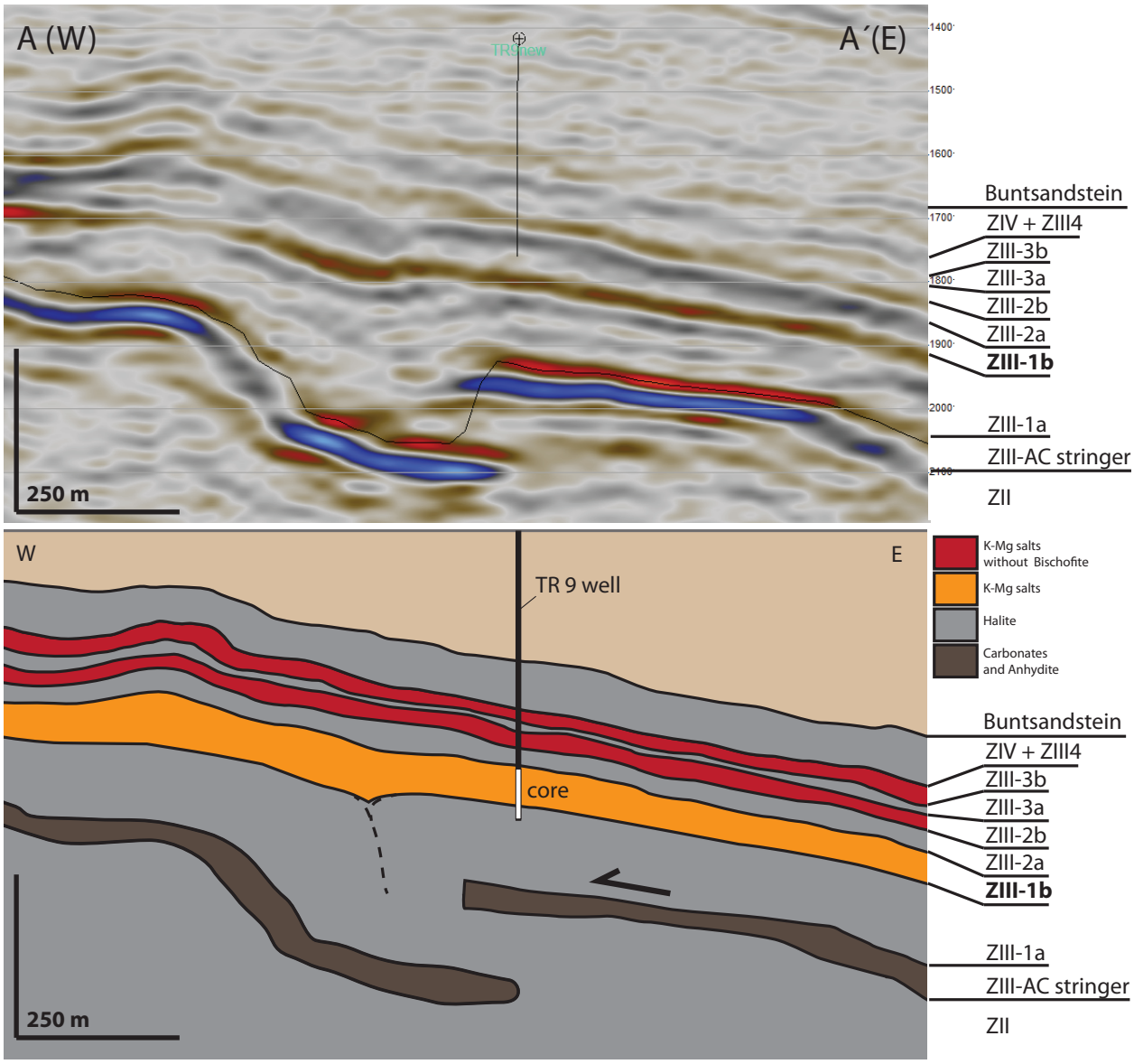


Fig. 5.2: E-W profile (A-A´) at the core location from seismic interpretation (Raith et al. 2016).

ly consist of halite (>95%) in the lower part (Z3-1a,2a,3a) followed by a K–Mg salt part (Z3-1b,2b,3b) (Geluk et al., 2007). The Z3-4 contains no K–Mg salt. While the K–Mg salts in the Z3-2b and -3b were interpreted as intimate mixing of carnallite and halite crystals as the result of co-precipitation (Coelewij et al., 1978), the much thicker Z3-1b consists of numerous thin layers dominated by one mineral type and metre-thick layers of bischofite. The massive occurrence of bischofite was interpreted as being the result of accumulation of bittern brines in a local depression formed by an active graben in the subsalt Rotliegend (Raith et al., 2016).

Corresponding to the regional development, salt flow in the Veendam Pillow can be divided into three main phases (Raith et al., 2016): (1) early extensional salt flow during the Triassic and Jurassic leading to the break-up of the 3Z3-AC stringer, (2) a tectonically quiet phase that lasted until the early Late Cretaceous, and (3) onset of the basin inversion during the late Cretaceous that led to overburden

buckling and downbuilding of sediments around the Veendam Pillow forming the structure present today. The salt flow was convergent towards the pillow centre, causing folding and thrusting of the competent Z3-AC stringer. This folding had a dominant influence on the overlying soft K–Mg salts, which were concentrated into areas above the stringer synclines (Raith et al., 2016). This deformation history suggests intense lateral salt flow in the Z3-1b with high strain, complex folding and boudinage, although in the core photos of Coelewij et al. (1978) this is not readily visible.

5.3 Data & Methods

The Tr9 well was cored over 81 m in December 2012 starting at a 1781.25 m true vertical depth (TVD) (drillers depth of 2420 m). The drilling itself and the first processing of the cores was part of the magnesium-salt exploration of Nedmag B.V. and not part of this research project focusing on the internal deformation of soft K–Mg salts. The core was described on site (ECOSPLAN), and one-quarter of the core (parallel to core axis) was cut out for chemical analysis of 20–40 cm long pieces which were dissolved and analysed for K, Na, Mg, Ca and S content using ICP-MS (inductively coupled plasma--mass spectrometry) (Appendix 1). In this paper, we always quote TVD.

For further analysis, 2 cm thick slabs were cut (parallel to core axis) using a diamond saw blade and a small amount of saturated Na, Mg and K chloride brine for cooling and cleaning the diamond blade. We note that when cutting the core, the 1 m core segments were unfortunately not marked to allow orienting the segments with respect to north. When preparing for slabbing, the core segments were matched as well as possible. This was complicated by fact that the quarter of the core that was extracted directly after drilling was cut randomly and the slabs had to be aligned with the existing cuts to produce continuous pieces from the centre of the core axis. Hence, the slabs and photos shown do not always match in orientation, and therefore dip directions are random. As a result, it is not possible to recognise folds directly by change of dip angle if the fold wavelength exceeds the core segment length of about 1 m.

The core slabs were photographed using reflected and transmitted light and subsequently stitched together to images with a resolution of about 250 pixels per cm (Fig. 5.3). The pictures were taken under constant artificial light conditions to be able to compare colours and identify grain boundaries. The work on the core was carried out in a dry laboratory with a constant relative humidity under 15%. Under these conditions thin sections containing soft and hygroscopic salts like bischofite can be prepared using dry sanding paper with incremental grit sizes from 300 to 4000. During the grinding of bischofite, the top few μm of the polished surface immediately recrystallised; this fine-grained recrystallised layer was removed in a last step with a slightly damp polishing cloth as described in Urai (1983). After the first round of analyses, the core was subdivided into six main lithoclasses with ad-

a
1781 m
Top
1782.24 m
1783.22 m
1784.18 m
1785.16 m
1786.11 m
1787.1 m
1787.94 m
1788.9 m
1789.82 m
1790.81 m
1791.81 m
Fig. 5.4
1m
Halite
Halite + Kieserite
Halite + Carnallite
Halite + Carnallite + Kieserite
Kieserite
Kieserite + Halite
Kieserite + Bischofite
Carnallite
Carnallite + Halite + Kieserite
Carnallite + Kieserite + Bischofite
Bischofite
Bischofite + Carnallite (+- Kieserite)

Halite
Halite + Kieserite
Halite + Carnallite
Halite + Carnallite + Kieserite
Kieserite
Kieserite + Halite
Kieserite + Bischofite
Carnallite
Carnallite + Halite + Kieserite
Carnallite + Kieserite + Bischofite
Bischofite
Bischofite + Carnallite (+- Kieserite)
1m
1801.5 m
1802.45 m
1803.42 m
1798.52 m
1799.52m
1800.51m
1795.78 m
1796.7 m
1797.52 m
1792.8 m
1793.8 m
1794.79 m
Top
Fig. 5.8
Fig. 5.10
b

Halite
Halite + Kieserite
Halite + Carnallite
Halite + Carnallite + Kieserite
Kieserite
Kieserite + Halite
Kieserite + Bischofite
Carnallite
Carnallite + Halite + Kieserite
Carnallite + Kieserite + Bischofite
Bischofite
Bischofite + Carnallite (+- Kieserite)
1m
1813.52 m
1814.52 m
1815.53 m
1810.53 m
1811.53 m
1812.51 m
1807.61 m
1808.56 m
1809.55 m
1804.39 m
1805.36 m
1806.19 m
1806.61 m
Fig. 5.7
Fig. 5.11
Top
c

Halite
Halite + Kieserite
Halite + Carnallite + Kieserite
Halite + Carnallite
Kieserite
Kieserite + Halite
Kieserite + Bischofite
Carnallite
Carnallite + Halite + Kieserite
Carnallite + Kieserite + Bischofite
Bischofite
Bischofite + Carnallite (+- Kieserite)
1m
1825.35 m
1826.36 m
1827.35 m
1822.46 m
1823.46 m
1824.43 m
1819.53 m
1820.5 m
1821.5 m
1816.56 m
1817.53 m
1818.53 m
Top
d

Halite
Halite + Kieserite
Halite + Carnallite
Halite + Carnallite + Kieserite
Kieserite
Kieserite + Halite
Kieserite + Bischofite
Carnallite
Carnallite + Halite + Kieserite
Carnallite + Kieserite + Bischofite
Bischofite
Bischofite + Carnallite (+- Kieserite)
1m
1836.51 m
1837.5 m
1838.49 m
1839.47 m
1834.17 m
1834.52 m
1835.54 m
1831.29 m
1832.23 m
1833.26 m
1828.34 m
1829.32 m
1930.31 m
Top
e

Fig. 5.3: Photographed TR-9 core slabs in transmitted and reflected light together with the interpretation into lithoclasses. Each core piece is numbered starting at the highest, first cored part. Missing core pieces are marked with blank panels.

ditional subcategories, defined by mineralogy and microstructure as recognizable with a hand lens. Thin sections and XRD analysis were used to determine the exact mineralogical composition of the lithoclasses. Detailed analysis of the microtextures in the thin sections was carried out using transmitted and reflected light polarisation microscopy. After gathering the data, the structures in the core were interpreted by identifying layer repetition, folding, faults, veins and fractures. Additionally, polished sections from halite-dominated samples were etched with a slightly under-saturated NaCl brine for about 30 s and dried using a jet of n-hexane to remove all brine. The etching makes halite subgrain boundaries visible in reflective light microscopy, and the halite subgrain sizes were used for halite subgrain piezometry (Carter et al., 1993; Franssen, 1993; Schléder & Urai, 2005).

5.4 Results

5.4.1 Lithoclasses

The layers in the core can be divided into five main lithoclasses (see below) based on the dominant evaporite mineral. These lithoclasses are briefly described below and can be subdivided into subcategories consisting of mixtures.

Halite (NaCl)

Almost pure halite is only present in the top few metres of the Z3-1b and in the Z3-1a cycles. In most cases, halite is mixed with kieserite and in some cases with carnallite. The halite at the top of 1b (under the 1.5 m thick breccia of halite in a carnallite matrix in the top) is divided in equiaxial very coarse-grained (up to 3 cm) layers and layers with <1 cm grain sizes (Fig. 5.4). In contrast to the rest of the Z3-1b a small amount of clay is common; there is no kieserite present. The coarse halite grains contain subgrains with an average size around 300 μm (Fig. 5.5). In some grains, chevron-shaped parallel bands of fluid inclusions are present. These have been interpreted as of primary fluid inclusions (Schléder & Urai, 2005).

The grey to light-brown halite in the Z3-1a contains layers of 5–40 cm thickness separated by thin (few mm) folded or boudinaged layers of fine-grained sulphates (Fig. 5.6). The up to 5 mm diameter equiaxed halite grains with 120° triple junctions of grain boundaries contain occasional subgrains of about 180 μm size.

In the Z3-1b subunit, halite is commonly interbedded with kieserite, forming Halite + Kieserite layers (Fig. 5.7& Fig. 5.8). The grey to white halite–kieserite layers are typically thin-layered and appear in layers from 1 to 30 cm thickness. The sub-mm elongated halite grains (Fig. 5.7& Fig. 5.8)

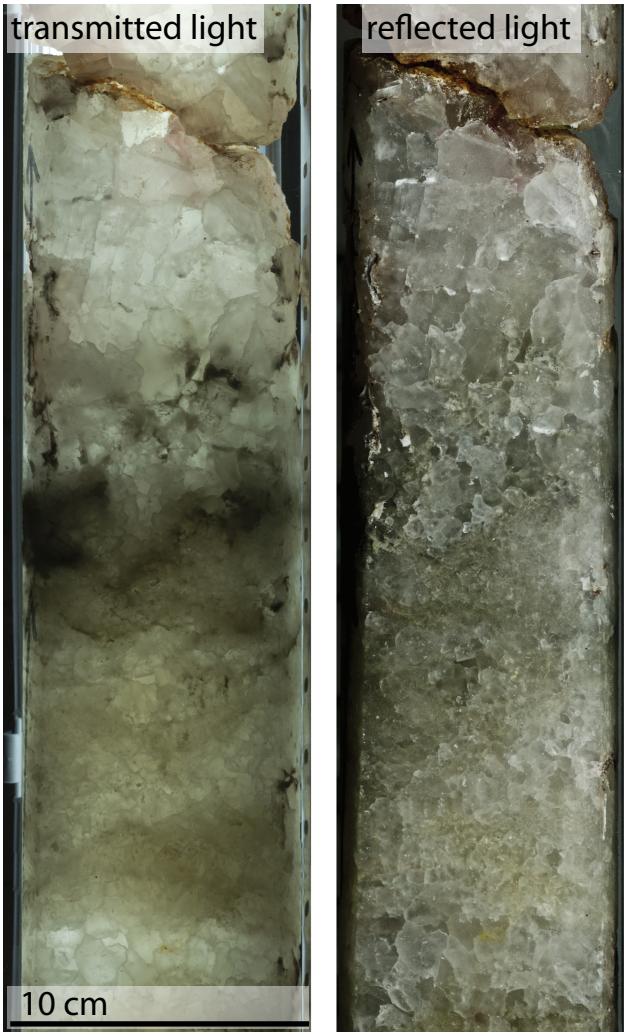


Fig. 5.4: Detailed pictures of core piece 1785.7–1786.1 m TVD in transmitted and reflected light showing large, >3 cm, equiaxial halite crystals.

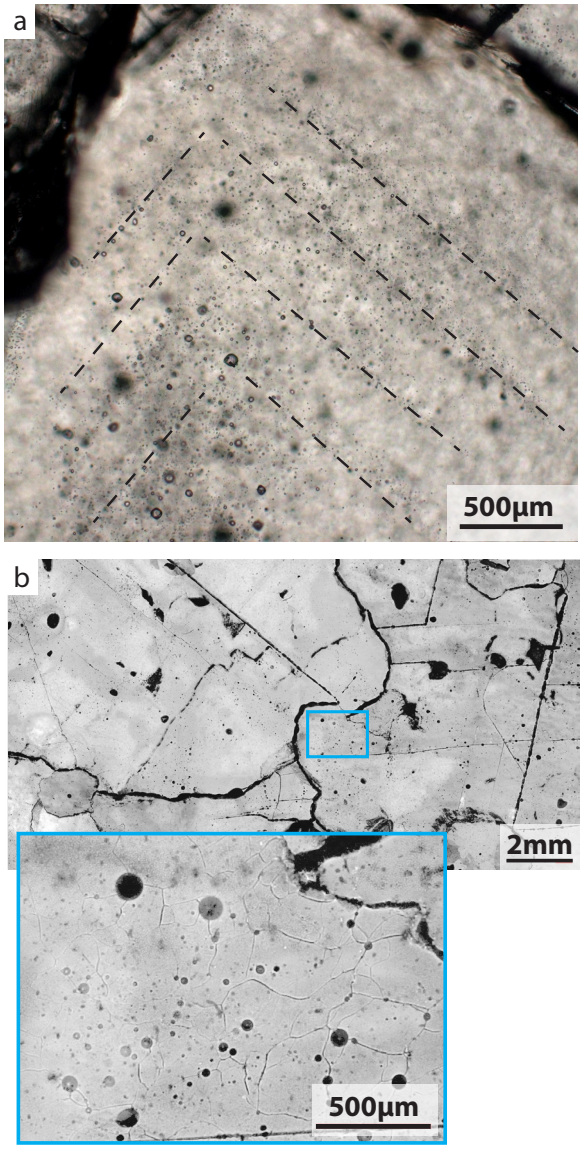


Fig. 5.5: (a) Polished section from top C_H-3 halite showing subgrains inside one big crystal with parallel straight fractures most likely originated from coring or sample preparation. (b) Example of parallel fluid inclusion lines, interpreted to be primary fluid inclusions built into the crystal during evaporation.

are mixed with kieserite and small amounts of other salts and sulphates. Commonly, these layers are fractured with carnallite/bischofite veins or are separated into fragments in a matrix of carnallite or bischofite. Thin separated halite/kieserite layers are often folded. In thin sections (Fig. 5.7& Fig. 5.8), a distinct elongation of the halite crystals parallel to bedding can be observed. Halite grain size tends to decrease with increasing kieserite content. The halite grains show an aspect ratio of about 3 : 1 and are on average 250 µm long and about 80 µm in the short axis. The kieserite grains are smaller than 20 µm and mostly euhedral (Fig. 5.8& Fig. 5.9).

In some layers halite or halite and kieserite is mixed with larger amounts of carnallite forming Halite + Carnallite and Halite + Carnallite + Kieserite layers. These layers have a grey to white colour and are less transparent than the Halite + Kieserite layers.

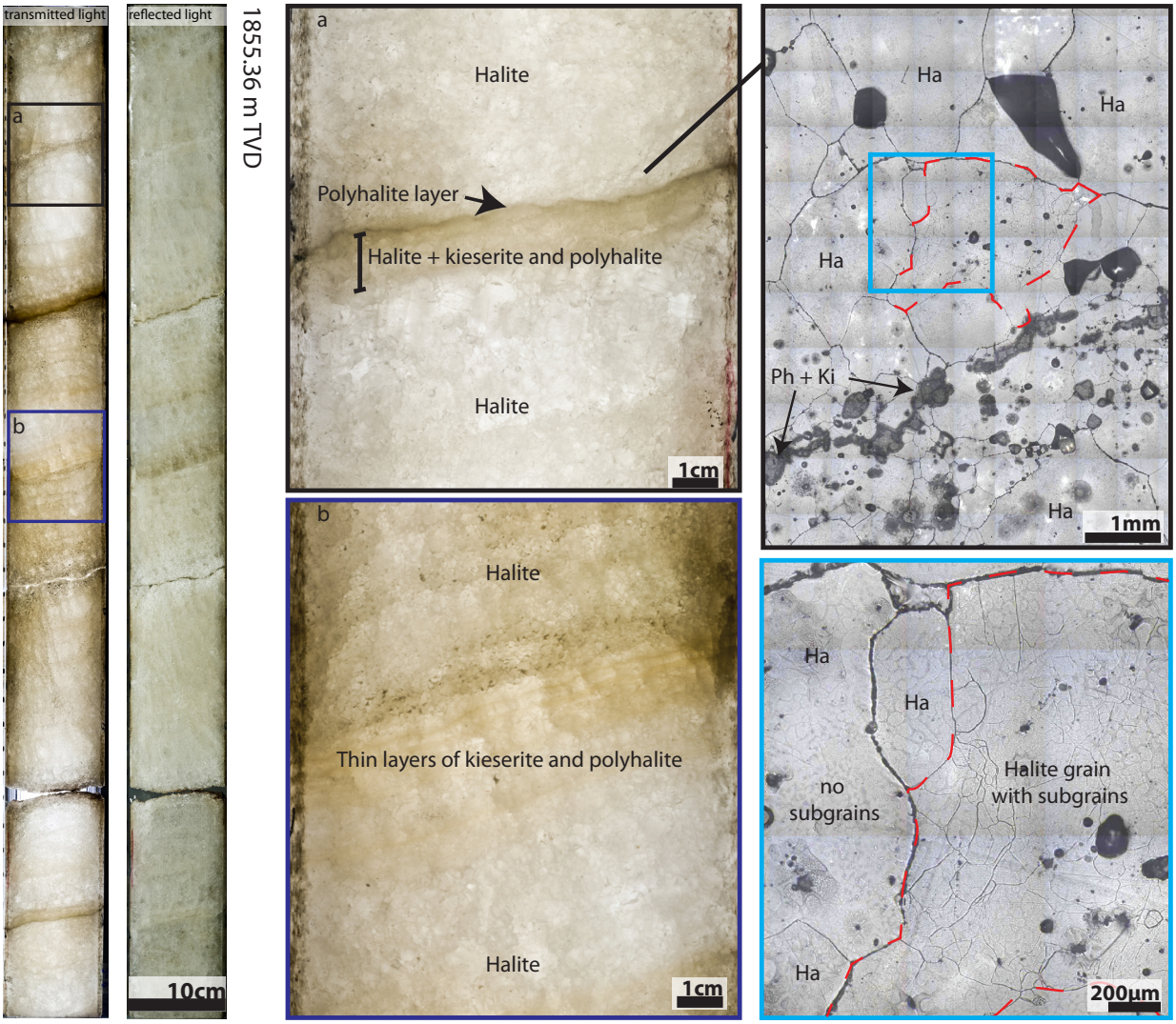


Fig. 5.6: Example of the Z3-1a halite. The halite layers are frequently interrupted by thin sulphate layers. The detailed pictures (a, b) show thin layers of slightly folded polyhalite and kieserite. (right) Reflected light microscopy pictures of an edged section showing halite grains of sizes up to several mm and one halite grain (red dashed line) containing subgrains <200 µm. The banding of the halite is very unclear and not distinguishable on this figure.

Kieserite (MgSo4*H2O)

Although kieserite layers in halite are common in the core, they are normally so thin (<50 µm) that they are mostly included in the Halite + Kieserite or Kieserite + Halite lithoclass, depending on the dominant mineral. The thin kieserite-dominated layers can easily be identified on the freshly cut core surface due to their lower solubility compared to the surrounding salts.

Small amounts of kieserite (<10%) are present in almost all layers as small (10–200 µm) euhedral crystals representing about 5% of the core. Intra- and intergranular kieserite makes up to 7% of the bischofite- or carnallite-dominated layers (Fig. 5.9). It is also present in mixtures with bischofite where it can make up <50% of the mixture forming thin (few cm) Kieserite + Bischofite layers.

Carnallite (KMgCl3*6H2O)

Carnallite is common in the Z3-1b part of the core (24 vol.% based on the chemical analyses)

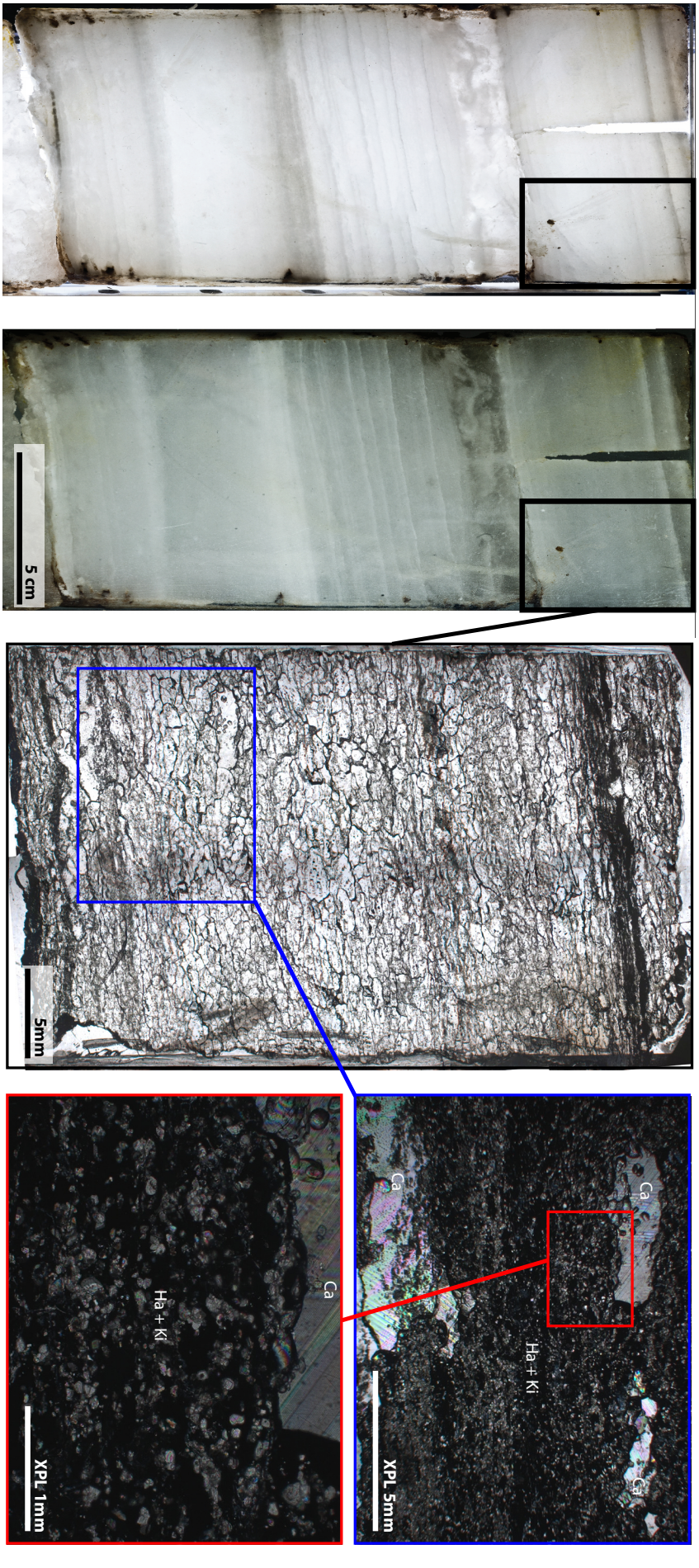


Fig. 5.7: Slab photographs and thin section of a halite–kieserite mix. Elongated (1 : 2–1 : 3) halite crystals smaller than 0.2 mm (long axis). Intra- and inter-crystalline kieserite is present. The kieserite content varies, forming a parallel layer of higher concentration or complete kieserite layers <0.5 mm. The halite grains are smaller in the layers of higher kieserite concentration. Carnallite is present in sparse layer-parallel lenses with irregular, often elongated (1 : 4), crystals up to 1 cm in size.

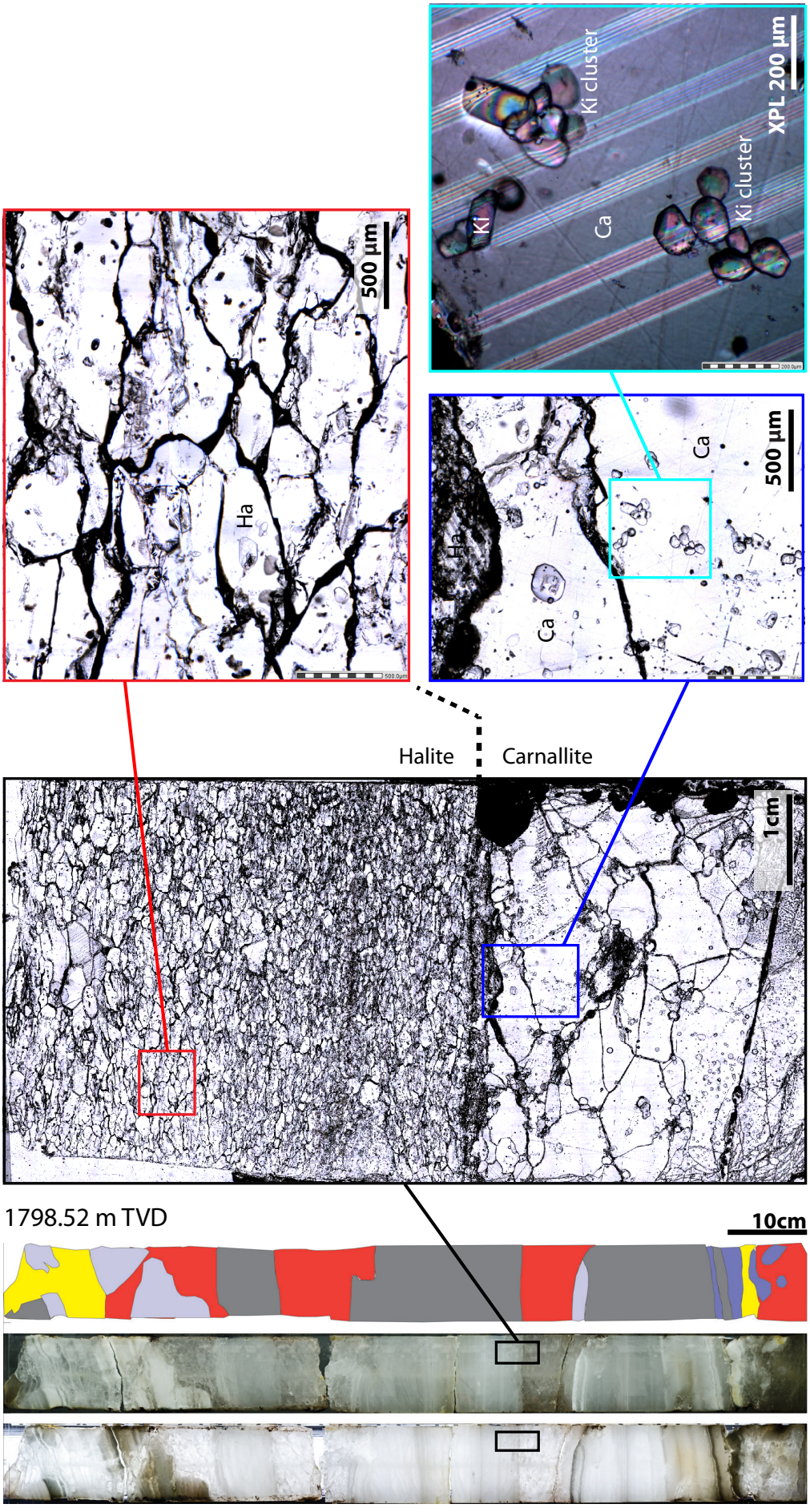


Fig. 5.8: Slab photographs and thin section of the contact between a halite + kieserite (top) and carnallite (bottom) layer. Colour code for the lithologies is given in figure 5.3.

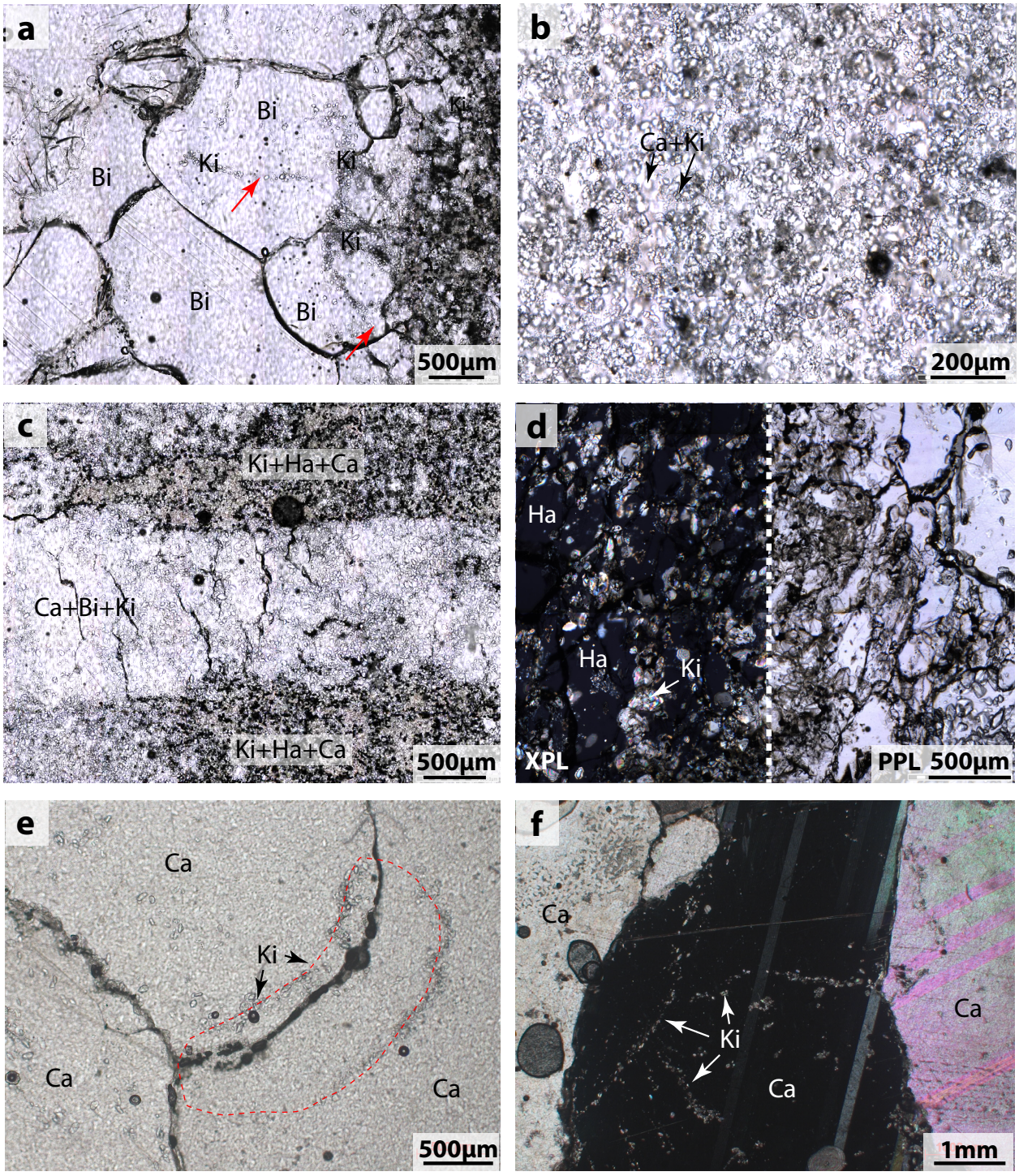


Fig. 5.9: Examples of kieserite in thin sections. (a) Bischofite and carnallite mixed layer with intra-crystalline kieserite marking old grain boundaries (red arrows). (b) Kieserite overgrown by one larger carnallite crystal. (c) Bischofite, carnallite and kieserite mixed vein in a hostrock of kieserite halite and carnallite. (d) Halite–kieserite mix in cross-polarised (XPL) and unpolarised (PPL) light. (e) Intra-crystalline kieserite in carnallite marking the outline of a recrystallised grain. (f) Kieserite tracks in carnallite crystals shown in XPL (red dashed line).

in up to 1.5 m thick layers consisting of up to 2 cm diameter elongated grains with wavy to straight grain boundaries and 120° triple points between grain boundaries (Fig. 5.8& Fig. 5.10). Many grains show (110) oriented twin lamellae (Tröger et al., 1982) and subgrains are rare. Wavy grain boundaries are common, indicating grain boundary migration recrystallisation (GBM). Minor clusters of kieserite

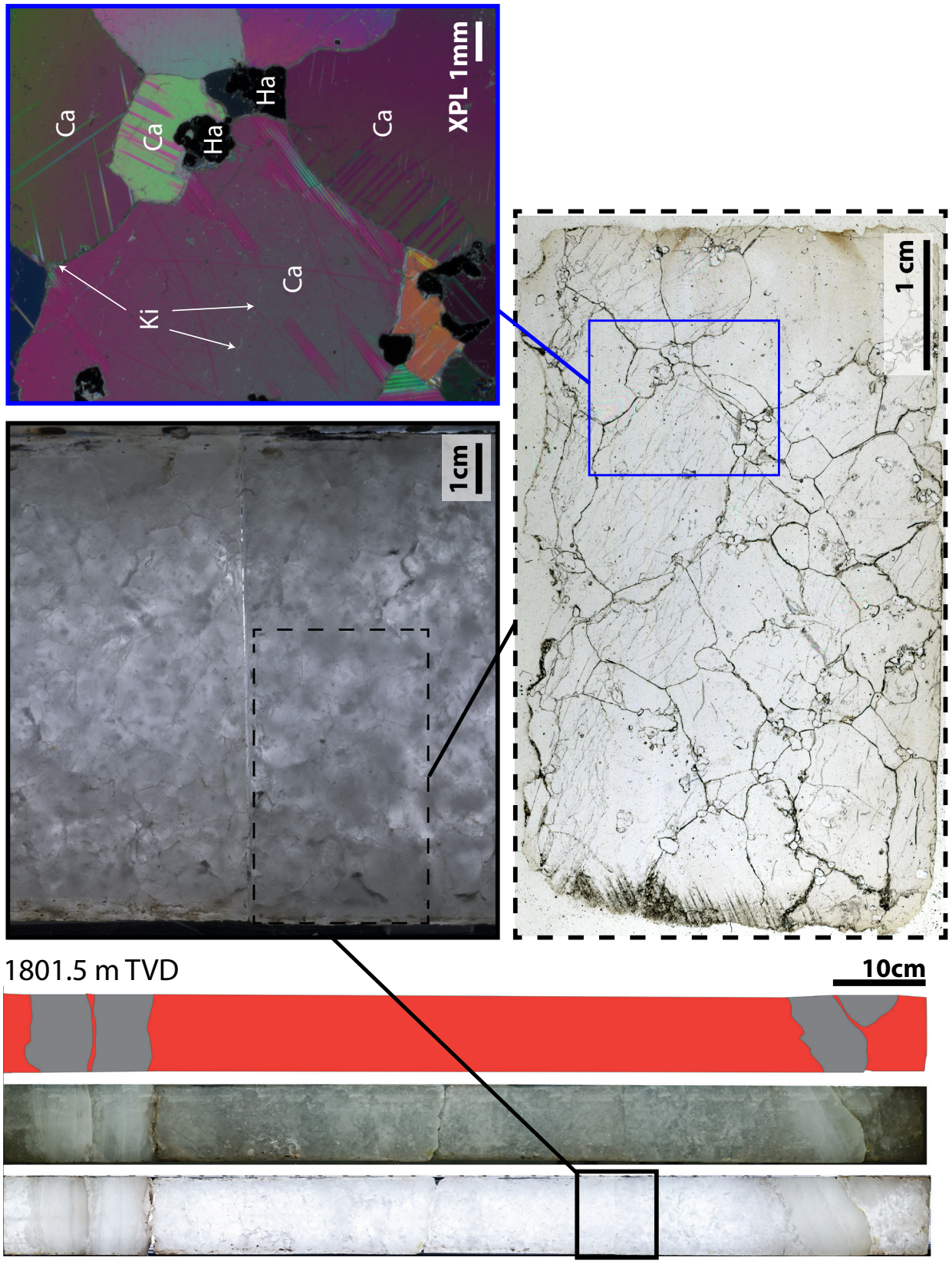


Fig. 5.10: . Slab photographs and thin section of a typical carnallite layer in the TR-9 core. In these layers, up to 1.5 cm partly elongated carnallite grains with mostly straight GBs. 120° triple points are common. Intra- and inter-crystalline kieserite is present (scattered and ghost grain boundaries). Halite is present, often in small clusters of rounded grains <1 mm. Colour code for the lithologies is given in Figure 5.3.

are present inside the grains and on the grain boundaries, while intra-crystalline inclusion trails of kieserite often mimic the structure of old grain boundaries (ghost grain boundaries; Fig. 5.9, cf. Urai and Boland, 1985). Clusters of rounded halite grains of up to 1 mm are often found between the carnallite grains. The carnallite is commonly transparent, grey to white except in the top (Fig. 5.3a: 1781–1784 m TVD) where it is red. Red carnallite from the Veendam Pillow has been studied by Urai and Boland (1985) and they found the red colour is caused by dislocation networks decorated by hematite. These hematite networks were not present in the samples studied here.

Carnallite is also present in mixed Carnallite + Halite + Kieserite and Carnallite + Kieserite + Bischofite layers. Here the carnallite is present in small <2 mm grains elongated parallel to the layering or as large amoeboid grains overgrowing kieserite. In veins, equiaxed carnallite is often mixed with equiaxed bischofite of similar grain size (<1 cm) and inter- and intra-crystalline euhedral kieserite (Fig. 5.13c).

Bischofite (MgCl2*6H2O)

Bischofite forms massive 5–8 m thick layers in the centre of the Z3-1b. These layers contain less than 20% other phases with up to 10 cm sized broken fragments of fine-grained, layered rock salt or single halite and carnallite grains inside the bischofite matrix (Fig. 5.11). Fine-grained equiaxed intra- and intergranular kieserite is commonly present. The bischofite grains are elongated, typically 2–5 cm in size, and some of the bischofite grains can grow to >15 cm. The grain texture shows frequent 120° grain boundary triple points and wavy grain boundaries. In some cases, GBM and grain overgrowths can be observed. While subgrains are very scarce, (110) twin lamellae are common, possibly caused by thin-section preparation. The bischofite layers are very similar to the carnallite layers in texture but have larger grain sizes and are more transparent. If small amounts of halite are mixed with bischofite the halite grains are rounded and accumulated in small clusters. In some layers bischofite is intergrown with carnallite, forming Bischofite + Carnallite (± Kieserite) layers that have a similar texture to the pure carnallite and bischofite layers.

Sulphate mineral layers (XSO4)

Beside kieserite, which is almost omnipresent in small quantities in the core, other sulphates forming mixed layers are also present. All layers dominated by sulphates beside kieserite (polyhalite, anhydrite, kieserite) are grouped into this lithoclass. These layers are only present in the top Z3-1a part of the core and are typically opaque, white to grey. Besides kieserite, polyhalite forming thin (up to 10 mm) layers and anhydrite as rare single <1 mm crystals are present.

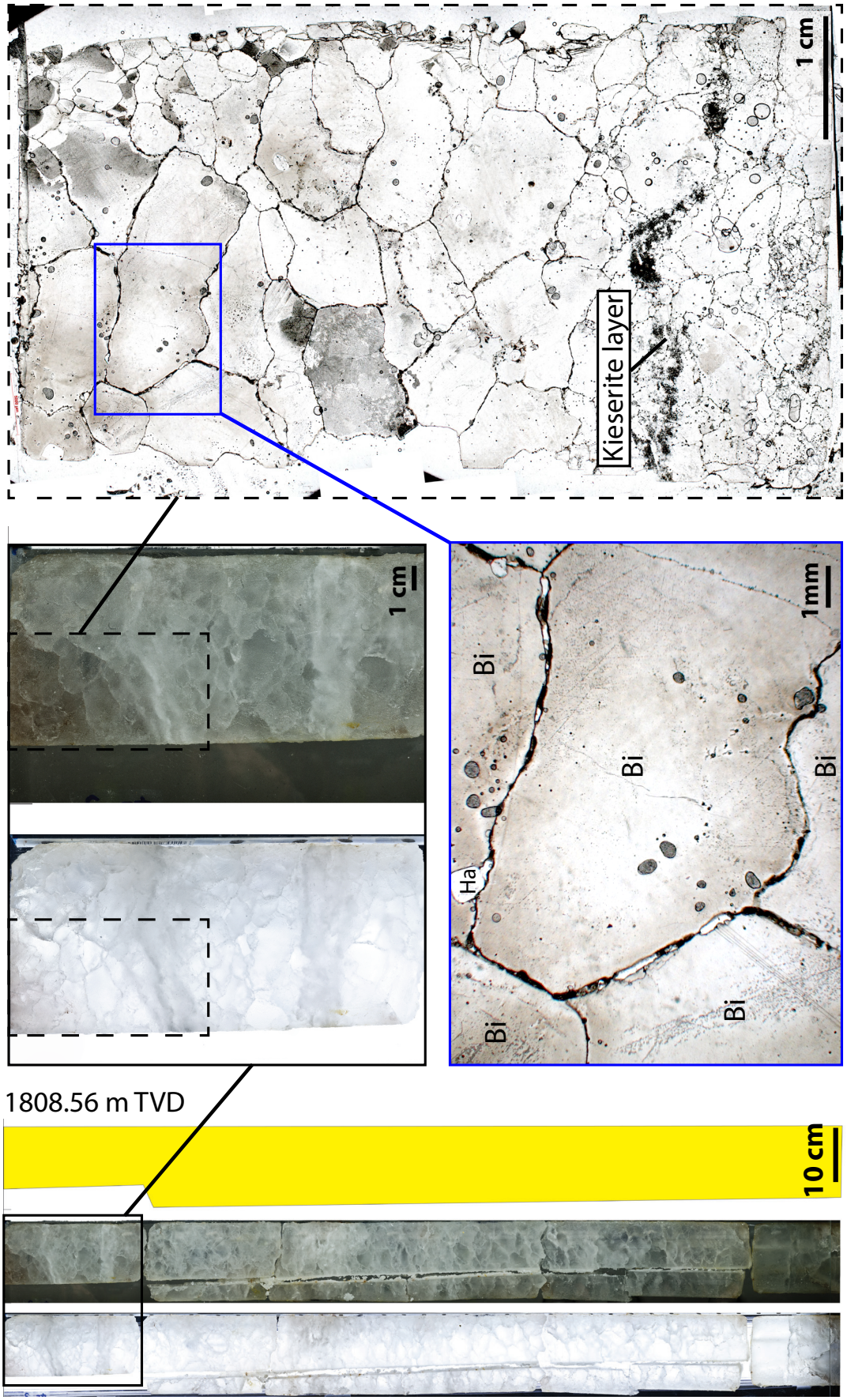


Fig. 5.11: Slab photographs and thin section of a typical bischofite layer. Up to 2 cm elongated bischofite grains with wavy grain boundaries and 120° triple points. Kieserite on grain boundaries and inside grains (scattered and ghost grain boundaries). Very small amount of <0.5 mm halite grains.

5.4.2 Structure of the core

The 81 m long TR9 core represents almost the entire Z3-1b subunit (from 1781.25 to 1837 m TVD) with the top 22 m of the Z3-1a (from 1837 to 1859.37 m TVD). While the Z3-1a mainly consists of halite (>95%) with thin (up to 1 cm layers) of sulphate minerals, the Z3-1b is dominated by K–Mg salts: interbedded, dm-scale halite–carnallite layers with minor kieserite and two massive (7 and 15 m thick) bischofite layers (Fig. 5.12). In what follows we describe the structure of the core, from top to bottom, divided into sections of similar composition and structure. An overview of these results is given in Table 1.

Carnallite/Halite 3 (C_H-3) (1781.25–1792 m TVD)

The top of the core consists of a 1.6 m thick layer with cm-sized fragments of fine-layered rock salt in a matrix of red carnallite with bischofite (Fig. 5.3a: 1781–1782.6 m TVD). This is followed by 0.7 m of coarse-grained rock salt and 0.7 m of interbedded cm-scale layers of halite and carnallite (Fig. 5.3a: 1782.6–1783.9). Unlike the deeper parts of the core a small amount of clay gives the top part a much darker colour. The lower part of this section (Fig. 5.3a: 1785.3–1792 m TVD) shows a gradual change from halite to K–Mg salts and increasing layer thickness. The top 3 m consists of alternating bands of fine- and coarse-grained halite with minor clay (Fig. 5.3a: 1784–1787.6 m TVD). The clay content decreases with depth, and no clay is visible after 3.5 m. This is where the first thin carnallite and halite–kieserite mix layers appear. With increasing depth, the carnallite and kieserite mix layers become thicker, reaching up to 30 cm thickness (Fig. 5.3a: 1791.2 m TVD). In the last metre (Fig. 5.3a: 1790.9–1791.8 m TVD) of this part, bischofite is present in the carnallite-dominated layers and in veins perpendicular to bedding.

Bischofite 2 (B-2) (1792–1798 m TVD)

The upper bischofite section consists of very coarse-grained (1–3 cm diameter) bischofite with some grains larger than 10 cm (Fig. 5.3c: 1810.3 and 1811.8 m TVD). Minor halite and carnallite (up to 5%) are mostly present in clasts of 1–30 cm. These clasts range from rounded to angular, and contain fine-grained layered kieserite. They are locally boudinaged and contain veins filled with bischofite, carnallite and kieserite (Fig. 5.3b: 1796–1796.6 m TVD).

Carnallite/Halite 2 (C_H-2) (1798–1808 m TVD)

The top 1.5 m of this part consists of fragments of layered kieseritic rock salt in a matrix of carnallite and occasionally bischofite. This is followed by 3.5 m of 10–30 cm thick halite and halite/kieserite layers interbedded with carnallite forming metre-scale folds (Fig. 5.13 FZ-1). The fold axial planes are sub-horizontal and about 1–1.5 m from each other (Fig. 5.13). In the fold cores, faulting

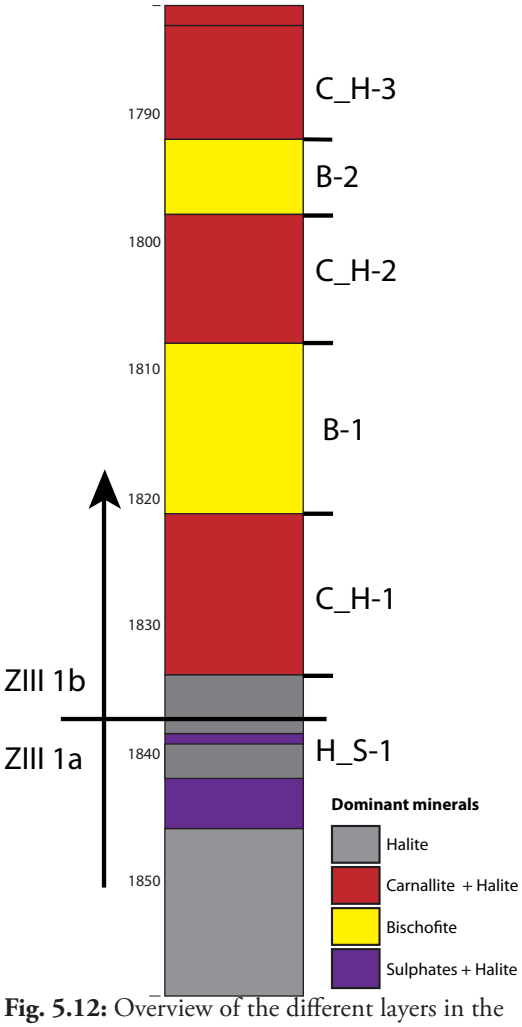


Fig. 5.12: Overview of the different layers in the TR-9 core.

of the kieseritic rock salt layers is common (Fig. 5.3b: 1801.2 m TVD). This folded area is followed by 0.7 m of broken kieseritic rock salt fragments (<10 cm), in a matrix of bischofite.

This is followed by 2 m of a recumbent fold (Fig. 5.13 FZ-2) with bischofite in the core (Fig. 5.3c: 1804.7 m TVD), and interbedded kieseritic rock salt and carnallite at the flanks on top and above the fold are cut off by a sub-horizontal discontinuity, followed by 3 m of folded kieseritic halite layers (Fig. 5.13 FZ-3) interbedded with carnallite (layer thickness 10–40 cm). The fold axial planes are sub-horizontal and about 1.5 m from each other (Fig. 5.13).

Bischofite 1 (B-1) (1808–1821.8 m TVD)

This 15 m bischofite- (90%) rich part of the core is similar to B-2 but with less kieseritic rock salt. It contains a 1.5 m thick layer of coarse-grained (1–2 cm) carnallite (Fig. 5.3c, d: 1815.7–1817.3 m TVD). No layering can be observed in the bischofite and carnallite sections, while the enclosed halite/kieserite fragments are fine-layered or cloudy.

Carnallite/Halite 1 (C_H-1) (1821.8–1834.7 m TVD)

The lowest part of the Z3-1b consists of 13 m folded and broken interbedded halite carnallite layers. Folding is present at mm to metre scale interrupted by common fracturing and highly deformed zones. In contrast to the C_H-2 layer, only minor bischofite is present in this part and no fragments in a carnallite or bischofite matrix were observed.

Halite/Sulphate 1 (H/S-1) (1834.7–1839.3 m TVD)

The halite-rich part at the top of the Z3-1a starts with 4.5 m of folded halite with 0.5–2 cm thick carnallite and sulphate mineral (kieserite, polyhalite, anhydrite)-rich layers. This halite-dominated part is followed by 7 m of halite with much higher sulphate mineral content and some boudinaged and faulted sylvite layers.

Halite (1839.3–1859.4 m TVD)

In the bottom part of the core the Z3-1a consists of halite layers with mm-scale folded sulphate (polyhalite, kieserite, anhydrite) and sylvite layers every 20–50 cm separating the halite layers (Fig. 5.6). The halite is slightly banded by different grain sizes of 0.5–1 mm in the coarse and <0.5 mm in the fine domain with unclear transitions.

5.4.3 Deformation structures

Visible macro-scale structures in the core are present in small halite/kieserite layers or at larger scale in the interbedded halite–carnallite layers. The common structures are folds, fragments of layered kieseritic rock salt in a matrix of carnallite or bischofite and veins in kieseritic rock salt layers.

Folds

Folds at different scales are interpreted to be common in the Z3-1b. Folding can only be observed if layering was originally present and preserved during deformation (Hirsinger & Hobbs, 1983). This is the case in the C_H-1 & 2 layers where metre-scale recumbent folding is interpreted by the closure in the core with correlation of layers on both limbs (Fig. 5.13). In C_H-2, faulting can be observed in the fold centres and at the hinges. The thickness of the carnallite layers interbedded with halite varies and sometimes the carnallite is completely absent between two corresponding halite layers (Fig. 5.13). Since the core can only provide 1D information, folds were identified by tracing distinct layer sequences that were found in upright and reversed order (see example in Fig. 5.13) that sometimes had well-preserved fold cores in the middle (see a fold core at 1806.2–1806.4 m TVD; Fig. 5.3c).

Folds in the C_H-1 are present on metre to cm scale. The observed fold axes are mostly sub-horizontal with a variety of axial planes from horizontal to vertical. Some observed folds have curved axial planes (Fig. 5.3d: 1824–1825 m TVD). Coherently folded sections of the core can rarely be traced over more than a few metres, when discontinuities (shear-zones or faults) interrupt the layering (Fig. 5.13). In bischofite- and carnallite-dominated layers, folded thin (<3 cm) halite/kieserite layers also show sub-horizontal fold axis but no preferred orientation of the axial planes.

Boudinage, veins and tectonic fragmentation

Halite and kieserite layers are frequently fractured. The fragments are either completely separated as fragments in a matrix of carnallite and bischofite or contain thin, up to 1 cm wide, veins which separate the boudins. These veins are filled with bischofite + kieserite, carnallite + kieserite or both and appear as bedding-parallel and bedding sub-normal veins. The veins at high angle to bedding are commonly observed in halite- or kieserite-rich layers interbedded with K–Mg salts and are often quite high in kieserite content.

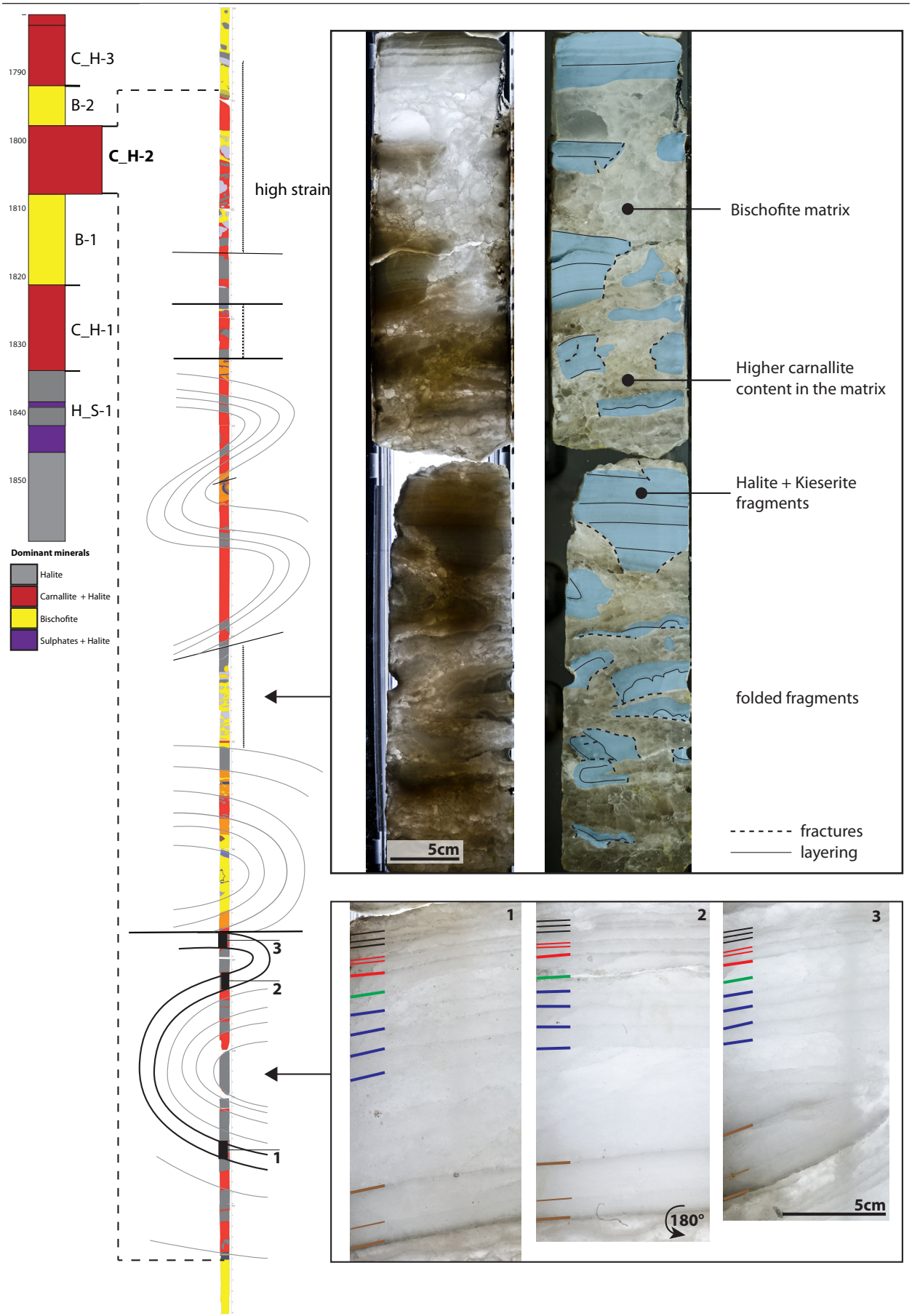


Fig. 5.13: Detailed view on the structure of C_H-2 showing a typical tectonic breccia of halite + kieserite fragments inside a bischofite matrix and an example of layer correlation in a folded segment (FZ-3). The three examples show the same layer sequence while #2 is overturned. Unlike most parts of the core, the core pieces in the C-H-2 part could be aligned reasonably well using the whole core pieces. The structural interpretation was performed using the whole core. Thus, the slabbed core pieces in this figure show only part of the available information and visible dips can be misleading.

5.5 Discussion

5.5.1 Sedimentation and diagenesis:

The Z3-1b represents the last stage of evaporation of seawater and is interpreted to have been deposited over numerous minor evaporation–refreshing events in the 1b sub-cycle. In the parts of the core where the original layering was not overprinted by high strain deformation, the core consists of thin usually monomineralic beds. This kind of texture is typical for shallow water precipitation (Coelewij et al., 1978). Changing conditions in temperature and composition of the brine by refreshing events lead to a switch in precipitation of one dominant phase. This is particularly clear in the C_H layers with alternating beds of halite and carnallite. Every halite layer could represent a minor refreshing event, raising the Na content of the brine (Borchert & Muir, 1964). The thin kieserite-enriched layers inside halite layers, on the other hand, can be interpreted as the result of annual temperature changes due to their mm-spaced periodic character and the thermophile precipitation of kieserite. The kieserite was either precipitated directly or was the result of a later metamorphosis from epsomite. For direct precipitation of kieserite, very high temperatures >55°C are necessary (Borchert & Muir, 1964). Although those high precipitation temperatures are rarely observed in other evaporite bodies, the unique abundance of massive bischofite layers in the core indicates precipitation from shallow, hot brine pools during Z3-1b time.

Most layers show sharp contacts to other lithologies, and gradual transitions are rarely present on the cm scale. However, as shown below, primary gradual transitions could have been overprinted by layer-parallel shearing concentrated in the softer layers.

Beside the numerous minor refreshing events, two major events are interpreted (Fig. 5.14). Those events caused a change in precipitation from Mg-rich to halite-rich salt while preventing full dissolution of the underlying bischofite layers. These events are present at the B-1/C_H-2 and B-2/C_H-3 contacts. While the B-1/C_H-2 is rather sharp, the B-2/C_H-3 contact is a gradual transition from pure bischofite to pure halite over 5 m vertical distance.

In many locations across Europe, Z3 K–Mg salt deposits show mineral alterations during metamorphosis, caused by the dewatering of gypsum in the underlying Z3-AC stringer (Borchert & Muir, 1964). The result of this process is the rise of Na-chloride and sulphate-rich brines forming ‘Hartsalz’ (sylvinitic halite + sulphates) deposits when they come into contact with carnallite. In the TR-9 core Hartsalz is not present in Z3-1b. That does not mean that the usual gypsum–anhydrite transition did not take place, but we see no evidence for interaction with the fluids (30% vol. loss) in the core. Nevertheless, some of the sulphate-rich halite layers in the top of the Z3-1a are enriched in sylvite and

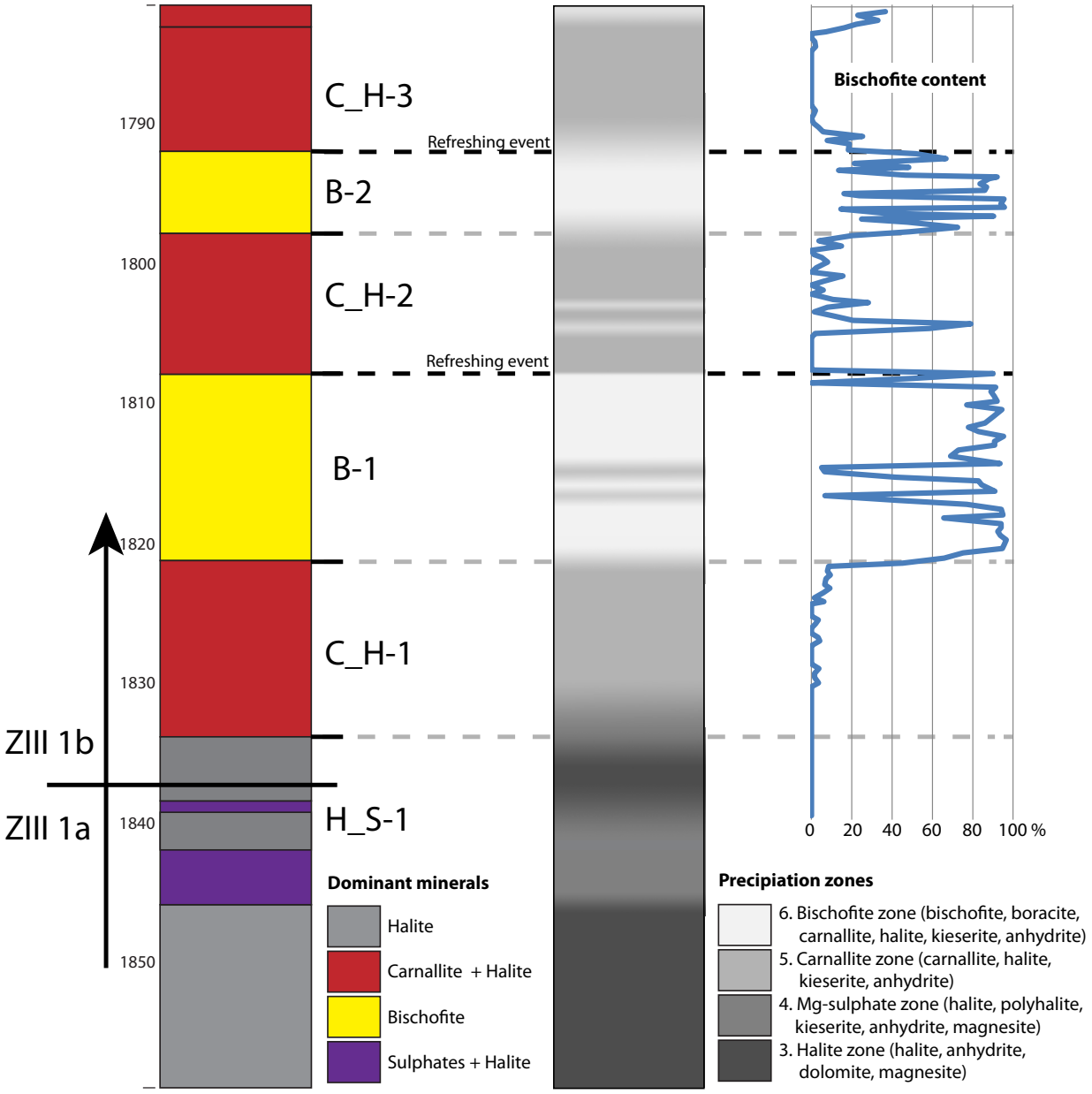


Fig. 5.14: Core overview showing the precipitation zones (after Pohl, 2011) and bischofite content (from ICP analysis). Starting from the 1a halite, the 1b composition slowly develops from sulphate-rich halite (S_H-1) to an interbedding of carnallite with halite (C_H-1). Towards the top of the C_H-1 layer, the carnallite content increases and first bischofite crystals appear inside the carnallite layers. At a depth of 1822 m the composition changes to strongly bischofite-dominated, ending the evaporation sequence in the B-1. Thin halite/kieserite layers and the 1.5 m of carnallite in the middle of the B-1 indicate refreshing events bringing in new sodium and sulphate. At the contact to the overlaying C_H-2 at a depth of 1808 m the composition changes to an interlayering of halite with carnallite, which is interrupted by two bischofite-rich layers at a depth of 1805 and 1802.5 m. The C_H-2 is interpreted to represent a refreshing event bringing the precipitation back into the carnallite zone. Towards the top of the C_H-2 the carnallite content increases and the transition to the B-2 is gradual from carnallite-dominated to bischofite-dominated at a depth of 1797.5 m. The B-2 bischofite is not as pure as the B-1, with more fragments of broken kieserite/halite layers. At the C_H-3 contact at 1791.8 m depth, 10–20 cm thick halite layers appear that are interbedded with bischofite, carnallite and kieserite layers. The thickness and bischofite content of these layers gradually decreases towards the top until pure halite is present from 1787.5 to 1784.1 m. In the top 2 m a gradual increase of bischofite (up to 30%) and carnallite (20%) is present. Here bischofite and carnallite form the matrix of a breccia with halite clasts. TR9 log data indicate that the following 5 m above the core are still rich in carnallite and bischofite until pure halite is reached at a depth of 1776 m.

could result from gypsum dewatering by derived brines. In summary, the mono-mineralic character in combination with thin layering in most Z3-1b layers indicates only minor alterations during prograde (increasing temperature and pressure) salt metamorphosis. Since those material alterations are highly dependent on temperature as long as the influence of alternating brines is small, a primary mineral paragenesis, evaporated under high temperatures, would be much more stable under in situ conditions during the deformation and today. Thus, high temperature precipitation of the K–Mg salt found in the core seems very likely.

5.5.2 Deformation:

Microstructure

In a section of 81 m, the core displays a large variety of structures from gently dipping intact layers to intensely folded sections disrupted into tectonic breccias, indicating a complex heterogeneous deformation. The bischofite- and carnallite-dominated layers are completely recrystallised and parts of the core containing mostly these minerals show hardly any layering (Fig. 5.10& Fig. 5.11).

Large grains of halite in the top of the C_H-3 with remnants of primary fluid inclusion bands (Fig. 5.5) are interpreted to show low strains (<20%; (Jessell et al., 2003). The observed subgrain sizes in these crystals (250–300 μm) indicate differential stresses of about 0.7–1 MPa during the last deformation phase (Carter et al., 1993; Franssen, 1994; Schléder & Urai, 2005). Comparable subgrain sizes are present in the Z3-1a halite. However, the halite grains are much smaller (<5 mm) with a grain texture typical for dynamical recrystallisation and without preserved remnants of primary fluid inclusions. The halite layers inside the C_H 2 & 1, on the other hand, show much smaller <250 μm) elongated halite grains with a grain texture typical for pressure solution processes. Thus we infer higher strains in the Z3-1a than in the top of the Z3-1b and possibly larger contribution of pressure solution processes in halite layers in the middle of the Z3-1b. 3

The microstructure in the carnallite and bischofite with 120° triple-points, grain boundary migration, elongated grains and wavy grain boundaries indicates extensive dynamic recrystallisation. The observed grain sizes of >2 cm in these layers are interpreted to have formed at very low differential stresses (<0.1 MPa) (van Eekelen et al., 1981; Muhammad, 2015), much lower than those inferred in the halite layers in the C_H-3 and in the Z3-1a.

In the halite/kieserite layers in the centre of the Z3-1b, the halite grains are much smaller (<350 μm) and show a completely different grain texture than the halite below or in the top of the Z3-1b. The small grain size together with a strong elongation of these grains is typical for fluid-assisted dissolution/precipitation creep (Urai et al., 1987; Závada et al., 2012). In summary, the microstructures

indicate a heterogeneous stress distribution in the Z3-1b subunit, with lower differential stress in the softer K–Mg salt layers and in the fine-grained halite.

Strain

Together with the microstructure, larger structures like folds and breccia are used to relate parts of the core to areas of low, intermediate and high strain. The lack of strain markers in most parts of the core only allows a qualitative description.

Low-strain areas: The lowest strains are observed in the halite-dominated layers in the top and bottom of the TR 9 core. In these low-strained parts the original layering is fully preserved and primary microstructures can be found indicating strain of no more than 20%. The halite with grain sizes >1 cm in the top part of the C_H-3 (Fig. 5.3a: 1784.1–1787.6 m TVD) have remnants of primary fluid inclusions and show no sign of strong deformation (Fig. 5.5). In the rest of the C_H-3 the interbedded thin carnallite/kieserite layers with halite are parallel and show small-scale folding with limb dips <30°. Relatively low strains can also be inferred in the Z3-1a, (Fig. 5.2), although the small-scale folded, faulted and boudinaged thin layers of sulphate minerals and sylvite in this part show evidence for stronger deformation than in the top of the Z3-1b (Fig. 5.2).

Intermediate-strain areas: The intermediate-strained parts are characterised by strong metre-scale folding, frequent boudinaged layers and indicators for localised salt flow. In the interlayered halite with carnallite or carnallite with sulphate minerals, folding (present in the C_H-1 & 2), fracturing (boudinage) and veins can be observed (Fig. 5.3b: 1803.8 m TVD). Thickness variations in the carnallite layers can be the result of local flow into the fold flanks or into saddle reef structures. The folded carnallite/halite parts in the C_H-2 (Fig. 5.13) are interrupted by shear zones, and the folded layers cannot be traced further than a few metres. Since the axial planes are horizontal, layers should be repeated if they were continuous. Fold limbs that could be followed in the core are therefore limited to a couple of metres, and the changes in composition and layering make it very unlikely that they are repeated in the core. A possible explanation for the limited limb length could be that the folded layers fragmented into blocks. Thus they are in fact 1–4 m-sized fragments of folded carnallite/halite layers separated by veins and shear zones analogous to that observed at smaller scales (e.g. Fig. 5.3b: 1801.1).

High-strain areas: The high-strained parts are characterised by the lack of visible layering and strongly deformed fragments. The bischofite-dominated layers were dynamically recrystallised and it is likely that all original layering was completely overprinted by intense deformation. Although ghost grain boundaries decorated by kieserite occur in some areas, they are not as common as in the carnallite layers. Stronger materials like halite and kieserite, included in a matrix of bischofite, are fractured

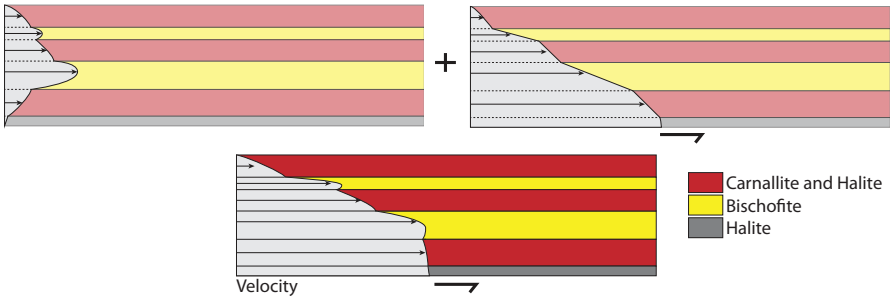


Fig. 5.15: Simplified example of the combination of Poiseuille and Couette flow inside a salt package with layered viscosities similar to the TR9 core, showing the displacement field and folding inside the different layers.

(Fig. 5.3b: 1794.7–1795 m TVD). This was observed at small-scale in the form of sheared and disrupted halite grain clusters in bischofite and in breccias of stronger layers in a bischofite-rich matrix at larger-scale (Fig. 5.3a: 1781–1783 m TVD). While deformation structures are visible everywhere in the core, the amount of strain varies and can be correlated to the mineralogical composition and hence the rheology of the layers. The highest strains are therefore interpreted to be concentrated in the weakest layers. Bischofite is the weakest material, followed by carnallite. Halite and sulphate represent rather strong materials in this environment. In addition, numerous examples of brittle deformation and veins indicate that at one point during the deformation, dilatant (mode one) fracturing was taking place in the stronger layers. This is interpreted to indicate high fluid pressures leading to tensile effective principal stress (Schléder et al., 2008). In summary, the structures observed in the drill core form, depending on the original content of soft K–Mg salts and position in the core, are either (1) weakly deformed parallel layers, (2) a mélange of folded layers in fractured blocks or (3) completely overprinted highly strained layers.

Local deformation history compared to the structures observed in the core

The salt deformation in the Veendam Pillow was interpreted to have started with a phase of extension followed by radial convergent salt flow into the Veendam Pillow (Raith et al., 2016). It is likely that the common tensile fractures in the core occurred in this early phase, forming disrupted layers that were folded in a later shortening stage. The folding of the disrupted, mechanically much stronger Z3-AC stringer had a dominant influence on the salt flow in the soft Z3-1b K–Mg salts above. Although the salt was generally thickened towards the pillow crest, the Z3-1b salts are interpreted to have been locally squeezed away from the stringer anticlines towards the areas above the stringer synclines (Raith et al., 2016). The folding of the Z3 AC results in the formation of areas of local extension and areas of local compression above the stringer, leading to local Poiseuille flow in the Z3-1b unit and a great variance in thickness. While layers below the Z3-1b are folded, the layers above the Z3-1b are parallel to top salt, which is on average about 180 m above top Z3-1b. We infer that the weak K–Mg-rich Z3-1b functioned as a decoupling layer between Z3-AC stringer deformation and the suprasalt sediments.

Salt flow below the Z3-1b that is locally more competent than above would cause intense shearing and therefore Couette flow inside the weak subunit (Fig. 5.2& Fig. 5.15).

The TR9 well is located on the edge of a small Z3-AC stringer syncline. The syncline is about 500 m wide, with the fold axis striking NW–SE. The NE flank close to the TR9 well the top is thrust about 100 m to the west (Fig. 5.2). The overlying Z3-1a halite and the stringer are most likely folded into this syncline. The Z3-1a halite almost doubles in thickness into this syncline. However, the section above the Z3-1a (i.e. the Z3-1b) appears hardly disturbed. This is good evidence for strain partitioning across the Z3-1b zone.

The expected salt flow in the Z3-1b at this position would be a combination of general Poiseulle flow towards the pillow crest to the W-SW and Couette flow caused by the movement of the Z3-AC stringer and the Z3-1a halite towards the small syncline NW of the TR9 well after an early extensional phase. The almost exclusively horizontal fold axial planes in the centre of the Z3-1b indicate Couette flow dominant in this layer (Fig. 5.2& Fig. 5.13). Additionally, we expect early salt flow during Triassic extension to have caused ruptures in halite and kieserite layers inside the Z3-1b. Thus, many of the observed veins and boudinaged layers could already be present prior to the main pillow evolution in the Cretaceous. In the late Triassic, the Z3-AC exceeded a depth of 1 km and reached pressure and temperature conditions that would lead to gypsum dehydration. It is therefore possible that the early salt extension was concurrent with the dehydration leading to additional fluids in the Z3 and possible overpressures. Under those conditions, open fractures can produce the veins we observe in the core today. Taking this into account, the fractures observed in the stronger layers originated either from early extension accompanied by fluid overpressures or during later folding and shearing. The observable extent of fractures and veins is strongly limited by the core diameter (fractures and veins in layers thinner than 1 m). By core observations it cannot be determined if the veins present are big enough to separate the C_H-2 layers and connect the B-1 to the B-2. Nevertheless, the multitude of fractures and the high strain deformation in the Z3-1b unit make the existence of larger fractures, veins or faults likely. It is possible that B-1 and B-2 are connected by a matrix of bischofite- and carnallite-filled veins and the Z3-1b is fragmented at the scale of the internal C_H-2 layer the same way as observed in the core at cm-scale. Higher differential stresses observed in the halite in the top and bottom of the ZII-1b than in the bischofite and carnallite layers indicate that these layers were still intact and not separated fragments in a K–Mg salt matrix.

The initial bulk rheology of the Z3-1b consisting of continuous layers with high viscosity contrasts was anisotropic. We conclude that the deformation accompanied by folding and fracturing produced a tectonic mélange of layered carnallite and halite fragments of mm to possibly tenths of metres

in size in a matrix of carnallite and bischofite. The result is a less anisotropic bulk rheology dominated by the soft K–Mg salts low viscosity and therefore possibly strain softening of the Z3-1b subunit.

5.6 Conclusions

- Although the ZIII sub-units appear as rather simply deformed parallel layers on seismic images (e.g. Raith et al., 2016), they can show highly strained and complex internal structures.
- The Z3-1b was strongly deformed during the subsequent phases of salt tectonics (Raith et al., 2016). The combination of Couette and Poiseuille flow inside the subunit forms a tectonic mélange of metre- to mm-scale horizontal folds, fractures, boudinaged layers, breccias and complete overprinting of the original texture, depending on the mineral content of the layers.
- The amount of strain correlates with the viscosity of the layers and therefore with the carnallite and bischofite content.
- Stronger layers out of halite and sulphate minerals were either folded or fractured. The observed folds show sub-horizontal fold axes, mostly horizontal axial planes and wavelength from mm <2 m.
- While the differential stress during deformation was heterogeneous and lower than 1 MPa, fluid over-pressures were possibly present during the development, leading to brittle mode one deformation and veins.
- The brittle deformation of stronger halite and kieserite layers commonly results in boudinaged layers and breccias with fragments of different scales in a bischofite–carnallite matrix.
- It is possible that the Z3-1b is internally completely ruptured, leading to connection of the bischofite layers in the subunit and therefore strain softening of the bulk viscosity.
- Continuous K–Mg salt layers can act as an internal detachment layer during salt deformation. The result is strain concentration in the K–Mg layers and Couette flow producing sub-horizontal fold axial planes.

5.7 Acknowledgements

We thank Nedmag for providing the core, chemical and seismic data. We also would like to thank the reviewers Mark Geluk, Carl Fiduk and an anonymous reviewer for their constructive comments and improvements to this article.

Table 1

Carnallite/Halite 3	1781.3 to 1792 m	Top: Breccia 1.6 m + 1.4 m fine layered carnallite halite (kieserite)
		Followed by 8 m banded rock-salt layers (5-60 cm thickness) interlayered with Carnallite layers (<1-30 cm thickness).
Bischofite 2	1792 to 1798 m	6 m of massive bischofite (<70%) with strongly deformed halite pieces.
Carnallite/Halite 2	1798 to 1808 m	10 m of interlayered carnallite with halite, showing meter scale folds divided by high strain (shear) zones.
Bischofite 1	1808 to 1821.8 m	14 m of massive bischofite (<90%) with strongly deformed halite pieces interrupted by a 1.5 m thick layer of carnallite.
Carnallite/Halite 1	1821.8 to 1834.7 m	13 m complex folded and broken interbedded halite carnallite layers.
ZIII-1a:		
Halite/Sulphate	1834.7 to 1839.3 m	4.5 m of halite with carnallite and sulphate mineral (kieserite, polyhalite, anhydrite) rich layers followed by 7 m of halite with high sulphate mineral content.
Halite	1839.3 to 1859.4 m	Banded halite (95%) with thin (<1 cm) sulphate layers.

5.8 References

Behlau J, Mingerzahn G (2001) Geological and tectonic investigations in the former Morsleben salt mine (Germany) as a basis for the safety assessment of a radioactive waste repository. Eng Geol 61:83–97. doi: 10.1016/S0013-7952(01)00038-2

Bérest P, Ghoreychi M, Hadj- Hassen F, Tijani M (eds) (2012) Mechanical Behaviour of Salt VII. CRC Press

Borchert H, Muir R (1964) Salt deposits: the origin, metamorphism and deformation of evaporites. D. Van Nostrand Company. Ltd, London

Bornemann O, Behlau J, Fischbeck R, et al (2008) Projekt Gorleben, Standortbeschreibung Gorleben. Teil 3: Ergebnisse der über- und untertägigen Erkundung des Salinars. Bundesanstalt für Geowissenschaften und Rohstoffe (BGR), Hannover

Bornemann O, Fischbeck R (1991) Zur geologie des salzstocks Gorleben nach den Bohrergebnissen. Deutschland Bundesamt für Strahlenschutz, Salzgitter

Burliga S (1996) Kinematics within the Klodawa salt diapir, central Poland. Geol Soc London, Spec Publ 100:11–21. doi: 10.1144/GSL.SP.1996.100.01.02

Carter N., Horseman S., Russell J., Handin J (1993) Rheology of rocksalt. J Struct Geol 15:1257–1271. doi: 10.1016/0191-8141(93)90168-A

Cartwright J, Jackson MPA, Dooley T, Higgins S (2012) Strain partitioning in gravity-driven shortening of a thick, multilayered evaporite sequence. Geol Soc London, Spec Publ 363:449–470. doi: 10.1144/SP363.21

Cerqueira RM, Chaves APV, Pessoa AFC, et al (1997) Principais depositos minerais do Brasil. In: Rochas e minerais industriais [Pricipal mineral deposits of Brazil, v. 4, Industrial rocks and minerals]: Brasilia, [Brazil] Departamento Nacional de Producao Mineral. pp p. 277–312.

Coelewij P, Haug G, Kuijk H Van (1978) Magnesium-salt exploration in the northeastern Netherlands. Geologie en Mijnbouw 57:487–502.

De Jager J (2007) Geological development. In: Wong TE, Batjes DAJ, De Jager J (eds) Geology of

the Netherlands. Royal Netherlands Academy of Arts and Sciences, pp 5–26

Fiduk JC, Rowan MG (2012) Analysis of folding and deformation within layered evaporites in Blocks BM-S-8 & -9, Santos Basin, Brazil. Geol Soc London, Spec Publ 363:471–487. doi: 10.1144/SP363.22

Franssen RCMW (1993) Rheology of synthetic rocksalt with emphasis on the influence of deformation history and geometry on on the flow behaviour. Rijksuniversiteit Utrecht

Franssen RCMW (1994) The rheology of synthetic rocksalt in uniaxial compression. Tectonophysics 233:1–40. doi: 10.1016/0040-1951(94)90218-6

Geluk MC, Paar W a, Fokker PA (2007) Salt. In: Wong TE, Batjes DAJ, De Jager J (eds) Geology of the Netherlands, 10th edn. Royal Netherlands Academy of Arts and Sciences, pp 283–294

Geluk MC, Röhling H, Brückner-Röhling S (2000) Salt occurrences in the Netherlands and Germany: new insights in the formation of salt basins. In: Geertman, R.M. (ed.): Proceedings of the 8th World Salt Symposium, May 2000, The Hague. Elsevier, pp 126–131

Hammer J, Behlau J, Mingerzahn G, Mertineit M (2014) The mechanical behavior and geometry of anhydrite layers in rock salt: Observations from nature. In: Natural Analogues for Safety Cases of Repositories in Rock salt - "Salt Club" Workshop Proceedings Braunschweig, Germany, 05.-07.September 2012. Hosted by Gesellschaft für Anlagen und Reaktorsicherheit (GRS) mbH, Braunschweig and Project Management Agency.

Hirsinger V, Hobbs BE (1983) A general harmonic coordinate transformation to simulate the states of strain in inhomogeneously deformed rocks. J Struct Geol 5:307–320.

Jackson CA-L, Jackson MPA, Hudec MR, Rodriguez C (2014) Internal structure, kinematics, and growth of a salt wall: Insights from 3-D seismic data. Geology 42:307–310. doi: 10.1130/G34865.1

Jackson CA-L, Jackson MPA, Hudec MR, Rodriguez CR (2015) Enigmatic structures within salt walls of the Santos Basin—Part 1: Geometry and kinematics from 3D seismic reflection and well data. J Struct Geol 75:135–162. doi: 10.1016/j.jsg.2015.01.010

Jackson MPA, Talbot C (1989) Anatomy of mushroom-shaped diapirs. J Struct Geol 11:211–230. doi: 10.1016/0191-8141(89)90044-8

Jessell MW, Kostenko O, Jamtveit B (2003) The preservation potential of microstructures during static grain growth. J Metamorph Geol 21:481–491. doi: 10.1046/j.1525-1314.2003.00455.x

Langbein R (1987) The Zechstein sulphates: The state of the art. In: Peryt TM (ed) The Zechstein Facies in Europe, Lecture Notes in Earth Science, Vol .10. Springer- Verlag Berlin, Heidelberg, pp 143–188

Martini HJ (1953) Salzsättel und Deckgebirge. In: Frühjahrestagung "Salzlagerstätten" der Deutschen Geologischen Gesellschaft in Goslar, Mai 1953. pp 823–836

Mohr M, Kukla PA, Urai JL, Bresser G (2005) Multiphase salt tectonic evolution in NW Germany: Seismic interpretation and retro-deformation. Int J Earth Sci 94:917–940. doi: 10.1007/s00531-005-0039-5

Muhammad N (2015) Deformation and transport processes in salt rocks : An experimental study exploring effects of pressure and stress relaxation. UU Dept. of Earth Sciences

Pohl WL (2011) Economic Geology: Principles and Practice. John Wiley & Sons

Poiate EJ, Costa AM, Falcao JL, Petrobrás SA (2006) Well Design for Drilling Through Thick Evaporite Layers in Santos Basin- Brazil. In: IADC/SPE Drilling Conference , 21-23 February 2006, Miami, Florida, USA. Society of Petroleum Engineers, p 16

Raith AF, Strozyk F, Visser J, Urai JL (2016) Evolution of rheologically heterogeneous salt structures: A case study from the NE Netherlands. Solid Earth 7:67–82. doi: 10.5194/se-7-67-2016

Richter-Bernburg G (1987) Deformation within salt bodies. In: Lerche I, O´Brien JJ (eds) Dynam-

ical Geology of Salt and Related Structures. Academic Press, London, pp 39 –75

Roth H (1968) Deformations in sub-horizontal salt deposits of German Zechstein 1: Hannover symposium. Geology of Saline Deposits. In: Proceedings of UNESCO. Hannover, pp 225–233

Schenk O, Urai JL (2005) The migration of fluid-filled grain boundaries in recrystallizing synthetic bischofite: First results of in-situ high-pressure, high-temperature deformation experiments in transmitted light. J Metamorph Geol 23:695–709. doi: 10.1111/j.1525-1314.2005.00604.x

Schléder Z, Urai JL (2005) Microstructural evolution of deformation-modified primary halite from the Middle Triassic Röt Formation at Hengelo, The Netherlands. Int J Earth Sci 94:941–955. doi: 10.1007/s00531-005-0503-2

Schléder Z, Urai JL, Nollet S, Hilgers C (2008) Solution-precipitation creep and fluid flow in halite: A case study of Zechstein (Z1) rocksalt from Neuhof salt mine (Germany). Int J Earth Sci 97:1045–1056. doi: 10.1007/s00531-007-0275-y

Scott Duncan EJ, Lajtai EZ (1993) The creep of potash salt rocks from Saskatchewan. Geotech Geol Eng 11:159–184. doi: 10.1007/BF00531249

Siemeister G (1969) Primärparagenese und Metamorphose des Ronnenberglagers nach Untersuchung im Grubenfeld Salzdetfurth. Bundesanstalt für Bodenforschung, Geologische Landesämter der Bundesrepublik Deutschland, Hannover

Spiers CJ, Urai JL, Lister GS, et al (1983) The influence of fluid-rock interaction on the rheology of salt rock and on ionic transport in salt. Report over the period nov. 1981- Dec. 1983. 131.

Strozyk F, Urai JL, Gent H Van, et al (2014) The internal structure of salt : insights from a regional 3D seismic study of the Permian Zechstein 3 intra-salt stringer in the Northern Netherlands and its implications for salt tectonics. Interpretation 2:101–117. doi: 10.1190/INT-2014-0037.1

Talbot CJ, Tully CP, Woods PJE (1982) The structural geology of boulby (potash) mine, Cleveland, United Kingdom. Tectonophysics 85:167–204. doi: 10.1016/0040-1951(82)90102-0

Tröger WE, Bambauer HU, Taborszky F, Trochim H-D (1982) Optische Bestimmung der gesteinsbildenden Minerale - Teil I.: Bestimmungstabellen.

Urai JL (1983) Water assisted dynamic recrystallization and weakening in polycrystalline bischofite. Tectonophysics 96:125–157. doi: 10.1016/0040-1951(83)90247-0

Urai JL (1985) Water-enhanced dynamic recrystallization and solution transfer in experimentally deformed carnallite. Tectonophysics 120:285–317. doi: 10.1016/0040-1951(85)90055-1

Urai JL, Boland JN (1985) Development of microstructures and the origin of hematite in naturally deformed carnallite. Neues Jahrb für Mineral Monatshefte H.2:58–72.

Urai JL, Schléder Z, Spiers CJ, et al (2008) Flow and Transport Properties of Salt Rocks. In: Dynamics of Complex Intracontinental Basins: The Central European Basin System. Springer Science & Business Media, pp 277–290

Urai JL, Spiers CJ, Peach CJ, et al (1987) Deformation mechanisms operating in naturally deformed halite rocks as deduced from microstructural investigations. Geologie en Mijnbouw 66:165–176.

van Eekelen HA, Urai JL, Hulsebos T (1981) Creep of Bischofite. In: Proceedings, 1st Conference on the Mechanical Behaviour of Salt. Pennsylvania,

Van Gent H, Urai JL, de Keijzer M (2011) The internal geometry of salt structures - A first look using 3D seismic data from the Zechstein of the Netherlands. J Struct Geol 33:292–311. doi: 10.1016/j.jsg.2010.07.005

Vysotskiy EA, Kislik VZ (1987) Epochs of bischofite deposition in geologic history. Int Geol Rev 29:134–139. doi: 10.1080/00206818709466130

Warren JK (2006) Evaporites:Sediments, Resources and Hydrocarbons. Springer Science & Business Media, Berlin Heidelberg

Williamson MD, Murray SJJ, Hamilton TAPAP, et al (1998) A Review of Zechstein Drilling Issues. In: Offshore Europe Conference in Aberdeen, Scotland, 9-12 September 1997. pp 189–196

Závada P, Desbois G, Schwedt A, et al (2012) Extreme ductile deformation of fine-grained salt by coupled solution-precipitation creep and microcracking: Microstructural evidence from perennial Zechstein sequence (Neuhof salt mine, Germany). J Struct Geol 37:89–104. doi: 10.1016/j.jsg.2012.01.024

Ziegler P a. (1978) North-Western Europe: Tectonics and Basin Development. Geologie en Mijnbouw 57:589–626.

Zirngast M (1996) The development of the Gorleben salt dome (northwest Germany) based on quantitative analysis of peripheral sinks. Geol Soc London, Spec Publ 100:203–226. doi: 10.1144/GSL.SP.1996.100.01.13

5.9 Appendix

1. Chemical analysis of the Tr-9 Core

2. XRD analysis of the samples used in the chapter

3. Tr -9 Core pictures

Further thinsections/XRD analysis and photographs from other cores near Tr-9 are in the digitalappendix.

1

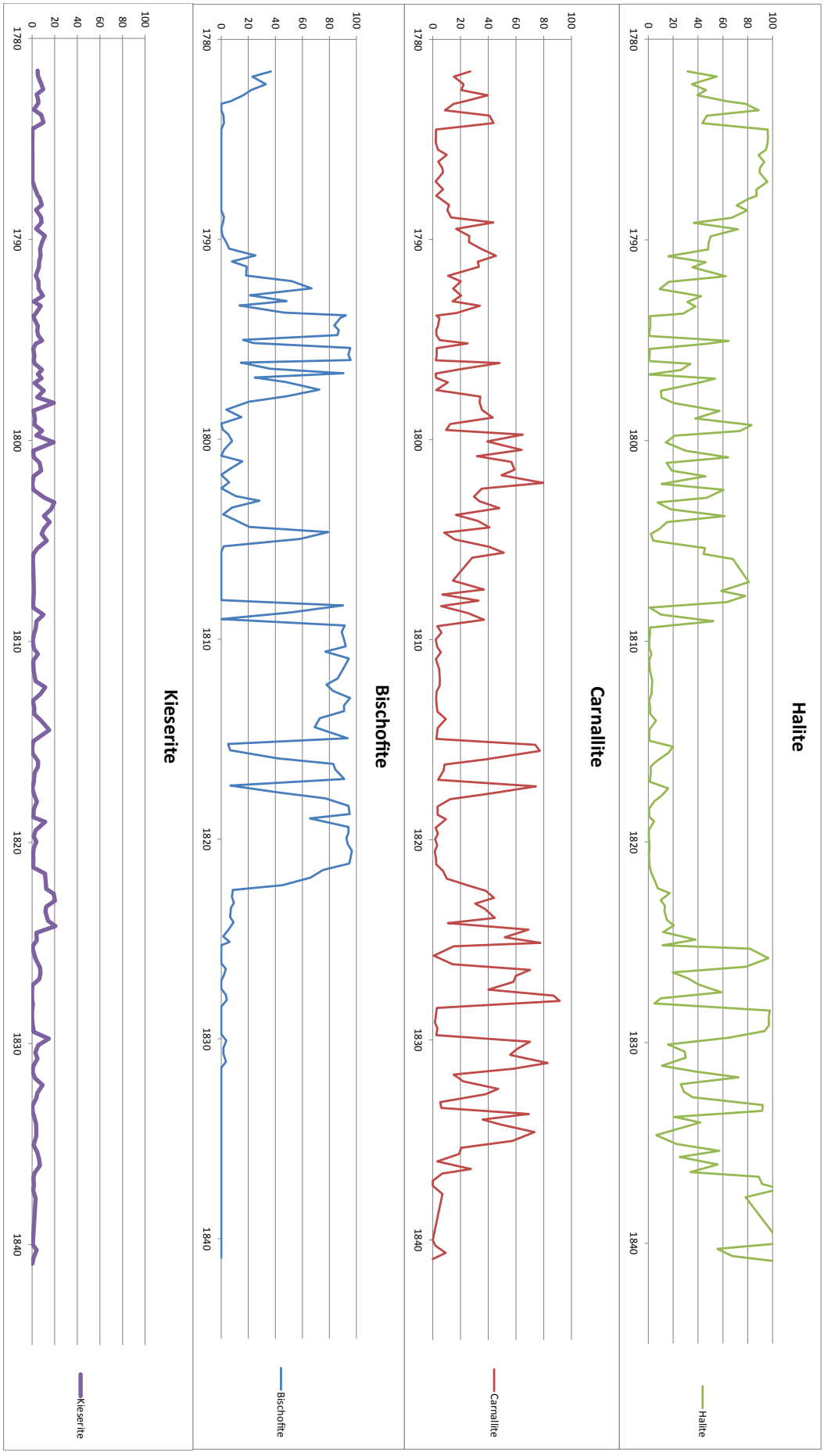
From [TVD]	To [TVD]	SO4 [Vol%]	K [Vol%]	Mg [Vol%]	Na [Vol%]	Ca [Vol%]	Cl [Vol%]	Sum [Vol%]
1781	1781.35	4.03	3.81	7.62	12.41	0.26	42.29	70.42
1781.35	1781.61	4.21	2.15	5.01	21.65	0.24	47.27	80.54
1781.61	1781.99	5.78	3.13	7.28	13.8	0.12	41.29	71.4
1781.99	1782.28	7.28	2.91	6.19	18.26	0.19	43.81	78.64
1782.28	1782.54	3.26	5.58	6.13	15.51	0.19	44.78	75.44
1782.54	1782.84	4.45	3.24	3.85	24.76	0.24	49.48	86.02
1782.84	1782.97	4.46	2.19	2.28	30.76	0.27	53.26	93.22
1782.97	1783.29	2.05	1.4	1.03	34.92	0.42	57.34	97.16
1783.29	1783.56	5.91	5.76	5.22	18.55	0.09	44.85	80.38
1783.56	1783.93	7.38	6.17	5.86	17.1	0.14	43.86	80.51
1783.93	1784.25	1.87	0.44	0.27	37.79	0.68	59.28	100.34
1784.25	1784.58	2.08	0.36	0.26	37.86	0.77	59.31	100.64
1784.58	1784.91	1.54	0.38	0.24	37.79	0.57	59.2	99.72
1784.91	1785.26	1.41	0.64	0.37	37.23	0.51	58.94	99.1
1785.26	1785.52	1.45	1.61	0.94	34.89	0.53	57.85	97.26
1785.52	1785.86	1.98	0.71	0.4	36.69	0.74	58.23	98.75
1785.86	1786.17	2.41	1.09	0.65	35.29	0.91	57.15	97.51
1786.17	1786.39	1.34	1.21	0.71	35.18	0.48	57.28	96.2
1786.39	1786.85	1.24	0.39	0.24	37.7	0.44	59.03	99.04
1786.85	1787.24	2.3	1.19	1.14	34.2	0.17	55.73	94.72
1787.24	1787.56	4.22	0.42	1.09	34.22	0.31	53.78	94.04
1787.56	1787.69	5.27	0.74	1.64	31.86	0.25	51.15	90.91
1787.69	1788.03	6.4	1.75	2.56	27.95	0.15	47.72	86.54
1788.03	1788.28	2.71	1.57	1.54	31.29	0.12	52.38	89.61
1788.28	1788.65	5.74	1.85	2.78	26.35	0.1	46.36	83.19
1788.65	1788.9	6.13	6.15	5.45	14.41	0.11	39.38	71.64
1788.9	1789.22	2.77	2.47	2.1	28.33	0.12	50.22	86.02
1789.22	1789.57	8.02	3.71	4.41	19.73	0.06	40.85	76.79
1789.57	1789.88	6.39	3.67	4.27	19.1	0.08	40.65	74.15
1789.88	1790.22	5.16	4.92	5.01	18.91	0.09	44.58	78.67
1790.22	1790.56	5.44	6.41	8.35	6.32	0.07	36.04	62.63
1790.56	1790.86	4.59	4.56	4.87	18.2	0.11	43.21	75.54

1790.86	1791.11	4.48	4.68	6.23	13.98	0.09	40.84	70.3
1791.11	1791.56	2.62	1.56	3.74	24.52	0.13	48.43	81.01
1791.56	1791.84	4.05	2.85	8.99	6.5	0.05	35.92	58.36
1791.84	1792.2	4.09	2.06	10.29	3.53	0.03	34.36	54.37
1792.2	1792.55	6.85	2.88	6.03	16.69	0.06	40.96	73.47
1792.55	1792.84	1.2	2.01	7.28	12.33	0.07	41.32	64.21
1792.84	1793.06	5.6	4.78	5.93	14.95	0.12	40.77	72.16
1793.06	1793.42	2.65	2.41	7.68	10.99	0.09	39.73	63.56
1793.42	1793.55	0.97	0.37	11.49	0.43	0	33.81	47.07
1793.55	1793.68	1.27	0.68	11.27	0.58	0	33.45	47.25
1793.68	1794.06	3.61	0.54	11.24	0.68	0	31.66	47.73
1794.06	1794.3	3.14	0.36	11.41	0.42	0	31.92	47.24
1794.3	1794.54	3.82	0.39	11.49	0.32	0	31.53	47.55
1794.54	1794.78	6.22	0.71	3.93	25.35	0.02	46.63	82.86
1794.78	1794.94	2.81	3.55	5.63	17.78	0.2	45.35	75.32
1794.94	1795.18	0.76	0.41	11.86	0.5	0	35.18	48.71
1795.18	1795.53	1.44	0.41	11.86	0.4	0	34.52	48.63
1795.53	1795.79	1.07	0.33	11.92	0.25	0	34.66	48.23
1795.79	1795.92	1.8	6.78	6.32	13.37	0.15	44.13	72.55
1795.92	1796.23	6.14	2.81	7.63	10.35	0.03	36.27	63.23
1796.23	1796.45	3.58	0.31	11.9	0.42	0.01	33.02	49.24
1796.45	1796.66	5.91	0.34	4.67	21.12	0.01	42.17	74.23
1796.66	1796.89	1.65	1.54	7.03	15.41	0.08	44.57	70.29
1796.89	1797.27	7.18	0.36	10.7	3.99	0.01	32.41	54.64
1797.27	1797.6	3.31	4.83	9.63	4.15	0.05	36.51	58.49
1797.6	1797.88	13.48	4.75	8.76	8.06	0.04	32.39	67.48
1797.88	1798.27	1.15	5	3.78	22.56	0.11	49.68	82.27
1798.27	1798.65	1.94	6.08	6.01	14.84	0.07	44.63	73.57
1798.65	1798.97	1.74	1.95	1.48	32.67	0.12	55.37	93.33
1798.97	1799.27	6.27	1.36	2.55	28.98	0.04	48.8	88
1799.27	1799.5	2.76	9.14	6.96	8.35	0.06	39.52	66.78
1799.5	1799.84	13.34	5.53	7.76	5.54	0.03	26.4	58.61
1799.84	1800.26	0.97	9.02	6.06	11.88	0.12	43.66	71.7
1800.26	1800.58	1.37	4.7	3.04	25.27	0.15	51.37	85.91
1800.58	1800.86	4.71	7.98	7.98	5.77	0.05	36.02	62.51
1800.86	1801.25	5.78	8.3	7.29	7.48	0.09	36.23	65.17
1801.25	1801.53	1.35	7.08	4.59	18.16	0.14	47.06	78.37
1801.53	1801.91	0.55	11.2	7.7	4.24	0.17	39.06	62.93
1801.91	1802.2	1.11	5.18	3.29	23.79	0.14	50.42	83.93
1802.2	1802.6	7.89	4.18	5.8	18.43	0.11	43.5	79.9
1802.6	1802.83	13.72	4.75	9.8	2.91	0	27.26	58.45

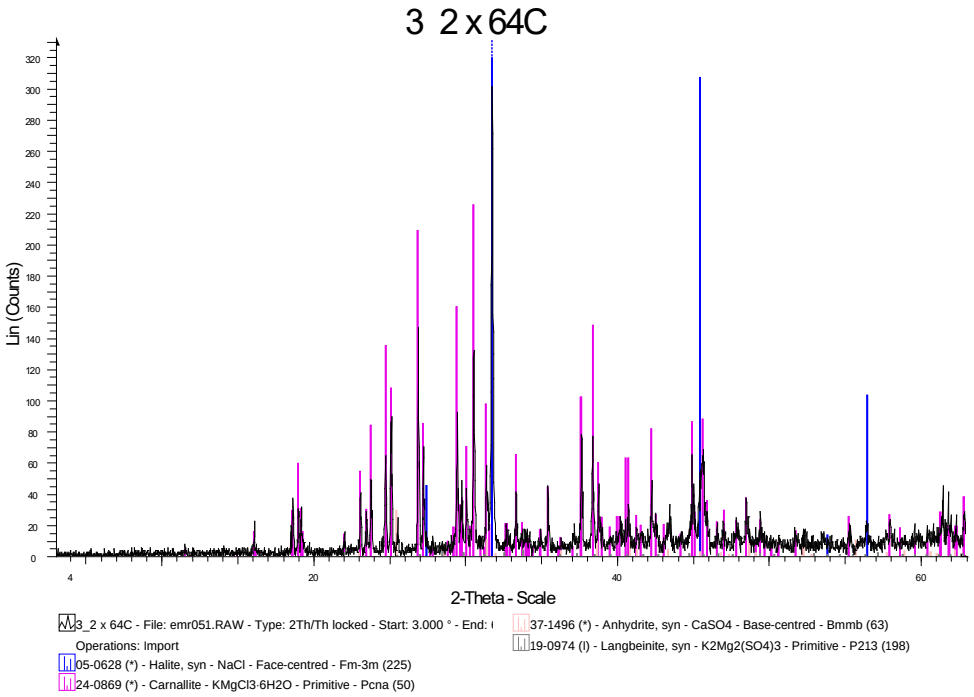
1802.83	1803.17	11.76	6.77	8.12	7.04	0.02	32.01	65.71
1803.17	1803.51	7.33	2.35	3.46	24.18	0.04	44.17	81.53
1803.51	1803.81	10.83	4.58	6.86	5.94	0.03	25.37	53.6
1803.81	1804.14	7.35	5.78	7.91	3.61	0.02	28.48	53.14
1804.14	1804.4	5.86	1.16	11.67	0.78	0	31.95	51.42
1804.4	1804.74	9.04	2.24	10.66	1.63	0.01	29	52.59
1804.74	1805.11	3.69	5.73	4.64	17.98	0.12	43.93	76.07
1805.11	1805.4	1.14	7.23	4.69	17.5	0.13	46.61	77.29
1805.4	1805.65	0.86	4.23	2.6	26.78	0.16	52.37	87.01
1805.65	1806.8	1.3	2.19	1.52	31.82	0.13	54.75	91.71
1806.8	1807.24	1.37	5.35	3.5	23.08	0.11	49.85	83.26
1807.24	1807.49	1.44	1.17	0.85	30.7	0.19	50.17	84.52
1807.49	1807.8	0.91	4.9	3.06	24.81	0.1	51.14	84.93
1807.8	1808.07	0.72	0.85	11.48	0.45	0	34.42	47.93
1808.07	1808.42	7.06	3.57	10.06	4.08	0.02	33.72	58.51
1808.42	1808.75	2.9	5.38	3.91	20.61	0.11	46.1	79.01
1808.75	1809.07	2.31	0.46	11.8	0.55	0	33.96	49.08
1809.07	1809.39	1.17	0.89	11.5	0.55	0	34.35	48.46
1809.39	1809.74	0.42	0.31	11.14	0.29	0	32.92	45.09
1809.74	1810.11	1.11	0.46	11.58	0.37	0	33.92	47.43
1810.11	1810.38	3.56	0.82	10.61	0.98	0	30.58	46.56
1810.38	1810.72	0.62	0.33	11.65	0.27	0	34.24	47.1
1810.72	1811.22	0.96	0.65	11.46	0.53	0	34.12	47.73
1811.22	1811.72	2.21	0.73	11.3	1.26	0.01	33.94	49.45
1811.72	1812.03	8.17	0.7	11.79	1.13	0.03	30.79	52.62
1812.03	1812.35	5.29	0.39	11.49	1.03	0.01	31.57	49.79
1812.35	1812.7	0.45	0.34	11.73	0.3	0	34.64	47.46
1812.7	1813.07	1.44	0.41	11.47	0.61	0.01	33.72	47.66
1813.07	1813.35	1.21	0.49	11.48	0.54	0	33.86	47.56
1813.35	1813.71	5.76	1.33	11	2.42	0.01	32.77	53.29
1813.71	1814.16	10.58	0.5	11.24	0.33	0.02	25.95	48.61
1814.16	1814.71	0.71	0.37	11.59	0.34	0.01	34.15	47.17
1814.71	1815	0.42	10.4	7.11	7.81	0.11	42.1	67.95
1815	1815.31	0.38	10.86	7.58	6.36	0.07	41.61	66.85
1815.31	1815.72	3.84	5.45	9.35	2.66	0.06	33.56	54.92
1815.72	1815.99	3.55	1.19	11.54	0.77	0	33.32	50.38
1815.99	1816.28	1.59	1.11	11.18	0.81	0.01	33.7	48.41
1816.28	1816.75	1.12	0.55	11.5	0.48	0.01	33.95	47.61
1816.75	1817.08	0.32	10.45	7.34	6.3	0.06	40.49	64.96
1817.08	1817.43	1.67	5.88	9.22	4.3	0.04	37.69	58.8
1817.43	1817.72	3.07	1.77	11.08	1.96	0.03	34.7	52.61

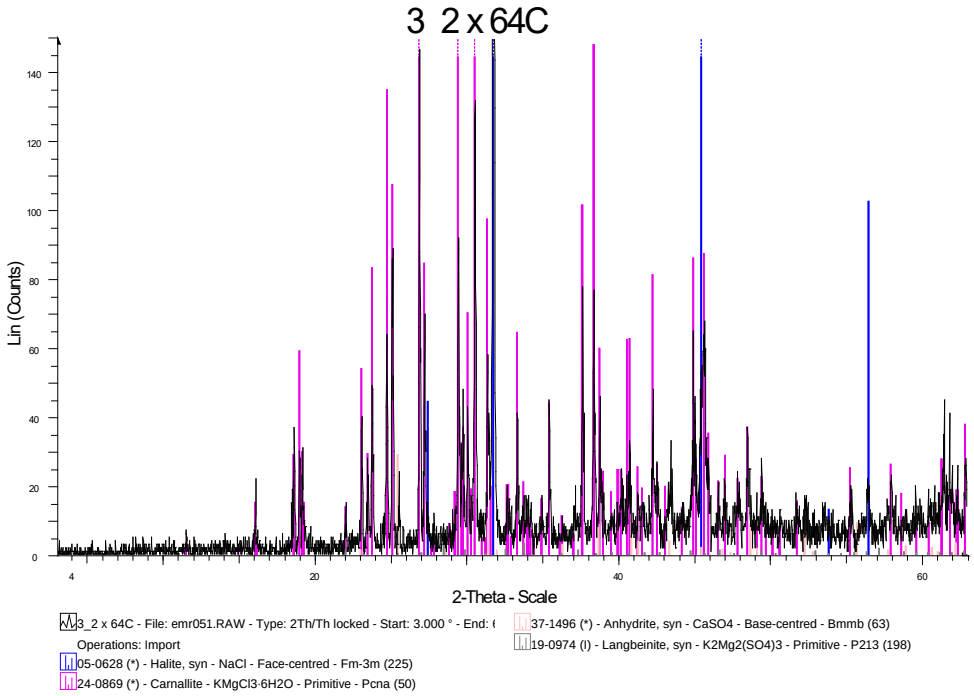
1817.72	1818.09	1.07	0.49	11.83	0.25	0	34.54	48.17
1818.09	1818.5	0.84	0.51	11.89	0.31	0	34.99	48.54
1818.5	1818.72	8.11	1.35	10.72	1.82	0.03	29.37	51.41
1818.72	1819.15	2.2	0.29	11.99	0.18	0	33.88	48.55
1819.15	1819.44	0.97	0.53	11.82	0.2	0	34.56	48.08
1819.44	1819.72	2.66	0.24	11.87	0.32	0.01	33.39	48.49
1819.72	1820.01	1.06	0.46	11.75	0.42	0	34.56	48.25
1820.01	1820.34	0.72	0.21	11.85	0.25	0.03	34.66	47.73
1820.34	1820.69	0.81	0.34	11.85	0.3	0	34.72	48.02
1820.69	1820.98	0.46	0.37	11.67	0.47	0	34.76	47.73
1820.98	1821.3	7.97	1.04	11.65	0.95	0.02	30.54	52.17
1821.3	1821.69	8.4	1.43	10.87	2.08	0.03	30.06	52.88
1821.69	1822.06	8.79	3.76	9.95	2.99	0.02	30.6	56.12
1822.06	1822.3	13.43	5.38	7.73	6.74	0.06	28.01	61.35
1822.3	1822.65	14.15	6.21	8.37	3.93	0.02	25.71	58.4
1822.65	1822.94	8.86	4.31	6	5.28	0.06	23.13	47.64
1822.94	1823.2	8.28	5.27	6.21	5.12	0.04	24.74	49.67
1823.2	1823.65	10.12	6.31	7.2	5.93	0.11	28.6	58.28
1823.65	1823.91	14.5	1.54	5.68	8.09	0.06	19.85	49.72
1823.91	1824.24	2.74	9.71	7.44	4.67	0.02	35.71	60.29
1824.24	1824.62	3.12	7.31	5.45	14.96	0.1	43.45	74.38
1824.62	1824.9	0.51	10.91	7.62	4.53	0.06	38.82	62.44
1824.9	1825.07	1.04	2.39	1.45	32.11	0.22	55.55	92.78
1825.07	1825.54	2.57	0.36	0.62	38.02	0.17	59.17	100.92
1825.54	1825.97	5.22	2.19	2.48	30.84	0.15	53.2	94.08
1825.97	1826.25	5.36	9.87	7.84	7.7	0.09	39.9	70.75
1826.25	1826.55	4.73	8.43	6.59	12.57	0.14	42.99	75.44
1826.55	1826.85	0.23	8.2	5.12	15.79	0.05	46.65	76.04
1826.85	1827.24	0.18	5.89	3.51	23.15	0.07	51.28	84.08
1827.24	1827.54	0.03	12.25	8.01	3.97	0	40.58	64.84
1827.54	1827.8	0.47	12.88	8.63	1.92	0	39.45	63.34
1827.8	1828.15	0.31	0.92	0.27	38.47	0.12	60.92	101.01
1828.15	1828.53	0.77	0.69	0.21	38.08	0.31	59.94	100.01
1828.53	1828.88	0.62	0.5	0.25	38.22	0.07	59.79	99.45
1828.88	1829.17	0.98	0.71	0.54	36.88	0	58.39	97.5
1829.17	1829.51	10.31	0.43	2.82	25.2	0.02	39.92	78.7
1829.51	1829.84	3.77	9.87	7.53	6.23	0.01	37.75	65.16
1829.84	1830.2	2.13	8.55	6.01	11.55	0.05	41.61	69.91
1830.2	1830.5	3.4	7.85	5.9	11.84	0.03	40.15	69.18
1830.5	1830.9	0.69	11.64	7.8	4.27	0.05	39.48	63.94
1830.9	1831.19	0.5	8.22	5.2	14.87	0.05	45.28	74.13

1831.19	1831.48	1.96	2.5	1.78	28.5	0.06	50.07	84.88
1831.48	1831.82	6.4	13.77	3.55	10.28	0	33.97	67.96
1831.82	1832.2	3.45	10.68	4.97	11.3	0.06	39.14	69.59
1832.2	1832.47	2.65	10.86	3.97	14.05	0.02	41.16	72.71
1832.47	1832.86	0.67	1.3	0.52	36.24	0.21	58.45	97.38
1832.86	1833.15	0.42	1.31	0.64	36.03	0.01	58.33	96.75
1833.15	1833.45	1.64	10.8	6.44	8.21	0.06	40.14	67.3
1833.45	1833.73	2.57	7.1	3.76	16.47	0.05	41	70.95
1833.73	1833.98	2.66	9.78	4.96	10.83	0.03	38.12	66.38
1833.98	1834.36	2.69	12.09	7.08	2.51	0.03	33.54	57.92
1834.36	1834.8	0.97	11.93	5.23	8.95	0.05	39.24	66.37
1834.8	1835.14	3.17	5.63	2.58	22.45	0.03	44.96	78.82
1835.14	1835.45	4.24	13.46	2.73	9.94	0.02	32.4	62.78
1835.45	1835.82	4.87	5.57	1.51	21.95	0.01	39.73	73.64
1835.82	1836.2	1.5	9.8	2.78	13.36	0.02	36.51	63.97
1836.2	1836.43	0.88	2.13	0.81	34.96	0.04	57.62	96.44
1836.43	1836.79	1.27	1.86	0.32	36.02	0.03	57.3	96.82
1836.79	1837.04	0.73	0.78	0.18	41.79	0.05	65.2	108.72
1837.04	1837.45	2.3	3.93	1.15	30.79	0.07	52.82	91.05
1837.45	1839.75	0.46	0.54	0.11	41.92	0.03	65.17	108.23
1839.75	1840.03	2.88	8.09	0.89	21.87	0.01	41.53	75.26
1840.03	1840.39	1.02	8.38	1.07	26.61	0.02	51.02	88.12
1840.39	1840.7	0.21	0.35	0.04	43.26	0.02	67.04	110.92

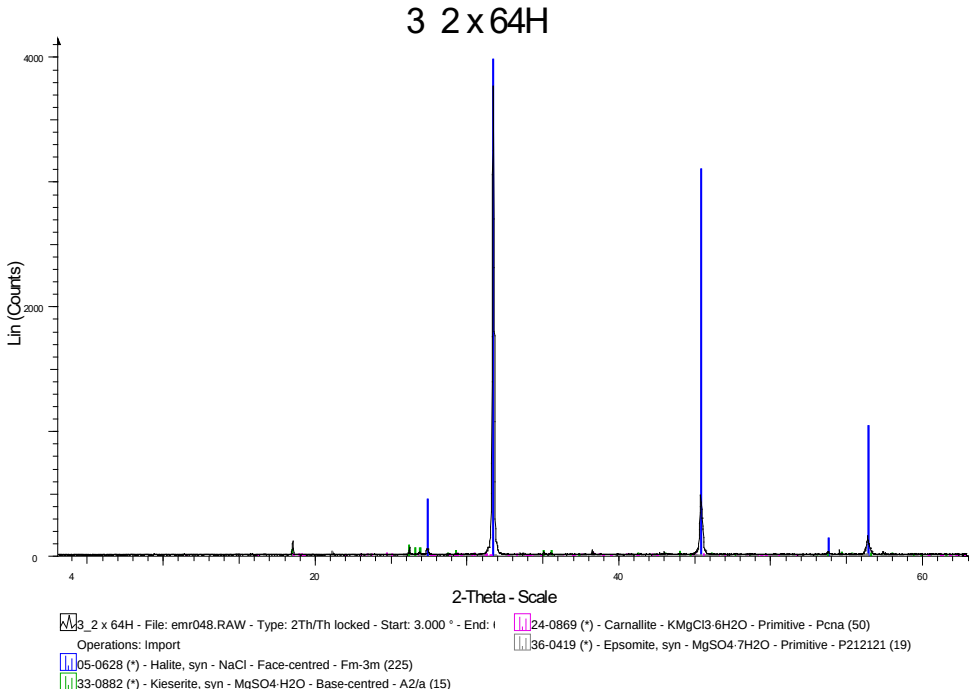

Halite
Carnallite
Bischofite
Kieserite
100
80
60
40
20
0
1780
1790
1800
1810
1820
1830
1840
Halite
Carnallite
Bischofite
Kieserite

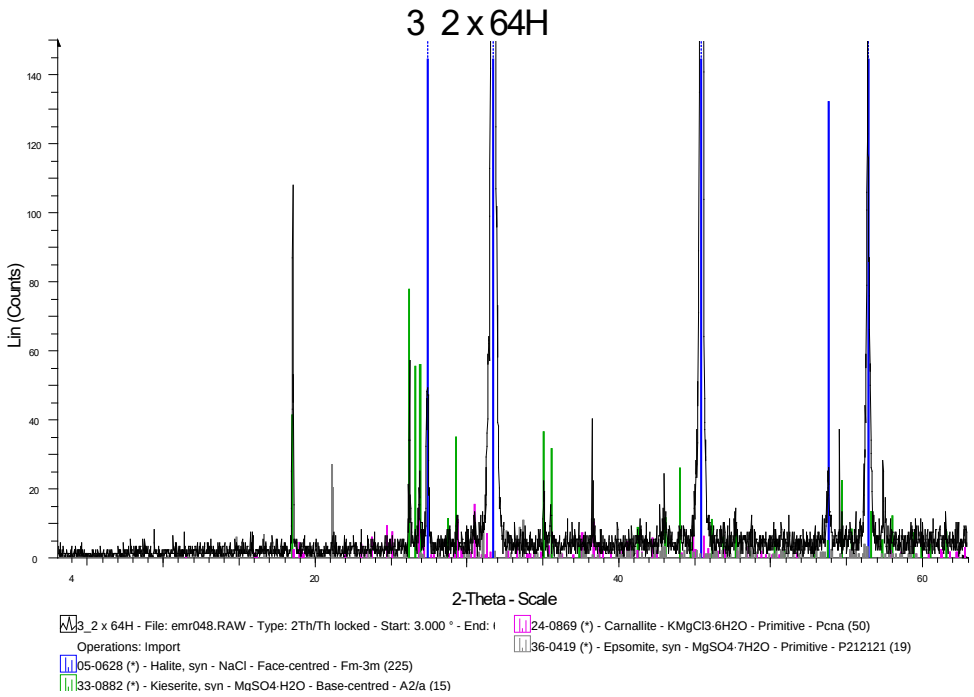
2 Sample taken from the carnallitic part of Fig. 5.8



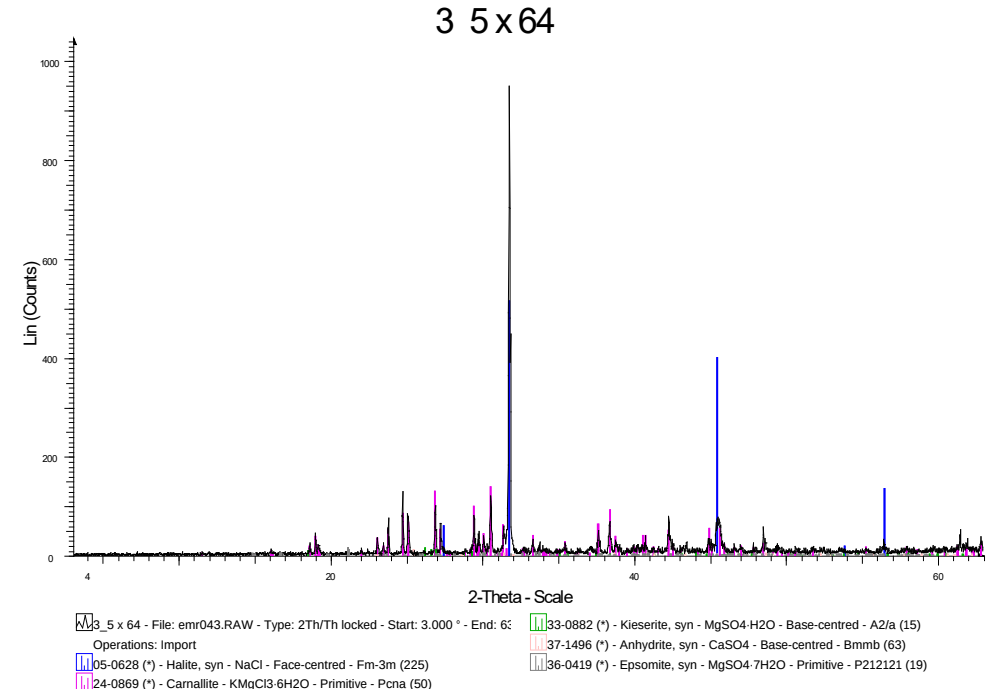


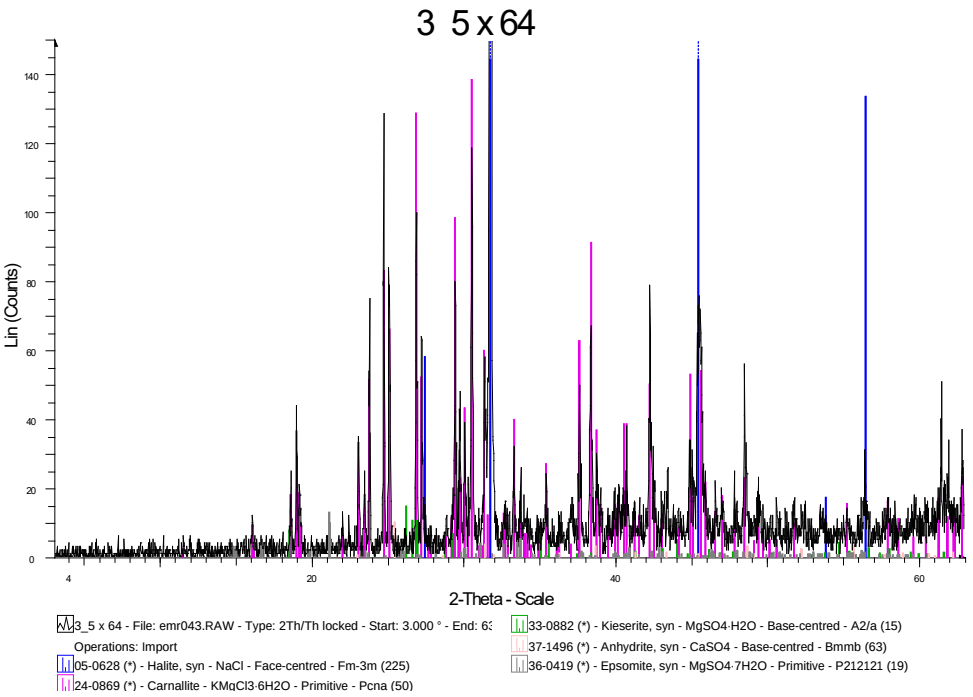
Sample taken from the halite part of Fig. 5.8



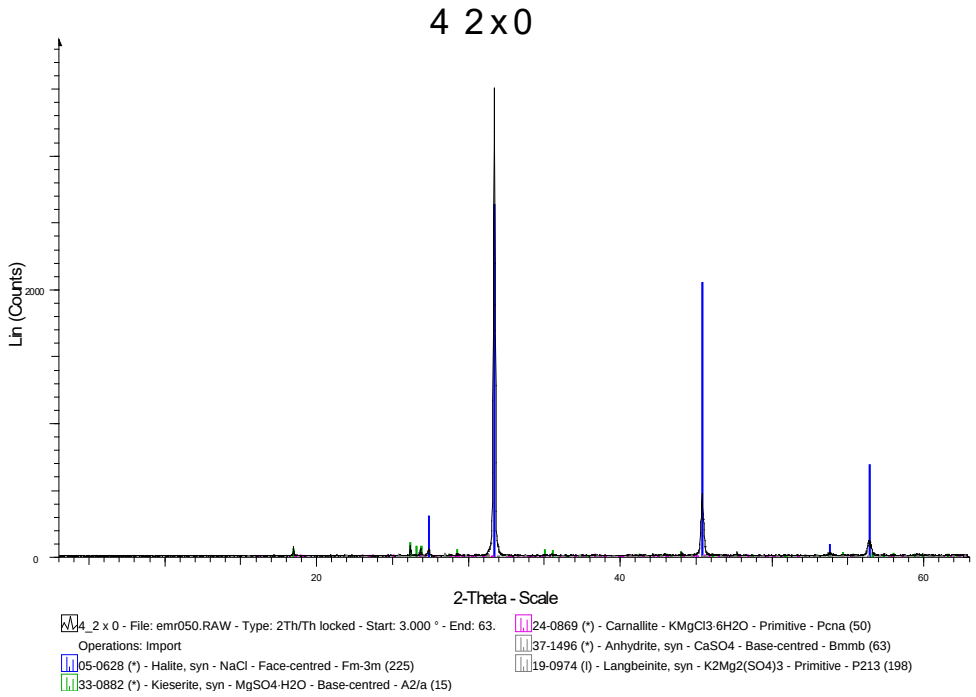


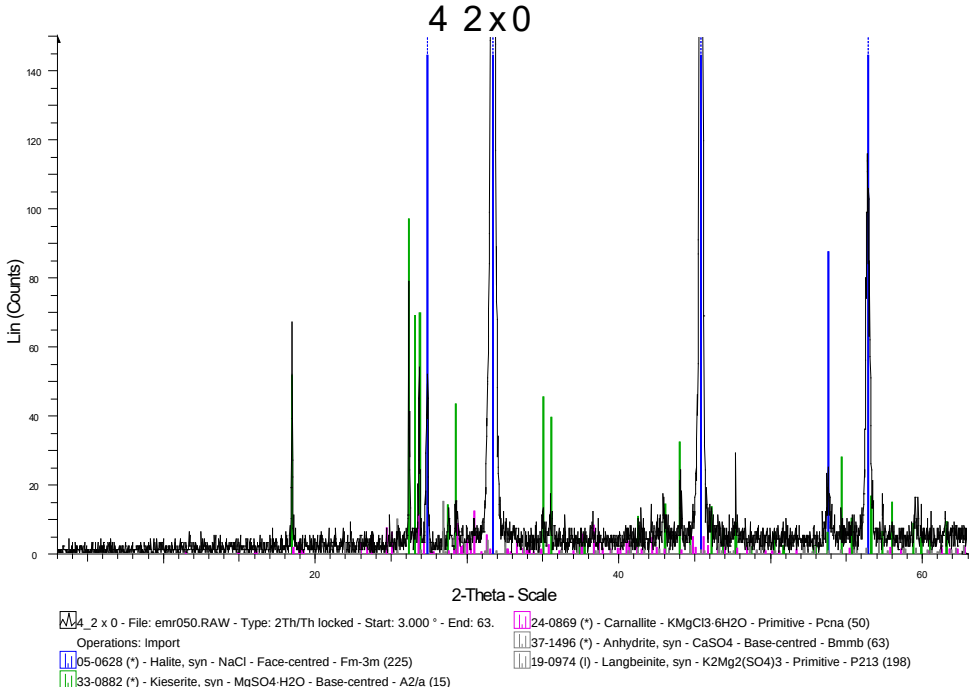
Sample shown in Fig. 5.10



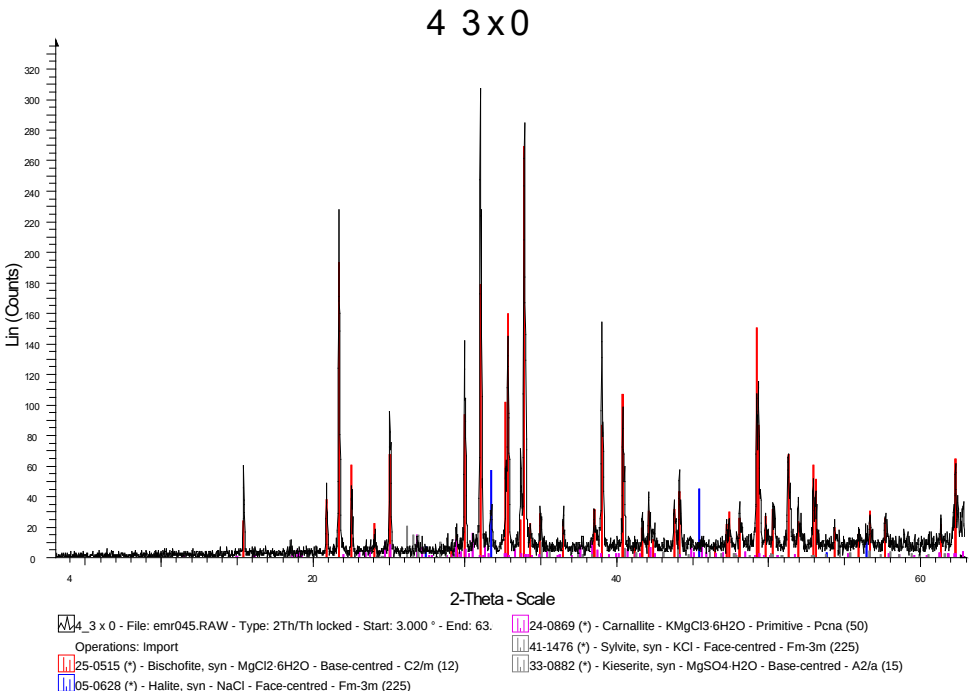


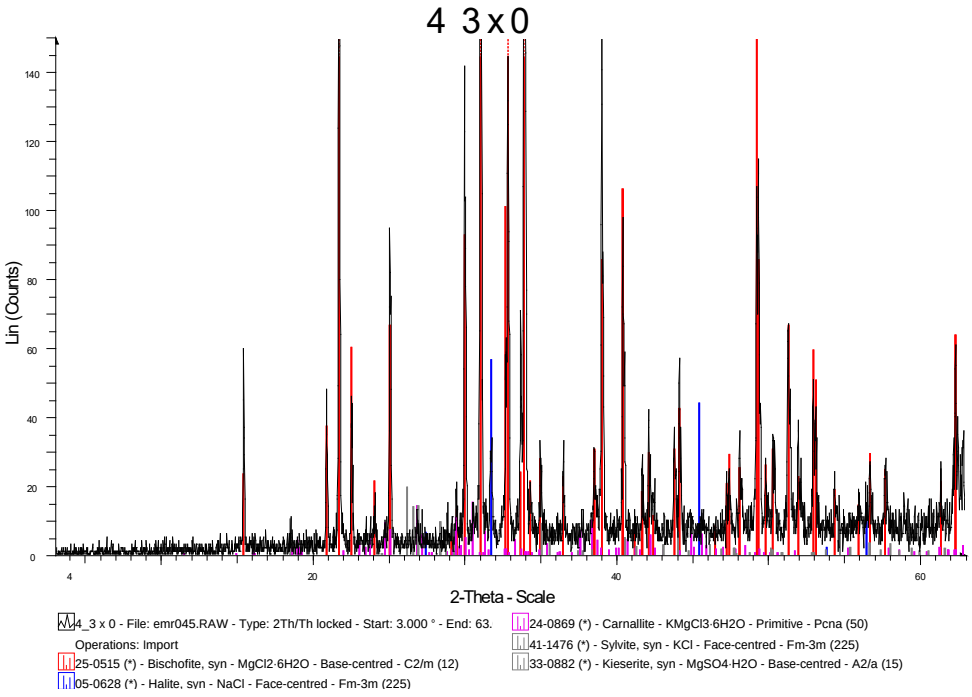
Sample shown in Fig. 5.7



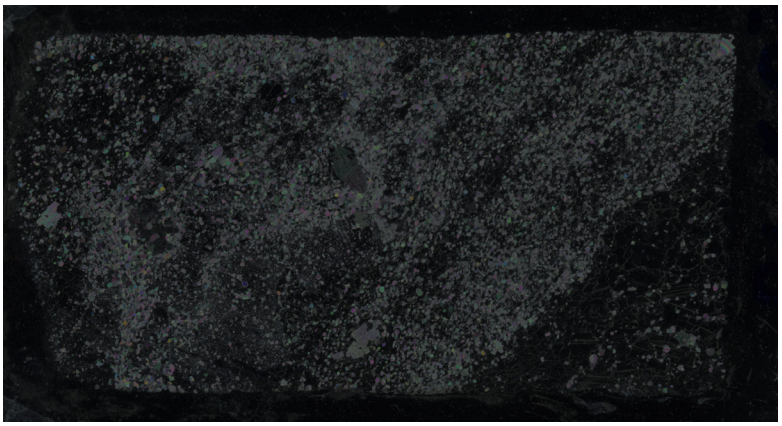


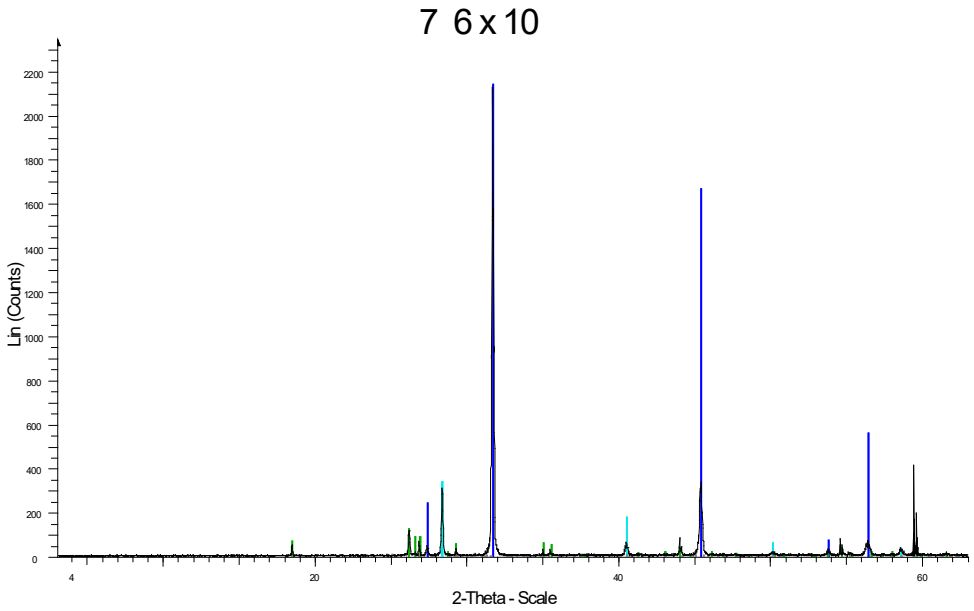
Sample shown in Fig. 5.11

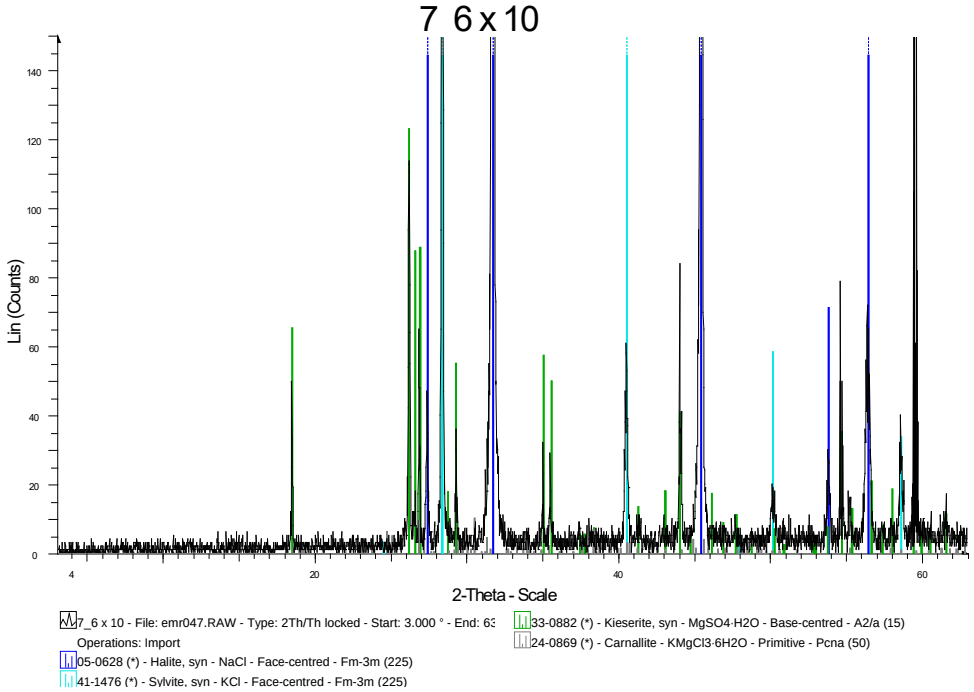




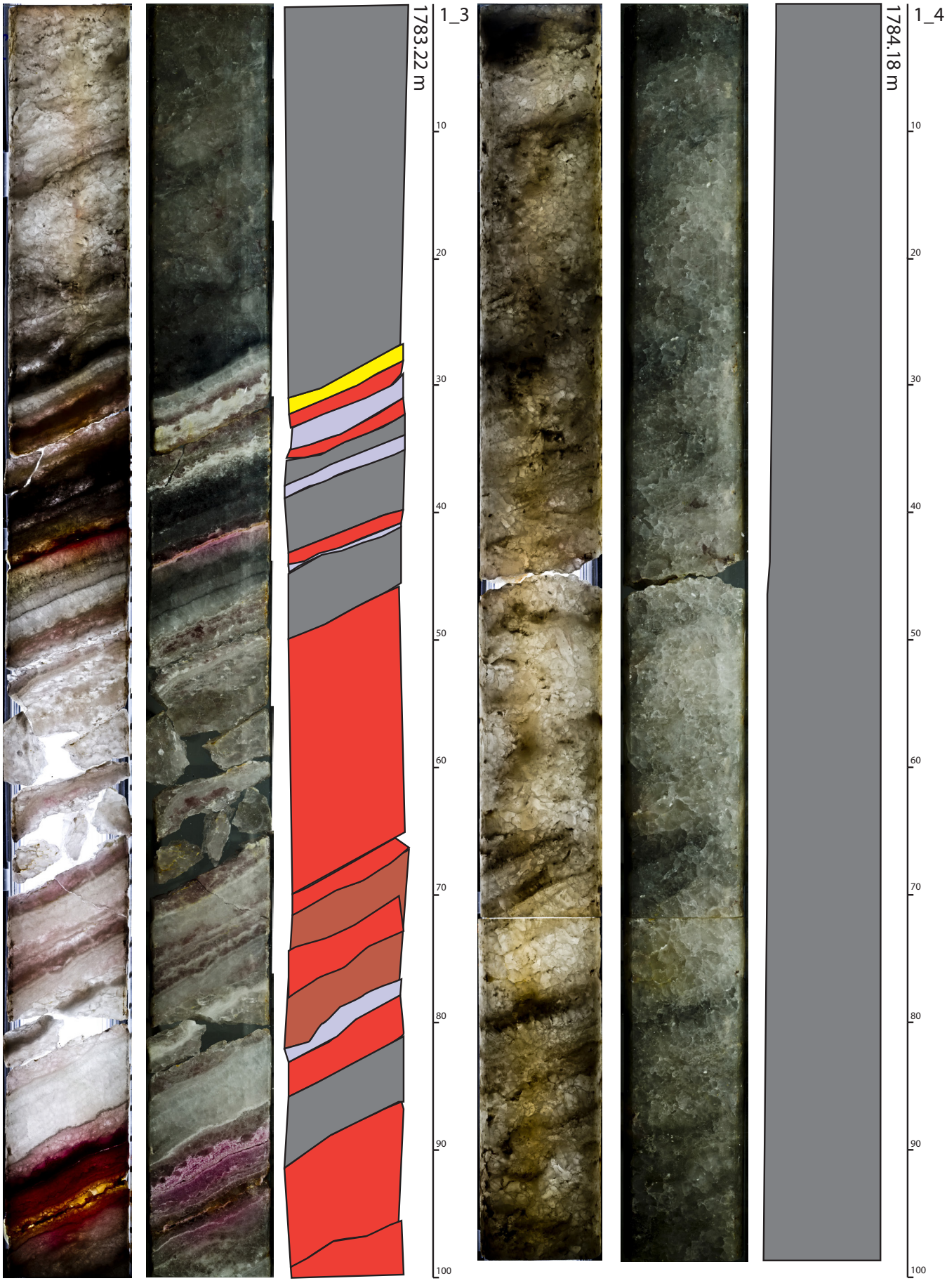
Sample taken from the top of core 7_6

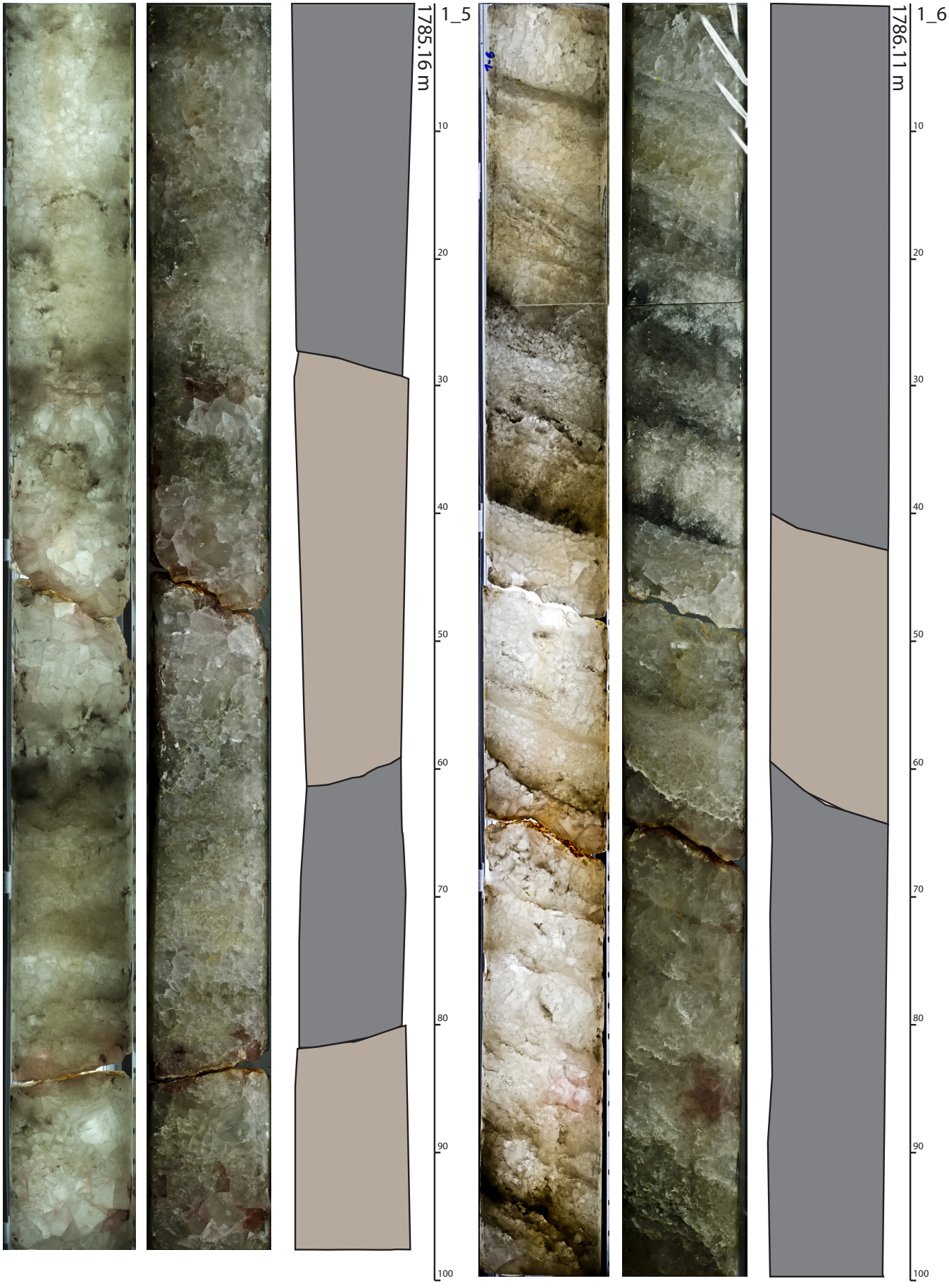


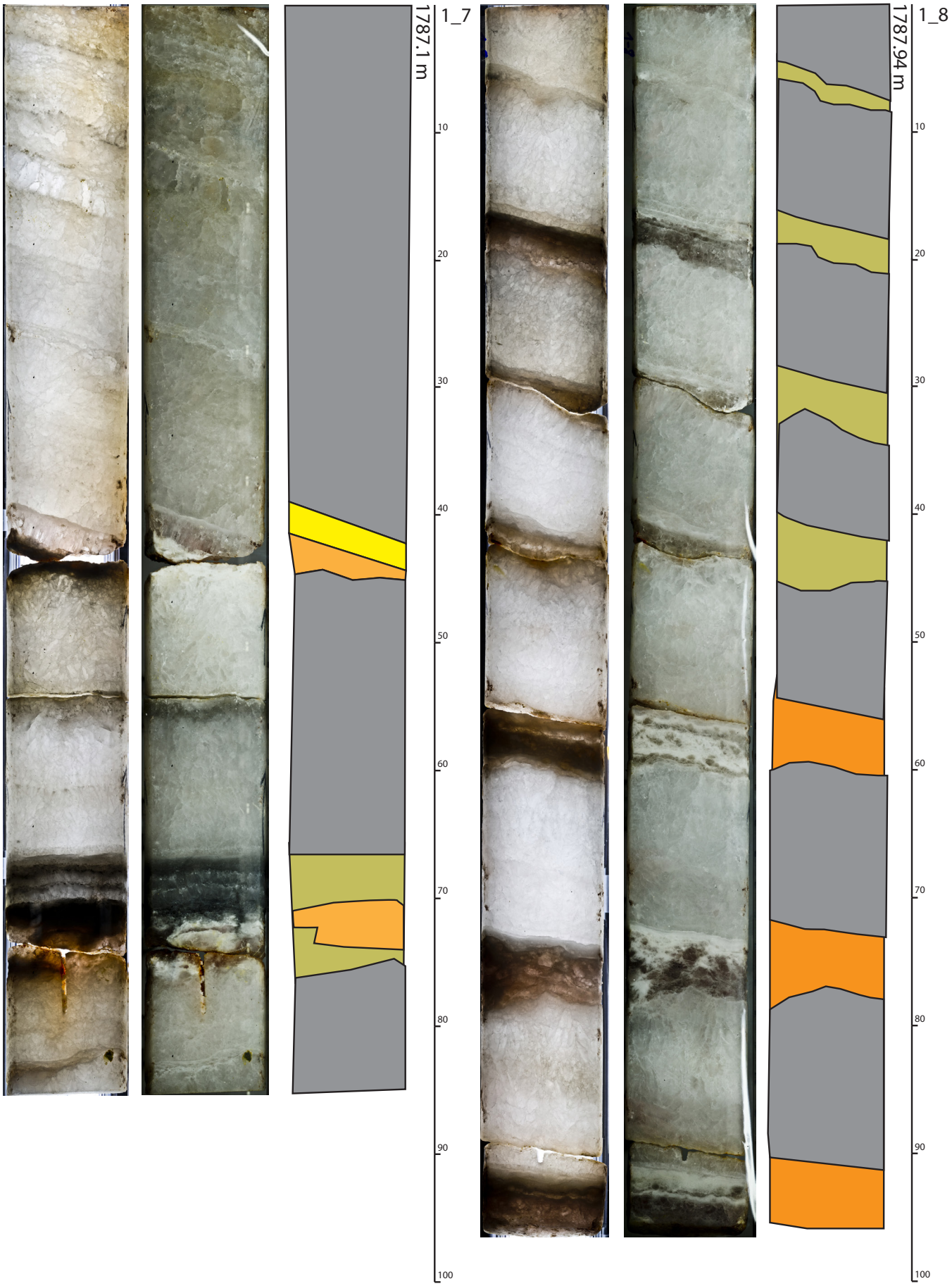


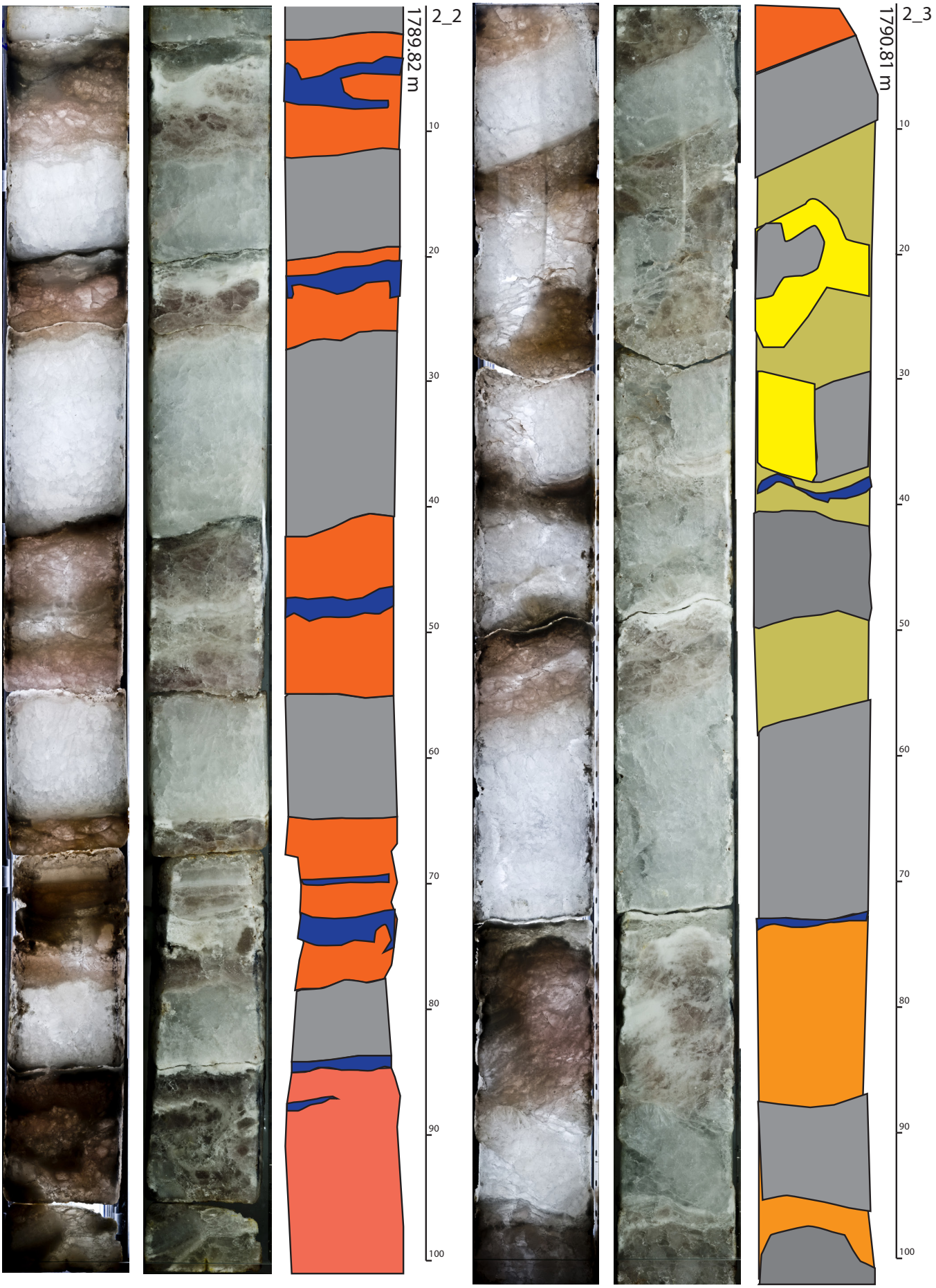


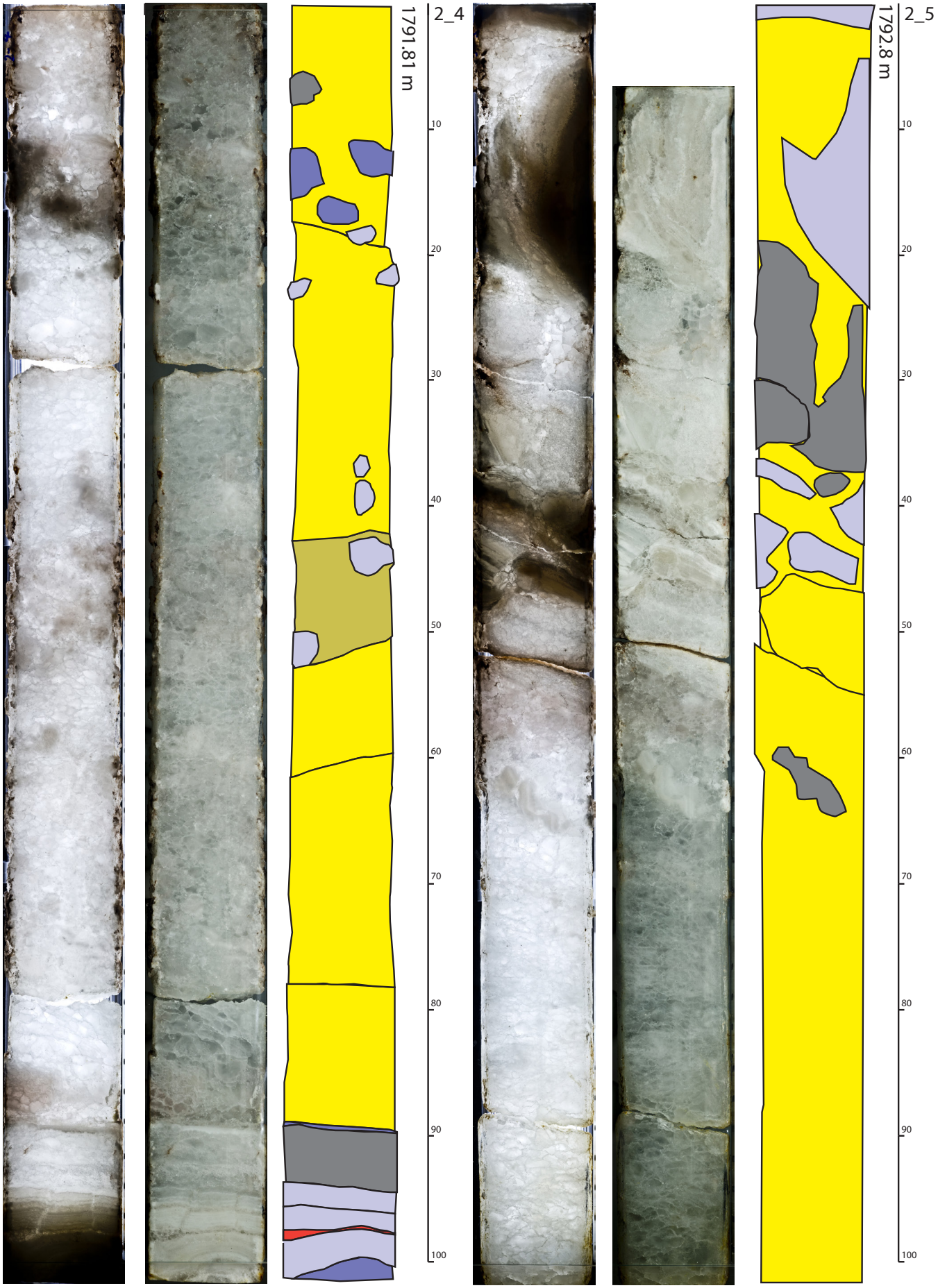

3
1781 m
1_1
1782.24 m
1_2
10
20
30
40
50
60
70
80
90
100


1783.22 m
1_3
10
20
30
40
50
60
70
80
90
100
1784.18 m
1_4
10
20
30
40
50
60
70
80
90
100

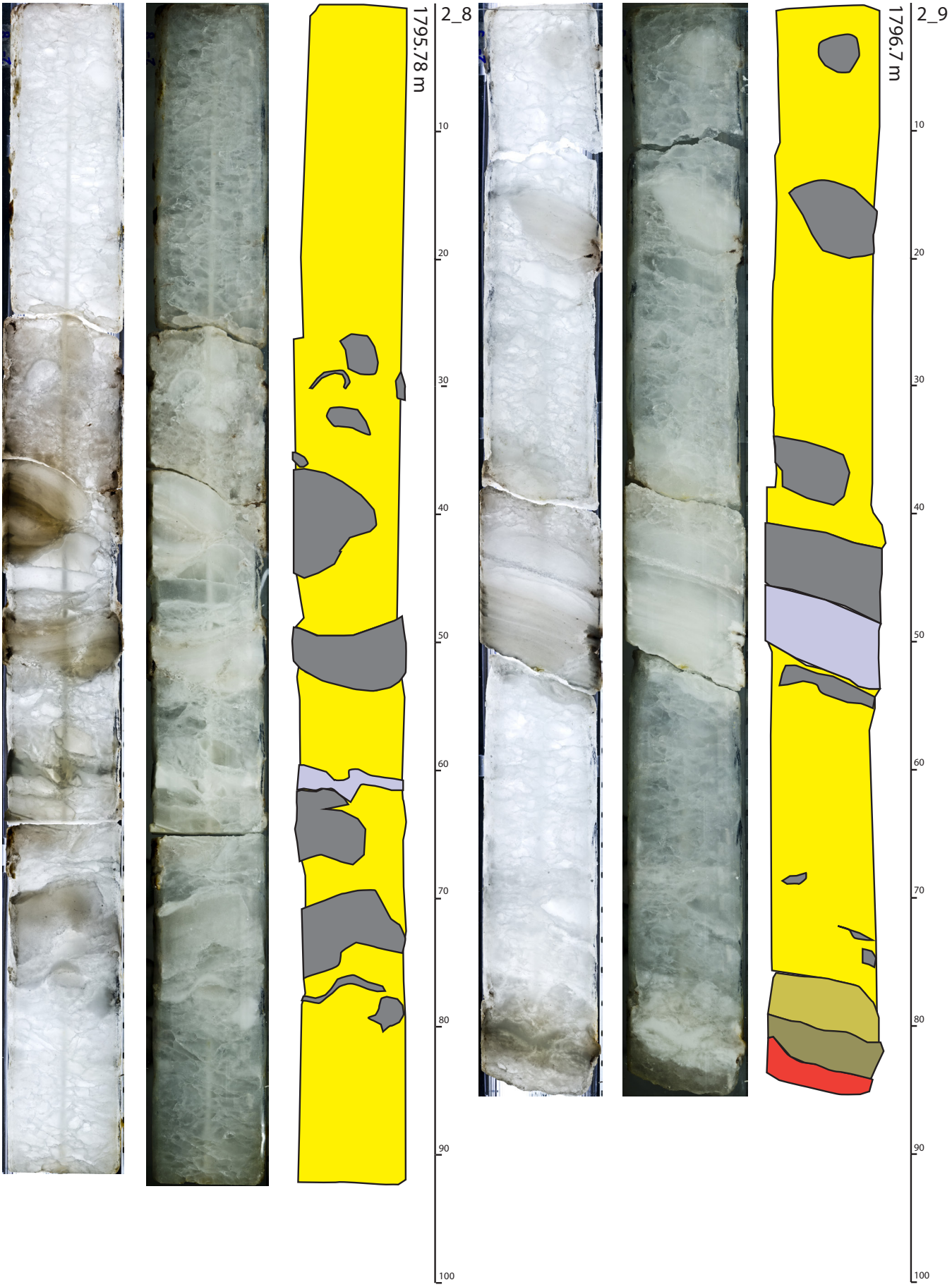

1785.16 m
1_5
1786.11 m
1_6
10
20
30
40
50
60
70
80
90
100

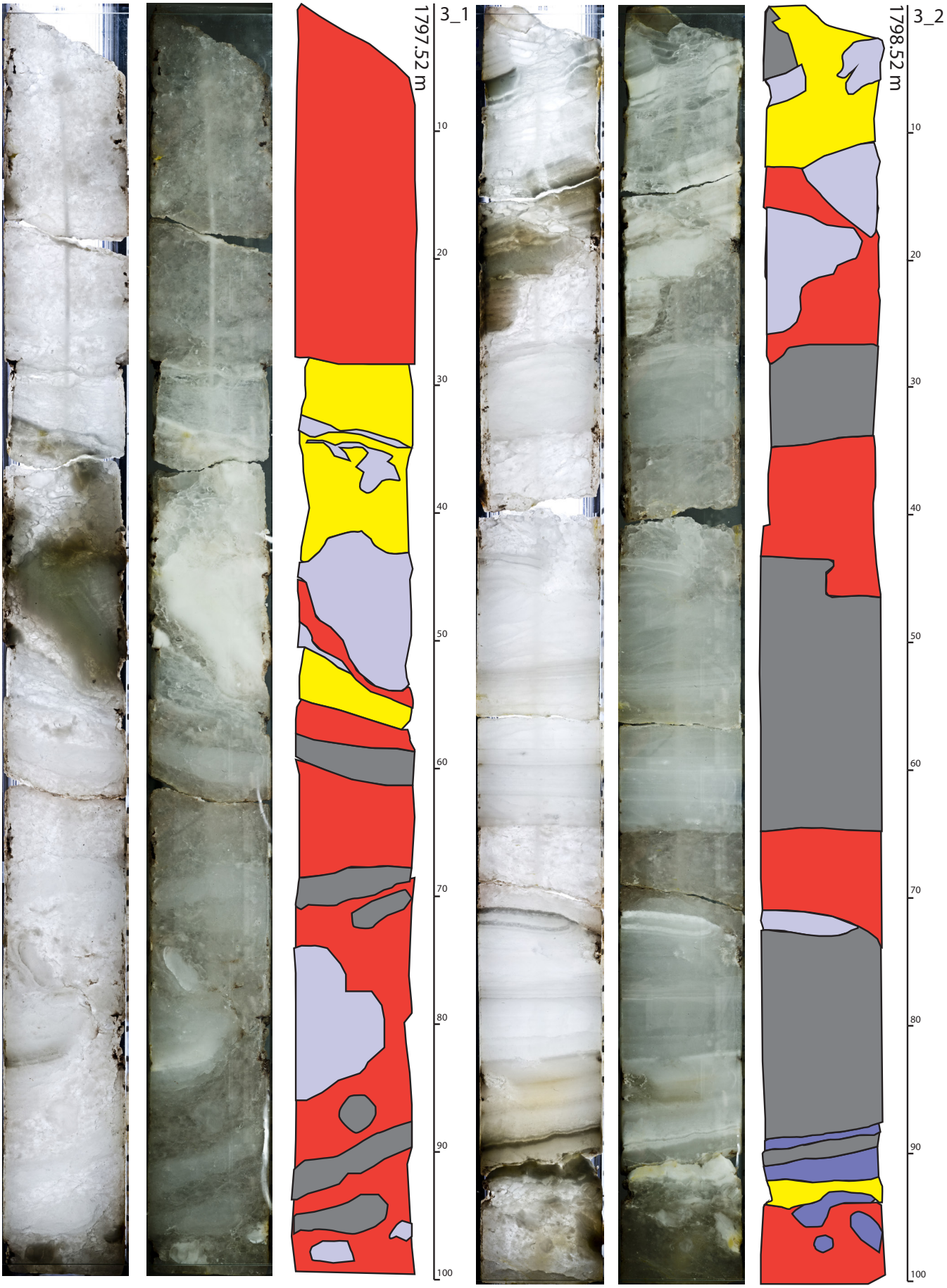

1_7
1787.1 m
1_8
1787.94 m
10
20
30
40
50
60
70
80
90
100

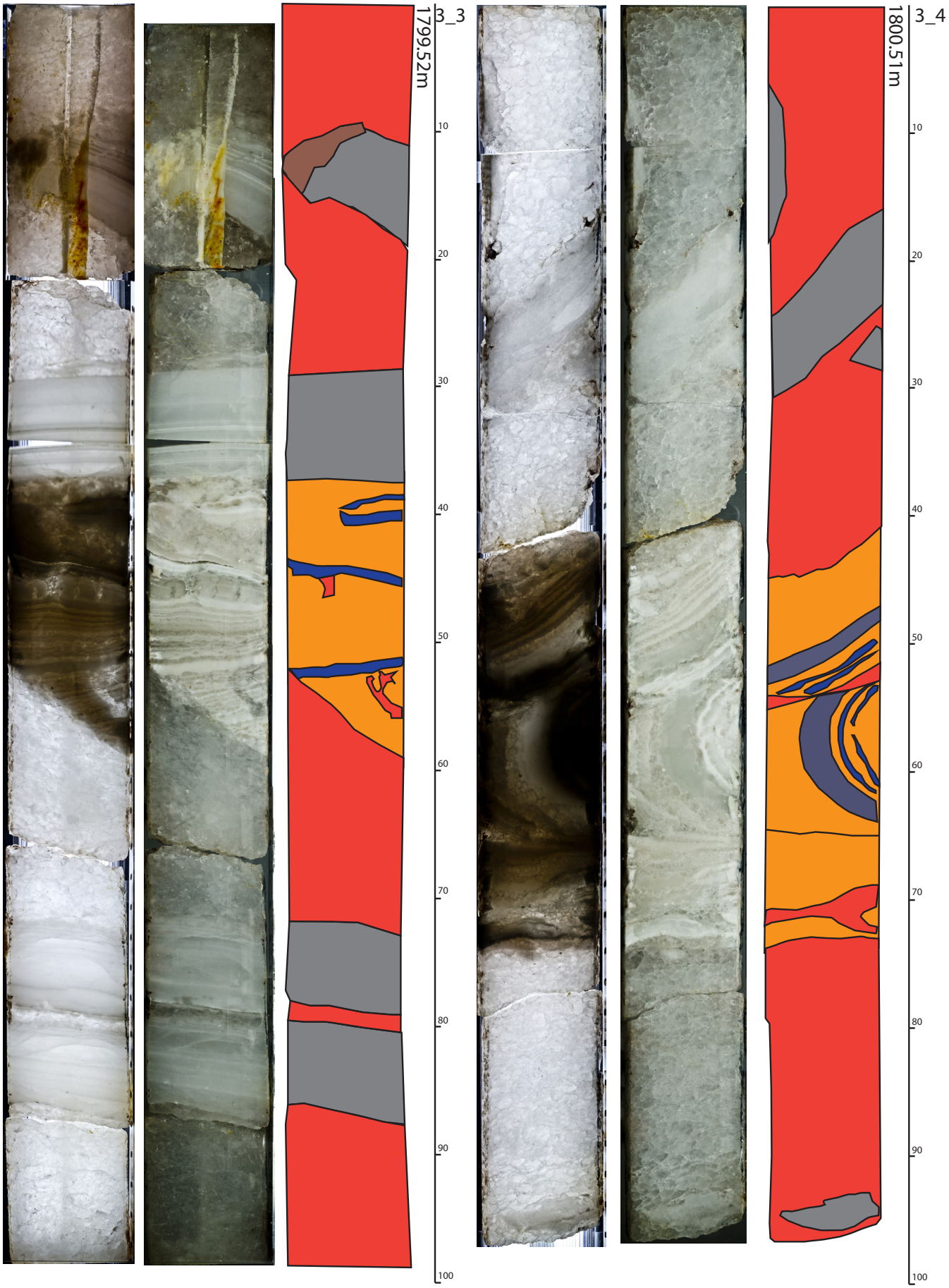

1789.82 m
2_2
10
20
30
40
50
60
70
80
90
100
1790.81 m
2_3
10
20
30
40
50
60
70
80
90
100

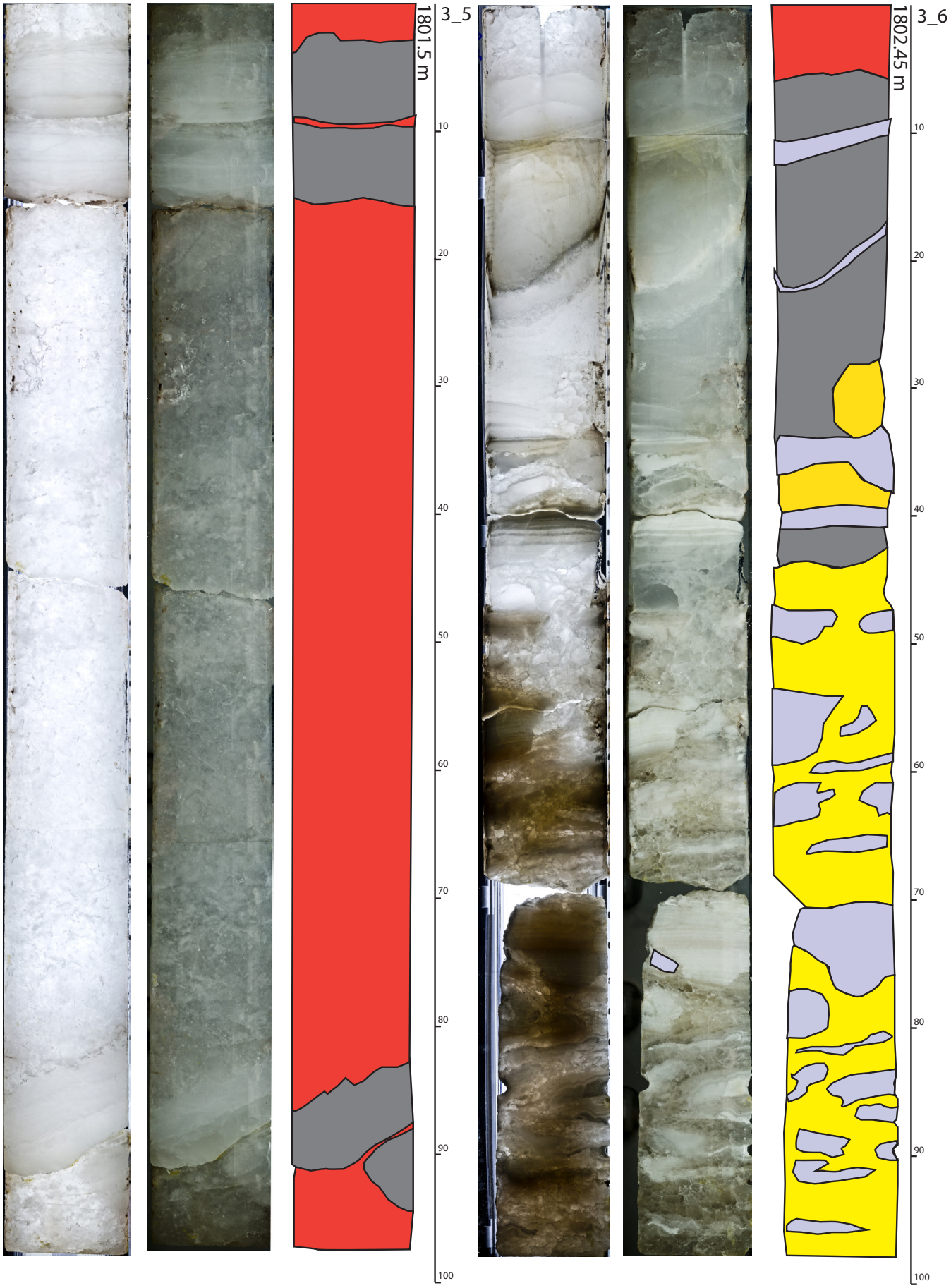

2_4
1791.81 m
2_5
1792.8 m
10
20
30
40
50
60
70
80
90
100

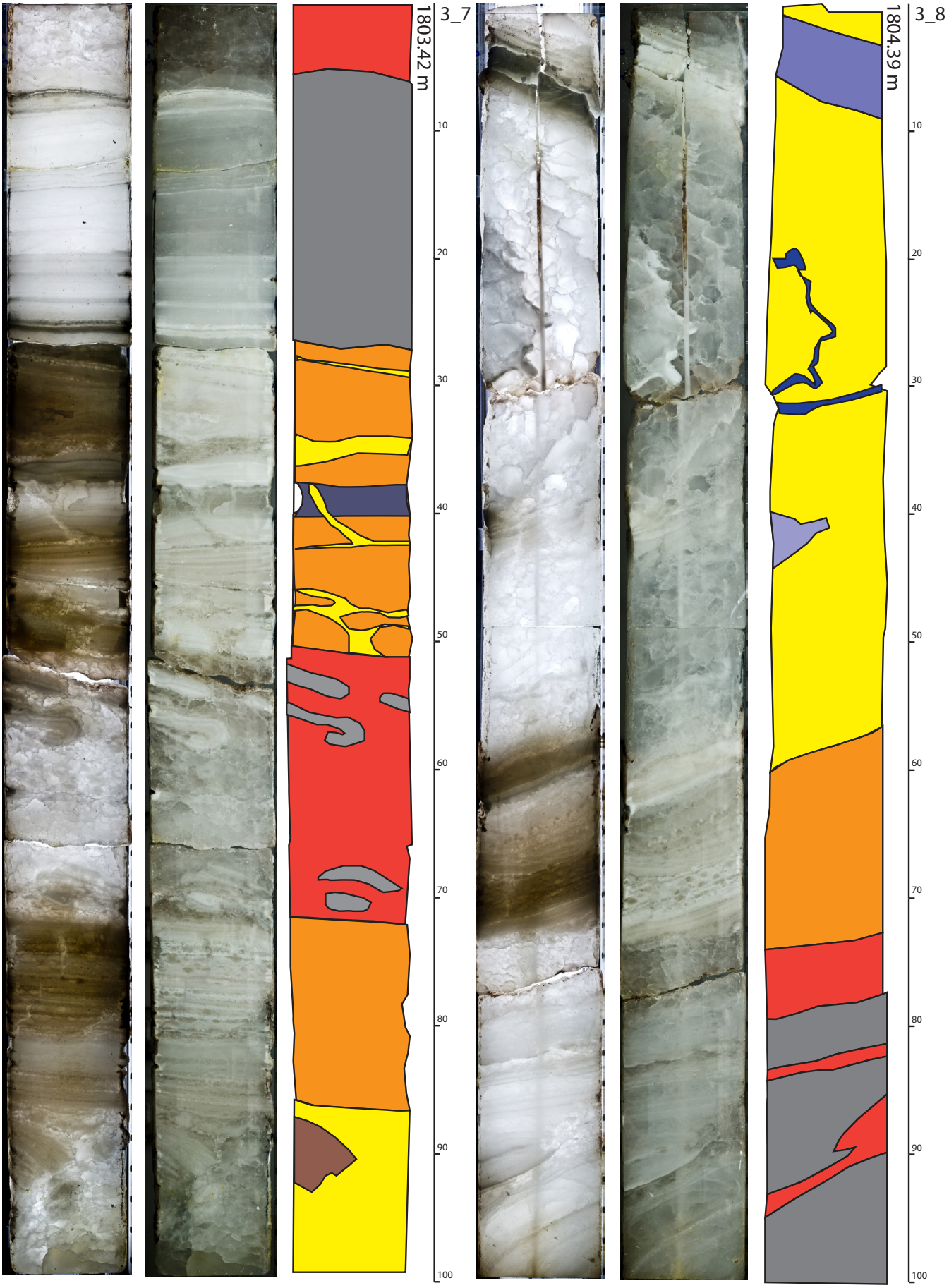

1793.8 m
2_6
1794.79 m
2_7
10
20
30
40
50
60
70
80
90
100

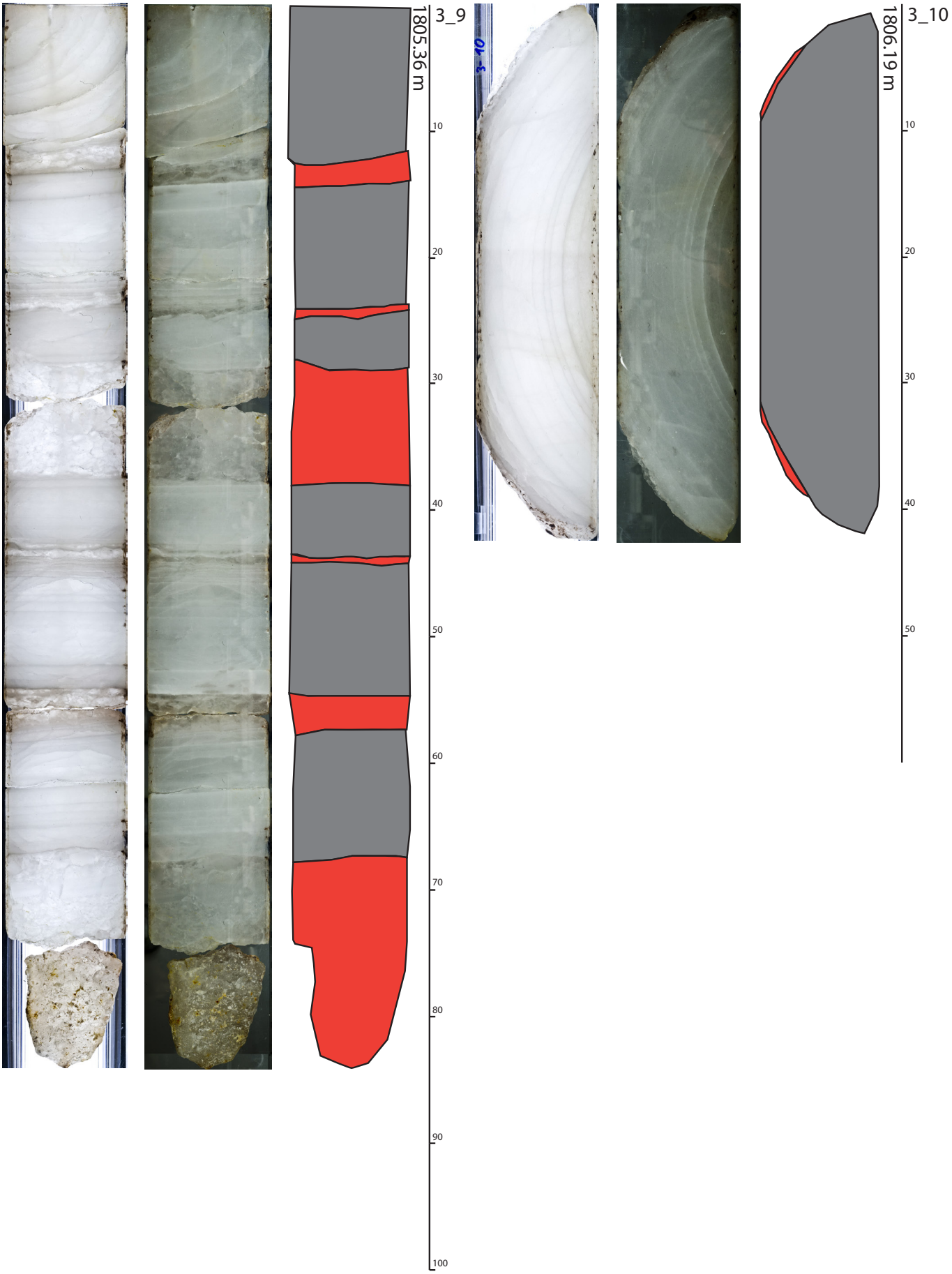

1795.78 m
2_8
10
20
30
40
50
60
70
80
90
100
1796.7 m
2_9
10
20
30
40
50
60
70
80
90
100

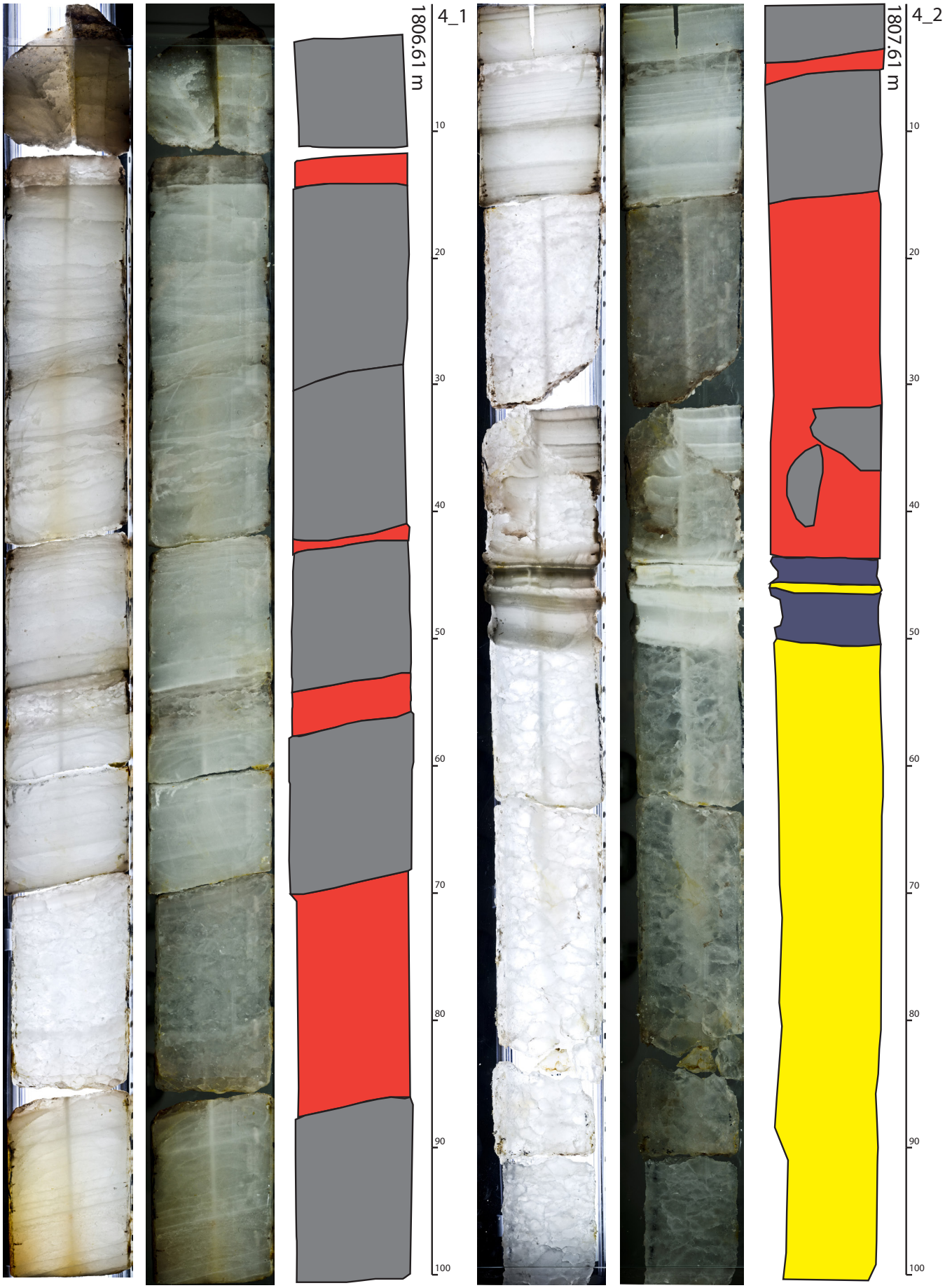

1797.52 m
3_1
10
20
30
40
50
60
70
80
90
100
1798.52 m
3_2
10
20
30
40
50
60
70
80
90
100

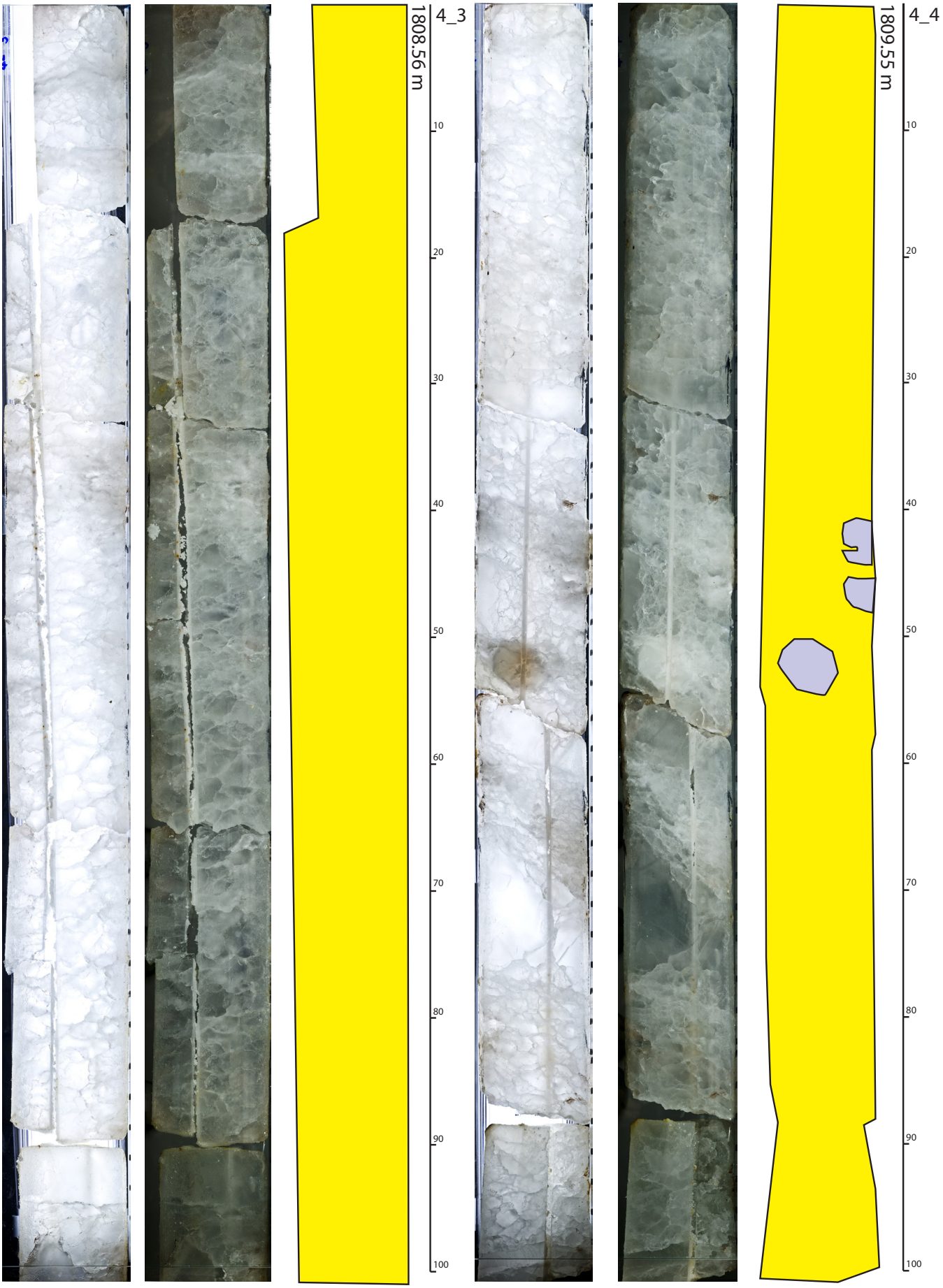

3_3
1799.52m
3_4
1800.51m
10
20
30
40
50
60
70
80
90
100

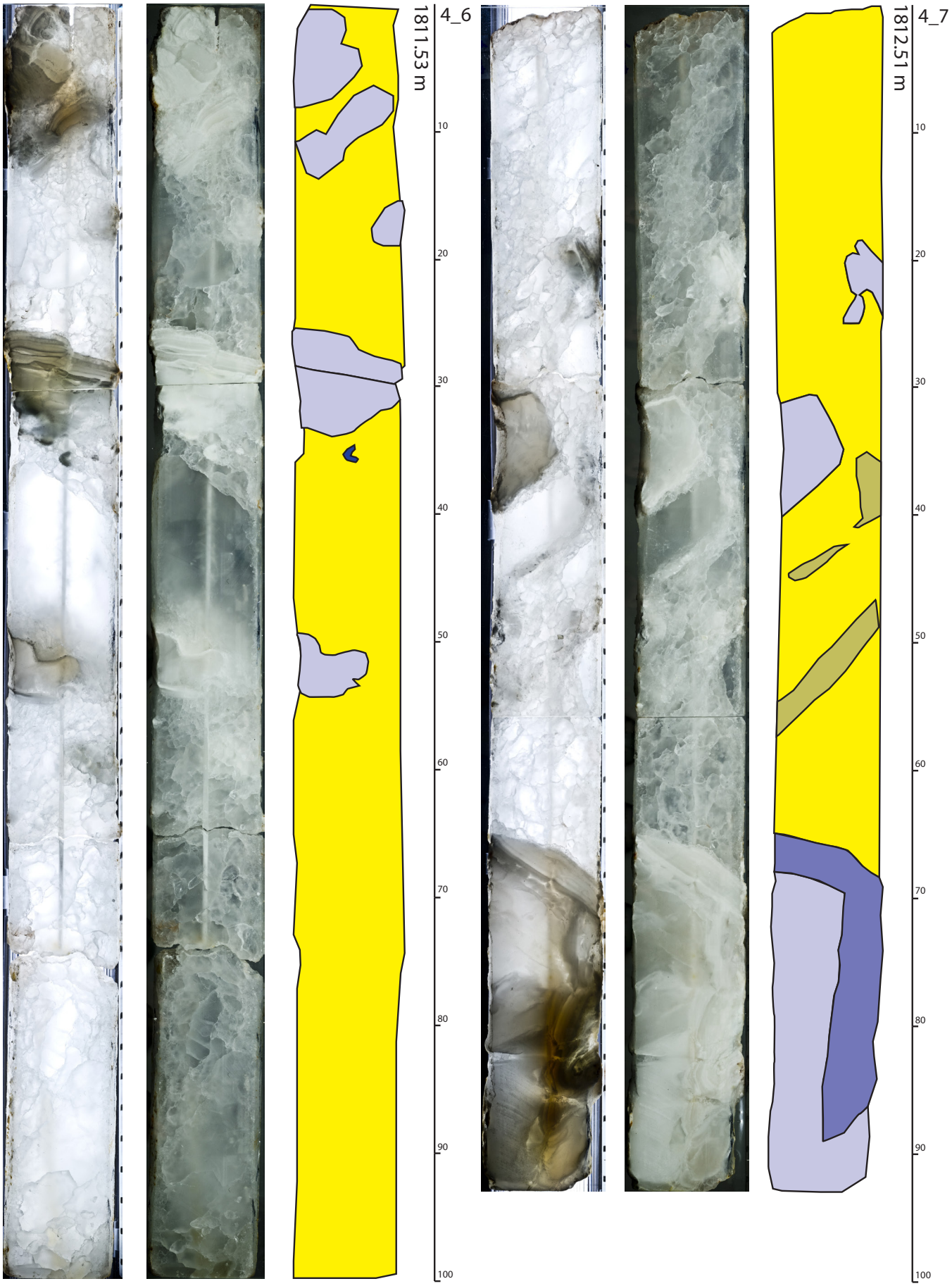

3_5
1801.5 m
10
20
30
40
50
60
70
80
90
100
3_6
1802.45 m
10
20
30
40
50
60
70
80
90
100

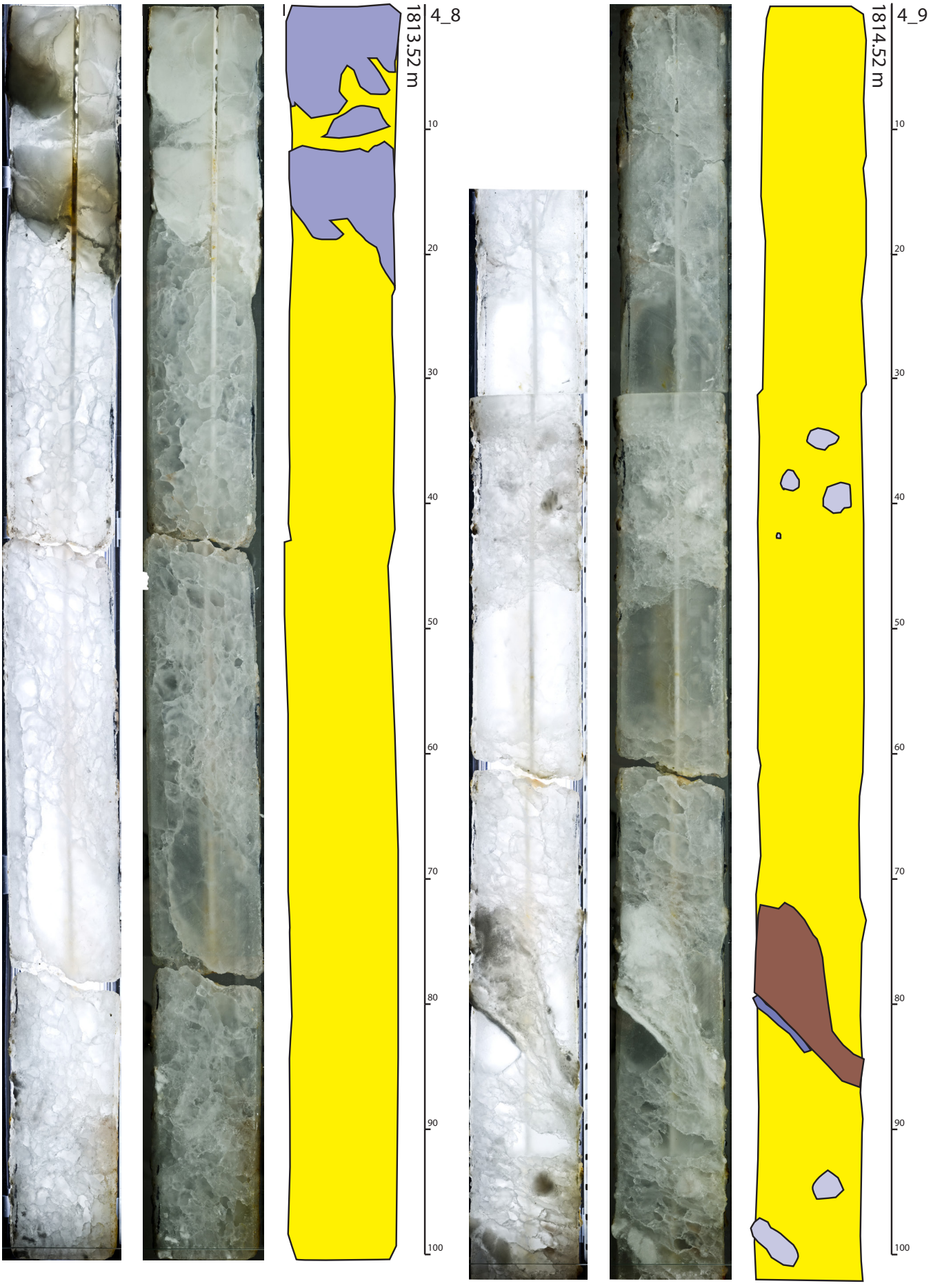

1803.42 m
3_7
10
20
30
40
50
60
70
80
90
100
1804.39 m
3_8
10
20
30
40
50
60
70
80
90
100

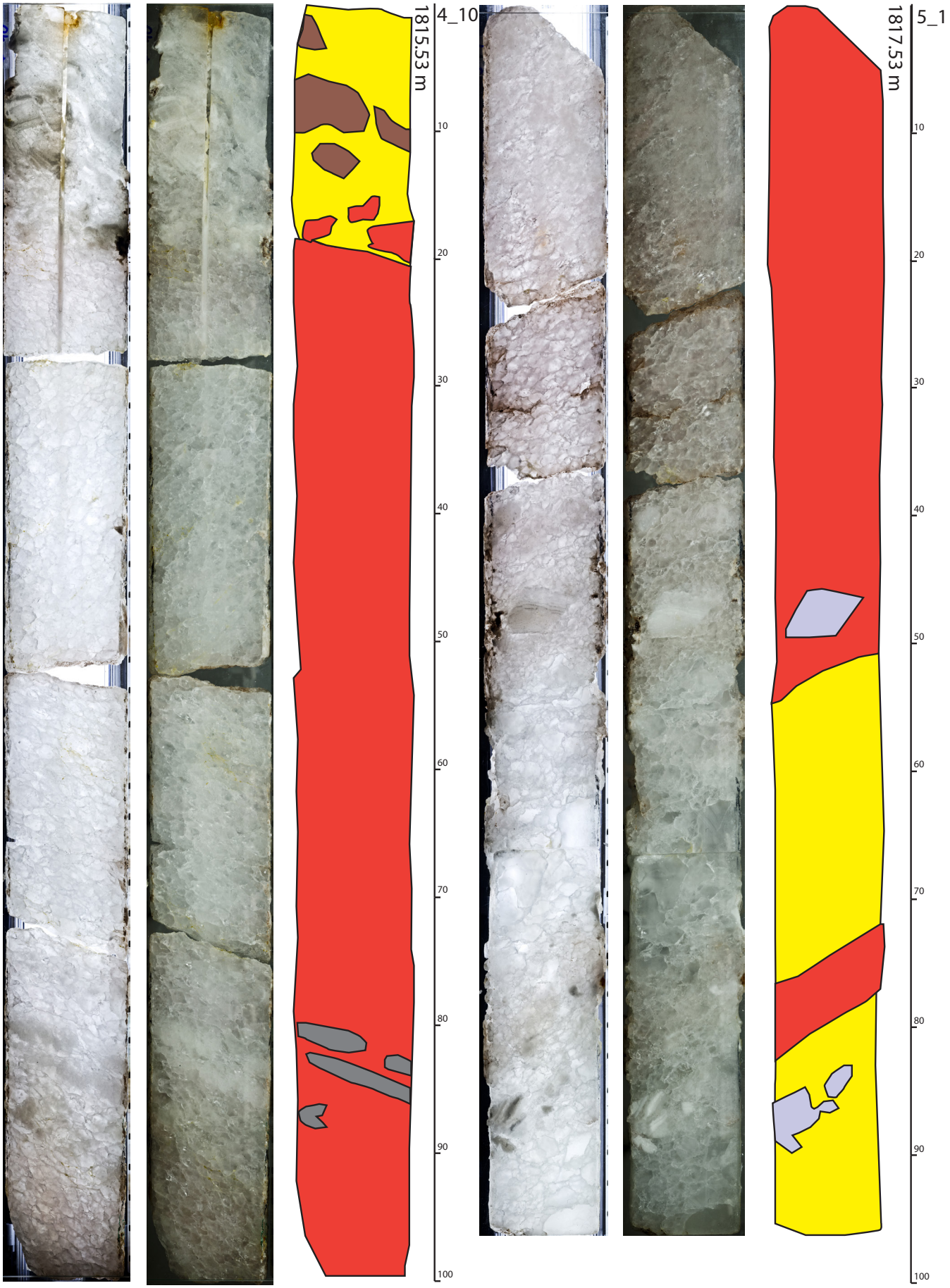

3_9
1805.36 m
10
20
30
40
50
60
70
80
90
100
3_10
1806.19 m
10
20
30
40
50

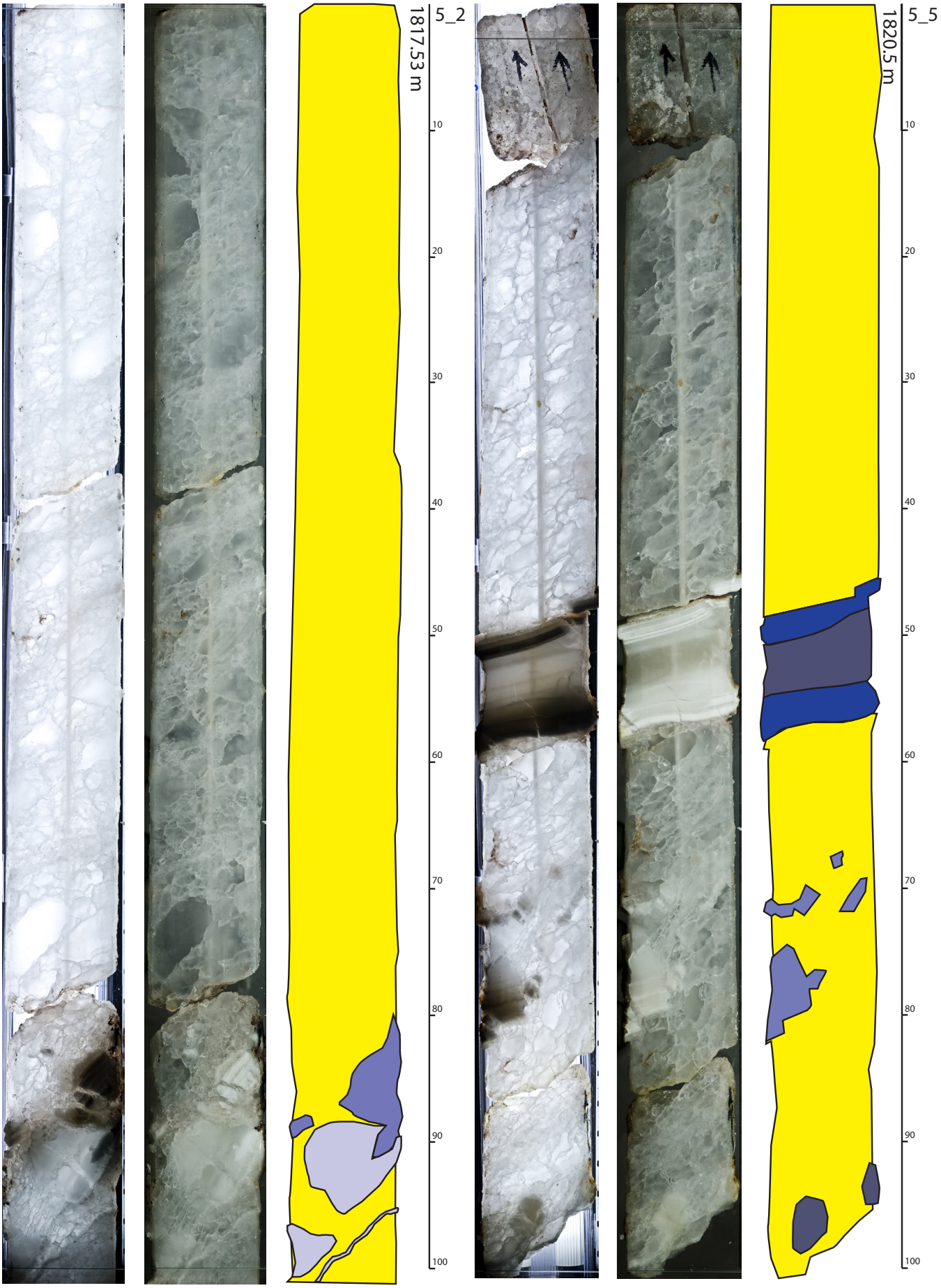

1806.61 m
4_1
10
20
30
40
50
60
70
80
90
100
1807.61 m
4_2
10
20
30
40
50
60
70
80
90
100

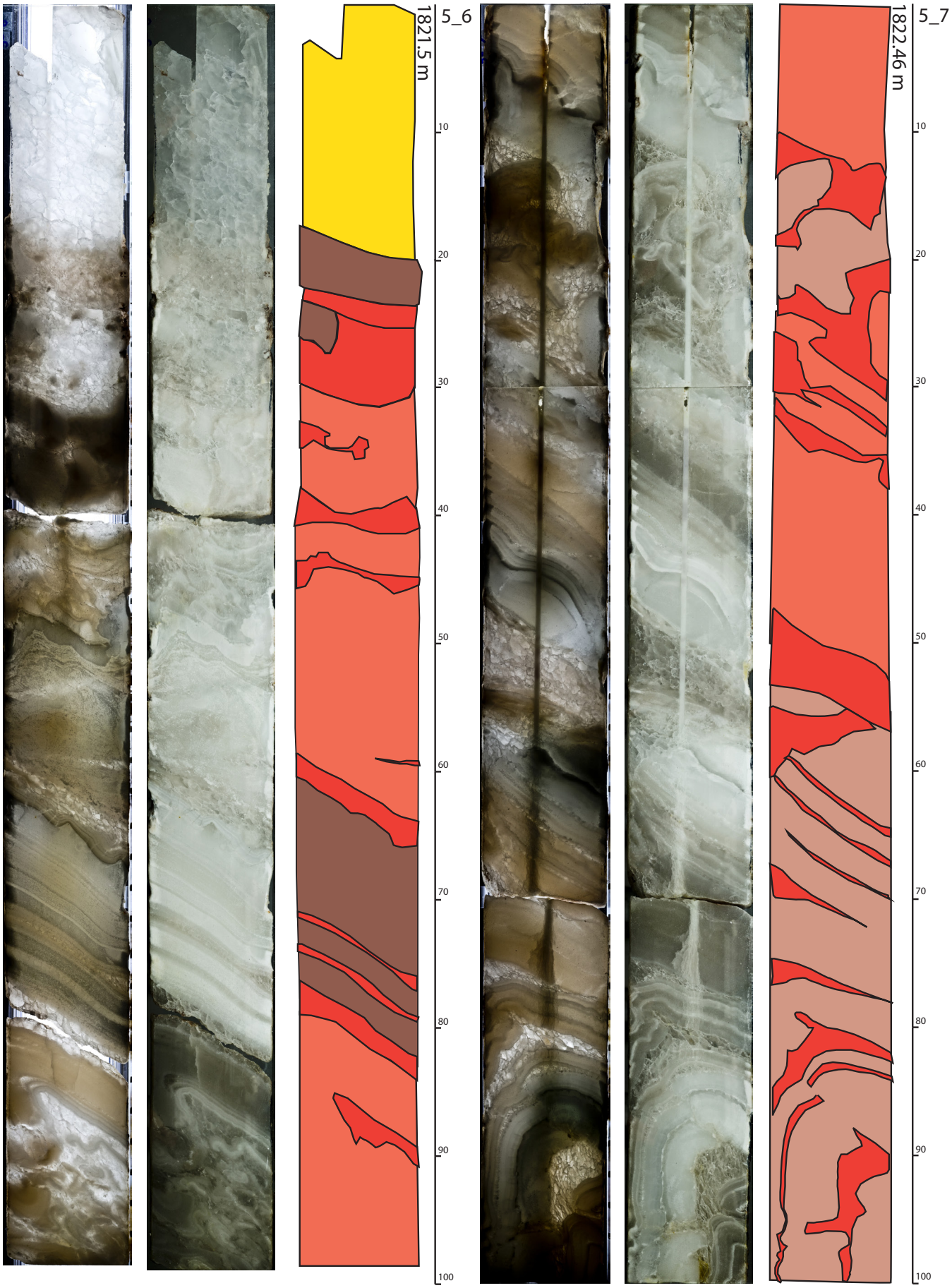

1808.56 m
4_3
10
20
30
40
50
60
70
80
90
100
1809.55 m
4_4
10
20
30
40
50
60
70
80
90
100

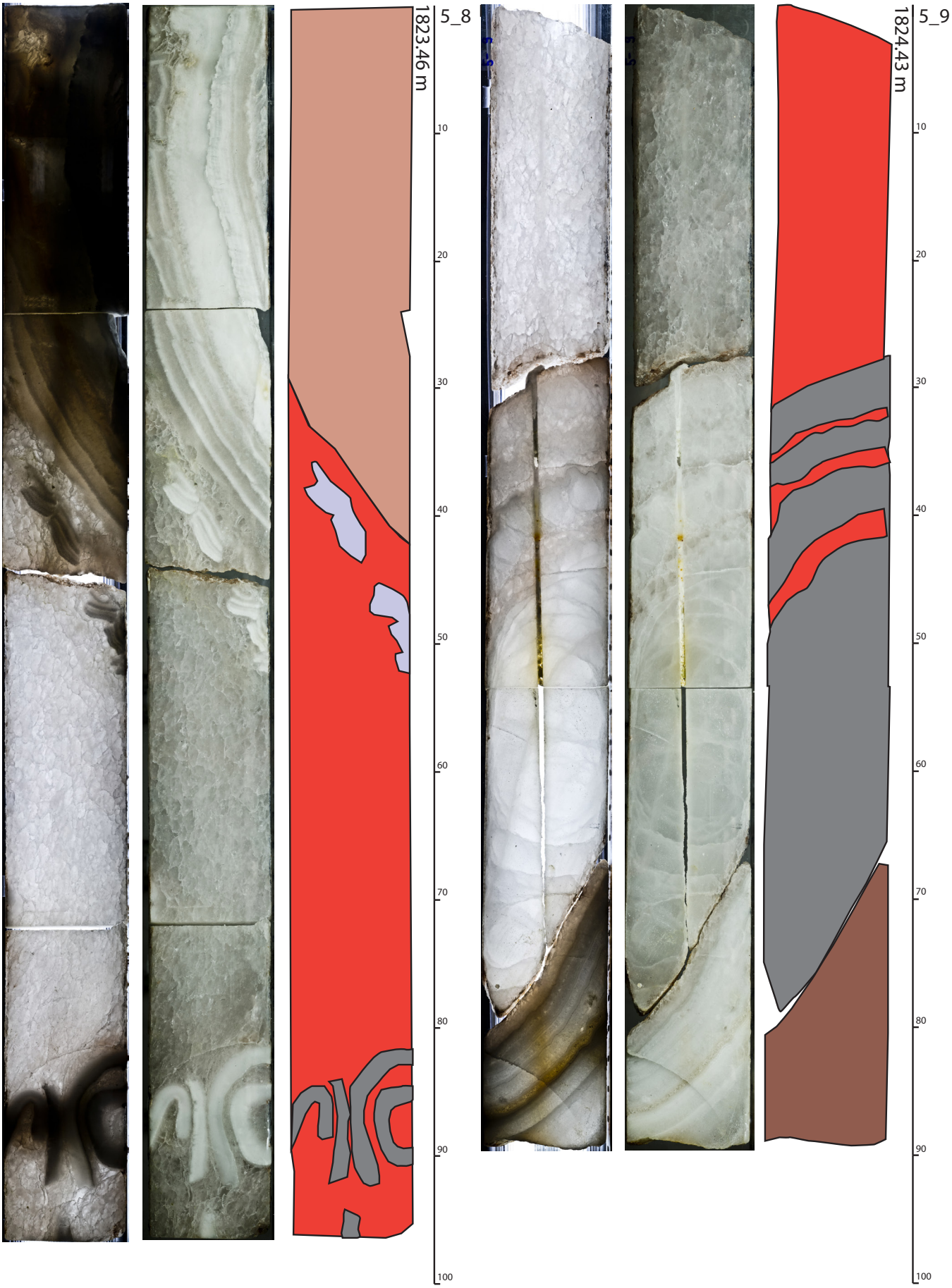

4_6
1811.53 m
4_7
1812.51 m
10
20
30
40
50
60
70
80
90
100

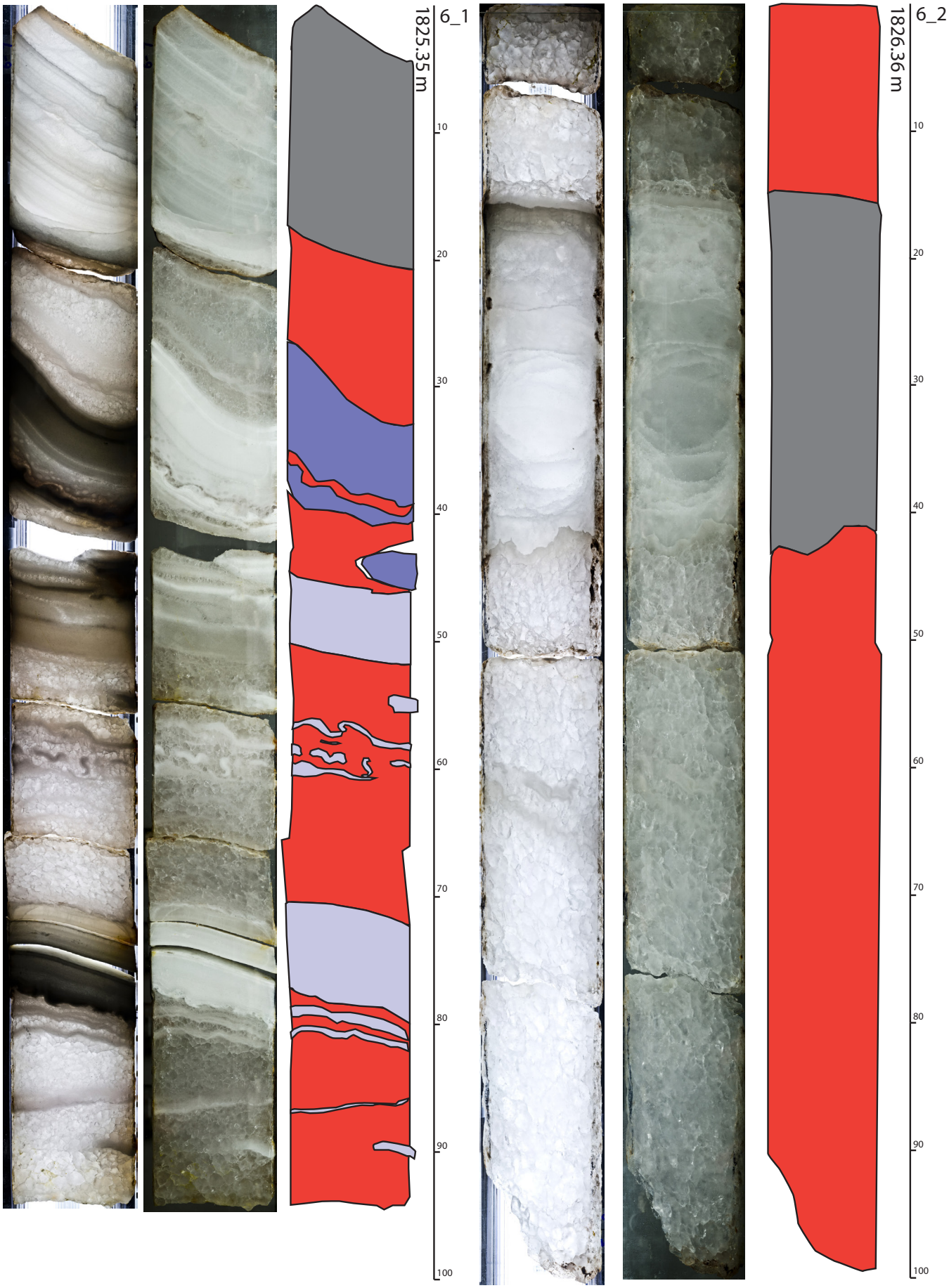

4_8
1813.52 m
4_9
1814.52 m

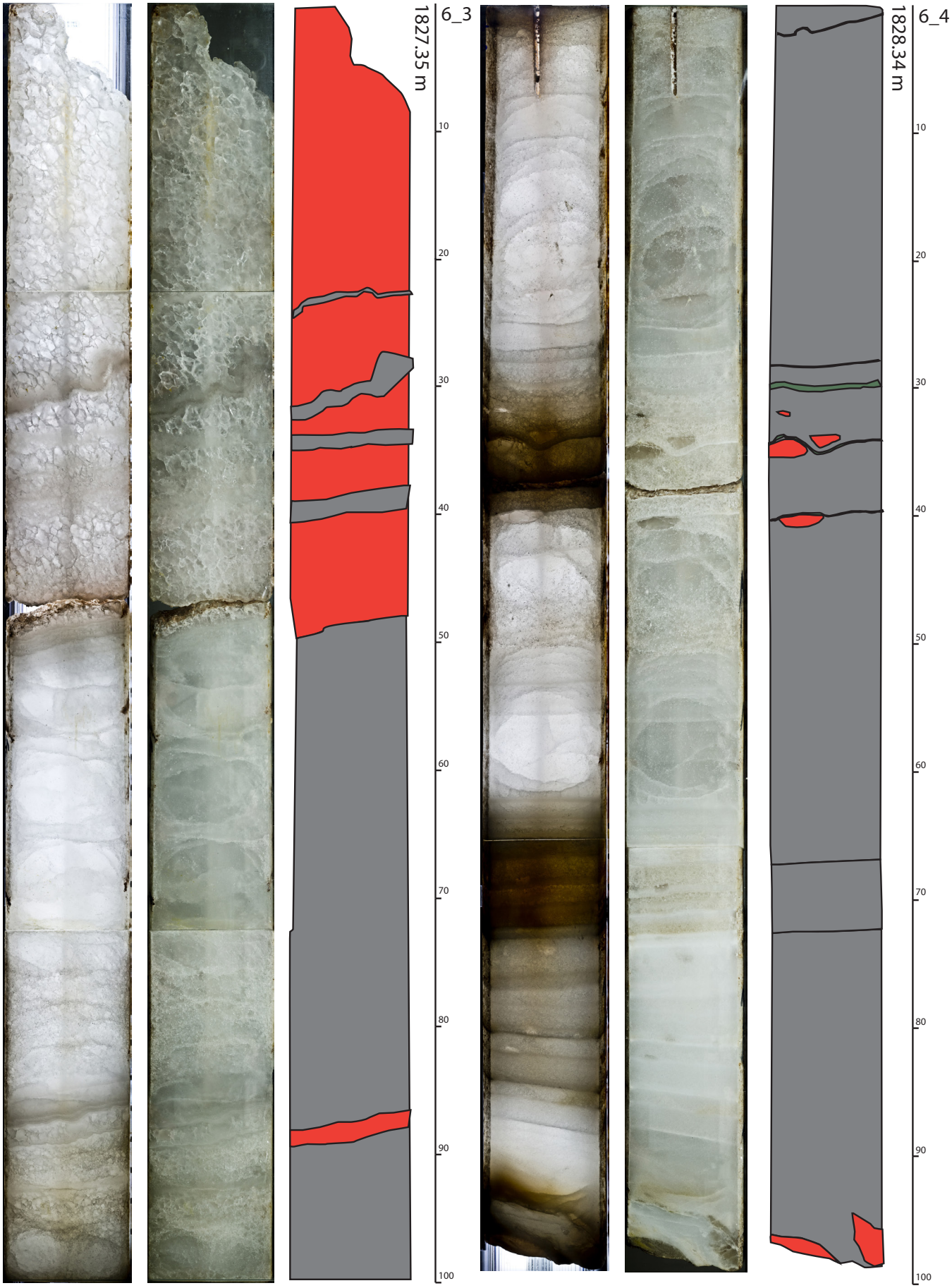

1815.53 m
4_10
1817.53 m
5_1
10
20
30
40
50
60
70
80
90
100

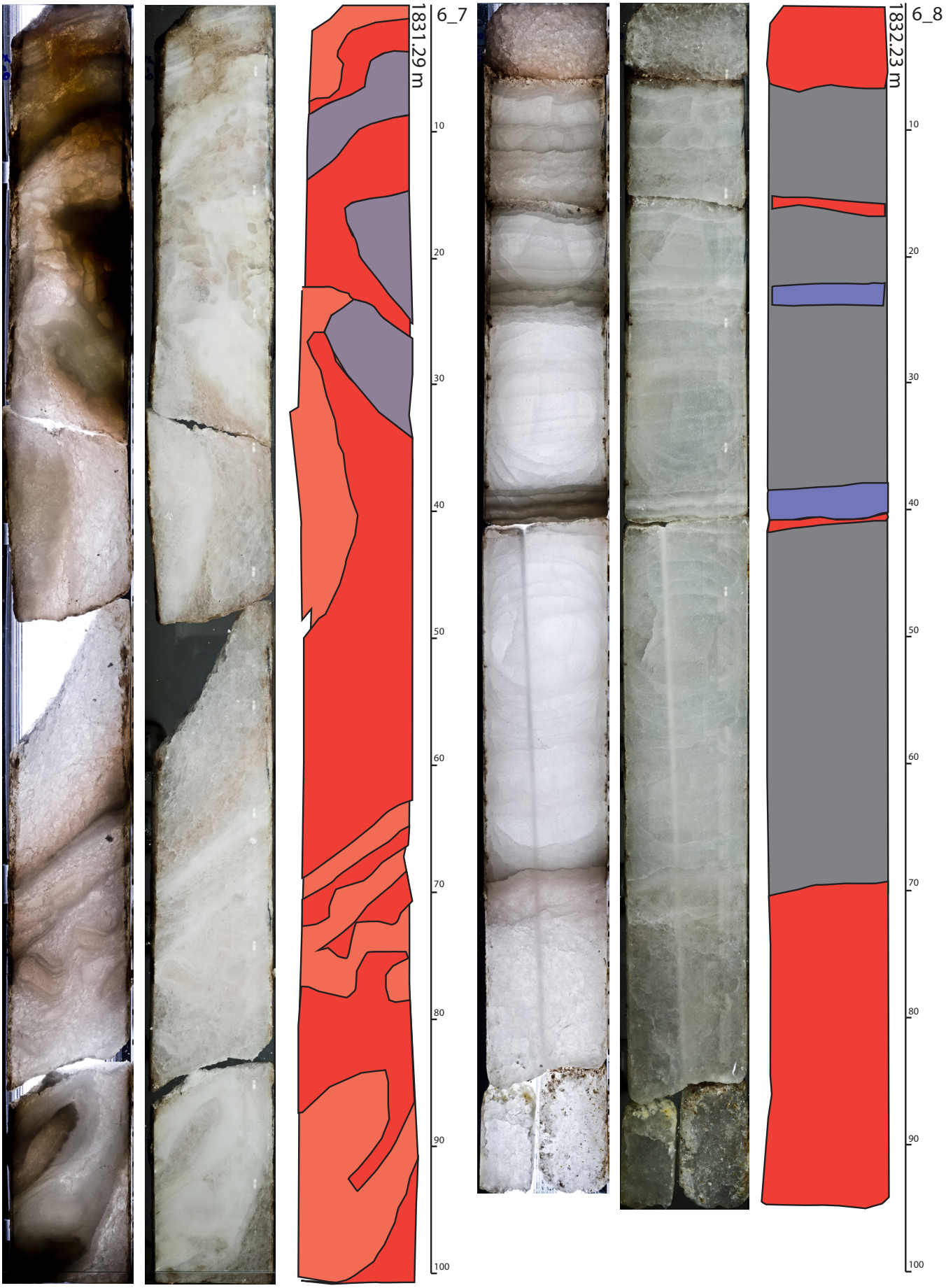

5_2
1817.53 m
5_5
1820.5 m
10
20
30
40
50
60
70
80
90
100

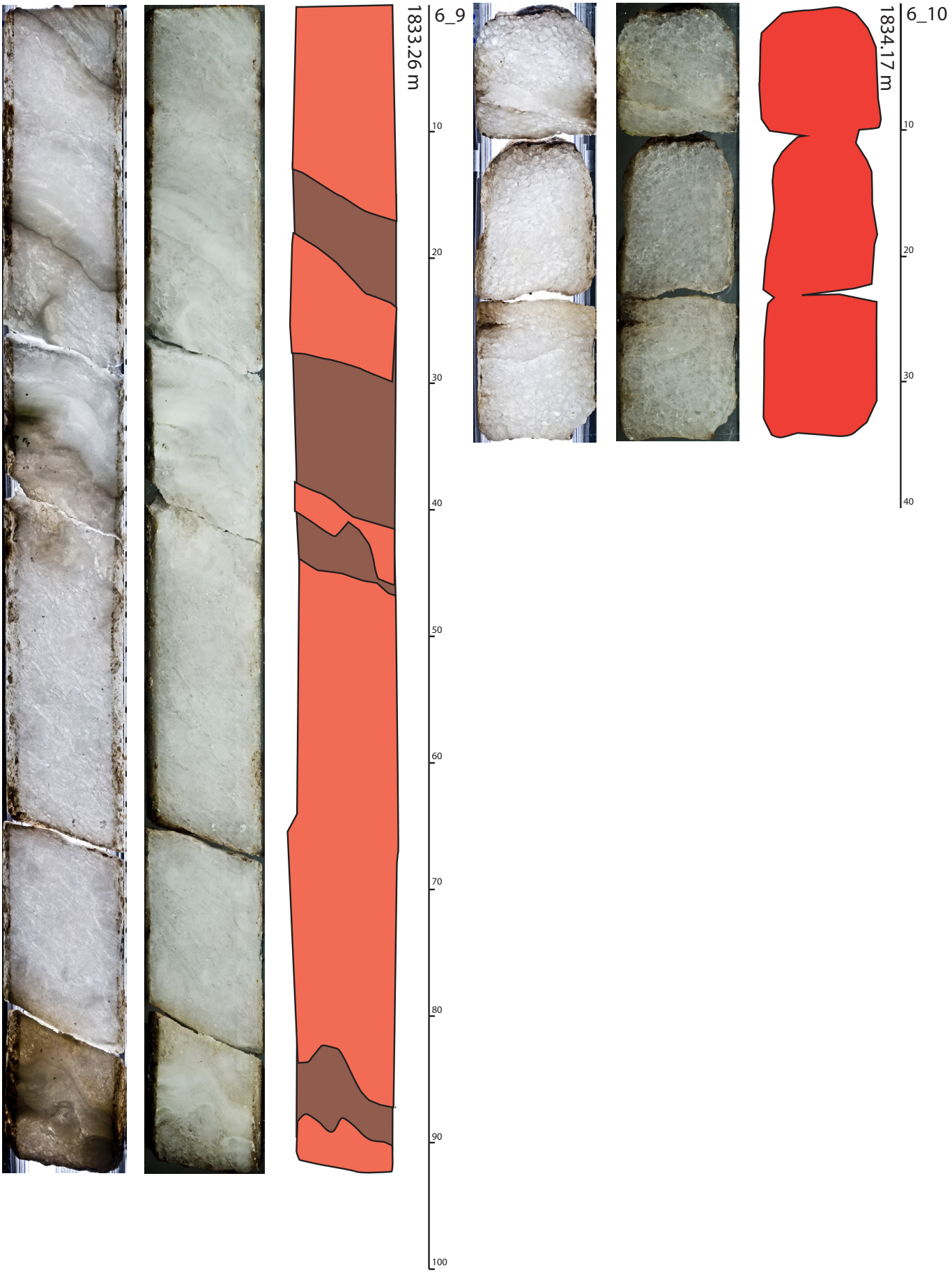

1821.5 m
5_6
10
20
30
40
50
60
70
80
90
100
1822.46 m
5_7
10
20
30
40
50
60
70
80
90
100

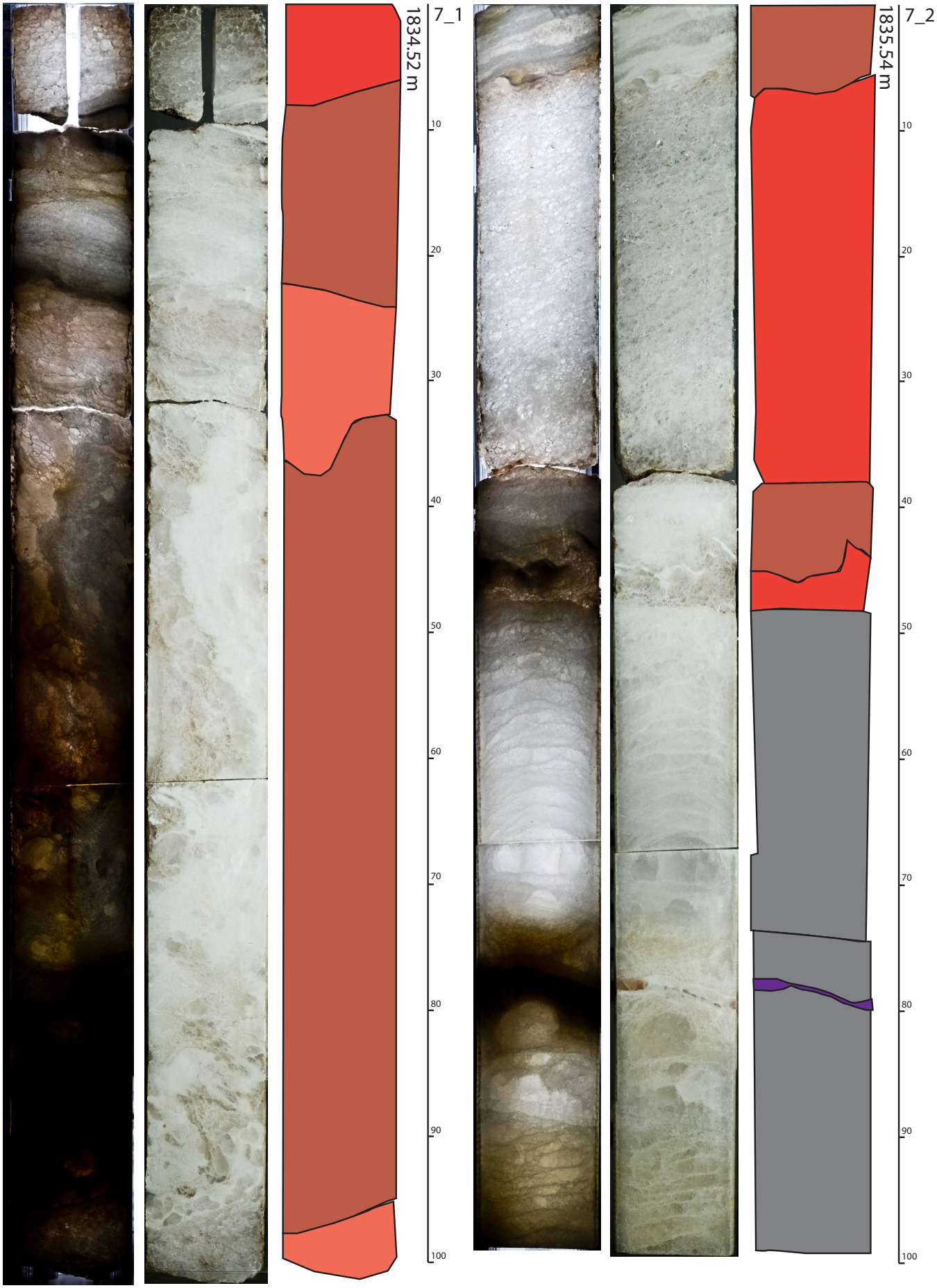

5_8
1823.46 m
10
20
30
40
50
60
70
80
90
100
5_9
1824.43 m
10
20
30
40
50
60
70
80
90
100

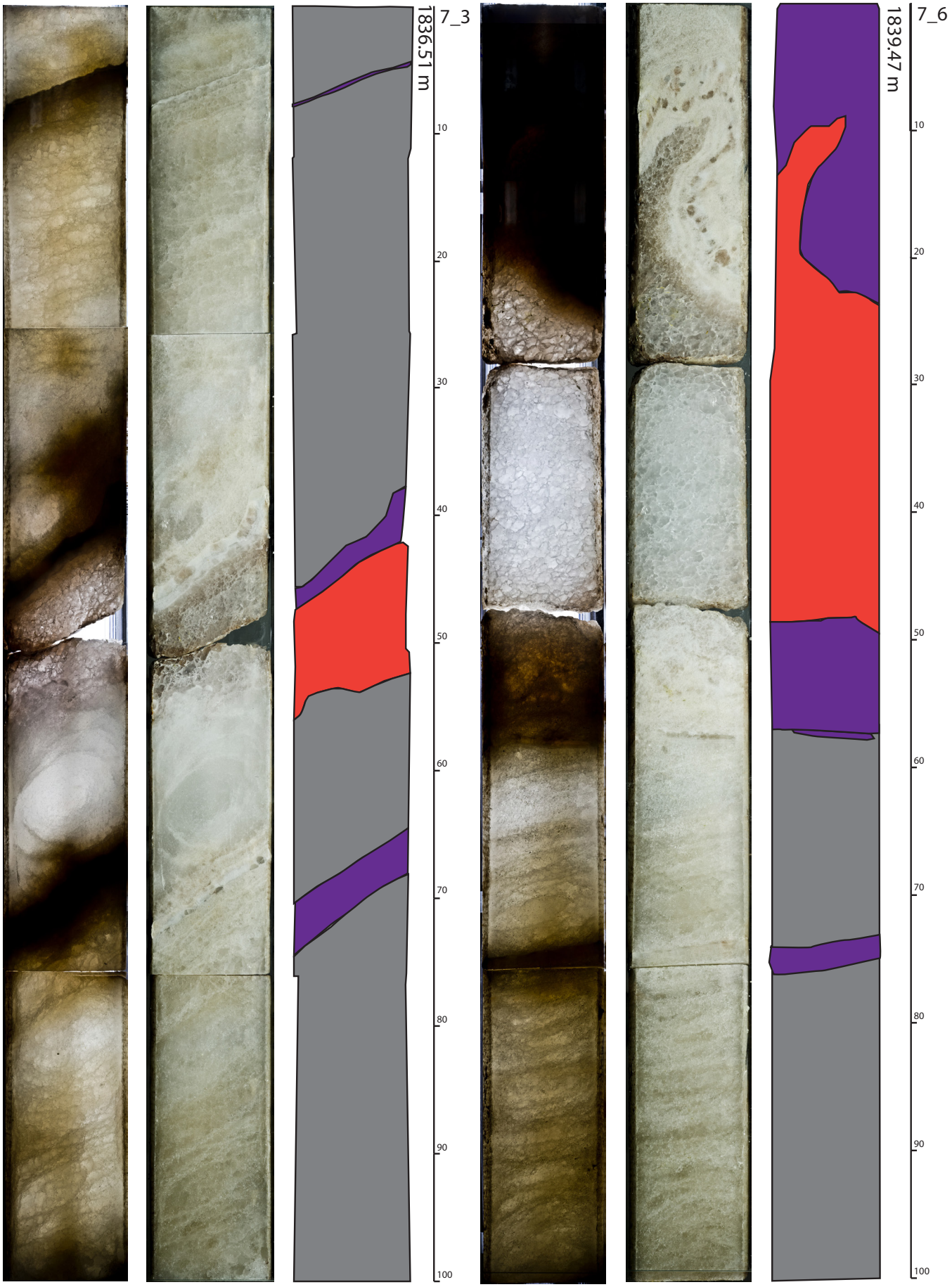

6_1
1825.35 m
6_2
1826.36 m
10
20
30
40
50
60
70
80
90
100


6_3
1827.35 m
6_4
1828.34 m
10
20
30
40
50
60
70
80
90
100


6_7
1831.29 m
6_8
1832.23 m
10
20
30
40
50
60
70
80
90
100


6_9
1833.26 m
10
20
30
40
50
60
70
80
90
100
6_10
1834.17 m
10
20
30
40


7_1
1834.52 m
7_2
1835.54 m
10
20
30
40
50
60
70
80
90
100


7_3
1836.51 m
10
20
30
40
50
60
70
80
90
100
7_6
1839.47 m
10
20
30
40
50
60
70
80
90
100

6. Squeeze mining- induced stress changes in the faulted overburden of the Veendam salt Pillow

This chapter was submitted to be published at the SaltMech IX conference, Sebtember 2018 in Hannover, Germany

6.1 Summary

The aim of this work was to quantify the stress development in the faulted overburden of the Veendam Salt pillow, induced by squeeze mining in a salt cavern field, and to evaluate those changes regarding the mechanical stability of the faulted overburden.

Faults in the overburden were mapped in a 3D seismic dataset, and shown to be normal faults with N-S and NE-SW strikes. None of the faults can be shown to continue to the surface, in agreement with the absence of neotectonic activity in the area.

A Finite Element model was used to calculate the stress changes in the Veendam Salt Pillow and its overburden, caused by squeeze mining. We built a model with radial symmetry, and let it develop a geologically stable in-situ stress field as a starting point for the squeeze mining simulations. Using reasonable values of the input geometry and the material properties, the model was ran until about 60 cm of subsidence in 50 years above a 2.4 km wide cavern field.

In most of the overburden, stress changes correspond to reduction of the shear stress and thus mechanically more stable conditions, in agreement with earlier simulations. In a limited volume of the overburden, shear stresses increase, but this increase is small and the stress path is likely to be far from the Mohr-Coulomb failure criterion for fault reactivation. The calculated stress changes are therefore very unlikely to lead to reactivation of the faults in the overburden.

6.2 Method

The geomechanical modelling approach used in this study is similar to that of Fokker et al., 1995. To simulate the stress changes in the Veendam Salt Pillow and its overburden, caused by squeeze mining of a cavern field, the Finite Element Method (FEM) software 3DS Abaqus was used. Abaqus is widely used for engineering and material science applications and sets a benchmarked industry standard (http://www.3ds.com/).

Results were evaluated considering a Mohr-Coulomb criterion for the brittle overburden. If this criterion is reached in a point where there is a pre-existing fault which is conservatively assumed to be cohesionless and optimally oriented for slip, it is considered to correspond to reactivation of the fault. Existing fault planes were not included into the model since the simulation aims to evaluate if faults could be activated not the plastic movement of the overburden itself. Here we note that a reactivated fault may or may not move seismically. The model was calculated in four steps. In the first stage a geo-

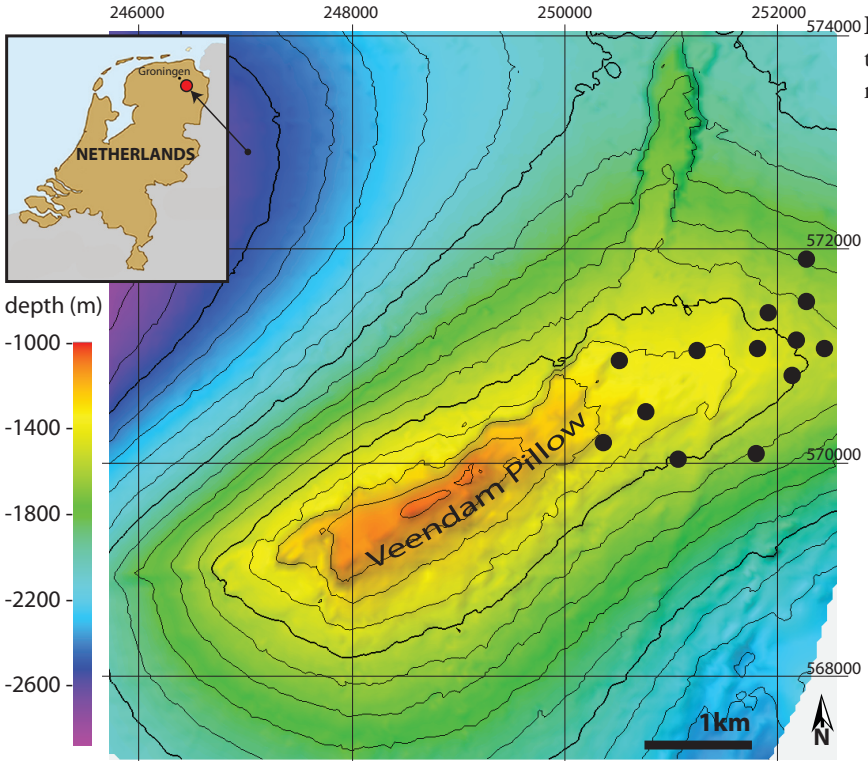


Fig. 6.1: Depth map of top salt at the Veendam Pillow. Black points mark the position of the wells.

static stress is established which is followed by a second 3.15e11 s (10,000 years) long step to let the model equilibrate the stress field in the gravity field. In the third phase the pressure in the cavern field is lowered to finally produce about 50 cm of maximal subsidence. Here we report the stress development during cavern convergence in the third model step. In the fourth step abandonment was simulated by keeping the cavern pressure lithostatic for a long period. These results are not discussed here.

6.3 FE model setup

The Veendam Pillow has an elliptical shape striking NE-SW and an average diameter of about 10 km (Fig. 6.1). It is surrounded by salt withdrawal basins in all directions and other salt structures (i.e. pillows or diapirs) further away (Raith 2016). The Veendam and Tripscompagnie cavern field is located around the crest at the eastern part of the pillow. The 13 wells are distributed within an area with a diameter of 2590 m (Fig. 6.1) inside the Zechstein-III 1b to 3b K-Mg salt layers, with an irregular and not well understood shape.

The calculated model is axisymmetric and centered in the middle of the salt pillow and the cavern field Fig. 6.2. This is a simplification to allow axisymmetric modeling which is computationally much less expensive, while preserving the essential mechanical elements of the system. The salt pillow is 10 km in diameter and is 600 m high. The central pillow is surrounded by a ring of thicker salt, representing the salt highs surrounding the Veendam Pillow. Although, the axisymmetric geometry of the model does not represent the real Veendam geometry in detail, it is adequate to represent a

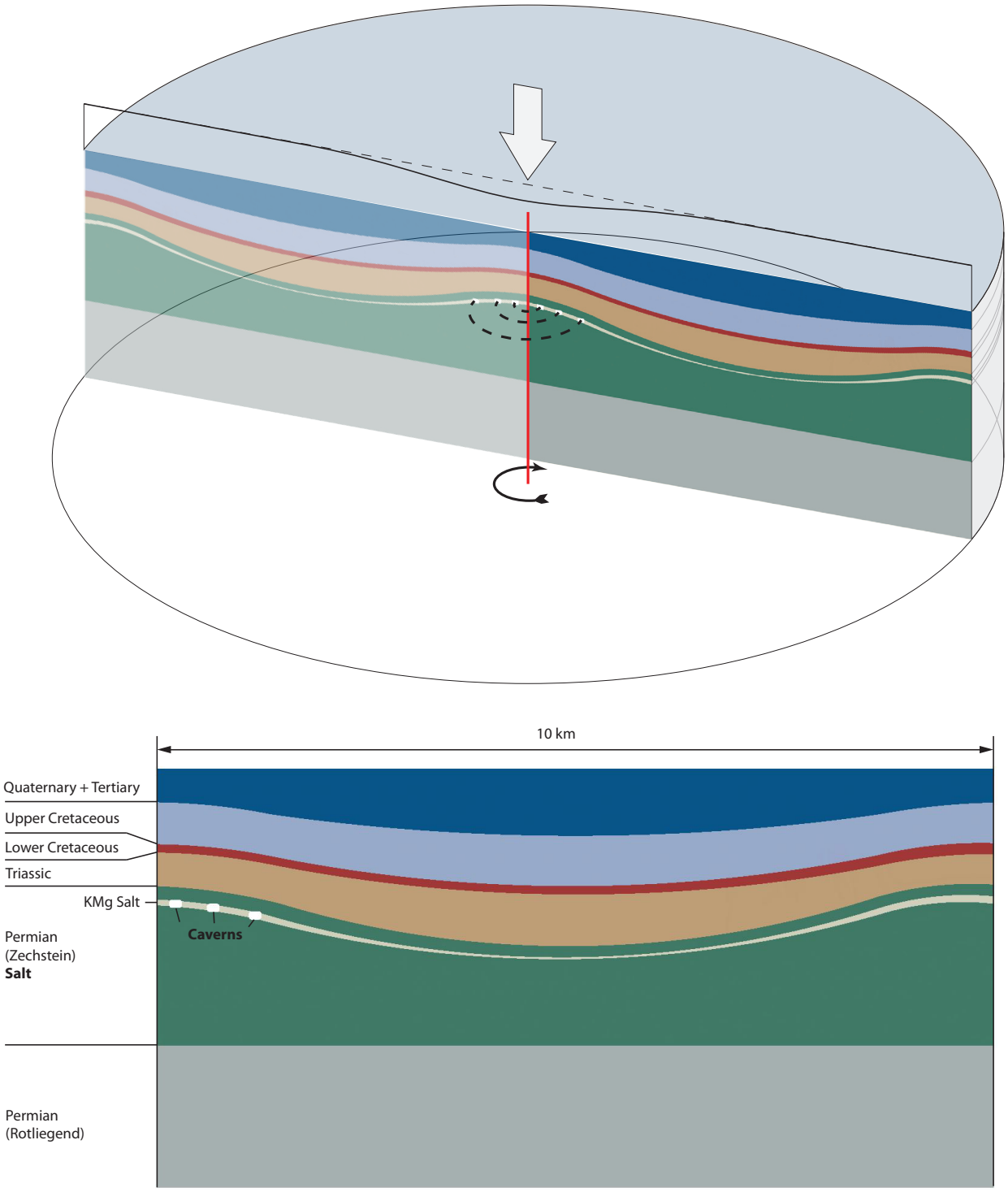


Fig. 6.2: Geometry of the axisymmetric ABAQUS model (red line is the model center). The cavern field is modeled as three rings around the pillow center (dashed black lines). (Horizontal scale equals vertical scale)

circular salt pillow with a cavern field in the crest of the structure. Thus, the stress changes calculated in the model are representative for a setting like the cavern field in the Veendam pillow. The model is meshed with quadrangular 8-node quadratic elements. The element size is kept detailed close to the model axis with sizes of 1 to 5 m and did not exceed 10m in the area above the caverns. Further away from the caverns, the elements reached sizes of about 50m. The solution mining field in this model is represented by three ring-shaped caverns with a radius of 220, 670 and 1170 m around the center. The

rings are each 100 m high and 150 m wide with rounded edges and located in the center of the K-Mg salt layer(Fig. 6.2). With this ring geometry, the deformation around the caverns is distributed over the whole cavern field while local effects of squeeze between caverns can still be resolved. The caverns themselves are not filed with elements. The convergence is modeled by applying pressure to the cavern walls by a fluid of 1300 kg/m³ with an additional wellhead pressure. The top of the models was a free surface, the bottom plate of the model had no degree of freedom while the walls could only move freely in vertical direction.

6.3.1 Layers

To model the mechanical response of the overburden to squeeze mining, the model was subdivided into several units with different rheologies and mechanical properties (Fokker, 1995; Fokker and Visser, 2014) (Fig. 6.2, Table 1). The Rotliegend subsalt layer is assumed flat, overlain by Zechstein salt. Inside the Zechstein halite unit one K-Mg salt layer is present to represent the softer ZIII 1b to 3b layers. The suprasalt sediments are simplified to a Triassic unit overlain by the Lower and Upper Cretaceous and the Tertiary - Quaternary sediments of the Upper North Sea Supergroup. These units are thicker in the basins than above the pillow center. While the rheology of the salt includes elastic and power law creep behavior (Table 1), the overburden is modeled as elastic: since the aim of this study is to clarify if the overburden stresses during elastic deformation can reach the Mohr Coulomb plasticity criterion, there is no need to include plasticity in the overburden. For the same reasons no faults were included into the model. The reactivation of faults with suitable orientation to the stress field would follow the same (cohesionless) Mohr Coulomb plasticity criterion as intact cohesionless layers.

6.3.2 Salt rheology

Under the conditions of squeeze mining, evaporites deform elastically and by creep, without dilatancy (Urai et al., 2008). The plastic deformation of evaporites is described by (power law) dislocation creep and (linear) fluid assisted pressure solution / precipitation (PS) creep. Since squeeze mining leads to a geologically rapid deformation, we decided to use power law creep only (Urai et al., 2008). We infer that including the PS creep, while possible, will not significantly change the conclusions relevant to this report. The rheology of the mixed potassium and magnesium (K-Mg) salts in the 1b layer was chosen to have the same stress exponent as Halite, but about 10 times weaker than rock salt, to simulate a package of Carnallite, Halite and Bischofite (Table 1, van Eekelen et al., 1981; Urai, 1983). Again, this is a strong simplification, but considering that the stress changes in the overburden occur at a distance from the 1b layer which is more than 10x the thickness of typical Bischofite layers, we infer that this will not significantly change the conclusions relevant to this report.

Table 1:

Name	Depth in pillow center [m]	Depth in the basins [m]	Density [Kg/m³]	Young's Modulus [GPa]	Poisson´s Ratio	Creep Multiplier [Pa/s]	Creep Exponent
Quaternary + Tertiary	0 to 400	0 to 800	2000	0.25	0.38	-	-
Upper Cretaceous	400 to 900	800 to 1400	2300	10	0.18	-	-
Lower Cretaceous	900 to 1000	1400 to 1500	2350	15	0.23	-	-
Triassic	1000 to 1400	1500 to 2100	2450	10	0.3	-	-
Halite	1400 to 3300	2100 to 3300	2040	30	0.25	1.00E-44	5
K-Mg salt	1560 to 1630	2230 2260	2040	30	0.25	1.00E-43	5
Rotliegend	3300 to 5000	3300 to 5000	2600	15	0.18	-	-

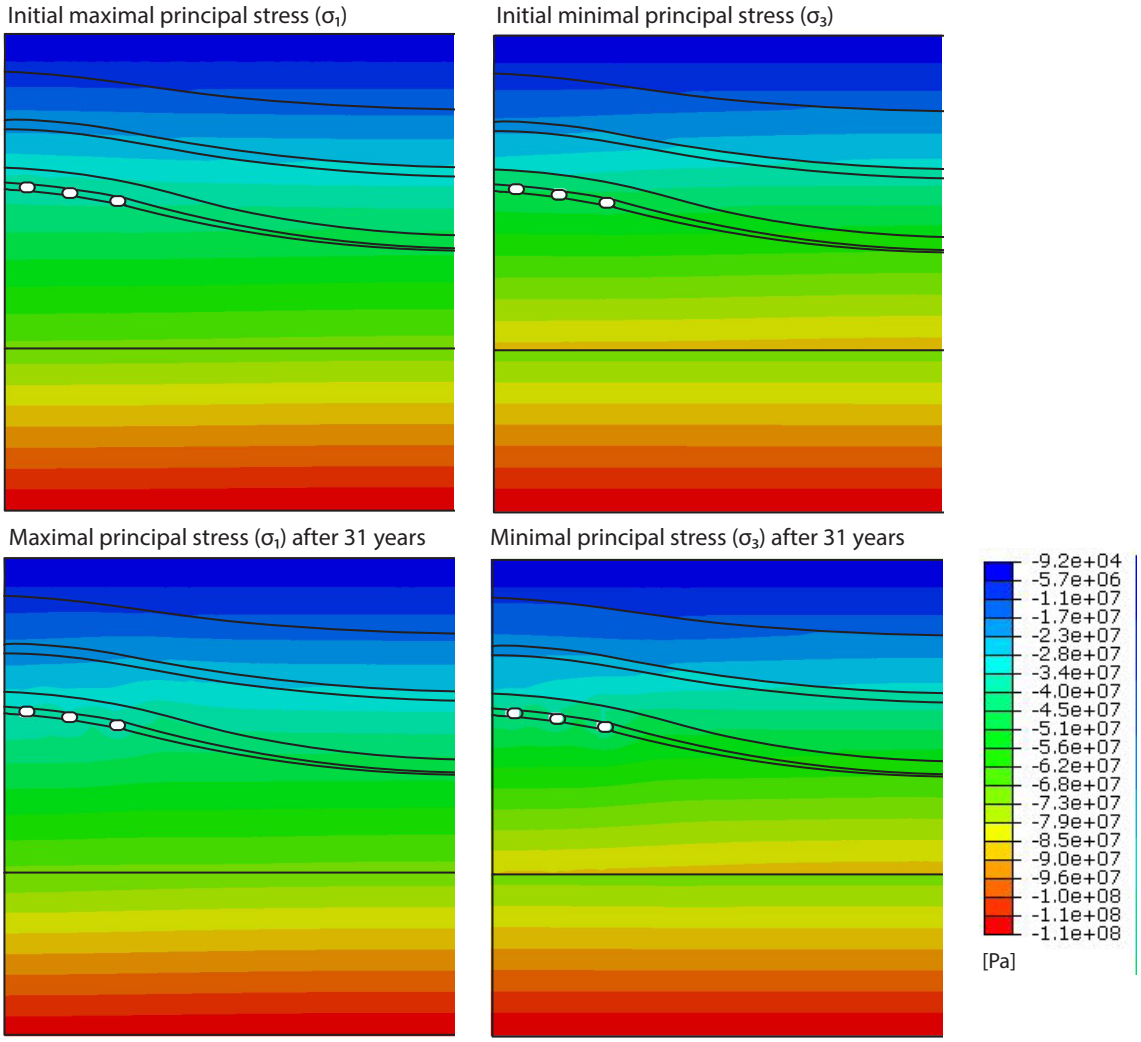


Fig. 6.3: Maximum and minimum principle stress in the model, above: initial geologically stable situation, below: after 52 cm subsidence in 31 years. Please note that the ABAQUS package uses tension as positive and in subsurface studies compression is taken as positive giving the slightly confusing color bar legend.

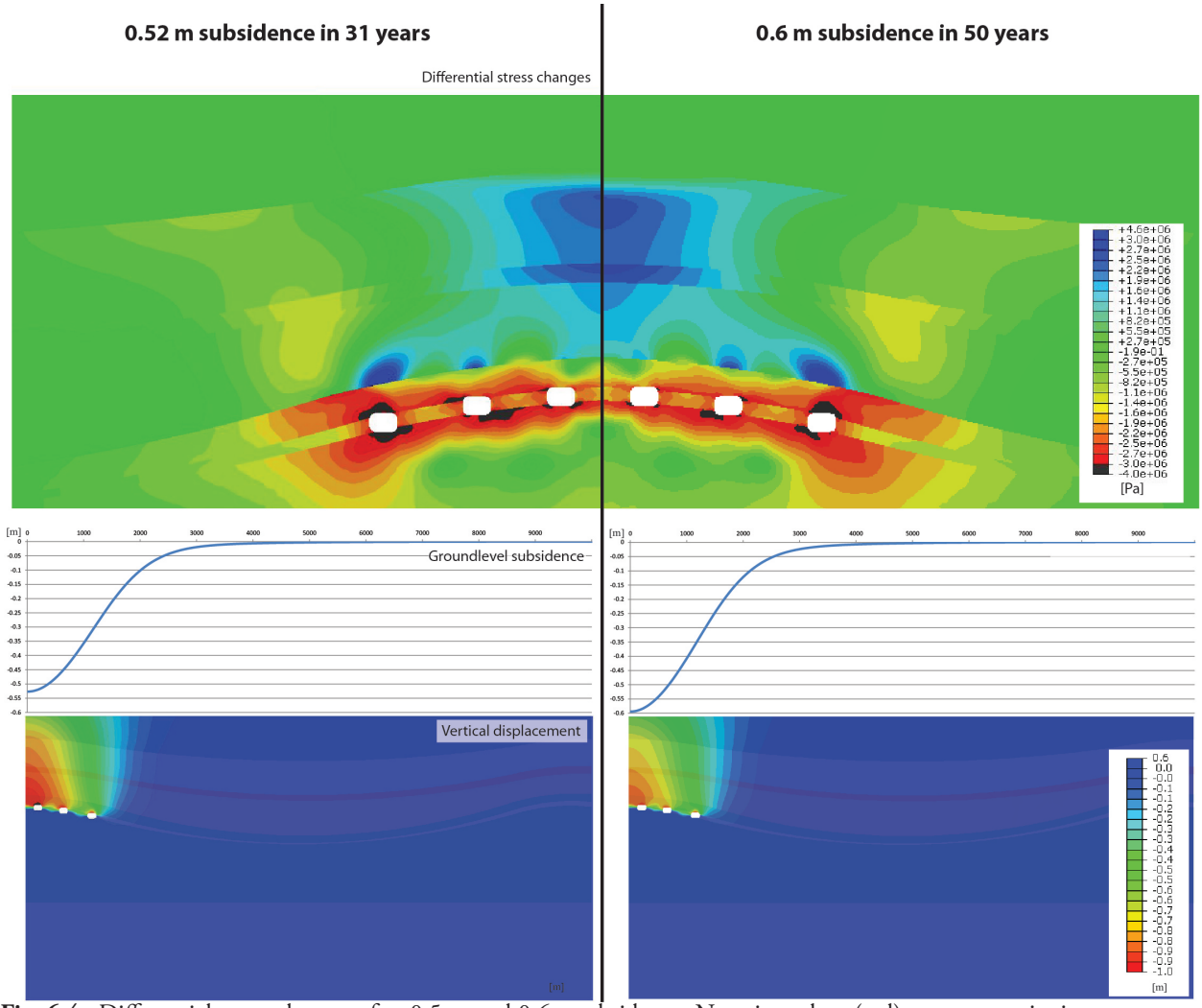


Fig. 6.4: Differential stress changes after 0.5m and 0.6m subsidence. Negative values (red) represent a rise in stress, while positive values (blue) represent a stress drop.

6.4 Model Results

6.4.1 Initial stress

Stresses in the models were computed as total stresses, assuming drained hydrostatic pore pressure everywhere. For stability analyses, effective stresses were computed, using hydrostatic pore pressure. Fig. 6.3 shows the trend of the minimum and maximum principle stresses in the model. Note that the stress contours in the starting model are not horizontal as commonly assumed, due to the stress redistribution required for a geologically stable situation above the Veendam pillow.

Here we note that in general the present day in-situ stress state in the Northern Netherlands is not well known in the absence of measurements. This causes a significant uncertainty in subsurface integrity analyses which compute the changes in stress, starting from the initial stress. In this study (in contrast to other studies, we aimed to establish an initial stress state which is geologically stable, as a first step towards addressing this issue.

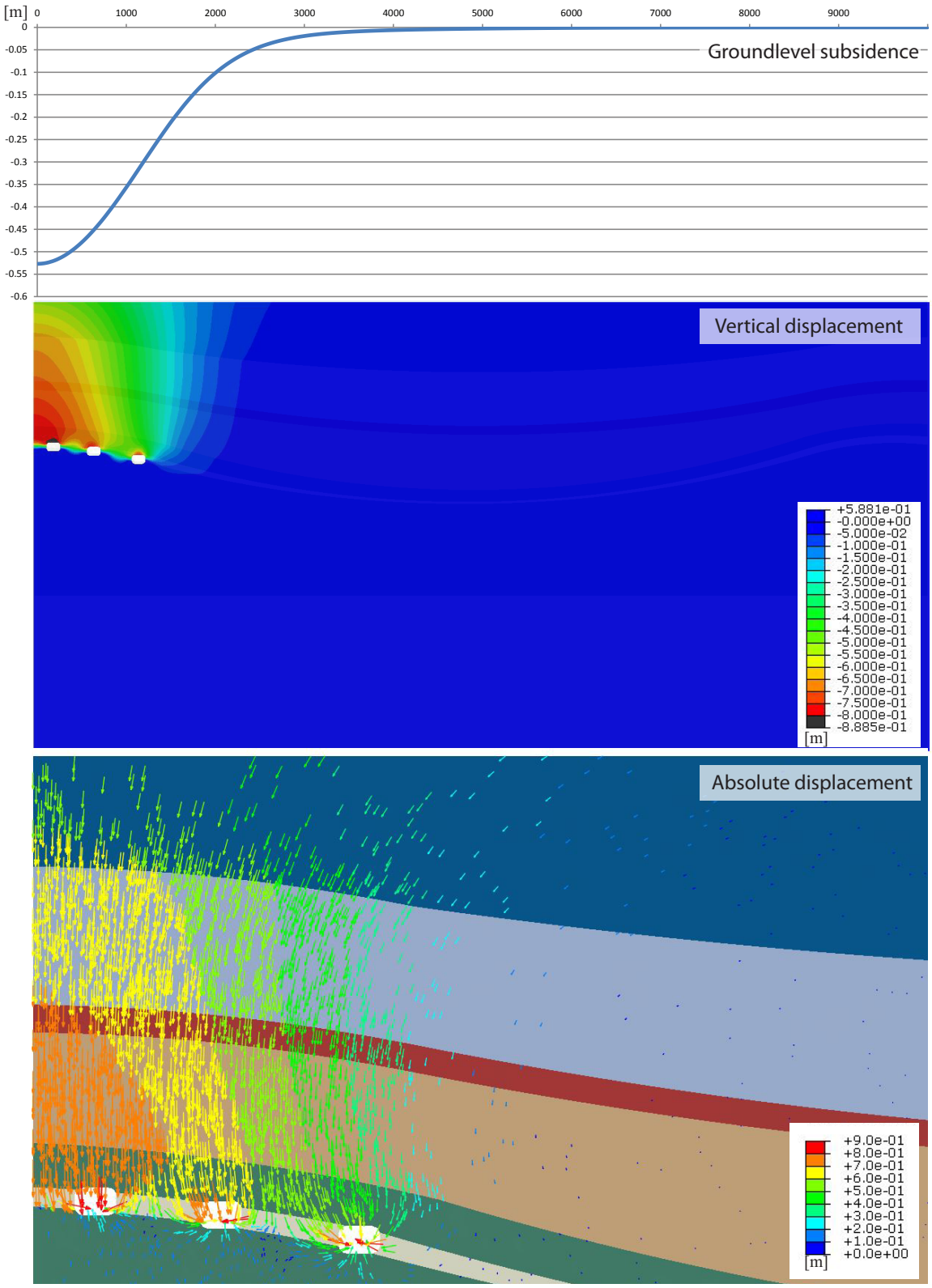


Fig. 6.5: Displacements in the model after 1e9s (50 cm subsidence in 31 years).

6.4.2 Subsidence

We computed two sets of models (Fig. 6.4): The first one (A) was computed to reach 52 cm subsidence (in the center of the subsidence bowl) in 31 years, and another (B) 60 cm subsidence in 50 years. The subsidence bowl geometry closely resembles the results by Fokker and Visser (2014). The

displacement is dominantly vertical with small horizontal components (Fig. 6.4). In the layers above the Triassic, the zone of vertical motion gets wider, as expected and therefore a horizontal component of movement towards the center of the cavern field is also significant. Inside the Triassic, minor local horizontal stretching in the areas between the caverns can be observed.

6.4.3 Stress development

Stress changes above the cavern field show the development of two different zones (Fig. 6.6,Fig. 6.7 and Fig. 6.8). Zone I is located directly above the caverns, while zone II is about 300 to 1000 m away from the caverns.

Zone I:

This zone is characterized by a drop of differential stress by up to 4.6 MPa. In the Triassic, above the caverns the decrease of differential stress ($\sigma1$ - $\sigma3$) is mostly caused by a reduction of the subvertical $\sigma1$ principle stress (please note that the ABAQUS package uses tension as positive and in subsurface studies compression is taken as positive giving the slightly confusing color bar legend). The sub-horizontal $\sigma3$ is also lowered in this area with smallest values in the area between caverns. Inside the Cretaceous, lower differential stress is mainly caused by an increase of the horizontal $\sigma3$.

Zone II:

In this zone increased differential stress values of up to 1 MPa can be observed. The increase is caused by a rise of vertical $\sigma1$ stress in that area.

6.5 Faults in the overburden

Faults in the overburden were interpreted in the 3D seismic cube used in Raith et al., (2016), as part of a study of the risk of fault reactivation in the overburden of the Veendam Pillow. While the quality of the 3D seismic is reasonable, only the general pattern of the faults could be mapped, keeping in mind the well-known problems and limitations of fault interpretations. Results are illustrated below.

In the overburden of the Veendam Pillow two dominant fault directions are present: NE-SW striking normal faults parallel to the crest and N-S striking normal faults in NE and SW of the Veendam Pillow (Fig. 8). About 60 faults were mapped in the seismic images. They are up to 800m long with throw up to 150m, dipping 35-55°. The length of the faults in strike direction is about 1.5- 2 times longer than in dip direction (Fig. 6.10).

The faults are well visible in the Cretaceous and at the top Triassic reflections. Inside the Triassic, the image rarely is good enough to allow accurate interpretation of the individual faults. None of the faults can be shown to continue to the surface, in agreement with the absence of neotectonic activity in the area (Fig. 6.9).

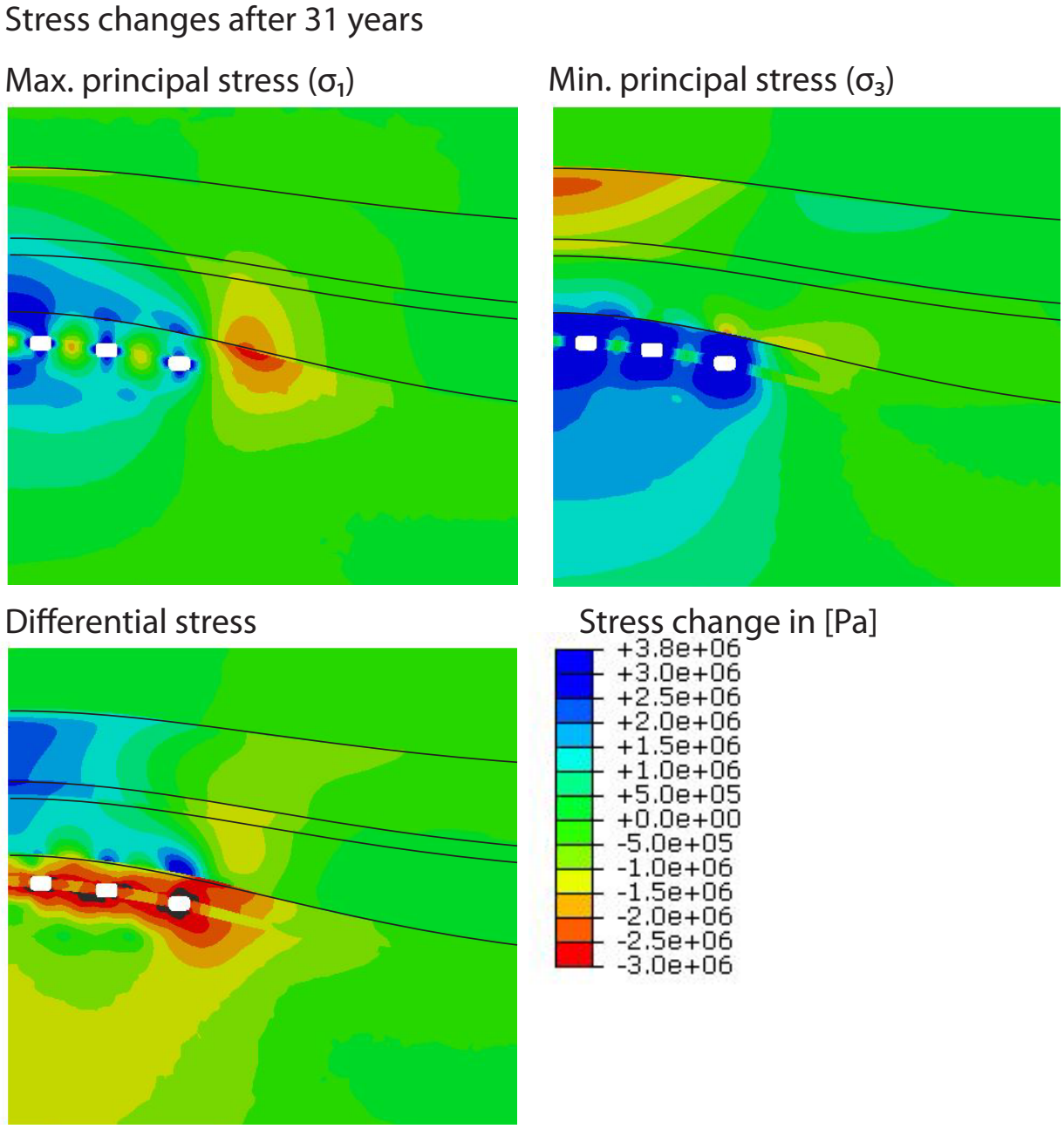


Fig. 6.6: Development of maximum principle stress, minimum principle stress and differential stress during squeeze mining. Negative values (red) represent a rise in stress, while positive values (blue) represent a stress drop.

Besides the smaller faults, two larger NE-SW striking faults parallel to the pillow's crest are present. These large faults extend from the Tertiary down to the Permian Top Salt over 1.1 km vertically with a maximal offset of about 300 m. They are up to 6 km long in strike direction. The offset of this fault is less than 150 m in the area above the caverns and is not present near the Tripscompagnie field. In the area above the active caverns, only smaller NE-SW striking faults parallel to the crest are present.

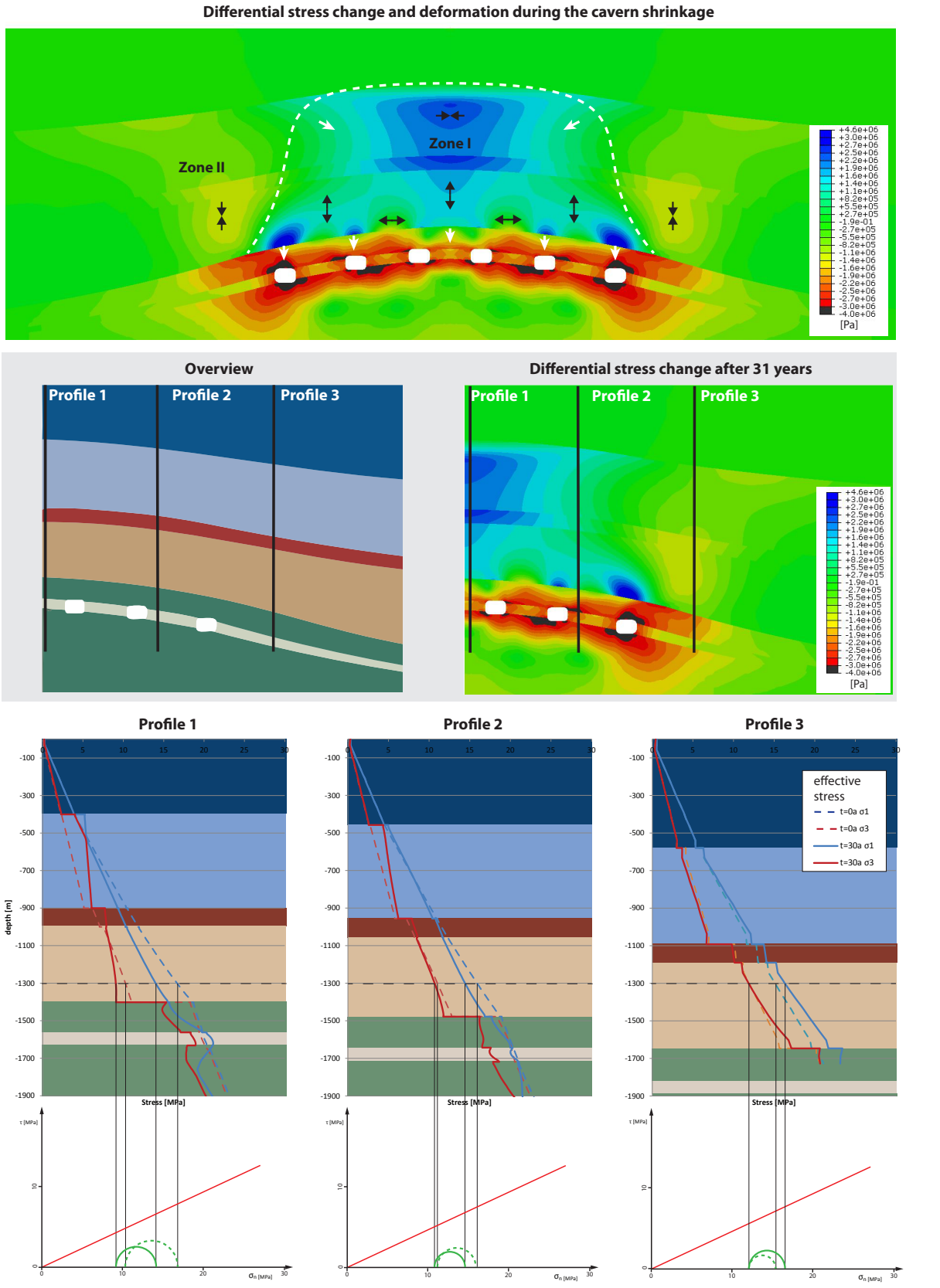


Fig. 6.7: Model A: 51 cm subsidence in 31 years. Stress development in the overburden divided into 2 zones. The arrows indicate the relevant principle strains. (Bottom) Stress development demonstrated at three vertical stress profiles showing minimum and maximum principal stress before and after 1e9 s. The MC plots show a conservative cohesionless plasticity criterion with a 25° friction angle at 1300 m depth.

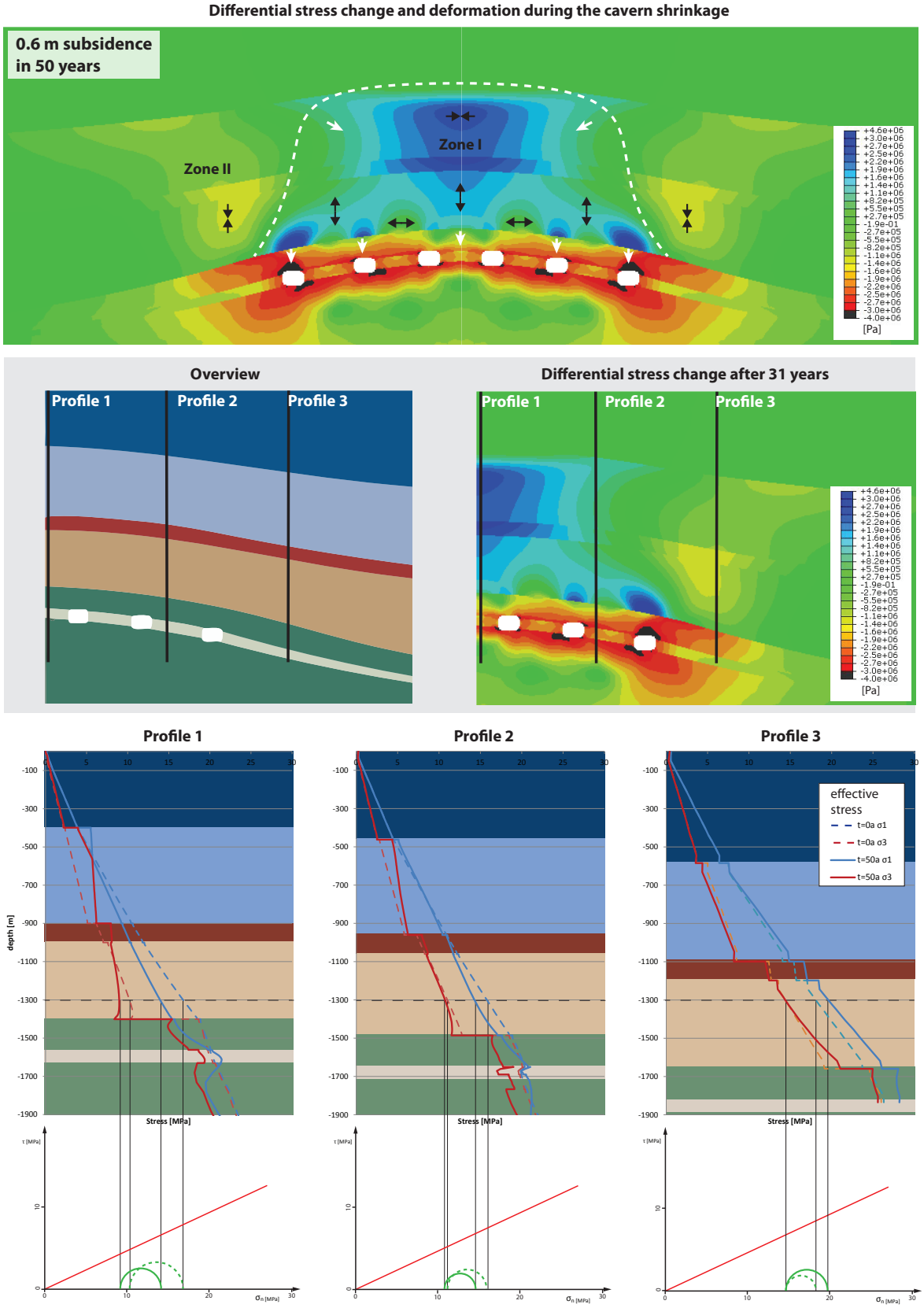


Fig. 6.8: Model B: 60 cm subsidence in 50 years. Stress development in the overburden divided into 2 zones. The arrows indicate the relevant principle strains. (Bottom) Stress development demonstrated at three vertical stress profiles showing minimum and maximum principal stress before and after 1e9 s. The MC plots show a conservative cohesionless plasticity criterion with a 25° friction angle at 1300 m depth.

6.6 Discussion

The models presented here are a subset of many different models, which can be used to match the observed subsidence and production over time. In our models, no history match with pressure data and squeeze volumes was attempted, and our ring-shaped caverns are a simplification compared with the details of the complex connected cavern network in the subsurface, in shape and volume. On the other hand, for a more representative model the details of the geomety of the cavern network would be required. In comparison with the models of Fokker et al., 1995, we have used a more complicated cavern model, and attempted to compute a more realistic initial stress distribution in the Veendam Pillow. The initial stresses are stable over geologic time, without plasticity in the overburden, consistent with the absence of neotectonics. Based on our results, we infer (because the models match the subsidence and because the overburden is elastic), that different realizations of this model would produce similar

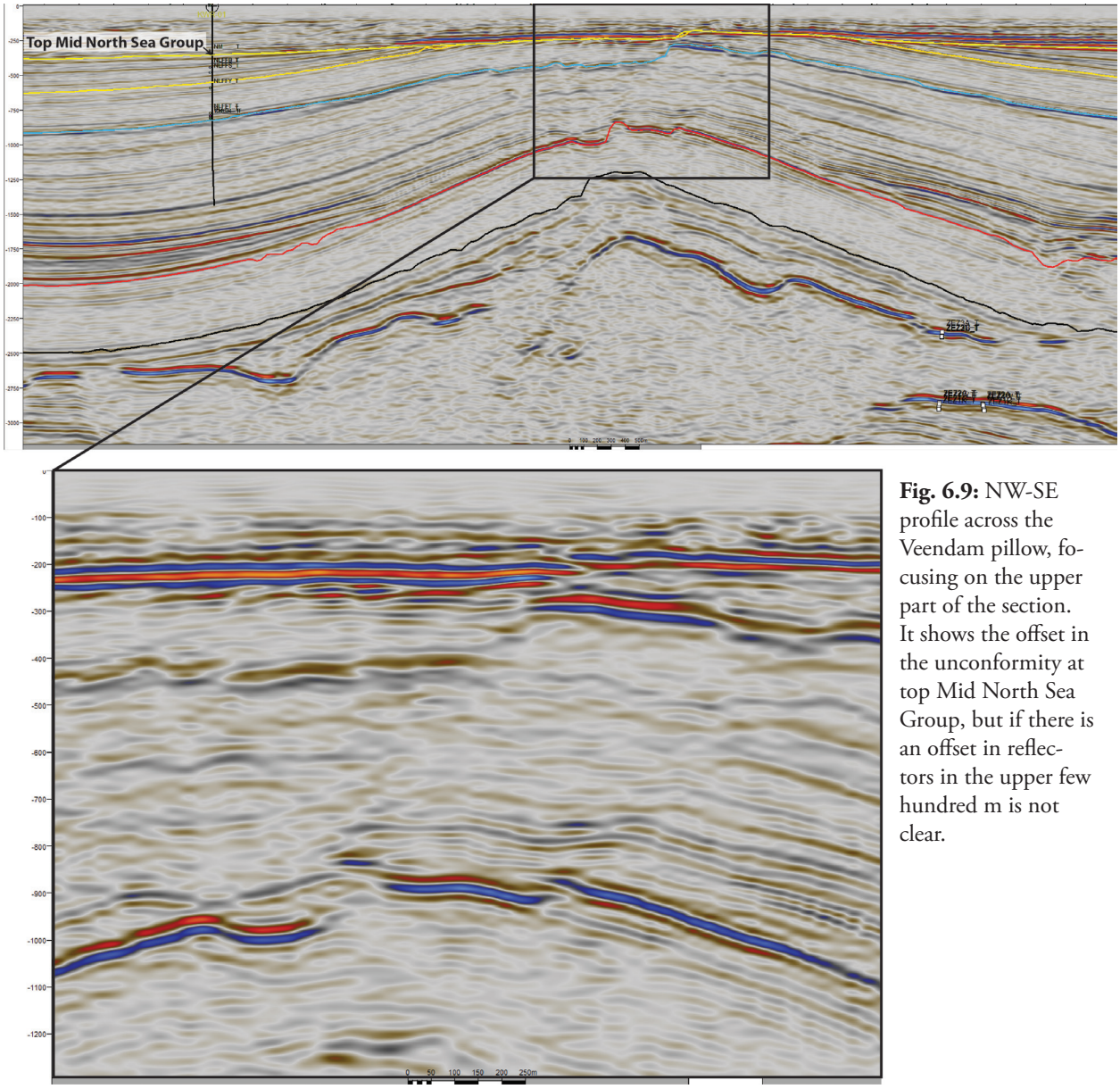


Fig. 6.9: NW-SE profile across the Veendam pillow, focusing on the upper part of the section. It shows the offset in the unconformity at top Mid North Sea Group, but if there is an offset in reflectors in the upper few hundred m is not clear.

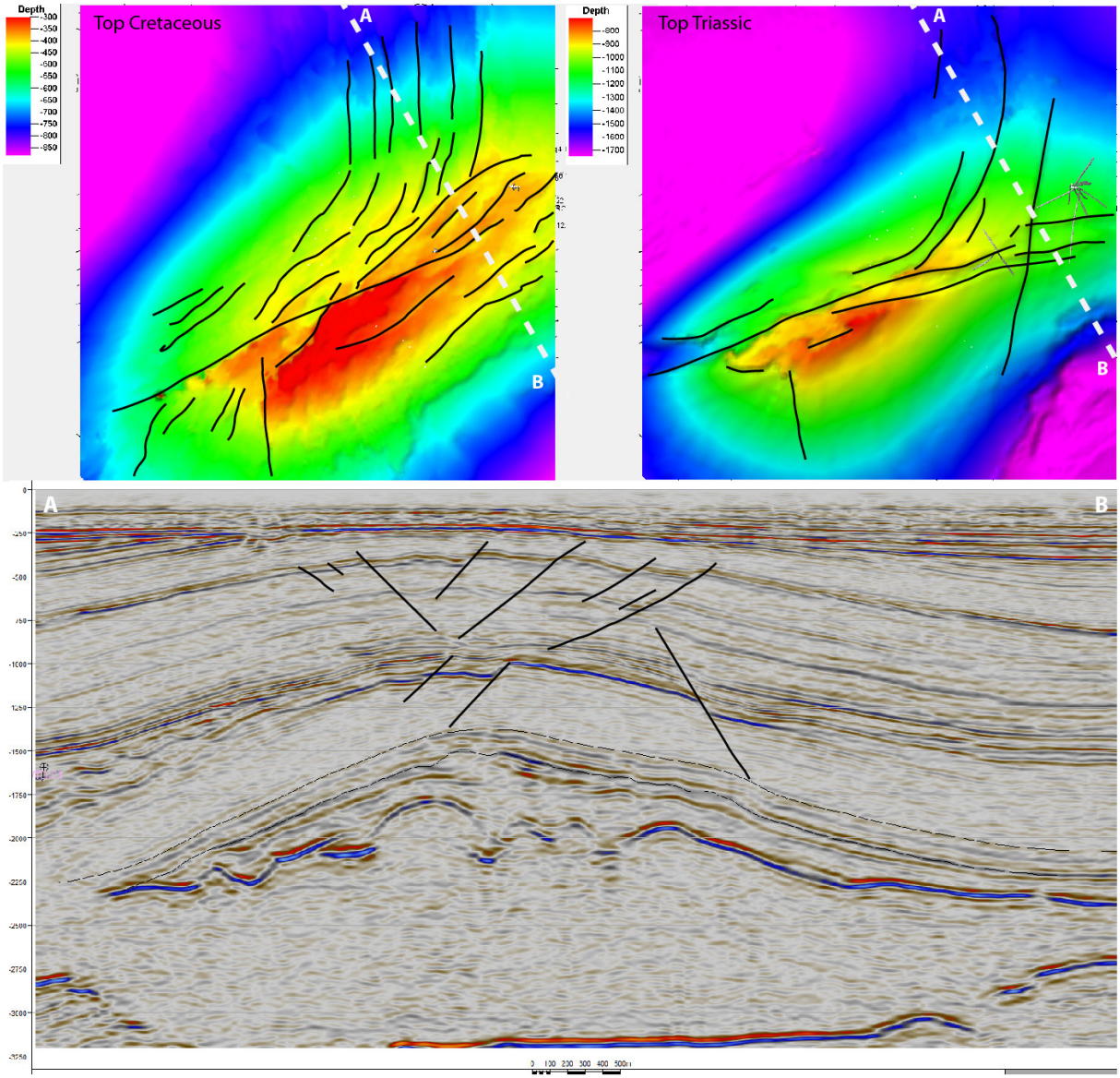


Fig. 6.10: Top: Top Cretaceous and Top Triassic depth maps with faults indicated with black lines. Bottom: Profile A-B (vertical = horizontal scale) showing normal faults above the cavern field.

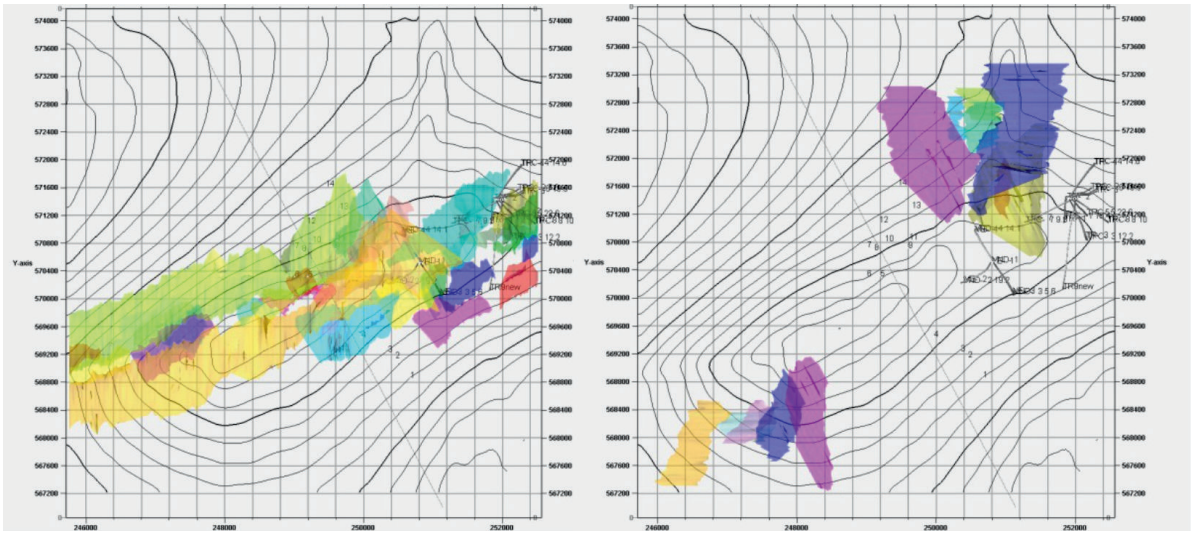


Fig. 6.11: Map view of N-S (left figure) and NE-SW (right figure) striking faults in the overburden. Each interpreted fault plane is shown by a different colour. Note that the 3D nature of these fault planes prevents better visualization in these images. The VE and TR wells are also shown. Depth of top salt is indicated by the black contour lines.

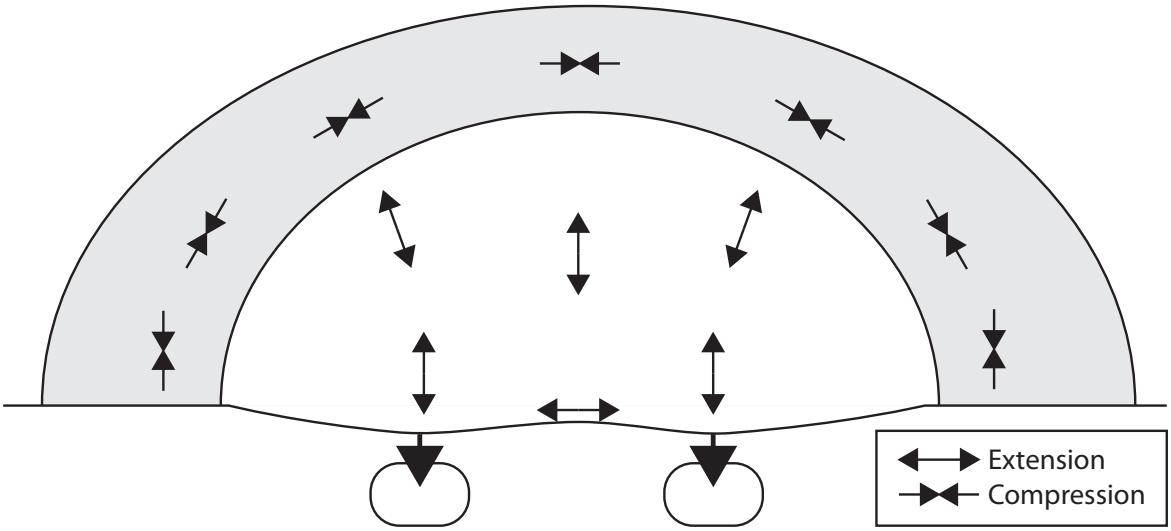


Fig. 6.12: Simplified sketch, showing direction of relevant principle strains in the overburden.

overburden stress changes.

Considering the deformations in the overburden, in zone I it can be clearly seen that the downward movement of Top Salt above the converging cavern field leads to a decrease of vertical stresses above this area. If the caverns are close to each other the effects overlap, forming one area of decreased differential stress above them. In the shallower Cretaceous on the other hand lower differential stresses are primarily caused by horizontal shortening and therefore higher horizontal stresses. Inside zone I small increases in differential stress can only be observed directly above cavern gaps. Here horizontal stretching due to salt flow towards the caverns decreases the horizontal stress.

The subsidence above the caverns associated by a decrease in vertical stress has to be compensated outside of zone I in zone II. Here the adjacent subsidence leads to an increased vertical $\sigma 1$ resulting in slightly higher differential stresses.

In summary, cavern convergence causes vertical extension in the area above the caverns that is compensated by compression in an arc around this area (Fig. 6.11).

If we consider a Mohr Coulomb yield criterion, the stress changes in zone I produces a more stable situation than in the initial state. The stress changes in zone II on the other hand could move slightly closer to the yield criteria (shown in figure 5 by a cohesion-less 25° MC criteria for comparison). However, since these stress changes are very small, zone II can also be considered to remain stable considering that initially the area was tectonically quiet.

6.7 Conclusion

The calculated stress development shows that cavern field convergence does not change the in-situ stress to values required for fault reactivation. Therefore, no fault reactivation in the suprasalt units at the Veendam Pillow is expected. The squeeze in the salt leads to a drop of vertical stress above the caverns. Lower vertical stress leads to smaller differential stress values and therefore to more stable conditions. Further away from the caverns a slight increase of differential stress could be observed in the super salt units. However, the magnitude of this unfavorable stress development is too small to induce plastic deformation.

6.8 References

Fokker, P.A., (1995). The behaviour of salt and salt caverns. Dissertation, Delft University of Technology.

Fokker, P.A., Visser, J., (2014). Estimating the distribution of salt cavern squeeze using subsidence measurements, in: 48 Th US Rock Mechanics / Geomechanics Symposium. American Rock Mechanics Association, Minneapolis, p. ARMA 14 – 7357.

Fokker, P.A., Urai, J.L. and Steeneken, P.V. (1995). Production-induced convergence of solution mined caverens in magnesium salts and associated subsidence. In: Barends, Brouwer and Schröder (eds): Land subsidence. Natural causes, measuring techniques, the Groningen gas field. Proceedings of the fifth international conference on land subsidence, Den Haag, the Netherlands, 16-20 Oct. 1995, p. 281-289.

Raith, AF F Strozyk, J Visser, JL Urai (2016) Evolution of rheologically heterogeneous salt structures: a case study from the NE Netherlands. Solid Earth 7 (1), 67

Schléder, Z., Urai, J.L., (2005). Microstructural evolution of deformation-modified primary halite from the Middle Triassic Röt Formation at Hengelo, The Netherlands. Int. J. Earth Sci. 94, 941–955. doi:10.1007/s00531-005-0503-2

Urai, J.L., (1983). Water assisted dynamic recrystallization and weakening in polycrystalline bischofite. Tectonophysics 96, 125–157. doi:10.1016/0040-1951(83)90247-0

Urai, J.L., Schléder, Z., Spiers, C.J., Kukla, P.A., (2008). Flow and Transport Properties of Salt Rocks, in: Dynamics of Complex Intracontinental Basins: The Central European Basin System. pp. 277–290. doi:978-3-540-85085-4

van Eekelen, H.A., Urai, J.L., Hulsebos, T., (1981). Creep of Bischofite, in: Proceedings, 1st Conference on the Mechanical Behaviour of Salt. Pennsylvania.

7. Finite element modeling of the deformation of ZIII-AC and ZIII K-Mg salts layers during pillow development

7.1 Summary

Simplified 2D plain strain models containing the key components of the Veendam Pillow were performed to analyze the influence and behavior of hard and soft layers on the internal deformation. The results show that the pre-fractured stringer is folded and thrusted in the pillow center during the development of the pillow. Depending on the viscosity of the stringer, the shortening is either compensated by folding or thrusting. We supposed that the stress exponent of halite and stringer deformation are most likely not the same and we could therefore expect a strain dependency of the effective viscosity contrast. Under this conditions, strong strain-rate changes during the pillow evolution could produce different dominant wavelengths. Fold analysis can therefore be used to estimate the in situ rheology of stringers or if the in situ rheology of anhydrite and salt is well known, might be used to estimate the in situ strain rates. We concluded from the models that the folding of the ZIII-AC observed in the Veendam pillow indicates an effective velocity contrast of about 100 between the stringer and the halite in most places. Nevertheless, a much larger wavelength folding could have been produced by early slow deformation forming the large syncline in the NW of the Veendam Pillow. Both soft K-Mg salt layers and strong stringers influence the deformation and salt flow inside the salt pillow. Strain is accumulated in the soft layers leading to stronger salt flow near these layers and extensive deformation inside of them. Thus, if a soft layer is present near a stringer, it will experience more deformation. On the other hand, the structure of the soft K-Mg salt layers and the salt flow inside of them is strongly influenced by nearby folding of a harder stringer. As a result, the soft K-Mg salts are withdrawn from areas above stringer anticlines to areas above stringer synclines.

7.2 Introduction

The seismic interpretation of the Veendam Salt pillow revealed a number of interesting structures (Raith et al. 2016) (chapter 2). It could be observed that the ZIII-AC stringer has a complex fracture pattern, lays parallel to top salt underneath the salt withdrawal basins and is strongly folded in the center of the pillow. This structure was interpreted to be the result of an early (Triassic) extension, generating fractures in the stringer, followed by later compression leading to salt flow into the pillow and simultaneously folding of the stringer. Furthermore, thickening of the soft K-Mg salt rich ZIII-1b layer above stringer synclines could be observed. The detailed analysis of a core cutting through the ZIII-1b revealed additional information (chapter 5). The internal structure of this layer resembles a tectonic mélange of intense recumbent folding, fracturing and shearing. The structure was interpreted

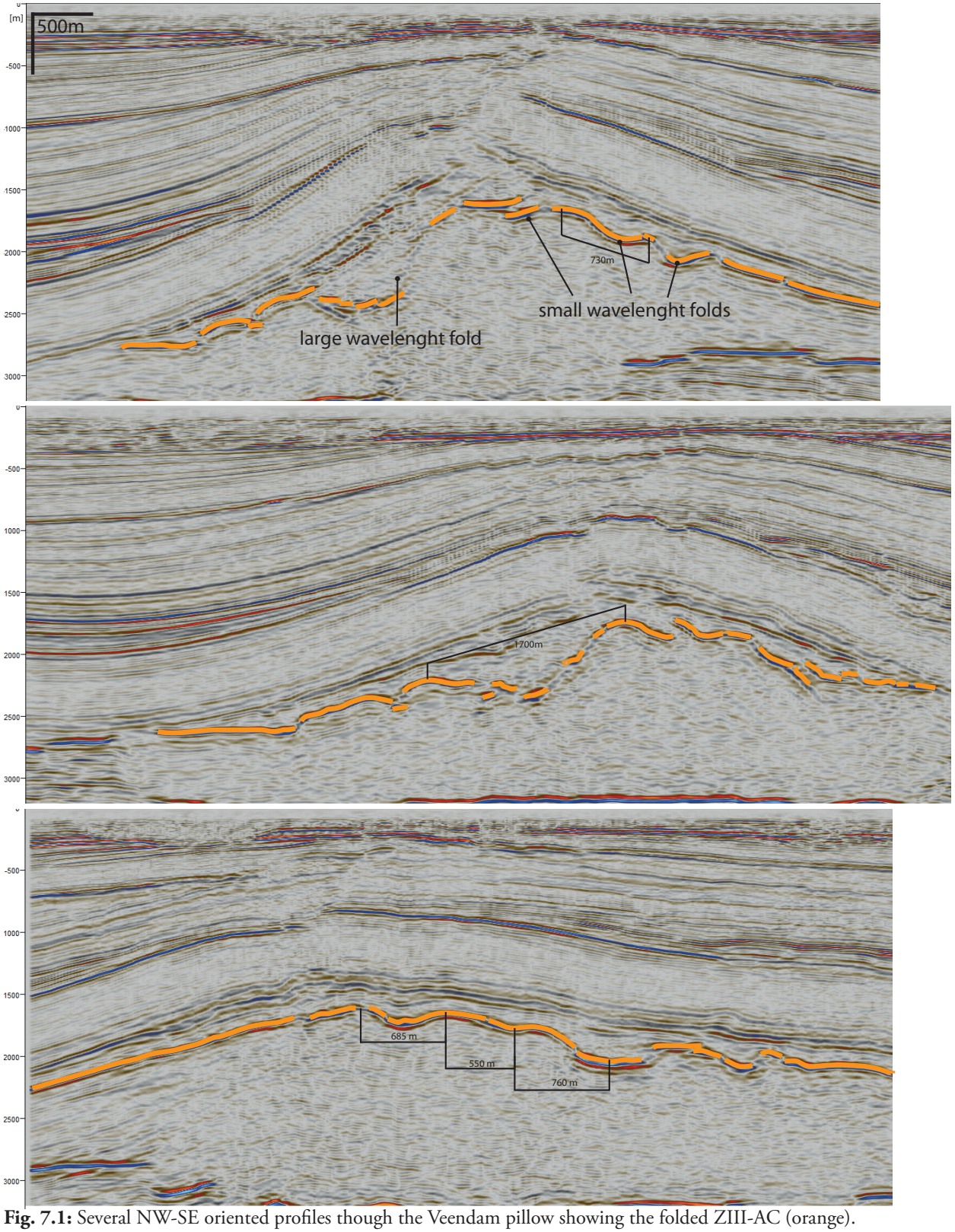


Fig. 7.1: Several NW-SE oriented profiles though the Veendam pillow showing the folded ZIII-AC (orange).

to indicate strain concentration in the soft layers during combined Couette and Poiseuille flow. Samples from thick halite layers in the ZIII-1a and top of the ZIII-1b indicated much less deformation than inside the ZIII-1b K-Mg salt dominated part, while the observed strain in the halite were lower than in the top of the core.

In the last step of this project we want to combine these information and investigate with the help of numerical models: (i) What kind of structures are produced by folding a pre-fractured stringer? (ii) Which rheology contrast between halite and ZIII-AC would produce the observed structures and are those structures influenced by deformation speed? (iii) How does the folding of the stringer influence the structure of the K-Mg salt layers above and, vice versa, how does the soft K-Mg salt influence the deformation on the deeper layers.

7.2.1 Folding

The principals of fold mechanics of infinite single layers had been analyzed and modeled for a large number of viscosity contrasts and stress exponent (Price and Cosgrove, 1990; Johnson and Fletcher, 1994; Johnson, 2012; for summary, see Schmalholz and Mancktelow, 2016). The initial wavelength and growth rates of Newtonian materials were described by Biot et al., 1961, while Fletcher, 1974 described the folding of power law materials. Schmid et al., 2004 analyzed the folding of single lens shaped layers and concluded that if the aspect ratio of a finite layer is not substantially larger than the effective viscosity contrast the conventional theories can not be applied. Although only minor changes of the initial wavelength can be observed in a linear viscous layer, the growth rates decrease strongly with increasing viscosity contrast and smaller aspect ratios. The Veendam case is complicated by the fact that the stringer is separated in finite fragments. These fragments could either interlock or slide along each other during contraction. Thus, if they are able to interlock, much higher growth rates are possible. Another complication could arise from possibly changing strain rates during pillow evolution causing the effective viscosity contrast to vary if the stress exponents of the different materials are not equal.

The folded ZIII-AC stringer in the Veendam Pillow has a typical wavelength of 600 to 1100 m. Considering the present amplitudes, the initial wavelength should be about 800 to 1600 m long (Fig. 7.1). Beside this dominant folding one much larger syncline on the NW flank of the pillow with a wavelength of about 1700 m is present with an initial wavelength of 2400 to 2600 m. With an average thickness of 50 ±10 m we could expect wavelength to thickness ratios of 16 to 30 leading to effective viscosity contrasts to be grater that 70.

7.2.2 Strain rates during deformation

The salt inside the Veendam pillow underwent much less deformation than in a more mature diapir. Today, the salt is about two to three times thicker in the center of the pillow, compared to its initial thickness. The resulting bulk strain is with 100 - 200 % not very high. Nevertheless, the strain can locally be orders of magnitude higher, due to strong mechanical contrasts and a complex internal deformation. The interpretation of the sedimentary strata around the Veendam pillow has shown, that

salt flow was not continuous but took place in several phases (chapter 2). Although the exact timing of those phases could not be reconstructed, the major part of salt deformation took place in the upper Chalk and during the Tertiary leaving a period of 30 to 100 Ma. The resulting mean strain-rate would therefore be lower than 1e-15 s^{-1}. Although strong variations from the mean value are possible, stress estimations from sub grain-sizes produce deviatoric stresses lower than 1 MPa (chapter 5) and therefore confirm low strain rates.

7.3 The model

Since the aim of the simulation is not a close nature reconstruction of the Veendam Pillow but the analysis of the principal processes acting in a salt body with fractured stringers and Soft K-Mg salt layers, the model can be strongly simplified to the key components: (i) salt flow into a pillow: (ii) a fractured anhydrite stringer with different fragment and hole sizes, (iii) soft K-Mg salt layers (the upper one representing the ZIII-2b+3b and the lower one with one internal halite layer representing the ZIII-1b). Therefore, layering and dimensions (such as pressures, depth to salt base, temperatures) of the model are oriented on the Veendam Pillow characteristics but do not represent all attributes exactly (Fig. 7.2).

The two dimensional plain strain model is 16 km wide with a 1.5 km thick salt body. The salt is underlain by a 500 m thick rigid base plate. The salt flow is directed by a sinusoidal vertical displacement of the upper model boundary reaching an amplitude of 1000 m after 1e15 s, while the walls are fixed in x direction. With this setup the salt is extruded from the sides into the center where more space is available. To establish correct confining pressures inside the model, 84 MPa pressure is applied to the rigid base plate corresponding to a base-salt depth of 3000 m (+ 500 m base plate). To allow a realistic vertical salt flow distribution in the salt pillow, a temperature field (from 70°C at the top to 115°C at the bottom) is established in the salt layers and the salt viscosity is temperature dependent

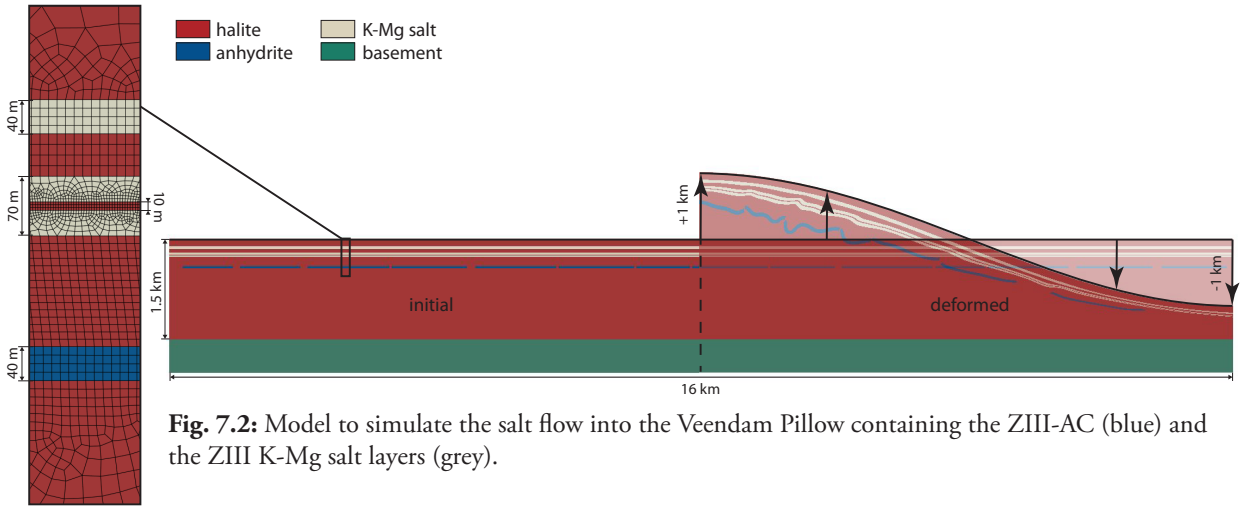


Fig. 7.2: Model to simulate the salt flow into the Veendam Pillow containing the ZIII-AC (blue) and the ZIII K-Mg salt layers (grey).

(Table 2). While the halite viscosity is kept constant in all experiments, the viscosity of K-Mg salts and the stringer are varied to study the effect of viscosity contrasts. The approach to model the known deformation of a salt body by implying deformation to the upper boundaries and stress to a rigid bottom plate was used and described by Li et al. (2012a) and Li et al. (2012b). It reduces the model expenses extremely by simplifying all supra salt processes to the resulting top salt deformation, which has to be well estimated beforehand. Although it is a strong simplification, it is permissible if the free development of the structure is not of importance for the processes of interest and the stress development in the models shows realistic (or calibrated) values. In the case of our models, this approach can be used because the pillow deformation can be estimated and the focus lies on the internal deformation of mechanically diverse layers during passive deformation.

The finite element models were calculated using the Abaqus/Standard solver. The mesh of dominantly tetragonal quadratic (8 nodes) elements was adjusted to allow at least 3 element vertically in each layer (Fig. 7.2,Fig. 7.9). A test if this setup is adequate to allow realistic folding is in the appendix of this chapter.

Rheology

The long term steady state deformation (secondary creep) of halite is dominated by non-Newtonian viscous, temperature dependent dislocation creep or Newtonian viscous, temperature and grain size dependent solution-precipitation creep. Under differential stresses smaller than 2.0 MPa the grain sizes can adapt to the pressures by dynamic recrystallization leading to a balance between dislocation and pressure solution creep (De Bresser et al. 2001). Therefore, some modelers chose an effective viscosity which is an implementation of power law creep (Li and Urai 2016) from a combination of both creep mechanisms (e.g. van Keken et al. 1993; Koyi 2001).

However, if the differential stresses are much lower, grain boundaries are immobilized by necking down of grain boundary fluids, preventing fluids assisted processes like pressure solution creep to

Materials	Elastic properties	Plastic properties
base	E=1e14 Pa v=0.4	---
halite	E=1e10 Pa v=0.35	exponential creep temperature dependent n=5
anhydrite	E=1e10 Pa v=0.4	Newtonian creep (n=1) A_0= 1e-22 to 1e-24 $MPas^{-1}$
K-Mg salt	E=1e10 Pa v=0.35	exponential creep temperature dependent n=5

Table 1: Mechanical properties details are given in table 2.

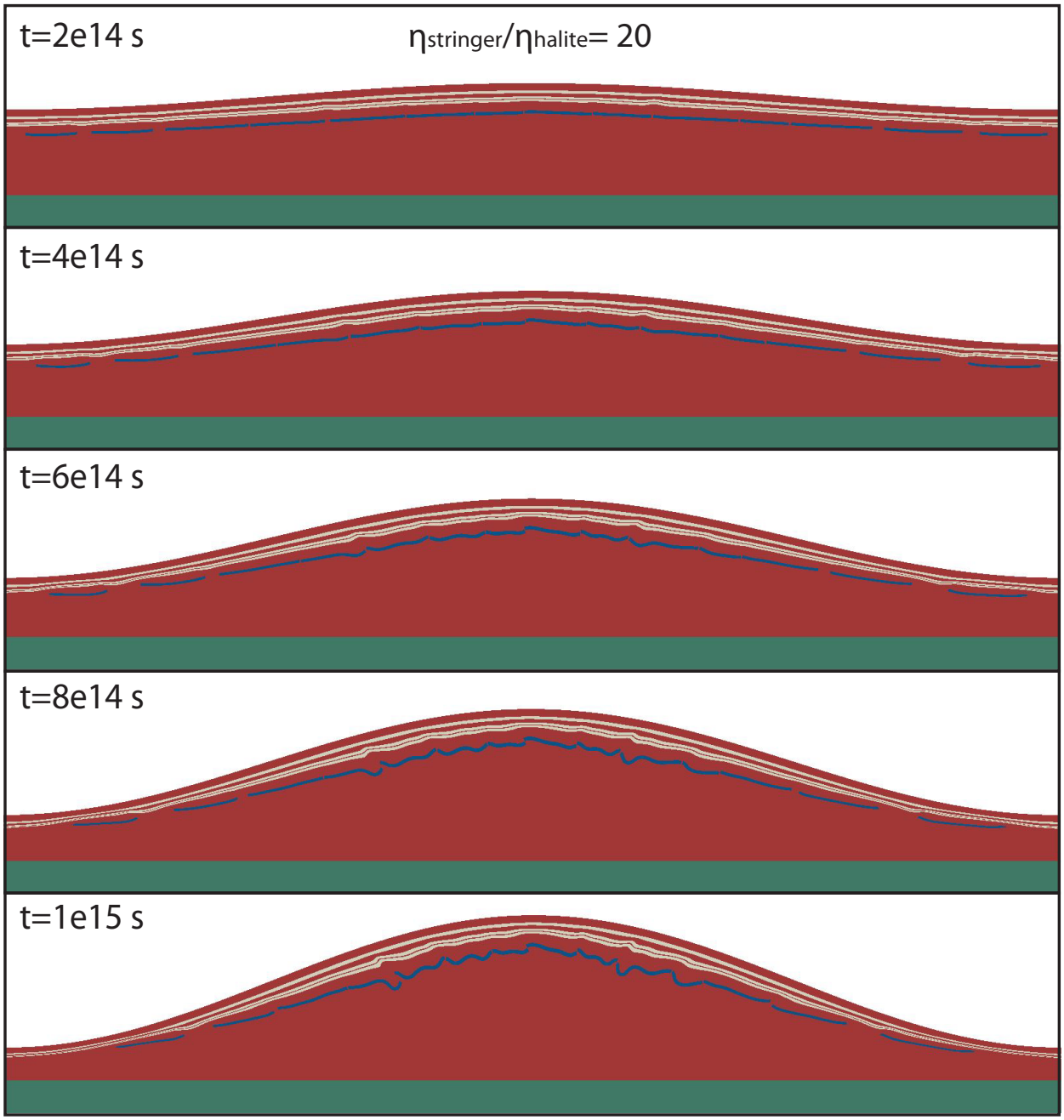


Fig. 7.3: Developement of a model with a halite / K-Mg salt contrast of 1.5 and a stringer/halite contrast of 20.

take place. This process is confirmed by natural observations of the anhydrite- carbonate stringers in the Zechstein salt, that do not sink over long geologic time periods (Van Gent et al. 2011). If pressure-solution creep was taking place, the low differential stresses caused by the weight of the denser stringers would produce enough strain to led the stringer sink though (Li et al. 2012b).

Considering the low bulk strain rates we expect in the Veedam Pillow and the rather low differential stresses (< 1 MPa) observed in the Tr-9 core we expect only minor pressure solution creep taking place. However, if pressure-solution creep could have taken place we can still expect dynamic recrystallization to establish a balance between dislocation and pressure solution creep. Either way, the salt could be modeled as a non-Newtonian viscoelastic material. Thus, the halite was modeled as a

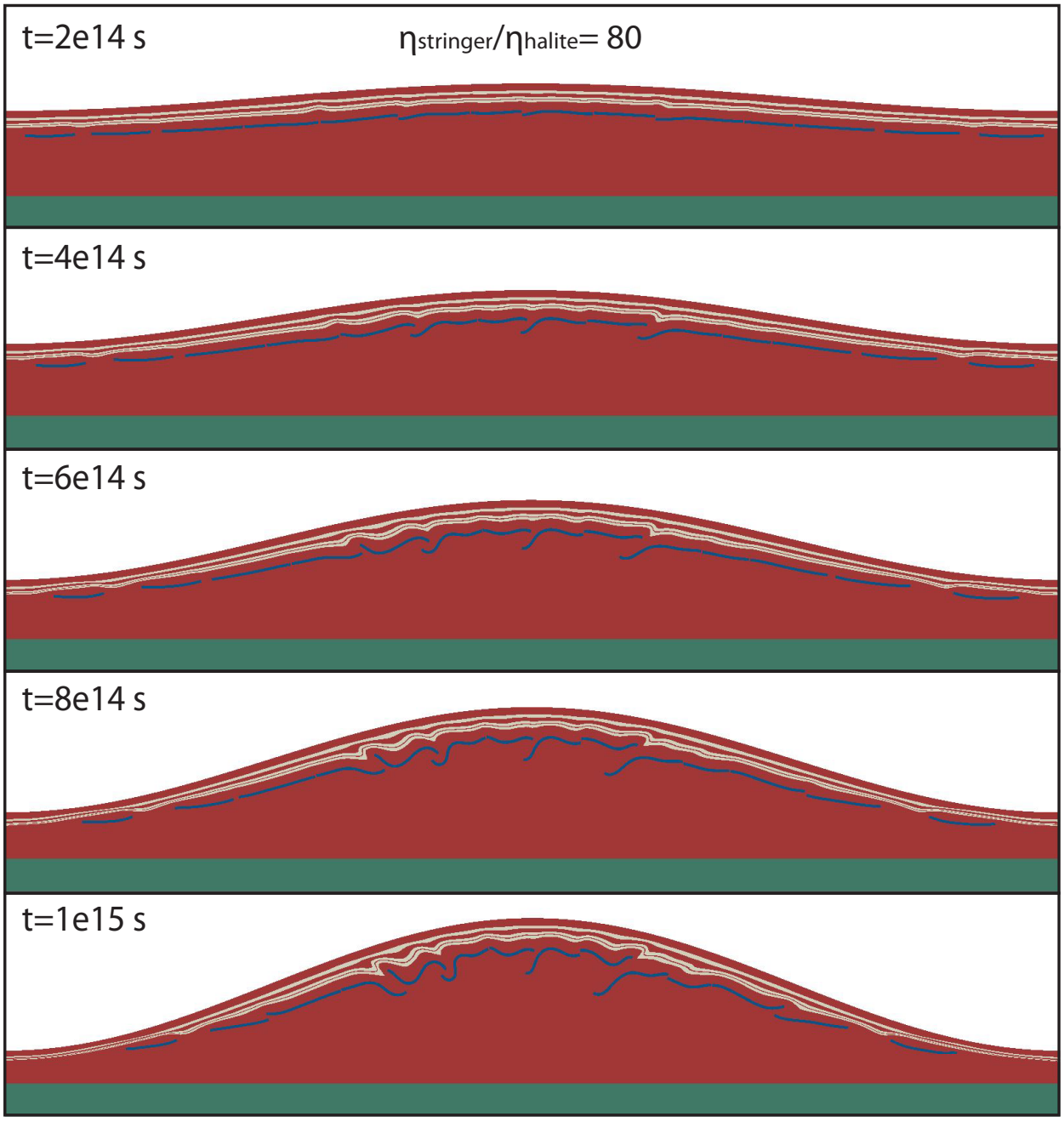


Fig. 7.4: Developement of a model with a halite / K-Mg salt contrast of 1.5 and a stringer/halite contrast of 80.

temperature dependent non- Newtonian (n=5) material $\dot{\varepsilon} = A_0(\sigma_1-\sigma_3)^n$ based on the creep multiplier by Wawersik and Zeuch (1986) (Table 1&2). The K-Mg salt rheology was set similar to the halite rheology but with a lower viscosity. Since an exact bulk viscosity of the strongly layered and deformed K-Mg salt layers are unknown several cases of K-Mg salt viscosity were simulated. (i) Halite dominated: the viscosity is just slightly lower than halite, resembling a strongly folded halite rich K-Mg salt layer where the halite is mostly interconnected and stress bearing (1.5 times lower effective viscosity than halite). (ii) K-Mg salt dominated: bulk viscosity similar to pure carnallite (10 times lower effective viscosity than halite). Additionally models with no K-Mg salt and with a viscosity contrast of 2 were performed.

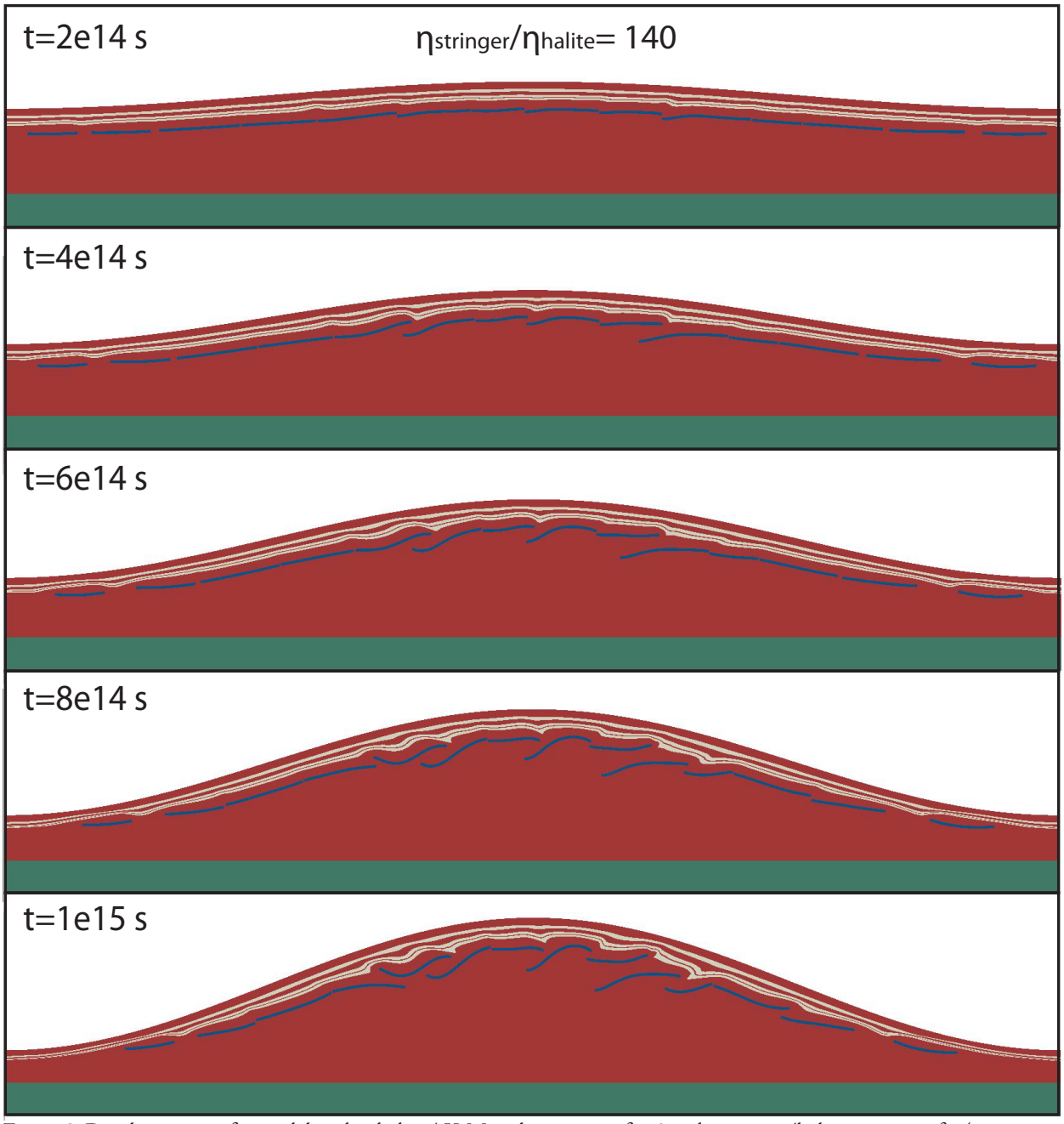


Fig. 7.5: Developement of a model with a halite / K-Mg salt contrast of 1.5 and a stringer/halite contrast of 140.

Anhydrite

Although low temperature triaxial experiments show dominantly brittle material behavior (Zulauf et al. 2010), exposures of folded anhydrite layers in mine galleries display typical characteristics of viscous buckle folding (constant layer thickness, regular fold hinge spacing) without brittle features (Brückner et al. 2007). Deformation experiments above 400°C show creep behavior due to diffusion and dislocation creep processes (Dell'Angelo & Olgaard 1995). Under high pressures the anhydrite deformed strain hardening (n=5) while Newtonian (n=1) creep was dominant at low pressures and strain rates. Neither, of these experiments can be directly applied to our in-situ conditions. We expect ductile behavior under compressional conditions at much lower temperatures and very small strain rates. It is

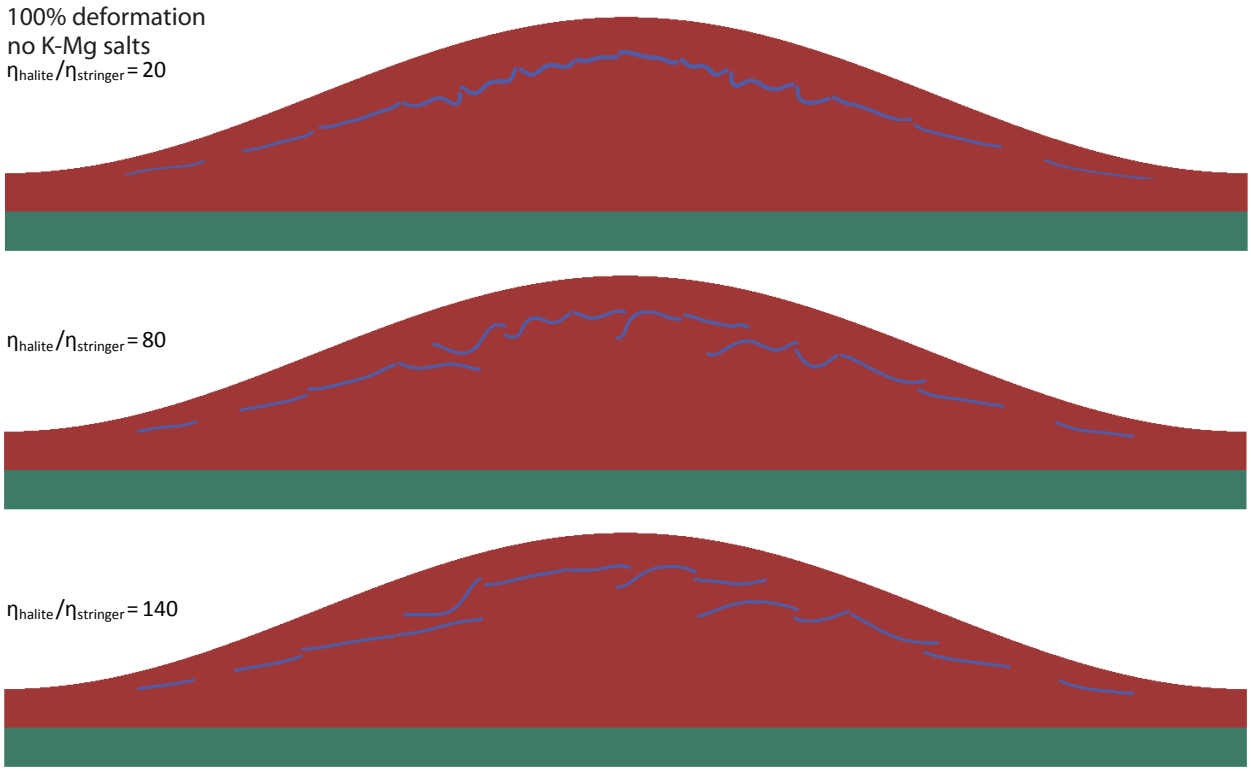


Fig. 7.6: Results of models without K-Mg salt with different stringer vicosities.

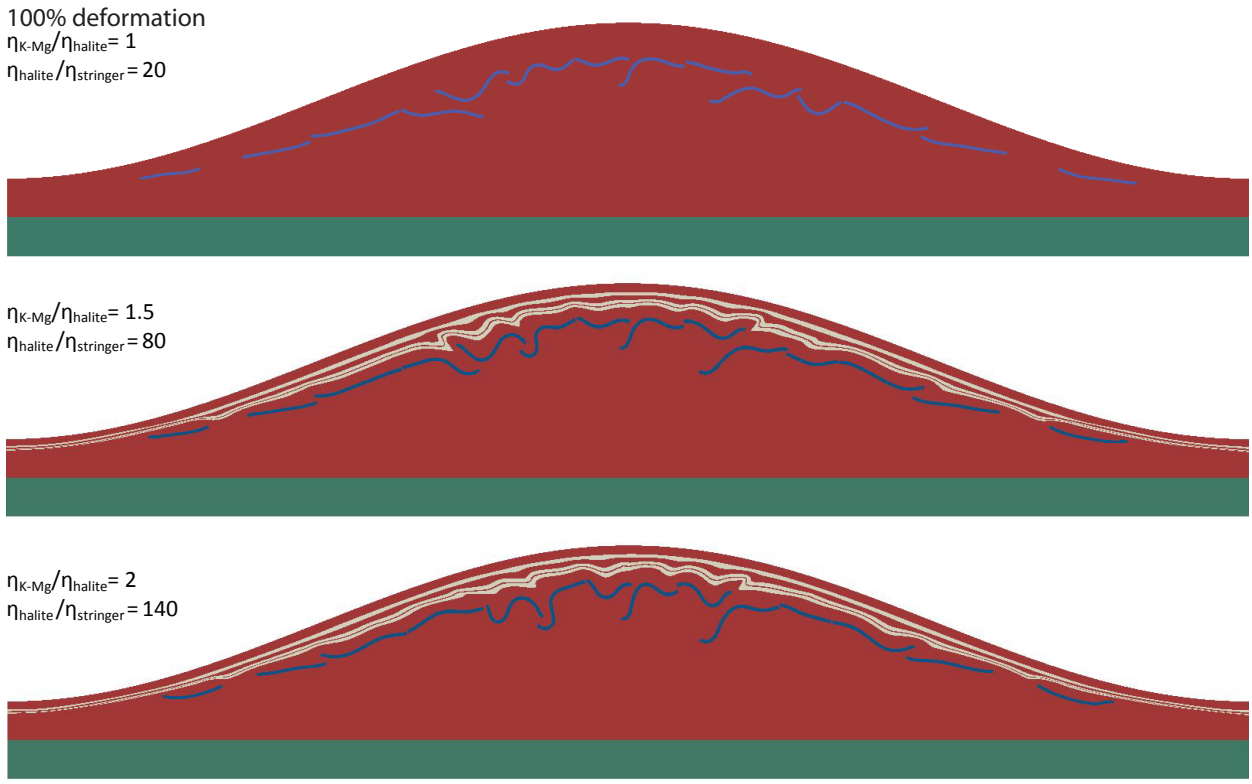


Fig. 7.7: Models with the same stringer viscosity but differend K-Mg salt viscosities.

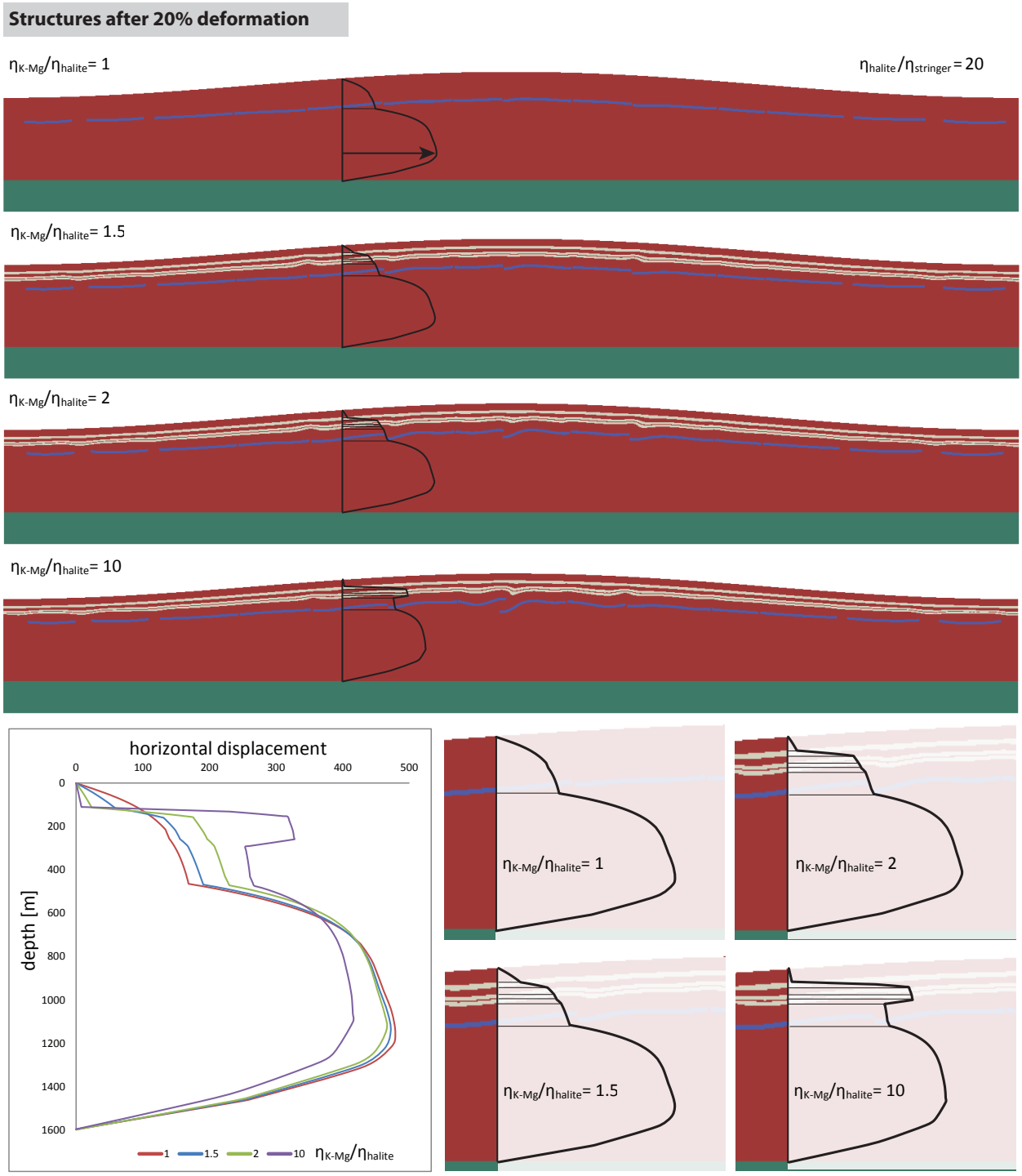
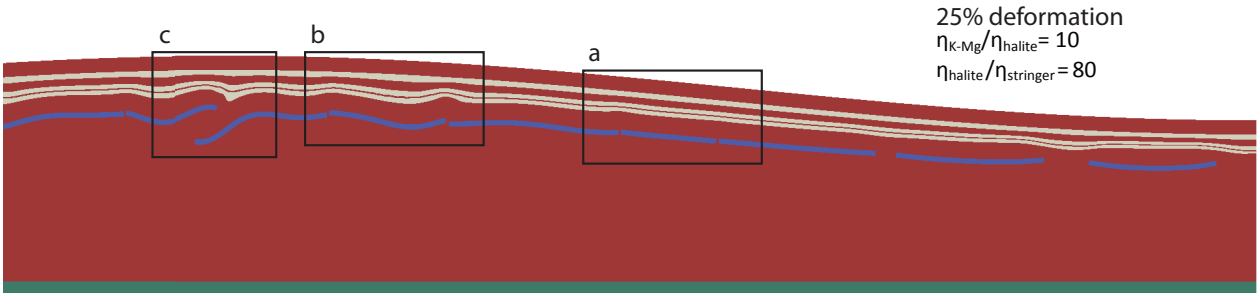
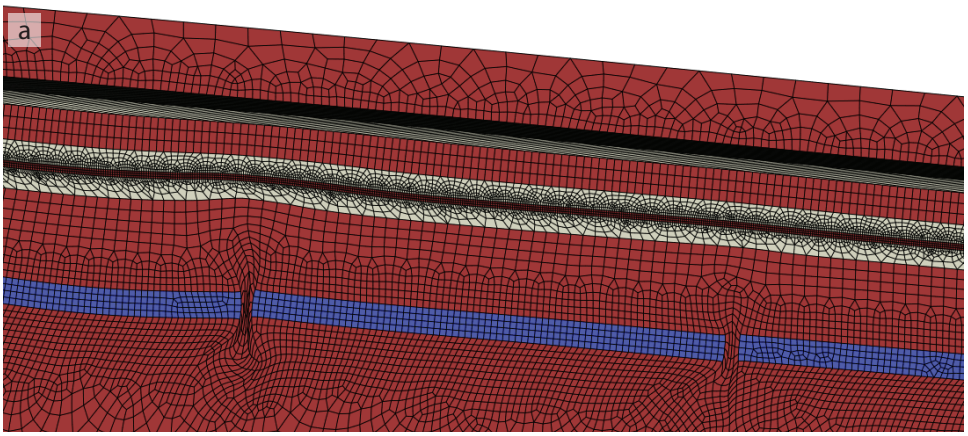
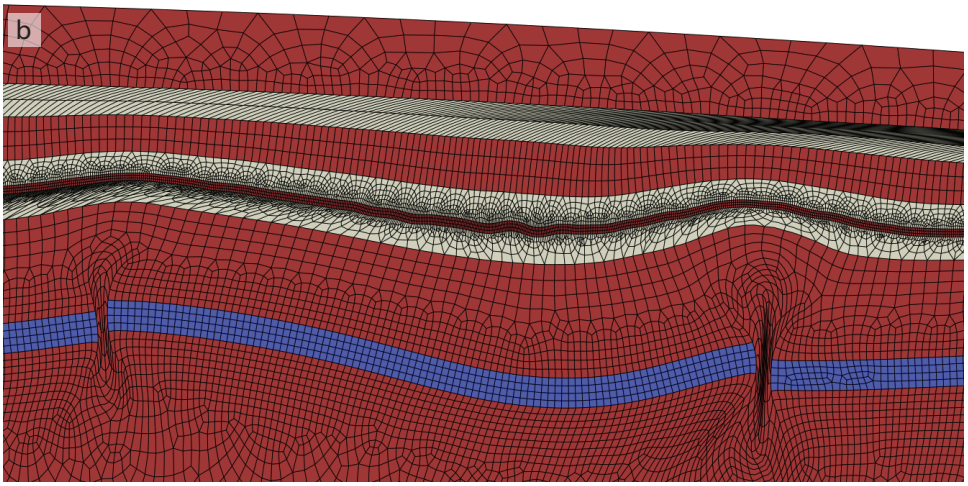


Fig. 7.8: Displacement field in different models after 20% deformation.

therefore likely that Newtonian creep is a dominant deformation process under low deviatoric stresses. The problem to observe these processes in laboratory experiments is, similar to halite, complicated by the extreme long experiment time needed. Although a power law behavior is also possible, prior simulations using this kind of material behavior produced strong strain localization. The structures produced with Newtonian creep resembled natural examples from seismic images much better. To evaluate the viscosity contrast simulations with an anhydrite viscosity of 1e22 to 1e24 $MPas^{-1}$ were performed.







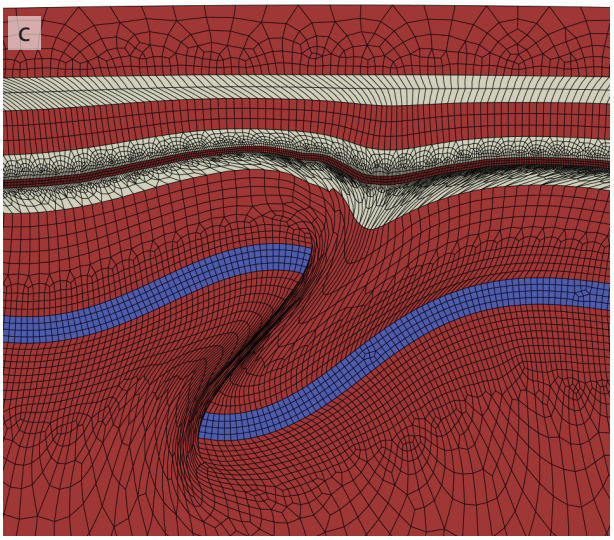


Fig. 7.9: Details of the salt deformation and the element mesh.

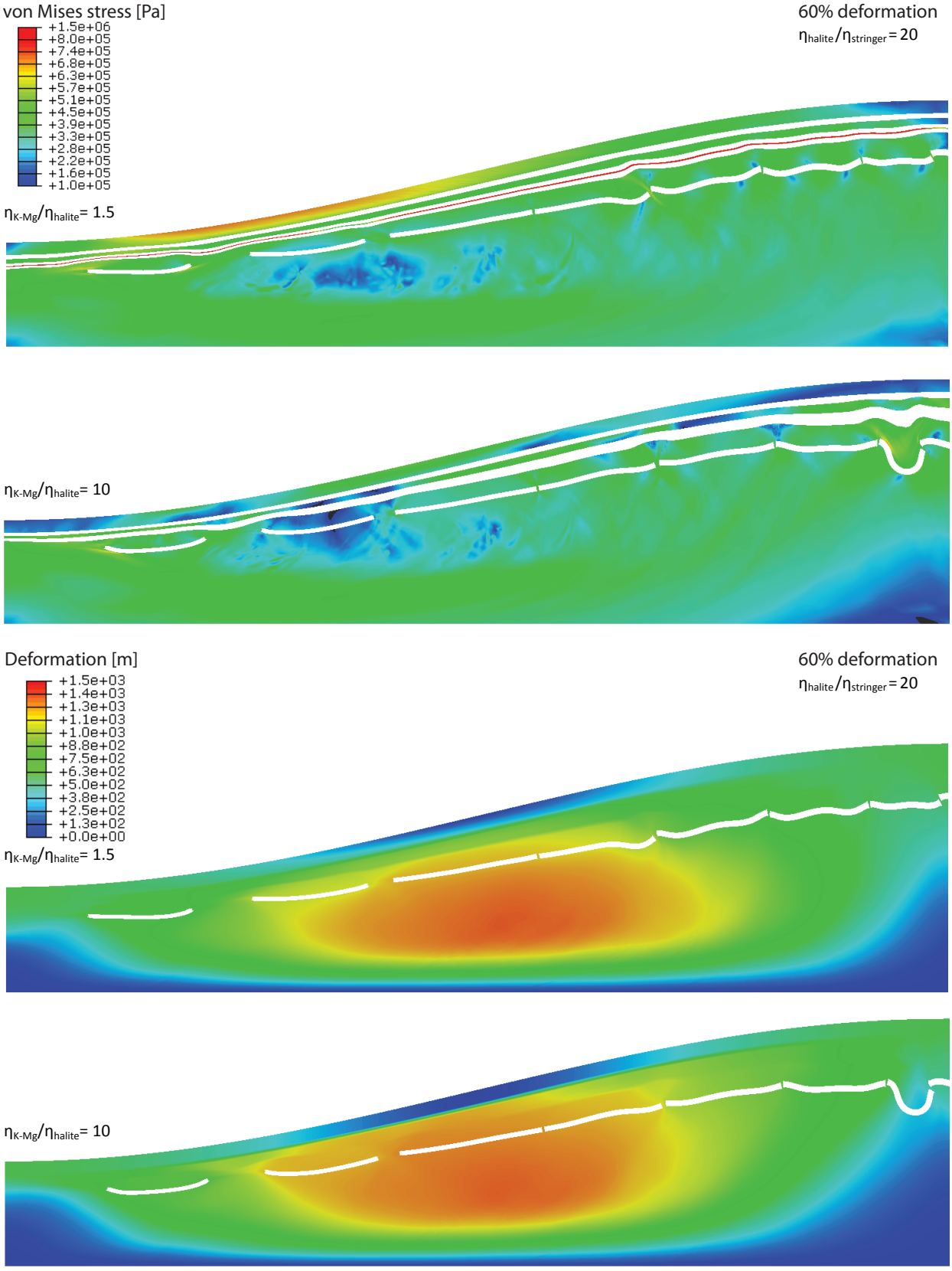


Fig. 7.10: Von Mises stress (= deviatoric stress * $\sqrt{3/2}$) and deformation after 60% of total deformation in a model with a slightly softer (1.5) and much softer (10) K-Mg salt. If the salt is much softer, the roof halite is decoupled from the main deformation leading to much lower stresses in that area. Additionally the decoupling leads to a shift of the bulk strain towards the layer under the K-Mg salt. As a result, less stringer buckling can be observed on the flanks while most buckling is taking place in the centre of the pillow.

7.4 Results

When the anhydrite stringer fragments are extruded into the pillow the shortening is either compensated by stringer folding or shearing of the fragments (Fig. 7.3,Fig. 7.4,Fig. 7.5). With decreasing viscosity contrast between the stringer and the halite, the wavelength of stringer folding decreases. In this case most of the shortening is compensated by folding. When the viscosity contrast increases, less shortening can be compensated by folding and more deformation is concentrated into stringer fragment shearing (Fig. 7.6). Once a shear zone is established its orientation remains relatively stable.

7.4.1 Influence of K-Mg salt layers on the internal deformation

The results with different viscosity contrasts between K-Mg salt and halite show a strong impact on the strain distribution in the salt pillow. The models without K-Mg salt have simple asymmetric Poiseuille flow restrained by the anhydrite stringer (Fig. 7.8). If K-Mg salt layers are present, deformation localizes in these layers above the stringer, leading to an upward shift of bulk deformation. With decreasing K-Mg salt viscosity the anhydrite stringer gets stronger deformed. Thus, folding and shearing of the stringer takes place much earlier during the pillow evolution.

7.4.2 Deformation of the K-Mg salt layers

The soft K-Mg salt layers can accumulate large strains depending on the viscosity. In case of a viscosity contrast of 10, the upper layer is sheared extensively in Couette flow while the lower K-Mg layer is deformed by a combination of Poiseuille and Couette flow (shear and extrusion)(Fig. 7.8). Which of the processes is dominant depends on the position in the pillow and the deformation of the underlying anhydrite stringer. At pillow scale the K-Mg salts are mostly sheared and extruded at the flanks, while being thickened in the pillow center. Additionally K-Mg salts are withdrawn from areas above stringer anticlines to areas above stringer synclines (Fig. 7.9). When the lower K-Mg salt layer is thickened, the internal halite layer starts to buckle.

7.5 Discussion

7.5.1 Mesh quality issues

The strongly localized deformation in the model leads to quick mesh distortions in the soft layers and at shear zones between stringer fragments. As a result, the elements are elongated to an extend, that the quality of the calculation is locally declined. To avoid these issues, frequent remeshing could be used. Nevertheless, frequent remeshing could also decline the quality in the whole model and would increase the calculation costs extremely. Thus, no remeshing was performed, leading to some areas of bad mesh quality that have to be considered:,

Very strong strain localization can be observed at the shear zones between stringer fragments.

Here, the elongated elements cause anisotropic deformation behavior that might lead to unrealistic deformation structures. The stability of the shear zones over time is therefore most likely an artifact of the mesh anisotropy. In the soft layers the distortion is especially high in the flanks of the pillow. Due to the less complex simple shear taking place, the mesh anisotropy has only minor effects on the resulting deformation.

7.5.2 Viscosity contrast of the stringer

The results show that the wavelengths observed in the Veendam pillow can be produced by effective viscosity contrast of about 100 (± 20). In the models with a viscosity contrast of 20, the (Fig. 7.3) wavelengths are too short, stringer shearing is not very common and a strong thickening of the layer towards the center, respectively a thinning below the basins can be observed. Such short wavelength and thickness changes cannot be observed in the seismic images. With a viscosity contrast of 80 (Fig. 7.4) the stringer thickness stays constant and the folding is comparable to the Venndam Pillow observations. Nevertheless, the fold grow rates are rather strong and the initial wavelength is on the lower end of the observations. With a decreasing K-Mg viscosity, this gets even more pronounced. With a viscosity contrast of 140 (Fig. 7.5) folding is less strong and most of the deformation is localized in the shear zones. In summary, the best fit could be established with a viscosity contrast between 80 and 140 but closer to the smaller value.

7.5.3 Multiphase tectonics and wavelength

If we consider the deformation history of the Veendam Pillow, we could expect a certain variance of strain rates during the pillows evolution. Given these circumstances, we also can expect a changing viscosity contrast, due to unequal stress exponents of halite and anhydrite. Even if anhydrite does not deform linear viscose, it is very likely its stress exponent does not equal the stress exponent of halite. Nevertheless once a dominate wavelength was able to develope, it will continue to grow. If a new dominant wavelength differs strong enough from the old one, it can also start to grow as long as the limbs are not to steep already.

If we apply this concept on the Veendam Pillow, the deep syncline NW of the pillow crest might be the result of early large wavelength folding. Later, faster salt flow established smaller wavelength folding of the stringer creating the structure visible today.

7.5.4 Influence of hard and soft layer on the internal deformation

Due to the temperature gradient in the models the horizontal Poiseuille flow is asymmetric, creating the largest displacements in the lower third of the model (ZII salt in the real case)(Fig. 7.8,Fig. 7.10). If a stronger layer like an anhydrite/carbonate stringer is present, the deformation is reduced

around it. In the case of a fractured stringer, this reduction is much weaker and could partly be compensated in the gabs between the stringers. These preexisting gaps react during the deformation in three different ways (Fig. 7.9). If they are in an area of salt withdrawal the salt in this area is stronger deformed to compensate the stiff anhydrite. If they are in an area of local compression, the salt is pushed together by the converging stringer fragments leading to local stress accumulation. The fragments either interlock or slide past each other. The sliding is accompanied by a shear zone of local stress and strain accumulation. Due to the power law creep behavior of the salt, these shear zones are nicely localized and stay stable. Softer layers could also change the internal deformation of salt bodies even if the contrast is rather small (1.5). They act as internal glide horizons and can shift the deformation field strongly (Fig. 7.10). Dependent on their position in the pillow, this could lead to a deformation increase in the layers closer to the center of deformation and also to a deformation decrease in the layers that get decoupled. The rough top salt contact of many salt structures causes good salt adhesion and prevents strong salt deformation along the contact. If a soft K-Mg salt layer is present the top is decoupled leading to much more deformation in the roof of the salt structure. Thus, if a stringer is present in the vicinity of a K-Mg salt layer it could either be much stronger deformed or if it is decoupled from the rest of the salt body by the soft salt, much less deformed.

7.5.5 Core structures compared to model results

Although, the internal deformation of the complex layered K-Mg salt layers is not resolved in these models, the bulk deformation of the layers could still indicate which kind of structures we could expect. As expected, the models confirm strain concentration in the soft layers as observed in the TR-9 core. While the K-Mg salt layers are deformed by simple Couette flow on the flanks of the pillow,

A_0 [$Mpa^{-5}s^{-1}$]	temperature [°C]	A_0 [$Mpa^{-5}s^{-1}$]	temperature [°C]	A_0 [$Mpa^{-5}s^{-1}$]	temperature [°C]
2.57E-45	25	9.85E-44	85	1.33E-42	145
3.67E-45	30	1.26E-43	90	1.59E-42	150
5.20E-45	35	1.61E-43	95	1.91E-42	155
7.28E-45	40	2.04E-43	100	2.27E-42	160
1.01E-44	45	2.57E-43	105	2.69E-42	165
1.38E-44	50	3.21E-43	110	3.18E-42	170
1.88E-44	55	4.00E-43	115	3.75E-42	175
2.53E-44	60	4.94E-43	120	4.40E-42	180
3.37E-44	65	6.08E-43	125	5.14E-42	185
4.46E-44	70	7.45E-43	130	5.99E-42	190
5.85E-44	75	9.07E-43	135	6.96E-42	195
7.62E-44	80	1.10E-42	140	8.06E-42	200

Table 2: Details of the halite viscosity.

structures that are more complex are visible towards the pillow crest, above the folded stringer. If the lower K-Mg salt layer is locally shortened, the thin internal halite layer is folded. If the shortening is accompanied by shear (which is often the case), we could expect recumbent folding as observed in the Tr-9 core. In addition, recumbent folding on scale of the K-Mg salt layers can be observed in the models at the boundary of dominantly sheared flanks to the dominantly folded crest above stringer shear zones (Fig. 7.4).

7.6 Conclusions

During the development of the pillow the pre-fractured stringer is folded and thrusted in the pillow center. Whether the shortening is mostly compensated by folding or thrusting depends on the stringer viscosity.

If the stress exponent of halite and anhydrite are unequal, the effective viscosity contrast is strain dependent. Thus, strong strain-rate changes during the pillow evolution could produce different dominant wavelengths.

The folding of the ZIII-AC observed in the Veendam pillow indicates an effective velocity contrast of about 100 between the stringer and the halite in most places.

Additionally, a much larger wavelength folding could have been produced by early slow deformation forming the large syncline in the NW of the Veendam Pillow.

Both soft K-Mg salt layers and strong stringers influence the deformation and salt flow inside the salt pillow. Strain is accumulated in the soft layers leading to stronger salt flow near these layers and extensive deformation inside of them. Thus, if a soft layer is present near a stringer, it will experience more deformation.

On the other hand, the structure of the soft K-Mg salt layers and the salt flow inside of them is strongly influenced by folding of a harder stringer close to them. The soft K-Mg salts are withdrawn from areas above stringer anticlines to areas above stringer synclines.

In summary, fold analysis can be used to estimate the in situ rheology of stringers or if the in situ rheology of anhydrite and salt is well known, might be used to estimate the in situ strain rates.

7.7 References

Biot MA, Odé H, Roever WL (1961) Experimental Verification of the Theory of Folding of Stratified Viscoelastic Media. Geol Soc Am Bull 72:1621. doi: 10.1130/0016-7606(1961)72[1621:EVOTTO]2.0.CO;2

Brückner D, Lindert A, Wiedenabb M (2007) The Bernburg Test Cavern - A Model Study of Cavern Abandonment. In: Proc. 6th Conf. on Mechanical Behaviour of Salt. London, pp 416–427

De Bresser J, Ter Heege J, Spiers C (2001) Grain size reduction by dynamic recrystallization: can it result in major rheological weakening? Int J Earth Sci 90:28–45. doi: 10.1007/s005310000149

Dell'Angelo LN, Olgaard DL (1995) Experimental deformation of fine-grained anhydrite: Evidence for dislocation and diffusion creep. J Geophys Res Solid Earth 100:15425–15440. doi: 10.1029/95JB00956

Fletcher RC (1974) Wavelength selection in the folding of a single layer with power-law rheology. Am J Sci 274:1029–1043. doi: 10.2475/ajs.274.9.1029

Johnson A (2012) Styles of folding: mechanics and mechanisms of folding of natural elastic materials.

Johnson A, Fletcher R (1994) Folding of viscous layers: mechanical analysis and interpretation of structures in deformed rock.

Li S, Abe S, Reuning L, et al (2012a) Numerical modelling of the displacement and deformation of embedded rock bodies during salt tectonics: A case study from the South Oman Salt Basin. Geol Soc London, Spec Publ 363:503–520. doi: 10.1144/SP363.24

Li S, Abe S, Urai J, Strozyk F (2012b) A method to evaluate long-term rheology of Zeichstein salt in the Tertiary. In: Mechanical Behaviour of Salt VII. Taylor & Francis Group, London, pp 215–220

Li S-Y, Urai JL (2016) Rheology of rock salt for salt tectonics modeling. Pet Sci. doi: 10.1007/s12182-016-0121-6

Price N, Cosgrove J (1990) Analysis of geological structures.

Raith AF, Strozyk F, Visser J, Urai JL (2016) Evolution of rheologically heterogeneous salt structures: A case study from the NE Netherlands. Solid Earth 7:67–82. doi: 10.5194/se-7-67-2016

Schmalholz SM, Mancktelow N (2016) Folding and necking across the scales: a review of theoretical and experimental results and their applications. Solid Earth Discuss 1–98. doi: 10.5194/se-2016-80

Schmid DW, Podladchikov YY, Marques FO (2004) Folding of a finite length power law layer. J Geophys Res 109:B03407. doi: 10.1029/2003JB002421

Van Gent H, Urai JL, de Keijzer M (2011) The internal geometry of salt structures - A first look using 3D seismic data from the Zechstein of the Netherlands. J Struct Geol 33:292–311. doi: 10.1016/j.jsg.2010.07.005

van Keken PE, Spiers CJ, van den Berg a. P, Muyzert EJ (1993) The effective viscosity of rocksalt: implementation of steady-state creep laws in numerical models of salt diapirism. Tectonophysics 225:457–476. doi: 10.1016/0040-1951(93)90310-G

Wawersik WR, Zeuch DH (1986) Modeling and mechanistic interpretation of creep of rock salt below 200°C. Tectonophysics 121:125–152. doi: 10.1016/0040-1951(86)90040-5

Zulauf G, Zulauf J, Bornemann O, et al (2010) Experimental deformation of a single-layer anhydrite in halite matrix under bulk constriction. Part 2: Deformation mechanisms and the role of fluids. J Struct Geol 32:264–277. doi: 10.1016/j.jsg.2009.12.001

Appendix

Shortened example of an Abaqus input file.

All element and node lists are kept out and marked with (…). All comments are markt with #. The full file is in the digital appendix.

```
*Heading
** Job name: dpiece6m Model name: Model-1
** Generated by: Abaqus/CAE 6.13-1
*Preprint, echo=NO, model=NO, history=NO, contact=NO
**
** PARTS
**
*Part, name=Part-1
*Node
#List of all 311475 nodes
*Element, type=CPE8
# List of all CPE8 elements
(...)
*Element, type=CPE6
# List of all CPE6 elements
(...)
*Nset, nset=K-MG
# List of all nodes in the K-Mg salt set
(...)
  *Elset, elset=K-MG
# List of all elements in the K-Mg salt set
(...)
 *Nset, nset=string
# List of all nodes in the Stringer set
(...)
   *Elset, elset=string
# List of all elements in the Stringer set
(...)
*Nset, nset=base
# List of all nodes in base plate set
(...)
*Elset, elset=base, generate
 1589,  1768,     1
*Nset, nset=halite
# List of all nodes in the halite set
(...)

*Elset, elset=halite
# List of all elements in the haliter set
(...)
** Section: Stringer
*Solid Section, elset=string, material=Stringer
,
** Section: Base
*Solid Section, elset=base, material=Base
,
** Section: Bischofite
*Solid Section, elset=K-MG, material=Bischofite
,
** Section: Halite
*Solid Section, elset=halite, material=Halite
,
*End Part
**
**
** ASSEMBLY
**
*Assembly, name=Assembly
**
*Instance, name=Part-1-1, part=Part-1
*End Instance
**
```

```
*Nset, nset=Set-4, instance=Part-1-1
# List of all nodes at the top boundary of the model
(...)

*Elset, elset=Set-4, instance=Part-1-1
# List of all elements at the top boundary of the model
(...)

*Nset, nset=tempAll, instance=Part-1-1
# List of all nodes that are influenced by the temperature field
(...)

*Elset, elset=tempAll, instance=Part-1-1
# List of all elements that are influenced by the temperature field
(...)

*Nset, nset=wände, instance=Part-1-1
# List of all nodes at the walls of the model
(...)

*Elset, elset=wände, instance=Part-1-1
# List of all elements at the walls of the model
(...)

*Nset, nset=_PickedSet5, internal, instance=Part-1-1
# List of all nodes at the bottom boundary of the model
(...)

*Elset, elset=_PickedSet5, internal, instance=Part-1-1
# List of all elements at the top boundary of the model
(...)

*Elset, elset=__PickedSurf7_S3, internal, instance=Part-1-1, generate
 1709,  1768,     1
*Surface, type=ELEMENT, name=_PickedSurf7, internal
__PickedSurf7_S3, S3
*End Assembly
**
** MATERIALS
**
# Material Properties
*Material, name=Base
*Density
2600.,
*Elastic
 1e+14, 0.4
*Material, name=Bischofite
*Creep, law=TIME
# creep multiplier, creep exponent,-,temperature
 3.49739e-41,  5.,  0.,  0.
 5.36173e-41,  5.,  0.,  5.
 8.09672e-41,  5.,  0., 10.
 1.20531e-40,  5.,  0., 15.
 1.77007e-40,  5.,  0., 20.
 2.56614e-40,  5.,  0., 25.
 3.67492e-40,  5.,  0., 30.
 5.20179e-40,  5.,  0., 35.
 7.28174e-40,  5.,  0., 40.
 1.00861e-39,  5.,  0., 45.
 1.38303e-39,  5.,  0., 50.
 1.87828e-39,  5.,  0., 55.
 2.52754e-39,  5.,  0., 60.
 3.37147e-39,  5.,  0., 65.
 4.45958e-39,  5.,  0., 70.
 5.85163e-39,  5.,  0., 75.
 7.61935e-39,  5.,  0., 80.
  9.8482e-39,  5.,  0., 85.
 1.26394e-38,  5.,  0., 90.
  1.6112e-38,  5.,  0., 95.
 2.04055e-38,  5.,  0.,100.
 2.56821e-38,  5.,  0.,105.
 3.21297e-38,  5.,  0.,110.
 3.99646e-38,  5.,  0.,115.
```

```
 4.94347e-38,  5.,  0.,120.
 6.08231e-38,  5.,  0.,125.
 7.44511e-38,  5.,  0.,130.
  9.0682e-38,  5.,  0.,135.
 1.09925e-37,  5.,  0.,140.
  1.3264e-37,  5.,  0.,145.
 1.59339e-37,  5.,  0.,150.
 1.90595e-37,  5.,  0.,155.
  2.2704e-37,  5.,  0.,160.
 2.69375e-37,  5.,  0.,165.
 3.18374e-37,  5.,  0.,170.
 3.74885e-37,  5.,  0.,175.
 4.39836e-37,  5.,  0.,180.
 5.14244e-37,  5.,  0.,185.
 5.99213e-37,  5.,  0.,190.
 6.95944e-37,  5.,  0.,195.
 8.05737e-37,  5.,  0.,200.
*Density
2040.,
*Elastic
 1e+10, 0.35
*Material, name=Halite
*Creep, law=TIME
 3.49739e-46,  5.,  0.,  0.
 5.36173e-46,  5.,  0.,  5.
 8.09672e-46,  5.,  0., 10.
 1.20531e-45,  5.,  0., 15.
 1.77007e-45,  5.,  0., 20.
 2.56614e-45,  5.,  0., 25.
 3.67492e-45,  5.,  0., 30.
 5.20179e-45,  5.,  0., 35.
 7.28174e-45,  5.,  0., 40.
 1.00861e-44,  5.,  0., 45.
 1.38303e-44,  5.,  0., 50.
 1.87828e-44,  5.,  0., 55.
 2.52754e-44,  5.,  0., 60.
 3.37147e-44,  5.,  0., 65.
 4.45958e-44,  5.,  0., 70.
 5.85163e-44,  5.,  0., 75.
 7.61935e-44,  5.,  0., 80.
  9.8482e-44,  5.,  0., 85.
 1.26394e-43,  5.,  0., 90.
  1.6112e-43,  5.,  0., 95.
 2.04055e-43,  5.,  0.,100.
 2.56821e-43,  5.,  0.,105.
 3.21297e-43,  5.,  0.,110.
 3.99646e-43,  5.,  0.,115.
 4.94347e-43,  5.,  0.,120.
 6.08231e-43,  5.,  0.,125.
 7.44511e-43,  5.,  0.,130.
  9.0682e-43,  5.,  0.,135.
 1.09925e-42,  5.,  0.,140.
  1.3264e-42,  5.,  0.,145.
 1.59339e-42,  5.,  0.,150.
 1.90595e-42,  5.,  0.,155.
  2.2704e-42,  5.,  0.,160.
 2.69375e-42,  5.,  0.,165.
 3.18374e-42,  5.,  0.,170.
 3.74885e-42,  5.,  0.,175.
 4.39836e-42,  5.,  0.,180.
 5.14244e-42,  5.,  0.,185.
 5.99213e-42,  5.,  0.,190.
 6.95944e-42,  5.,  0.,195.
 8.05737e-42,  5.,  0.,200.
*Density
2040.,
*Elastic
 1e+10, 0.35
*Material, name=Stringer
*Creep, law=TIME
 1e-23,1.,0.
*Density
2600.,
```

```
*Elastic
 1e+10, 0.4
** ----------------------------------------------------------------
**
** STEP: Step-1
**
*Step, name=Step-1, nlgeom=YES, inc=100000
*Visco, cetol=0.01
1000., 1e+15, 0.0001, 1e+15
**
** BOUNDARY CONDITIONS
**
** Name: BC-1 Type: Displacement/Rotation
*Boundary
wände, 1, 1
** Name: BC-3 Type: Displacement/Rotation Using Analytical Field: AnalyticalField-1
*Boundar
# Displacement of every node on the top boundary
(...)

**
** LOADS
**
** Name: Load-1   Type: Gravity
*Dload
, GRAV, 9.81, 0., -1.
** Name: Load-2   Type: Pressure
*Dsload
_PickedSurf7, P, 8.4e+07
**
** PREDEFINED FIELDS
**
** Name: temp   Type: Temperature Using Field: tempfield
*Temperature
#Temperature for every node
(...)

**
** OUTPUT REQUESTS
**
*Restart, write, frequency=0
**
** FIELD OUTPUT: F-Output-1
**
*Output, field
*Node Output
CF, COORD, NT, RF, U
*Element Output, directions=YES
CE, CEEQ, CEMAG, EE, EVOL, FV, IE, LE, PE, PEEQ, PEMAG, S, TEMP, UVARM
*Contact Output
CDISP, CSTRESS
**
** HISTORY OUTPUT: H-Output-1
**
*Output, history, variable=PRESELECT
*End Step
```

Fold test models

In the first simulations a simple three layer 2D model was deformed under pure shear. The models were initially 2000 high and 6000 m wide with a horizontal center layer of 50 m thickness. On the contacts between the central layer (layer) and the outer layers (matrix) brownian noise was added with a max amplitude of 1/20 to 1/30 layer thickness (depending on the mesh size). The model was horizontally shortened by 2000 m, resulting in 0.33 strain while the lower boundary was fixed and the upper boundary kept as a free surface . The horizontal shortening took place with constant wall movement over a time period of 3e13 to 3e17 seconds leading to bulk strain rates of 1e-14 to 1e-18. The results are summarized in the folowing figurs.

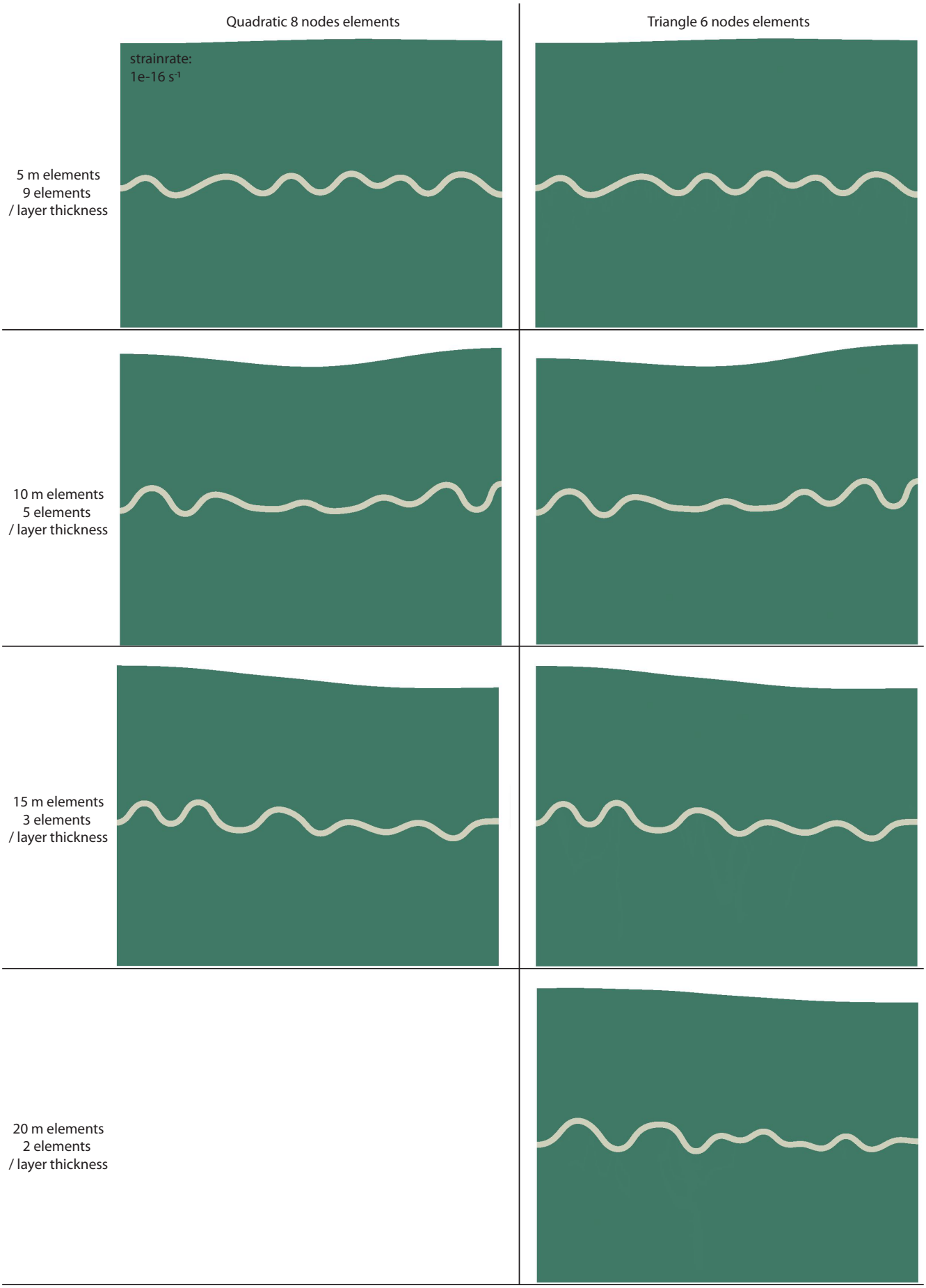


Fig. 7.11: Square elements compared to triangular elements with different element sizes producing the same wavelength.

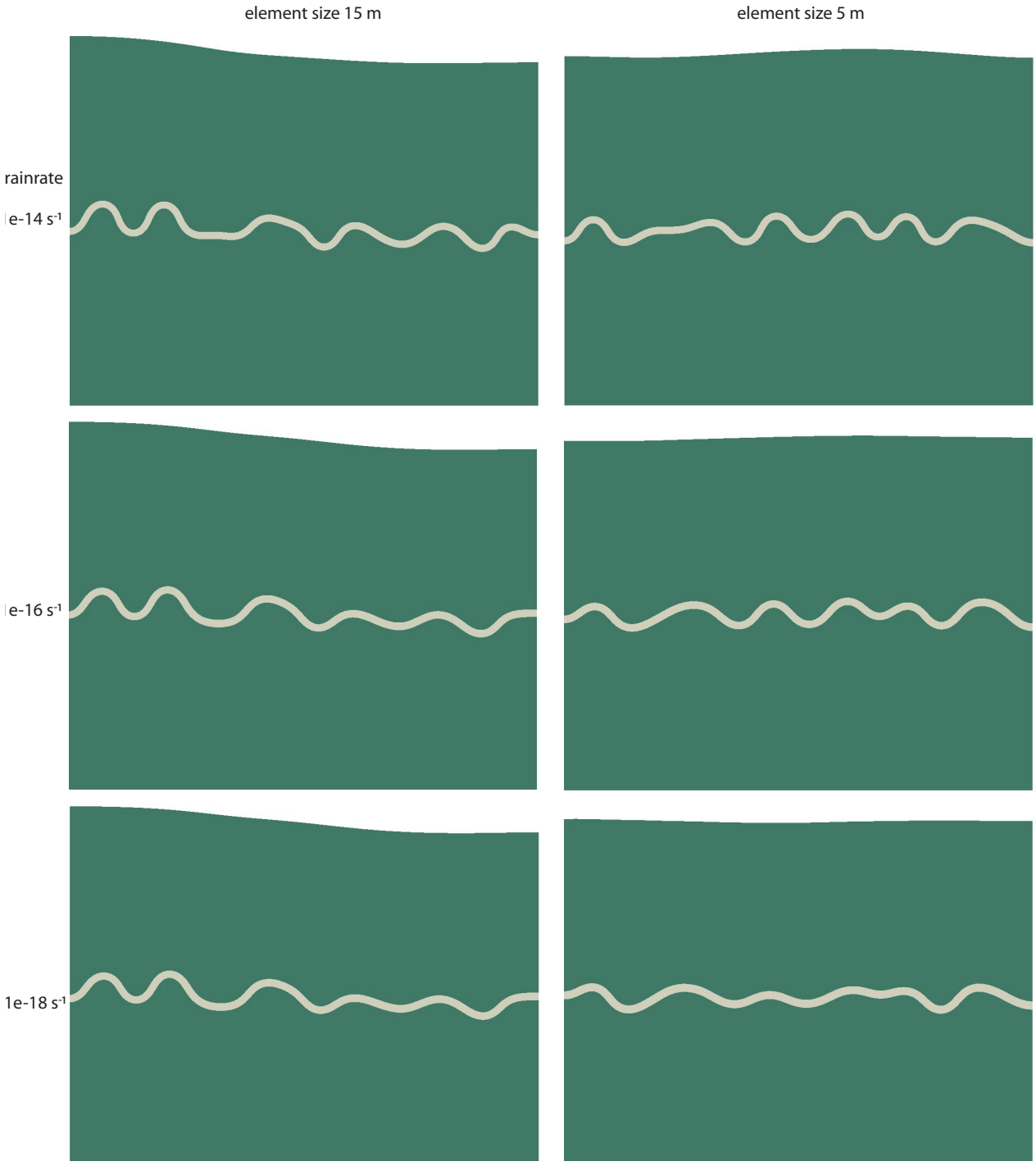


Fig. 7.12: Models with the same viscosity contrast but different element sizes develop the same fold wavelength at different strain rates.

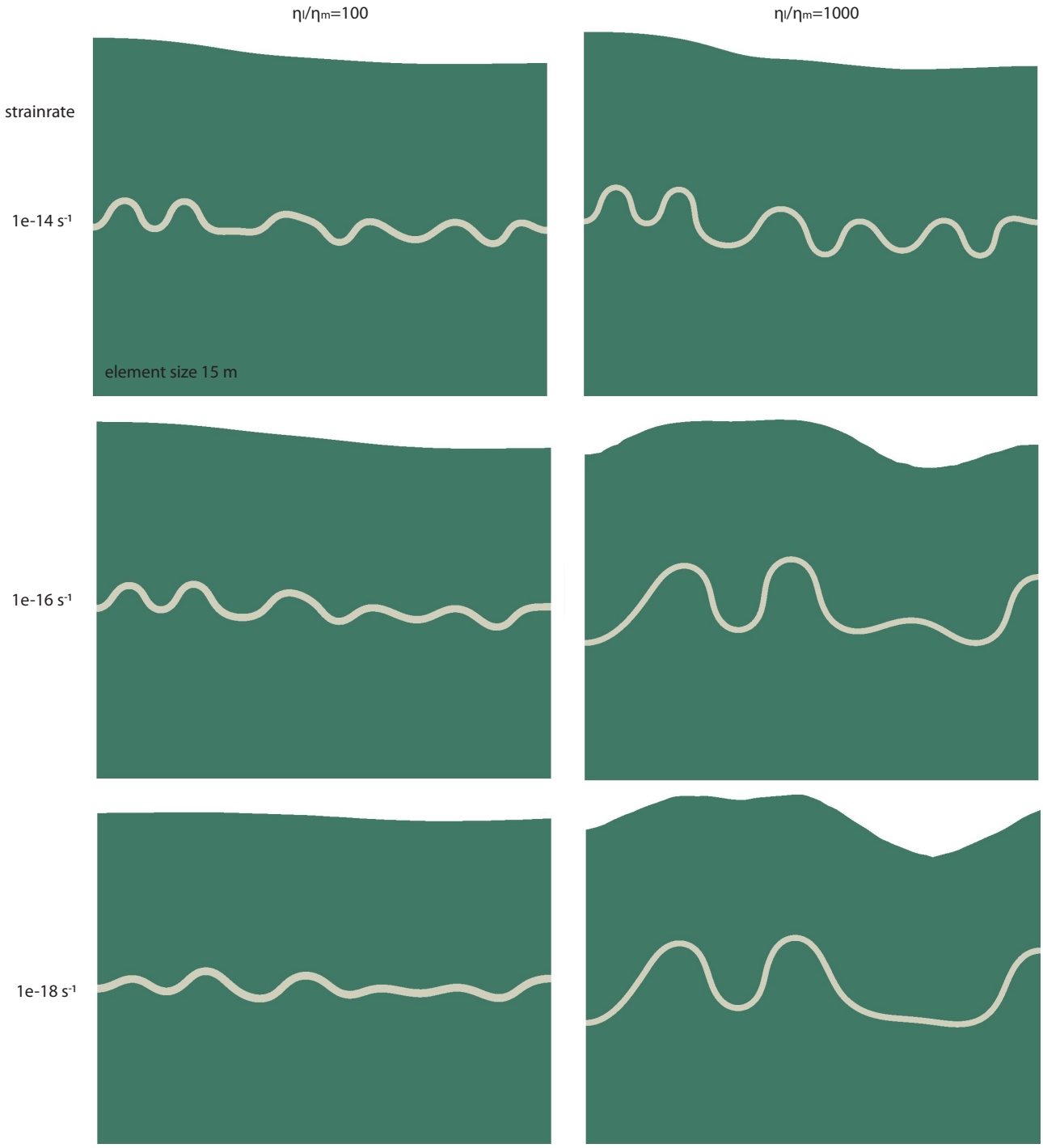


Fig. 7.13: Models with the different viscosity contrast develop different fold wavelength independent of the strain rate except for fast deformation and very high contrasts not reached in the pillow models.

8. Outlook

If we want to fully understand and model salt tectonics, we need a complete understanding of the rheologies of all evaporites present. Right now, empirical flow laws derived from deformation experiments are not fit to fully describe the spectrum of deformation processes under in situ conditions. To solve this issue, two possible approaches can be applied. The best, but also most elaborate solution would be to research and understand all microphysical processes involved. A second comparatively faster approach is to study structures in nature and to estimate the physical parameters that could produce these structures. Nevertheless, the number of unknown variables in nonlinear, repeatedly deformed, natural systems could be overwhelming. The challenge is to find nicely confined and simple natural examples, which could be dissected into single processes and parts to develop new models and test the existing. Although all observations can only witness the final stage of deformation, the evolution could be reconstructed from remnants of older stages, other structures with different maturity and the incorporation of all available information of the local tectonics. In the end, all models have to be tested to be physically correct and apply to realistic boundary conditions. At this stage, physical and numerical modeling is essential to the process. Modelling cannot only be used to test existing hypotheses, it is also a powerful tool to develop new models. Numerical models offer full control of all parameters, material laws, boundary conditions and access to all generated data.

In the process of this work we followed this approach by incorporating a widespread, multiscale dataset of 3D seismic, well logs and drill cores to evaluate the local sedimentation history, local tectonics and the salt body deformation down to the internal microscale processes. Finally, the key observations were combined in numerical simulations, to verify the importance of different components on the internal deformation of mechanically layered salt bodies. In the end, the possibilities of this extensive dataset are still not exhausted and some results can be improved by additional data that is not available yet.

The detailed analysis of the Veendam Pillow provided insights into one of the rare massive bischofite accumulations known. Nevertheless, it is not unique and to study the analogies and differences to other deposits might be of good use. Unfortunately, access to detailed information about other bischofite mines are very limited but more information might be available outside records written in English that are worth the effort.

One painful weakness of the Tr 9 drill core was the missing orientation corresponding to north and the resultant challenge to reconstruct the correct internal structure. If the possibility arises to obtain another core, this information has to be acquired to enable much better interpretations. Also considering new wells in the Veendam area, a good sonic log in combination with reliable elastic prop-

erties could improve the results of seismic inversion and interpretation process. Regardless of missing orientations, the existing Tr-9 core can still be explored further. A trace mineral analysis might offer new insight into the evaporation environment and internal structure of the almost pure bischofite layers. Gamma irradiation of halite samples could be used to analyze the deformation processes further to distinguish different deformation processes of halite outside the K-Mg salt and the thin layered halite inside the K-Mg salts. This information could eventually be incorporated into numerical models to study the internal deformation in greater detail. The calculated models so far, concentrated on the influence of soft and hard layers on the internal deformations of salt bodies. Hence, it was a useful simplification to force the deformation on the structure that was interpreted from the pillow evolution. The next step should be, to allow the free development of salt bodies by simulated sedimentation and regional tectonics. These models can evaluate how the overall salt structure and the development of the overlying strata are influenced by the internal layering, this might be especially interesting if the salt structure is not only passively deformed. By now, some efforts have been made to analyze the influence of folding stringers on the salt body morphology. Analyzing the role of decoupling soft salt layers could be of further interest. The crux of many numerical models are incomplete mechanical properties and rheological equations. Even if they could be reasonably estimated, the quality of the results increases strongly when uncertainties and extrapolation margins can be reduced. In particular, the in situ rheology and paleo behavior of anhydrite is of great interest. One could ask if all deformation took place after the initial gypsum dehydrated to anhydrite or if some early deformation took place before the transformation. The interpretation of the pillow evolution suggests early regional extension, thus an overlap of deformation and anhydrite dewatering is possible. In case of the Veendam Pillow hardly evidence for anhydrite dewatering was found in the Tr-9 core. Further investigations are needed to estimate where and how local the fluids passed through the ZIII salt layers and how the fluids and the possible overpressures influenced the K-Mg salts structure and composition. Besides the influence of mechanical contrast during the deformation of salt, one important question of salt tectonics is the long-term stability of complex deformed and layered salt bodies. This topic is essential to ensure safe storage of highly radioactive waste in salt diapirs. The development of detailed geometric models of suitable salt structures and in situ and paleo stress estimations have to be performed, to test the stability and sensitivity to stress changes of these salt bodies.

In the end, all aspects of salt deformation depend on our understanding of the microphysical processes. A reasonable approach could be to study bischofite deformation as a halite analog. The low viscosity of bischofite allows observations in much shorter time frames and at low stresses. At the same time, processes in the crystal lattice, at the grain boundaries and in grain boundary fluids are taking

place that could be applied to salt deformation in general (For example the evolution of grain boundary fluid films). The challenge is, to produce large grained polycrystalline samples, avoid reactions with humid air and to observe the fast processes before they are overprinted. A combination of cryogenic freezing with light and electron microscopy combined with ion milling, could be a good way to capture and study the acting processes.

9. Zusammenfassung

Das Ziel dieser Arbeit ist das Verständnis über die internen Strukturen und Prozesse in mechanisch geschichteten Evaporitkörpern während der Deformation zu erweitern. Ein besseres Verständnis wird für die Verfeinerung von Salzlagerstättenmodellen, der Reduzierung von Bohrrisiken und für die Vorhersage des Langzeitverhaltens komplexer Salzstrukturen benötigt. Genauer gesagt stellen sich die Fragen: welchen Einfluss haben sehr harte oder weiche Lagen auf die Salzdeformation? Was passiert in Kalium-Magnesium (K-Mg) Salz dominierten Schichten während der Deformation und welche Strukturen werden gebildet? Unter welchen Bedingungen (Rheologien, Viskositätskontraste, Verformungsgeschwindigkeiten, Spannungen, Schichtung oder Deformationphasen) konnten sich die beobachteten Strukturen bilden?

Durch die Synthese von Informationen vom Beckenmaßstab bis zur Mikrostruktur wurde die Entwicklung des Salzkörpers, der lokale Salzfluss, Materialvermengungen, Spannungsindikatoren und Verformungsakkumulation analysiert, auf der Basis existierender rheologischer Modelle und Konzepte der Salztektonik. Hierdurch ergab sich ein Model der Salzdeformation im Veendam Salzkissen unter Betrachtung der lokalen tektonischen Entwicklung sowie ein Model zur Entstehung der außerordentlich mächtigen Bischofit Ansammlungen. Zusätzlich wurde eine feinstratigrafische Analyse der bischofitreichen Zechstein III-1b Schicht mit einer detaillierten Betrachtung der vorhandenen Deformationsstrukturen an einem Bohrkern durchgeführt. Auf der Basis dieser Ergebnisse wurde die Deformation der ZIII Anhydrit/Karbonat (AC) Schicht und der weicheren K-Mg Salzschichten numerisch modelliert. Die produzierten Ergebnisse zeigen den dominierenden Einfluss der verschiedenen Rheologien auf die interne Deformation in dem Salzkissen und die Randbedingungen unter denen die beobachteten Strukturen geformt werden konnten.

Im ersten Abschnitt der Dissertation wird die Entstehung der Veendam und Slochteren Salzkissen am Südrand des Groningen Hochs, in den nördlichen Niederlanden, auf der Grundlage von hochauflösender 3D Seismik und Bohrlochdaten untersucht. Der interne Aufbau der Salzkissen zeigt starke Mächtigkeitsschwankungen der K-Mg salzreichen Zechstein III 1b Schicht, sowie komplexe Bruchmuster und Faltung der ZIII AC Lage. Die interpretierten Mächtigkeitsverteilungen der dem Salz aufliegenden Sedimentschichten wurden herangezogen um den anfänglichen Aufbau des Salzkörpers und die Deformationsgeschichte zu rekonstruieren. Die Ergebnisse legen nahe, dass die lokale Akkumulation hoch konzentrierter Salzsole und die Ablagerung von K-Mg Salzen durch die Existenz einer lokalen Depression in der Zechsteinoberfläche, verursacht durch einen aktiven Graben im Rotliegend, zustande kam. Während der ersten Salzdeformationsphase, ausgelöst durch ungleichmäßige Auflast von Buntsandstein Sedimenten, wurde die ZIII AC Lage boudiniert während die Linse aus Mg-Salz vergleichsweise undeformiert blieb. Es folgte eine konvergente Phase, in der die K-Mg Salzschichten stark in dem sich entwickelnden Salzkissen deformiert wurden. Diese

sehr disharmonische Deformation wurde hauptsächlich durch die Faltung der untergelagerten und fragmentierten ZIII AC Lage beeinflusst und führte zur lokalen Verdickung und internen Deformation der ZIII 1b K-Mg Salzschichten.

Um weitere Informationen über die Zusammensetzung des K-Mg reichen ZIII-1b Schicht zu erlangen wurde aus dem Seismikdatensatz durch Inversion die akustische Impedanz (AI) berechnet. Die ZIII-1b Schicht konnte gut als Körper niedriger akustischer Impedanz identifiziert und interpretiert werden mit einer gesteigerten Auflösung im Vergleich zum originalen Reflektionsdatensatz. Dies führte zur Identifikation von zusammenhängenden Bereichen besonders niedriger AI Werte die auf das Vorhandensein von Bischofit hinweisen. Die Ergebnisse ergaben eine verbesserte Interpretation der ZIII-1b Geometrie, insbesondere in den Bereichen in den der Reflektionsdatensatz von geringer Qualität war. Es ergibt sich, dass Bereiche mit geringen AI Werten in Kombination mit einer lokalen Deformationsanalyse, zur Identifikation von Gebieten mit hohem Magnesium Potential genutzt werden können.

Im zweiten Teil wurde ein Bohrkern von einmaliger Qualität aus der Carnallit und Bischofit reichen ZIII 1b Schicht aus dem Veendam Kissen analysiert. Der in Scheiben geschnittene Kern wurde hochauflösend fotografiert und unter Zuhilfenahme von chemischer Analyse, XRD und optischer Mikroskopie, feinstratigrafisch und strukturell analysiert. Die Ergebnisse zeigten eine starke Verformungskonzentration in den weicheren Bischofit und Carnallit reichen Lagen, assoziiert mit dynamischer Rekristallisation unter geringeren Differenzialspannungen die zur vollständigen Überprägung der Ausganstextur führte. Mechanisch stärkere Schichten die durch Wechsellagerung von Halit und Carnallit geformt wurden, zeigen komplexe und häufig liegende Faltung auf allen sichtbaren Maßstäben. Diese wird oft durch sub-horizontale Scherzonen unterbrochen, welche spröde Deformation mit Kluftfüllungen und Boudinage zeigen. Wir erwarten, dass diese tektonische Fragmentierung mit einer mechanischen Schwächung der gesamten ZIII- 1b Lage einhergeht. Das Ergebnis ist eine tektonische Melange aus Zentimeter bis zehner Meter großen Fragmenten die gefaltet und boudiniert sind. Wir gehen davon aus, dass diese Strukturen und Prozesse häufig in deformierten mit starken rheologischen Kontrast geschichteten Evaporiten anzutreffen sind.

Im letzten Abschnitt wurden auf die grundlegenden Komponenten des Venndam Salzkissen vereinfachte nummerische 2D Modelle berechnet um den Einfluss und das Verhalten von härteren und weicheren Schichten während der Salzdeformation zu analysieren. Die Ergebnisse zeigen, dass die vorgebrochene härtere Anhydrit Schicht während der Entwicklung des Veendamkissens im Zentrum der Struktur gefaltet wird und sich die einzelnen Fragmente übereinander schieben. Abhängig von der Viskosität der härteren Lage wird die Verkürzungen eher durch Faltung oder durch das Übereinanderschieben kompensiert. Es ist anzunehmen, dass die Spannungsexponenten von Halit und Anhydrit voneinander abweichen. Aus diesem Grund können wir erwarten, dass ihr effektiver

Viskositätskontrast von der Deformationsgeschwindigkeit abhängt. Unter diesen Bedingungen können starke Abweichungen in der Verformungsgeschwindigkeit des Salzkissens zu unterschiedlich dominanten Wellenlängen der Anhydrit Faltung führen. Die Modelle ergeben den Rückschluss, dass die Faltung der ZIII-AC Schicht wie sie im Veendamkissen sichtbar ist, unter einem Viskositätskontrast von ca. 100 zwischen Halit und Anhydrit erfolgte. Sowohl die weichen K-Mg Salz Schichten als auch der viel härtere Anhydrit beeinflussen die Deformation und den Salzfluss in dem Kissen. Ein Großteil der Deformation wird in den weichen Schichten akkumuliert, was zu stärkeren Deformation der Umgebung und zu beträchtlichen Deformationen in den Schichten selber führt. Während es durch die Konzentration der Verformung in den weichen Schichten in manchen Bereichen des Salzkörpers zu erhöhter Deformation kommt, können andere Bereiche von der Deformation durch die weichen Gleitschichten abgeschirmt werden. Dies bedeutet, dass eine kompetente Schicht wie der ZIII Anhydrit stärker deformiert wird, wenn er sich in der Nähe einer sehr weichen Schicht und auf der Seite der Hauptdeformation befindet. Andererseits ist die Deformation und Struktur der weichen K-Mg Salzlagen stark von der Faltung der härteren Schicht geprägt. Dies führt zur Auspressung von K-Mg Salzen über Anhydrit Erhöhungen in Gebiete über Anhydrit Vertiefungen.

10. Summary

The aim of this work is to improve our understanding of the internal structures and dynamics inside mechanically layered evaporite bodies during deformation. A better understanding is needed to improve salt reservoir models, reduce drilling risks and to understand the long-term behavior of complex salt structures.

In detail, we address the questions: What is the influence of extreme soft or much harder layers during deformation? What happens during this deformation inside K-Mg salt dominated layers and which structures are formed? Under which conditions (rheology, viscosity contrast, strain rates, stresses, layering, multiphase deformation) can the observed structures be formed?

With the synthesis of data from basin to micro scale structures, the salt body evolution, local salt flow, material mixing, stress indicators, strain concentration was analyzed based on existing rheology models and concepts of salt body deformation. Thus, a model of salt deformation inside the Veendam salt pillow in the framework of local tectonics was developed together with a concept of conditions leading to the local extreme accumulation of bischofite. A fine stratigraphic analysis of the bischofite rich ZIII-1b layer was performed with a detailed examination of the existing deformational structures. Based on these results, the deformation of the ZIII-AC stringer was modeled revealing the influence on the internal deformation and the boundary conditions to produce the observed structures.

In the first part, the evolution of the Veendam and Slochteren salt pillows at the southern boundary of the Groningen High, northern Netherlands is studied with high-resolution 3D seismic and well data. The internal structure of the two salt pillows shows areas in which the K-Mg salt-rich ZIII 1b layer is much thicker than elsewhere, in combination with a complexly ruptured and folded ZIII Anhydrite - Carbonate stringer. Thickness maps of supra-salt sediments and well data are used to infer the initial depositional architecture of the K-Mg salts and their deformation history. Results suggest that faulting and the generation of depressions on the top Zechstein surface above a Rotliegend graben caused the local accumulation of bittern brines and precipitation of thick K-Mg salts. During the first phase of salt flow and withdrawal from the Veendam area, under the influence of differential loading by Buntsandstein sediments, the ZIII stringer was boudinaged while the lens of Mg salts remained relatively undeformed. This was followed by a convergence stage, when the K-Mg salt-rich layers were deformed within the inflating salt pillows. This deformation was strongly disharmonic and strongly influenced by folding of the underlying, ruptured ZIII stringer, leading to thickening and internal deformation of the K-Mg salt layers.

To gain further information about the composition of the K-Mg salt rich ZIII-1b a seismic inversion was performed in order to obtain calibrated acoustic impedance values whilst at the same

time improving the temporal resolution compared to the reflectivity dataset. After seismic inversion, the structure of the Zechstein III- 1b subunit could be identified as a low acoustic impedance body. This led to the definition of bodies within the ZIII – 1 b subunit that exhibit low and connected AI values, a strong indicator for the presence of bischofite. Results show that the interpretation of AI data refined the geometric model of the salt body's structure especially in areas where the original reflection data quality was weak. Layer thicknesses conducted from the interpretation correlate reasonably with thicknesses measured in wells. We suggest that areas of low AI values, in combination with an analysis of local deformation structures can be used, to identify the most prospective areas of high magnesium content

In the second part, we analyzed a unique Tr-9 carnallite- and bischofite- rich drill core from the Zechstein III-1b subunit in the Veendam Pillow in the Netherlands. The slabbed core was analyzed by macroscale photography, bulk chemical methods, XRD and optical microscopy. Results show high strain in the weaker bischofite- and carnallite- rich layers, with associated dynamic recrystallization at very low differential stress, completely overprinting the original texture. Stronger layers formed by alternating beds of halite and carnallite show complex recumbent folding on different scales commonly interrupted by sub-horizontal shear zones with brittle deformation, veins and boudinage. We attribute this tectonic fragmentation to be associated with a softening of the complete ZIII-1b subunit during its deformation. The result is a tectonic mélange with cm - to 10m size blocks with internal folds and boudinage. We infer that these structures and processes are common in deformed, rheologically strongly stratified evaporites.

In the last part simplified 2D plain strain models containing the key components of the Veendam Pillow were performed to analyze the influence and behavior of hard and soft layers on the internal deformation. The results show that the pre-fractured stringer is folded and thrusted in the pillow center during the development of the pillow. Depending on the viscosity of the stringer, the shortening is either compensated by folding or thrusting. We supposed that the stress exponent of halite and stringer deformation are most likely not the same and we could therefore expect a strain dependency of the effective viscosity contrast. Under this conditions, strong strain-rate changes during the pillow evolution could produce different dominant wavelengths. Fold analysis can therefore be used to estimate the in-situ rheology of stringers or if the in situ rheology of anhydrite and salt is well known, might be used to estimate the in situ strain rates. We concluded from the models that the folding of the ZIII-AC observed in the Veendam pillow indicates an effective velocity contrast of about 100 between the stringer and the halite. Nevertheless, a much larger wavelength folding could have been produced by early slow deformation forming the large syncline in the NE of the Veendam

Pillow. Both soft K-Mg salt layers and strong stringers influence the deformation and salt flow inside the salt pillow. Strain is accumulated in the soft layers leading to stronger salt flow near these layers and extensive deformation inside of them. Thus, if a soft layer is present near a stringer, it will experience more deformation. On the other hand, the structure of the soft K-Mg salt layers and the salt flow inside of them is strongly influenced by folding of a harder stringer. Thus, the soft K-Mg salts are withdrawn from areas above stringer anticlines to areas above stringer synclines.